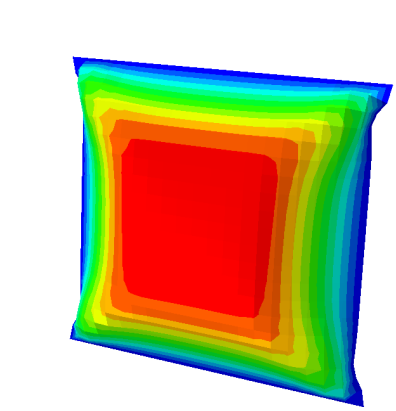

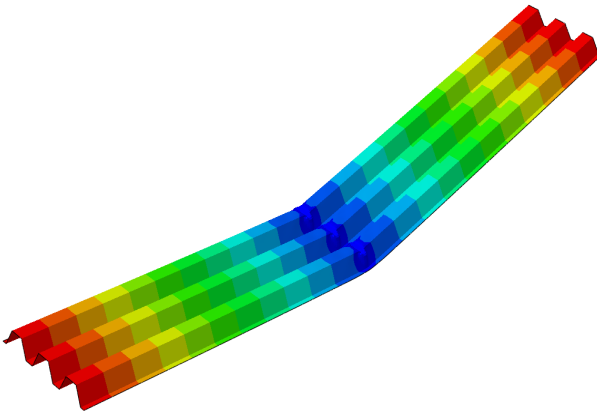

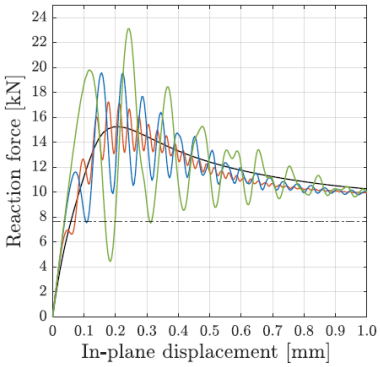

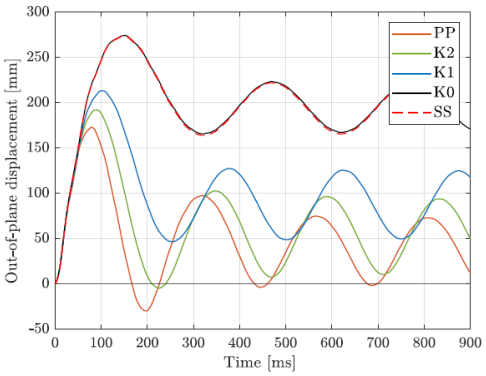

Structural response in thin-walled steel structures subjected to dynamic loading

Master's Thesis in the Master's Program Structural Engineering and Building Technology

LUCAS ANDRÉN

JAKOB ENGSTRÖM

DEPARTMENT OF ARCHITECTURE AND CIVIL ENGINEERING
DIVISION OF STRUCTURAL ENGINEERING

CHALMERS UNIVERSITY OF TECHNOLOGY
Master's thesis ACEX30
Gothenburg, Sweden 2025

MASTER'S THESIS ACEX30

Structural response in thin-walled steel structures subjected to compressive axial dynamic loading

Master's Thesis in the Master's Programme Structural Engineering and Building Technology

LUCAS ANDRÉN
JAKOB ENGSTRÖM

Department of Architecture and Civil Engineering
Division of Structural Engineering
Lightweight Structures
CHALMERS UNIVERSITY OF TECHNOLOGY
Gothenburg, Sweden 2025

Structural response in thin-walled steel structures subjected to dynamic loading

Master's Thesis in the Master's Programme Structural Engineering and Building Technology

LUCAS ANDRÉN
JAKOB ENGSTRÖM

Supervisor: Morgan Johansson, Norconsult
Examiner: Mohammad Al-Emrani, Department of Architecture and Civil Engineering

Examensarbete ACEX30
Institutionen för Arkitektur och Samhällsbyggnadsteknik
Chalmers Tekniska Högskola, 2025

Department of Architecture and Civil Engineering
Division of Structural Engineering
Lightweight Structures
Chalmers University of Technology
SE-412 96 Göteborg
Sweden
Telephone +46 31 772 1000

Cover:
To the left, the deformed shape (out-of-plane displacement) is shown and the response for a plate with a thickness of 1 mm subjected to different loading speeds. To the right, the the deformed shape for a CSM strip is shown and the dynamic response when different boundary conditions are used.
Department of Architecture and Civil Engineering
Göteborg, Sweden, 2025

Thin-walled steel structures subjected to dynamic loading
Master's thesis in the Master's Programme Structural Engineering and Building Technology

LUCAS ANDRÉN

JAKOB ENGSTRÖM

Department of Architecture and Civil Engineering
Division of Structural Engineering
Lightweight Structures
Chalmers University of Technology

ABSTRACT

As Swedish cities become increasingly dense, the distance between transportation routes and adjacent buildings decreases, heightening concerns about the potential effects of exceptional events on nearby structures, such as explosions originating from transport corridors. Structural members designed for static loads may not be suitable for dynamic loads from explosions. An example of such a structural member is corrugated sheet metal (CSM), commonly used in roofing applications. CSM falls into the category of thin-walled elements, meaning that it has a limited load capacity due to buckling. This also limits the capacity to resist dynamic loads from explosions, posing a risk to the overall structural integrity of the building. Current calculation methods may be overly conservative due to simplified and/or limited understanding of the post-buckling behaviour of CSM.

This thesis aims to investigate the structural response of thin-walled steel structures subjected to static and dynamic loading. Simplified models, consisting of steel plates classified into various cross-section categories and subjected to axial loading under both static and dynamic conditions, were employed to explore the fundamentals of dynamic buckling. Once the fundamentals of dynamic buckling had been investigated, a more complex geometry was analysed, involving a simplified CSM section. The methodology is based on numerical analyses conducted using the finite element software Abaqus CAE. The results were validated through comparison with analytical expressions derived from the Eurocode.

Findings from numerical analyses reveal that the structural response of both the steel plates and the CSM strip is primarily governed by buckling. At higher loading rates, the material exhibits a rate-dependent strengthening effect evident as an increased critical buckling load in the steel plates and reduced deflection in the CSM strip. Inertia effects, manifested as dynamic oscillations, become more pronounced at elevated strain rates, with their onset occurring earlier for slender structures. Increased slenderness and/or initial imperfections lead to a reduction in load-bearing capacity. Additionally, larger initial imperfections contribute to reducing the amplitude of dynamic oscillations.

Key words:
Steel plate, Buckling, Dynamic buckling, CSM, Explosions, Non-linear FE-analysis, Impulse load, Static loading, Dynamic loading

Tunnväggiga stålkonstruktioner utsatta för dynamisk last
Examensarbete inom masterprogrammet Konstruktionsteknik och Byggnadsteknologi

LUCAS ANDRÉN

JAKOB ENGSTRÖM

Institutionen för arkitektur och samhällsbyggnadsteknik
Avdelningen för konstruktionsteknik
Lättviktskonstruktioner
Chalmers tekniska högskola

SAMMANFATTNING

I takt med att svenska städer förtätas minskar avståndet mellan transportleder och intilliggande byggnader, vilket ökar oron för effekterna av exceptionella händelser, såsom explosioner från transportkorridorer på närliggande konstruktioner. I sådana scenarier är korrugerad plåt (TRP), som ofta används i takkonstruktioner, särskilt utsatt. Dessa tunnväggiga element har begränsad kapacitet att motstå dynamiska laster, vilket kan äventyra byggnadens strukturella integritet. Dagens beräkningsmetoder kan dessutom vara alltför konservativa på grund av begränsad förståelse för efterbucklingsbeteende.

Detta examensarbete syftar till att undersöka den strukturella responsen hos tunnväggiga stålkonstruktioner. Förenklade modeller, bestående av stålplåtar klassificerade enligt olika tvärsnittsklasser och utsatta för axiell belastning under både statiska och dynamiska förhållanden, används för att studera grunderna i dynamisk buckling. När dessa grundläggande mekanismer analyserats studerades en mer komplex geometri bestående av en förenklad TRP-plåt. Metodiken baserades på numeriska analyser med finita elementprogrammet Abaqus CAE. Resultaten validerades genom jämförelse med analytiska uttryck hämtade från Eurocode.

Resultat från de numeriska analyserna visar att den strukturella responsen hos både stålplåtar och korrugerad plåt huvudsakligen styrs av buckling. Vid högre lastningshastigheter uppvisar materialet en hastighetsberoende förstärkningseffekt, genom en ökad kritisk knäcklast för stålplåtarna och minskad deformation hos TRP-sektionen. Tröghetseffekter i form av dynamiska svängningar blir tydligare vid höga deformationshastigheter, där deras uppkomst sker tidigare för slanka konstruktioner. Ökad slankhet och/eller initiala imperfektioner leder till en minskning i bärförmåga. Dessutom bidrar större initiala imperfektioner till att dämpa amplituden hos de dynamiska svängningarna.

Nyckelord:
Stålplåt, Buckling, Dynamisk buckling, TRP, Explosioner, Icke-linjär FE-analys, Impulslast, Statisk last, Dynamisk last

Contents

Preface

This thesis investigates the structural response of thin-walled steel structures subjected to dynamic loading. It contributes to ongoing research on impulse-loaded structural systems within the field of structural engineering at Chalmers University of Technology. The work was conducted in collaboration between Norconsult and Chalmers during the period January to June 2025.

We would like to thank our supervisor, Morgan Johansson at Norconsult, for his guidance and support. His expertise in explosion loads has been valuable to the development of this work. We are also grateful to our examiner, Mohammad Al-Emrani from the Department of Lightweight Structures, for his helpful insights into steel structures.

Finally, we extend our thanks to the staff at the Bridge and Structural Analysis division at Norconsult in Gothenburg for their hospitality and for providing a supportive environment throughout the course of this thesis.

Gothenburg, June 2025
Lucas Andrén and Jakob Engström

Notations

Abbreviations

AI	Artificial Intelligence
BC	Boundary Condition
CAE	Computer Aided Engineering
C-S	Cowper-Symonds
CSM	Corrugated Sheet Metal / Corrugated Sheet Steel
CSC	Cross-section class
DLF	Dynamic Load Factor
DOF	Degree of Freedom
EC	Eurocode
FE	Finite Element
FEM	Finite Element Method
J-C	Johnson-Cook
LT	Lateral Torsional
LPF	Load Proportionality Factor
NDOF	Number of Degrees of Freedom
NLGEOM	Non-linear Geometry
NLA	Non-linear Analysis
S4R	Four-node Quadrilateral Shell Element
SDOF	Single Degree of Freedom
S.R	Strain Rate / Strain Rate Effect
TRP	Trapetskorrugerad plåt
TNT	Trinitrotoluene
DIF	Dynamic Increase Factor
DIF_i	Dynamic Increase Factor at Specific Strain
DIF_u	Dynamic Increase Factor for the Ultimate Strength
DIF_y	Dynamic Increase Factor for the Yield Strength
DIF_{avg}	Average Dynamic Increase Factor

Roman upper case letters

A	Area / Surface area / Material constant / Amplitude
A_{cs}	Cross-section Area
A_{eff}	Effective Area
B	Material Constant
C	Damping Matrix / Material Constant
D	Material Constant
D_{avg}	Material Constant Based on Average Increase of Strength
D_y	Material Constant Based on Dynamic Increase of Yield Strength
E	Elastic Modulus
E_k	Kinetic Energy
F	Force
$F(t)$	External Time-dependent Force / Impulse Load
$F(u)$	External Displacement-dependent Force
$F_{cr,dyn}$	Critical Dynamic Buckling Force
F_k	Characteristic Force / Characteristic Pressure Load
F_y	Force That Causes Yielding
I	Impulse / Second Moment of Inertia
I_{eff}	Effective Second Moment of Inertia for Cross-Sections in CSC4
I_k	Characteristic Impulse
K	Stiffness Matrix / Tangent Stiffness
L_{cr}	Critical Buckling Length
M	Mass Matrix / Moment
N	Normal Force
$N_{\mathrm{cr}}^{\mathrm{dyn}}$	Dynamic Critical Buckling Load
$N_{\mathrm{cr}}^{\mathrm{stat}}$	Static Critical Buckling Load
$P(t)$	External Time-dependent Pressure
P_{cr}	Critical Buckling Load
P_{max}	Maximum Load
Q	Equivalent Static Load
R	Internal Resisting Force / Reaction Force / Plastic Resistance / Rotation Matrix
$R(u)$	Internal Displacement-dependent Resisting Force
$RF2$	Reaction Force in Y-direction in Abaqus
$S1$	CSM Geometry 1
$S2$	CSM Geometry 2
$S3$	CSM Geometry 3
T	Temperature
T^*	Dimensionless Temperature
T_m	Melting Temperature
T_r	Room Temperature
U_{mag}	Magnitude of displacement
$U1$	Displacement in X-direction in Abaqus
$U2$	Displacement in Y-direction in Abaqus
$U3$	Displacement in Z-direction in Abaqus
$U_{u,dyn}$	Dynamic Ultimate In-plane Displacement
V	Velocity

V_0	Initial Velocity
W	Section modulus
W_{eff}	Effective Section Modulus for Cross-Sections in CSC4
W_E	External Work
W_I	Internal Work
X	Deflection Limit

Roman lower case letters

a	Height
b	Width
b_{eff}	Effective Width
e	Initial Imperfection
$f_{0.2}$	0.2 Offset Yield Strength
f_u	Ultimate Strength
$f_{u,A}$	Ultimate Strength for Material A
$f_{u,B}$	Ultimate Strength for Material B
$f_{u,C}$	Ultimate Strength for Material C
$f_{u,D}$	Ultimate Strength for Material D
f_y	Yield Strength
$f_{y,A}$	Yield Strength for Material A
$f_{y,B}$	Yield Strength for Material B
$f_{y,C}$	Yield Strength for Material C
$f_{y,D}$	Yield Strength for Material D
$f_{u,dyn}$	Dynamic Ultimate Strength
$f_{y,dyn}$	Dynamic Yield Strength
h	Height
i	Impulse Density
k	Spring Stiffness / Buckling Coefficient
m	Mass / Number of Half Sine Waves / Material Constant
n	Material Constant
p	Material Constant
p_{avg}	Material Constant Based on Average Increase of Strength
p_y	Material Constant Based on Dynamic Increase of Yield Strength
q	Material Constant
s_{eff}	Effective width of compressed part in CSM section
t	Thickness / Time
u	Displacement / In-plane Displacement
u_{el}	Elastic Displacement
u_{pl}	Plastic Displacement
v	Velocity
w	Out-of-plane Displacement
w_0	Initial Imperfection

Greek letters

Δt	Time Increment
$\Delta t_{initial}$	Initial Time Increment
Δt_{max}	Maximum Time Increment
Δt_{min}	Minimum Time Increment
ϵ	Strain
ϵ^*	Relative Strain Rate (divided by Reference Strain Rate)
ϵ_{eng}	Engineering Strain
ϵ_{sh}	Strain Hardening Strain
ϵ_{su}	Ultimate Steel Strain
ϵ_{true}	True Strain
ϵ_s	Steel Strain
$\dot{\epsilon}$	Strain Rate
$\dot{\epsilon}_0$	Reference Strain Rate
$\dot{\epsilon_{pl}}$	Plastic Strain Rate
λ	Eigenvalue / Slenderness
$\bar{\lambda}$	Relative Slenderness
$\bar{\lambda}_p$	Relative Plate Slenderness
$\bar{\lambda}_{LT}$	Relative Slenderness for Lateral Torsional Buckling
ν	Poisson's Number
ρ	Reduction Factor / Density
σ	Stress
σ_d	Dynamic Stress
σ_i	Stress at Specific Strain
σ_{cr}	Critical Stress
σ_{dyn}	Dynamic Stress
σ_{eng}	Engineering Stress
σ_{max}	Maximum Stress
σ_s	Steel Stress / Static Stress
σ_{true}	True Stress
σ_u	Ultimate Stress
$\sigma_{u,dyn}$	Dynamic Ultimate Stress
σ_y	Yield Stress
$\sigma_{y,dyn}$	Dynamic Yield Stress
χ	Reduction Factor
ω_{u}	Ultimate Out-of-plane Displacement
$\omega_{\mathrm{u,dyn}}$	Dynamic Ultimate Out-of-plane Displacement

1 INTRODUCTION

1.1 Background

As Swedish cities become increasingly dense, the distance between transportation routes and adjacent buildings decreases, heightening concerns about the potential effects of exceptional events on nearby structures, such as explosions originating from transport corridors. Structural members designed for static loads may not be suitable for dynamic loads from explosions. An example of such a structural member is corrugated sheet metal (CSM), commonly used in roofing applications. CSM falls into the category of thin-walled elements, meaning that it has a limited load capacity due to buckling. This also limits the capacity to resist dynamic loads from explosions, posing a risk to the overall structural integrity of the building. Current calculation methods may be overly conservative due to simplified and/or limited understanding of the post-buckling behaviour of CSM.

When exposed to compressive axial stresses, there is a risk that CSM buckles, leading to low deformation capabilities and reducing its energy absorption potential, which is a critical factor under dynamic loading. Further studies are necessary to better understand the post-buckling behaviour of current CSM structures under dynamic loads to see if it is possible to utilise a higher energy absorption capacity.

Under static loading, the structural response depends on factors such as material properties, slenderness, and initial imperfections. However, for dynamic loading, changes in material properties due to high strain rates (e.g., increased yield strength) and dynamic effects (e.g., inertia) may have an important influence. Key parameters of interest include structure slenderness, initial imperfections, material properties (including strain-rate effects), and load rates.

1.2 Similar previous Master's Thesis's at Norconsult

This master's thesis is the third conducted at Norconsult within the same subject area. In 2023, a numerical study was performed on a simply supported steel plate subjected to axial dynamic loads (Gerard & Larsson, 2023), and compared against a previously conducted experimental study on the same topic (Paik & Thayamballi, 2003a). Inconsistencies were found when comparing the results.

In 2024, a simplified model involving thin steel rods subjected to axial loads under both quasi-static and dynamic conditions was analysed to better understand the fundamentals of dynamic buckling (Sargsyan & Sargsyan, 2024). This study combined experimental testing with numerical analyses using the FE software Abaqus CAE, and demonstrated strong correlation between the two.

Building on the previous theses, this work aims to address the research questions presented in Section 1.3.

1.3 Aim and objectives

The aim of this master's thesis is to enhance the understanding of the structural response of thin-walled steel structures subjected to dynamic loading. A potential

application of this knowledge is to analyse the structural response of complex structures, such as CSM. To achieve this, it is first essential to understand the behaviour of simple structures, therefore plain steel plates subjected to compressive axial dynamic loads were initially studied. Once the fundamentals of dynamic buckling had been investigated, a more complex geometry was analysed, involving a simplified CSM section.

To achieve this goal, the following research questions are addressed:

- How can the effective stiffness at maximal load be accurately described when the structure buckles?
- What are the differences in response when the specimen is subjected to static versus dynamic loading?
- What effects, if any, occur under very rapid loading (e.g., explosion loads)?
- How do geometry, initial imperfections, material parameters, and dynamic effects (inertia and strain-rate effects) influence structural response?

To answer these research questions, the following specific objectives are formulated:

- Investigate the structural response of a compressed thin-walled structure using a simplified model, involving a plain steel plate subjected to compressive axial loads under both quasi-static and dynamic conditions.
- Analyse the combined influence of parameters on the structural behaviour of the studied plate(s), including strain-rate and inertia effects (dynamic effects), geometric initial imperfections, slenderness, and boundary conditions.
- Investigate the structural response of a thin-walled CSM structure subjected to distributed transversal loads under both quasi-static and dynamic conditions.

1.4 Limitations

The study is based on finite element (FE) modelling using Abaqus. Initially, to reduce complexity and facilitate potential future experiments, only the critical part of the CSM was considered, the compressed flange. The flange was simplified as a rectangular plate, laterally supported along its transverse edges, and allowed to deform out-of-plane under both static and dynamic axial loading. Finally, a simplified CSM strip without longitudinal stiffeners was analysed under static and dynamic loading.

1.5 Methodology

The three methods used in this project are a literature study, analytical analysis and numerical analysis.

The literature study aims to provide a deeper understanding of the topic, focusing on steel structures, dynamics and explosions, strain-rate effects, and related areas. It will also include a review of previous work on the subject.

The purpose of the analytical analysis is to validate the numerical analysis results and provide input for the Abaqus simulations.

The numerical analysis investigated the effects of quasi-static and dynamic loading on the simplified models. Both non-linear geometry and non-linear material behaviour was considered, using the FE-software Abaqus.

1.6 Use of AI in this project

AI can be a valuable tool in technical report writing when used judiciously to improve efficiency and clarity. It can assist with grammar, style, and formatting, helping to ensure that the text is both professional and easy to read. However, it is not suitable to use AI as a primary source of information, as the accuracy and originality of generated content cannot be guaranteed. AI-generated material may contain factual errors or misleading statements, and therefore requires careful verification.

In this report, AI has only been used to support visualization, automatically format equations, tables, and figures, and improve grammar for enhanced readability. It has not been used as a substitute for subject matter expertise or critical thinking.

2 THEORY

2.1 Explosions

2.1.1 What is an explosion

An explosion is defined as a sudden release of potential energy that is transformed into kinetic energy and ultimately into mechanical work (Johansson and Laine (2012a)). A common type includes gas explosions and detonations from explosives such as TNT, where the potential energy originates from a chemical reaction that releases heat and raises the temperature, leading to overpressure in the surrounding air. Alternatively, the source may be mechanical, such as the sudden release of compressed gas from a pressurised vessel (Johansson and Laine, 2012a). The potential energy is converted into kinetic energy due to the pressure difference between the gas and the surrounding air, causing the gas to expand outward from the explosion centre in an attempt to equalise the pressure. When the overpressure wave encounters objects such as buildings, it performs mechanical work, potentially causing structural damage.

The classification of strain rate is presented in Figure 2.1. Static loads has a strain rate of around 10^{-5} while the shock wave from an explosion results in a strain rate of around 10^{4}, around 10^{9} times higher than static loads. The high loading speed in combination with the change of the structure's material properties, see Section 2.1.4, may result in different structural response compared to the static load, highlighting the importance of dynamic loads such as explosions in structural design.

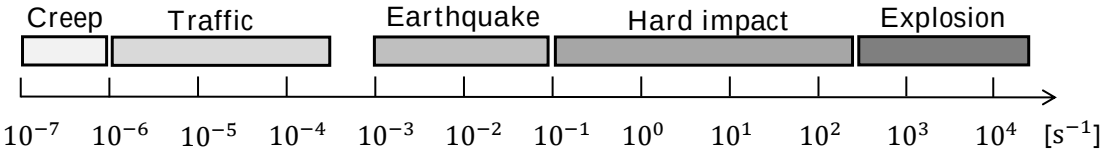

Figure 2.1: Classification of strain rates for different actions, explosions being way faster than any other load presented. Figure based on Yang et al. (2020).

2.1.2 Shock wave expansion

To get a better understanding of the explosion timeline the shock wave in a point within the blast zone can be visualized against time, see Figure 2.2. The shock wave expands outwards from the explosion center in a circular pattern and the energy is reduced in the shock wave front with increasing distance (Johansson and Laine, 2012a). The peak overpressure is reached just behind the shock wave front at the time of arrival, t_a, and then rapidly reduce with time until it reaches normal air pressure, P_0. The positive overpressure is considered most critical and used in explosion assessments while the negative pressure is neglected (Johansson and Laine, 2012a).

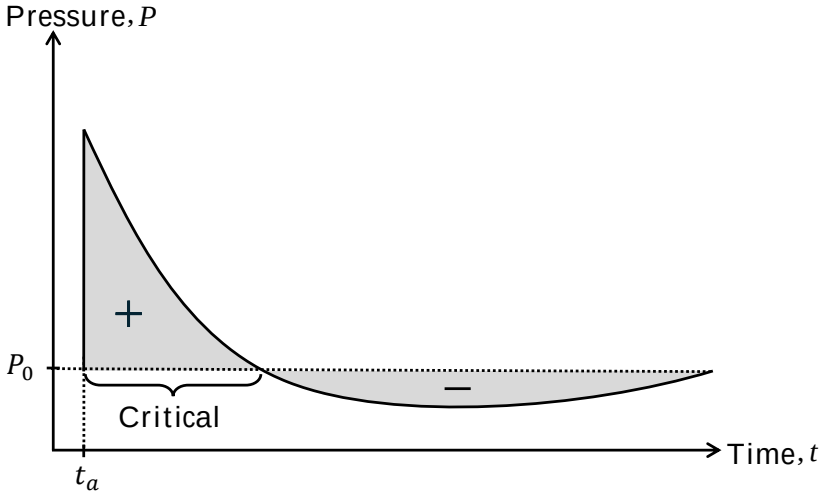

Figure 2.2: Ideal pressure-time curve for a blast wave caused by an explosion. Figure based on Johansson and Laine (2012a).

2.1.3 Explosion as an impulse load

To understand how a structure is affected by the shock wave the concept of impulse is introduced. Impulse I is defined as the change in a body's momentum due to a force $F(t)$ acting on it during a certain time interval $t_1 < t < t_2$ (Johansson and Laine, 2012b). The impulse is simply obtained by integrating the force with respect to the time, see Equation (2.1).

$$I = \int_{t_1}^{t_2} F(t)\, dt \tag{2.1}$$

To relate impulse to the shock wave, impulse density i is used. Impulse density is similar to impulse except that the force is applied as a pressure $P(t)$ on the body surface area A, see Equation (2.2).

$$I = A \cdot i = A \cdot \int_{t_1}^{t_2} P(t)\, dt \tag{2.2}$$

In an explosion, the load duration is short whereas the pressure is large. Johansson and Laine (2012b) thus concludes that the impulse load from an explosion often is similar to that of the characteristic impulse load I_k with infinitesimal load duration and infinitely large pressure, rather than the characteristic pressure load with infinite load duration and pressure amplitude P_k, see Figure 2.3.

Figure 2.3: Dynamic load cases starting at t_1, Characteristic impulse I_k and characteristic pressure load F_k. Figure based on Johansson and Laine (2012b).

2.1.4 Structural response

Dynamic loads can cause a delayed response in a structure compared to static loads because it takes time for the load to propagate through the material (Johansson and Laine, 2012b). If the impulse is large enough there is a risk of local failure before any other part of the structure has even responded to the load. The structure fails to redistribute the forces to adjacent parts and a major part of the load is resisted by only a small part of the structure. Conversely, if the load duration is longer, the structure has more time to redistribute the forces, resulting in a different overall response. Thus, the boundary conditions can be said to be time-dependent (Johansson and Laine, 2012b). Figure 2.4 illustrates the structural response of a impulse loaded frame structure. Initially, only the left column is affected but as time increases the other parts are affected as well.

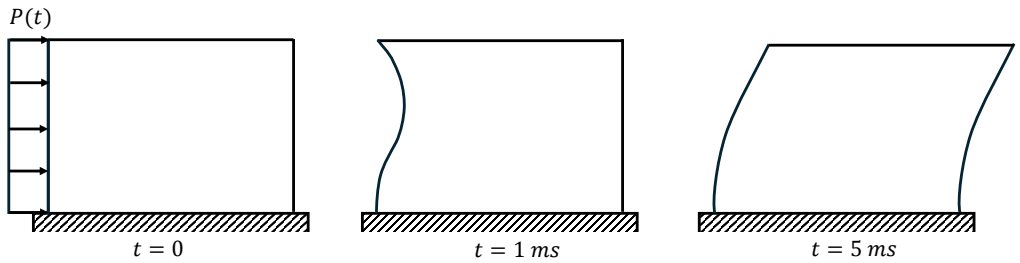

Figure 2.4: Delayed response in structure subjected to an impulse load with pressure $P(t)$. Figure based on Johansson and Laine (2012b).

Another characteristic of dynamic loading is that the reaction force at full load amplitude does not necessarily represent the actual imposed load. For a simply supported beam subjected to a dynamic load, the reaction force at one support can be described using Equation 2.3

$$R_{support} = \alpha R(t) + \beta F(t) \tag{2.3}$$

Where $R_{support}$ is the dynamic reaction force, $R(t)$ is the static reaction force that would result if the same load were applied statically, and $F(t)$ is the external time-dependent load. The coefficients α and β depend on the deflected shape of the beam and its dynamic response characteristics. Compared to the static case, where the reaction force is simply half of the external load for symmetric loading, the dynamic response includes an additional contribution due to mass inertia, represented by the term involving$F(t)$. This results in a reaction force that differs from the purely static value.

2.1.5 Energy absorption

To withstand dynamic loads, a structure must efficiently absorb and redistribute the energy from the load. This is achieved through ductile behaviour, allowing the structure to absorb energy effectively through controlled deformation.

According to Johansson and Laine (2012b) the ability of a structure to absorb energy can be explained using the energy balance between external and internal work. Work is a measure of energy and can in a simple context be defined as the work (energy) done by a force F when moving a point a distance u.

The impulse results in an external load F that transfers kinetic energy to the structure that can be seen as an applied external work W_e. Simultaneously, the structure deforms and energy is absorbed by the structure internally through internal forces R, described as an internal work W_i (internal energy absorption capacity). Since the structure is fixed in space the boundary conditions induce internal forces that result in either elastic or elasto-plastic deformation, thus absorbing the energy through deformation. The work can be seen as the area under the force-displacement relation (Johansson and Laine, 2012b), see Figure 2.5. If $W_i >= W_e$ the structure is able to absorb the external energy, however if $W_i < W_e$ the excess energy may cause structural collapse or failure.

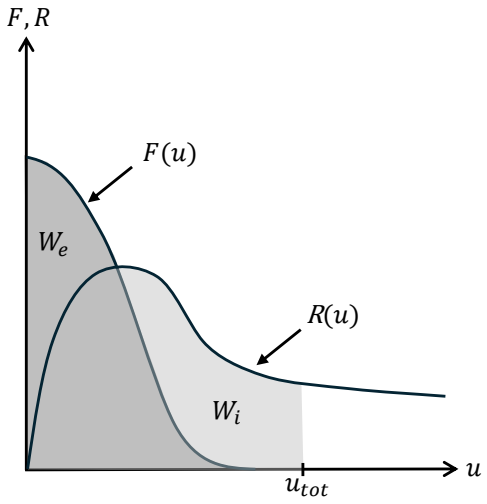

Figure 2.5: Internal and external work defined as the area under the external force-displacement relation $F(u)$ and internal force-displacement relation $R(u)$. Figure based on Johansson and Laine (2012b).

2.1.6 Influence of mass

The kinetic energy of a body subjected to an impulse load I can be described by Equation (2.4) (Johansson and Laine, 2012b) :

$$E_k = \frac{I^2}{2m_{ef}} \tag{2.4}$$

Where m_{ef} is the effective mass of the body, see Section 2.1.8. It can be seen that an increase in mass reduces the applied kinetic energy, thus reducing the applied external work. Increasing the mass of the structure is thus beneficial for dynamic loading since it results in reduced need for energy absorption.

2.1.7 Influence of stiffness, strength, and deformability

For static loads a high load capacity with low deformation is opted for. For dynamic loads however it is seldom possible to ensure that the load experienced by the structure will always remain below the maximum static load capacity (Johansson and Laine, 2012b). The design focus shifts to leveraging the structure's deformability to dissipate energy and prevent failure.

Energy absorption is governed by the structures ability to deform, thus a lower load capacity with good deformation capabilities prior to failure results in a higher energy absorption compared to the case when a structure is designed to withstand static loading, i.e. have a high load bearing capacity and limited deformations. (Johansson and Laine, 2012b), see Figure 2.6. This highlights the importance of ductile behaviour which is governed by the amount of plastic deformation before failure. Ductility is material dependant and has to be taken into consideration in design.

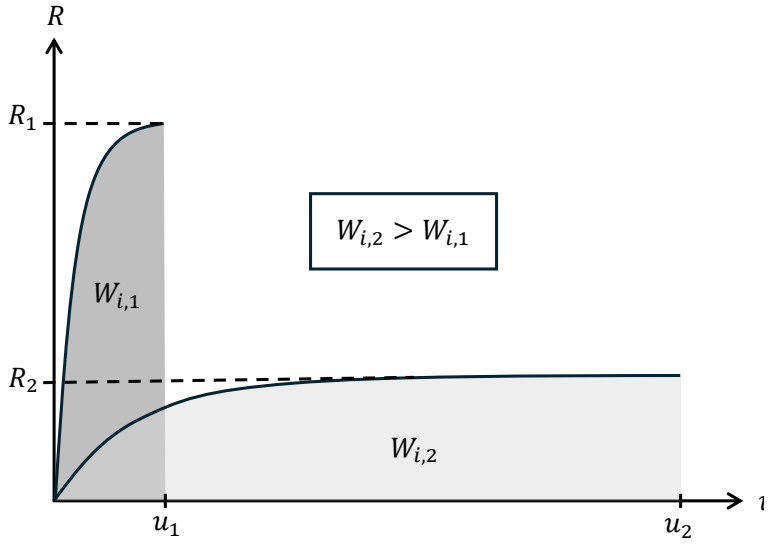

Figure 2.6: Internal energy for a stiff structure with load capacity R_1 and ductile structure with a lower load capacity R_2. Figure based on Johansson and Laine (2012b).

2.1.8 Simplification of dynamic systems

To reduce complexity Johansson and Laine (2012b) introduces a simplified method to calculate the dynamic response in a structure subjected to dynamic loading. In this method, the dynamic system can be described by a spring-mass system based on the structural dynamics equation (SDE), see Equation (2.5), Note that damping can be neglected, as it has minimal influence due to the short duration of loading and the primary focus being on the maximum deflection. The spring mass system is a single degree of freedom (SDOF) system meaning that only one displacement is considered. The system is shown in Figure 2.7 and features a body with mass m fixed to a spring with stiffness k. If the body is subjected to an impulse I the resulting deformation u depends on the spring stiffness, resulting in internal forces in the spring $R(u)$.

$$m\ddot{u}(t) + c\dot{u}(t) + ku(t) = F(t) \tag{2.5}$$

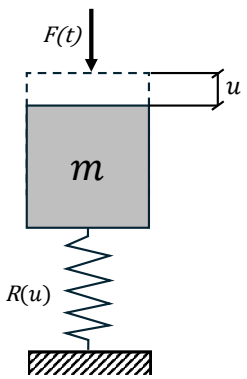

Figure 2.7: Spring-mass system used to describe the response of a dynamic system.

The engineer can use the SDOF-system to describe the dynamic response of a structure by estimating the maximum deflection. Exemplifying by using a beam, the beam may be transformed into a SDOF-system by assuming that the deflection shape remains the same for any load increase, under the assumption of linear elastic behaviour. This means that any point along the beam can serve as a reference point to describe its deflection, typically the point with the largest displacement is chosen (Johansson and Laine (2012b)).

Using transformation factors, denoted κ, the structural properties of the beam (mass, stiffness, damping and load) may be transformed into its effective counterpart to represent the structure as an SDOF-system. The SDOF-system then represents the displacement at the chosen reference point. The structural dynamics equation is thereby transformed into Equation 2.6.

$$\kappa_m m_b \ddot{u}(t) + \kappa_c c_b \dot{u}(t) + \kappa_k k_b u(t) = \kappa_{mF} F_b(t) \tag{2.6}$$

Where m_b, k_b, and c_b are the beam's mass, stiffness, and damping, and $F_b(t)$ is the load acting on the beam.

The transformation factors are derived based on the conservation of kinetic energy and the conservation of internal and external work during the transformation from the real structure to the SDOF-system. See Table 2.1 and Table 2.2 for examples of κ-factors for a beam with different boundary conditions, assuming a constant cross-section shape. Note that κ_m is omitted, as damping is typically neglected in this type of dynamic analysis.

Table 2.1: Transformation factors for a beam with different boundary conditions, pointload (Johansson and Laine, 2012b).

	Pointload			
	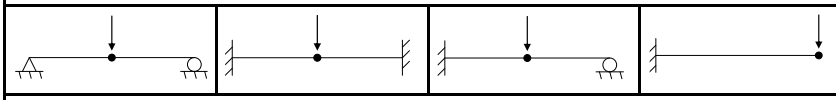			
	Deflection Shape – Elastic Case			
κ_m	0.486	0.371	0.445	0.236
κ_F	1.000	1.000	1.000	1.000
κ_{mF}	0.486	0.371	0.446	0.236
	Deflection Shape – Plastic Case			
κ_m	0.333	0.333	0.333	0.333
κ_F	1.000	1.000	1.000	1.000
κ_{mF}	0.333	0.333	0.333	0.333

Table 2.2: Transformation factors for a beam with different boundary conditions, uniformly distributed load (Johansson and Laine, 2012b).

	Uniformly Distributed Load			
	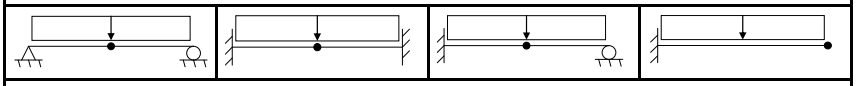			
	Deflection Shape – Elastic Case			
κ_m	0.504	0.406	0.483	0.257
κ_F	0.640	0.533	0.600	0.400
κ_{mF}	0.787	0.762	0.805	0.642
	Deflection Shape – Plastic Case			
κ_m	0.333	0.333	0.333	0.333
κ_F	0.500	0.500	0.500	0.500
κ_{mF}	0.667	0.667	0.667	0.667

2.1.9 Response of SDOF

The response of the SDOF-system may be described using a linear elastic or truly plastic behaviour, depending on the magnitude of the load (Johansson and Laine, 2012b), note that the response can be non-linear as well. The external work on a structure subjected to an impulse was presented in Section 2.1.5 as the transferred kinetic energy, stated in Equation (2.4). This can also be applied to the simplified SDOF-system.

Johansson and Laine (2012b) uses the following derivations to explain the different responses. Recall from Subsection 2.1.5 that the internal work can be seen as the area under the internal force-displacement relation. For a linear elastic response, the internal force in the spring can be described using Hooke's law, the force in the spring is the spring stiffness multiplied with the elastic displacement u_{el}, see Equation (2.7).

$$R(u) = k \cdot u_{el} \tag{2.7}$$

The internal work is thus the area under the internal force - elastic displacement relation, which is the area of a triangle, see Equation (2.8) and Figure 2.8.

$$W_{i,el} = \frac{k u_{el}^2}{2} \tag{2.8}$$

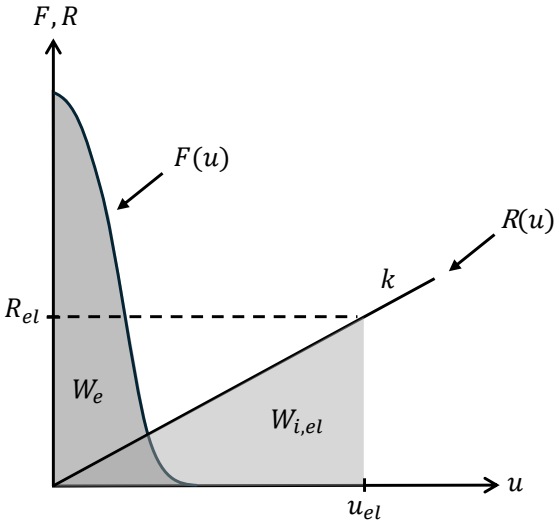

Figure 2.8: The internal work for a linear elastic elastic system is represented by the triangular area under the internal force-displacement relation, governed by the spring stiffness k. Figure based on Johansson and Laine (2012b).

The same can be done for a truly plastic system. Due to plasticity, the internal force is instead the plastic capacity, see Equation (2.9).

$$R(u) = R_{pl} \tag{2.9}$$

The internal work is thus the area under the internal force - elastic displacement relation, which is the area of a rectangle, see Equation (2.10) and Figure 2.9.

$$W_{i,pl} = R_{pl} \cdot u_{pl} \tag{2.10}$$

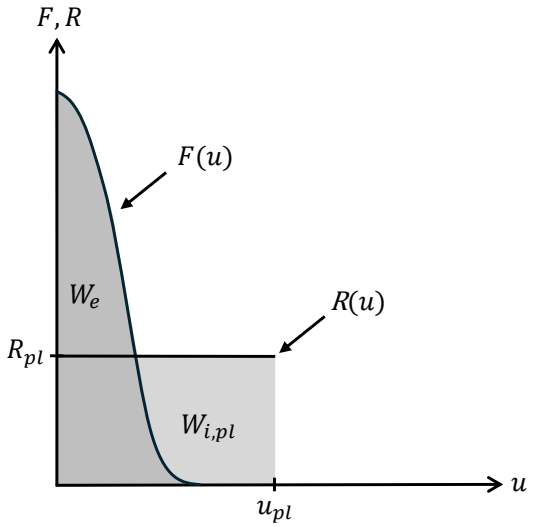

Figure 2.9: The internal work for a truly plastic system is represented by the rectangular area under the internal force-displacement relation, governed by the plastic resistance R_{pl}. Figure based on Johansson and Laine (2012b).

Consider the combination of an elastic and plastic system. The internal force in the spring is then in accordance with Equation (2.11).

$$R(u) = \begin{cases} ku, & u \leq u_{el,1} \\ R_{pl}, & u > u_{el,1} \end{cases} \tag{2.11}$$

The total elastic displacement $u_{el,1}$ before plastic deformation is initiated can be expressed using Equation (2.12) and the total internal work due to internal forces according to Equation (2.13), using that $W_i = W_e$, with W_e as in Equation (2.4).

$$u_{el,1} = \frac{R_{pl}}{k} \tag{2.12}$$

$$W_i = \frac{R_{pl}}{2}(u_{el,1} + 2u_{pl,1}) \tag{2.13}$$

The total plastic displacement $u_{pl,1}$ in Equation (2.13) can be expressed using Equation (2.14) where u_{pl} is the total plastic deformation for the truly plastic system.

$$u_{pl1} = \frac{I}{2mR_{pl}} - \frac{u_{el,1}}{2} = u_{pl} - \frac{u_{el,1}}{2} \tag{2.14}$$

The total displacement is then the sum of elastic and plastic deformation according to Equation (2.15).

$$u_{tot} = u_{el,1} + u_{pl1} = u_{pl} + \frac{u_{el,1}}{2} \tag{2.15}$$

The internal work due to elasto-plastic response is presented in Figure 2.10 where Equation (2.13) may be interpreted as the area under $R(u)$.

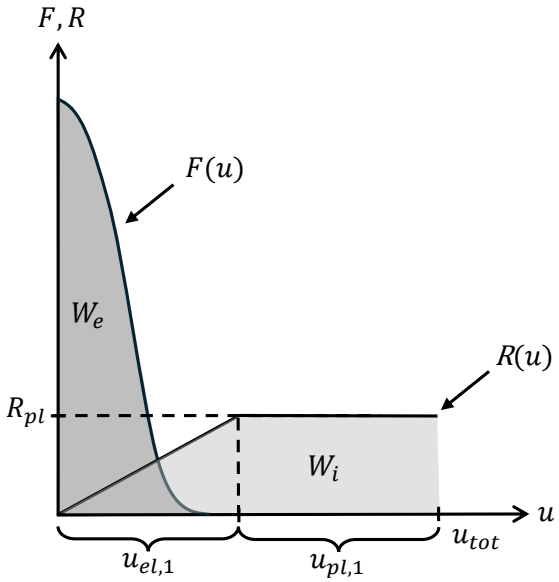

Figure 2.10: Resulting internal work for SDOF-system with elasto-plastic response. Figure based on Johansson and Laine (2012b).

2.1.10 Equivalent static load

It should be noted that dynamic loads are normally not considered in design. Instead the impulse load is usually transformed into an equivalent static load Q of which structural response is similar to that of the impulse load I (Johansson and Laine, 2012b). It is not however possible to derive the equivalent static load based on the impulse only. A structure may initially be transformed into an equivalent SDOF-system using transformation factors (see Section 2.1.8) and then using that the static load should result in the same amount of external work as the impulse load one can derive the equivalent static load. The load may be used as a distributed load in numerical or analytical calculations to compute stresses and moments. For further details see Johansson and Laine (2012b).

2.1.11 Catenary action

Catenary action is a structural mechanism that can develop in laterally restrained beams subjected to large deformations. It plays a critical role in enhancing resistance to progressive collapse, particularly in scenarios involving the sudden removal of a column in a frame structure. In conventional steel beam design, load-bearing capacity is primarily governed by flexural behaviour, with plastic hinges forming at critical sections. However, when axial restraints are present, there is an ability to balance a horizontal force at the ends of the beam during significant out-of-plane displacement. Catenary action may then be activated, allowing the beam to carry additional load beyond its flexural capacity (Harry and Lu, 2019). This mechanism is especially relevant under dynamic loading conditions, where larger displacements may be allowed, enabling the beneficial effects of catenary action to be utilized. The principle is illustrated schematically in Figure 2.11.

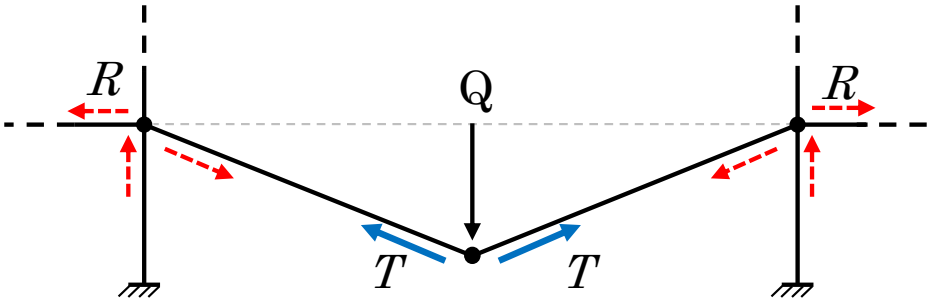

Figure 2.11: Tensile forces (T) appear in loaded member due to the support conditions. The member initially displaces vertically and then the load may increase until the tensile capacity is reached. The horizontal restraint forces (R) are necessary to obtain catenary action.

2.2 Steel

2.2.1 Corrugated Sheet metal

Corrugated sheet metal or corrugated sheet steel, abbreviated CSM, is an often effective and cheap solution when handling static loads. This is because of the strength to weight ratio; compared to the self weight, the strength is very high. Figure 2.12 shows an example of a typical CSM section. A common use of CSM is to span between a roof's main girders, meaning that CSM are optimized for transverse static loads. However, as mentioned in Section 1.1 there might be an increased risk of explosions in close proximity to buildings. Accordingly, if CSM is used as roof sheeting it will be loaded in bending, subjected to dynamic axial compressive loads in the flanges. Theoretically, CSM has low capabilities to withstand this type of load due to its geometry. Steel is a ductile material, but CSM falls into the category of thin walled structures, which means that the thickness is low compared the cross-section's height or width. his leads to buckling being the cause of failure, i.e. geometry being the governing factor of how much load a CSM structure can withstand. Consequently, the the ductility of the steel material is not utilized in an optimal way. Since CSM is stiff the deformation capabilities of CSM will be low, meaning that CSM has low capabilities of absorbing energy, which is a crucial parameter for withstanding explosions.

Figure 2.12: Typical Corrugated sheet metal section (Ruukki Sverige AB, 2025).

There is currently a lack of technical data and calculation methods for some steel profiles, one of these is corrugated sheeting. According to European Commission (2017), calculation methods are either not available or only partially included in the current version of Eurocode EN 1993-1-3, even though the use of the CSM is common practice. Because of this, conventional design approach may prove to be too conservative.

2.2.2 Mechanical properties of steel

Important material properties of steel that are relevant for this study are, among others, the yield strength f_y, This is the stress when the steel start to obtain plastic deformation, i.e. irreversible deformations which remains after unloading. Other important parameters are the ultimate strength f_u, which is the ultimate stress that the steel can withstand before failure, elastic modulus E, which is the stress to strain ratio in the elastic range, and the ductility, which is the ability to deform plastically without going to failure. In dynamic loading, the strain-rate sensitivity is also an important parameter, which depends on the just-mentioned material parameters. (Al-Emrani et al., 2019).

Steel products fall into two categories, they are either hot rolled or cold formed. The typical stress strain relationship for hot rolled steel can be seen in Figure 2.13. If a bar of hot-rolled steel is loaded so that the strain passes the yield point and is then unloaded, the steel in the bar has partially changed its properties. The steel is then said to be cold formed (Al-Emrani et al., 2019). The typical stress strain relationship for cold formed steel is presented Figure 2.14. CSM typically falls into the category of cold-formed steel, as the production process involves folding steel sheets into their characteristic shape, causing plastic deformation in the folds.

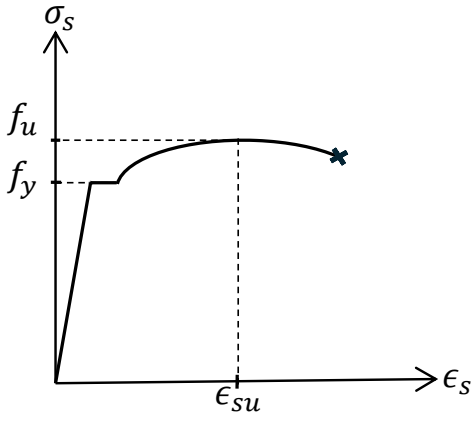

Figure 2.13: Example of stress strain relationship for hot rolled steel.

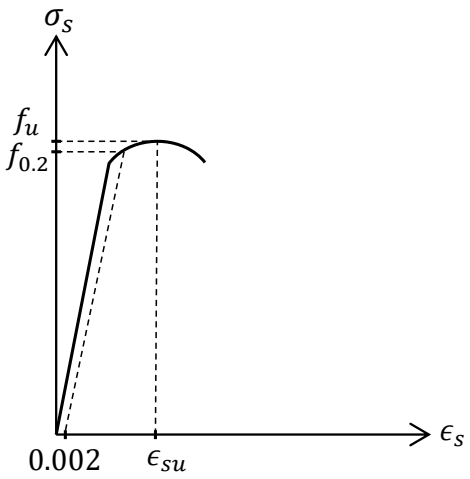

Figure 2.14: Example of stress strain relationship for cold formed steel.

2.2.3 Cross-section class

An important concept for different types of structural components made of steel is cross-sectional class (CSC). Eurocode defines four different classes, class 1-4. Each CSC is associated with a certain risk of local buckling. The parameter that governs what particular class a cross-section belongs to is the slenderness ratio λ of the plates composing the cross-section. Cross-sections in class 1 have the lowest slenderness and cross-sections in class 4 have the highest. The typical stress-strain relationship for the different CSC is presented in Figure 2.15. It can be seen that sections in class 1 reach plasticity and then goes into strain hardening, sections in class 2 reach full plasticity, sections in class 3 just reach plasticity and sections in class 4 will buckle elastically (Al-Emrani, 2023). To account for the risk of elastic buckling in sections classified as CSC 4, a reduced effective width b_{ef} is used for the individual members of the cross-section that are in CSC 4 during design, see Section 2.3.6.

It should be noted that in order to use plastic response in a global analysis, the cross-section must belong to class 1. However, CSM often exhibits class 3 or 4 behavior, which means that plastic redistribution in these sections is not possible and failure is governed by elastic buckling rather than yielding.

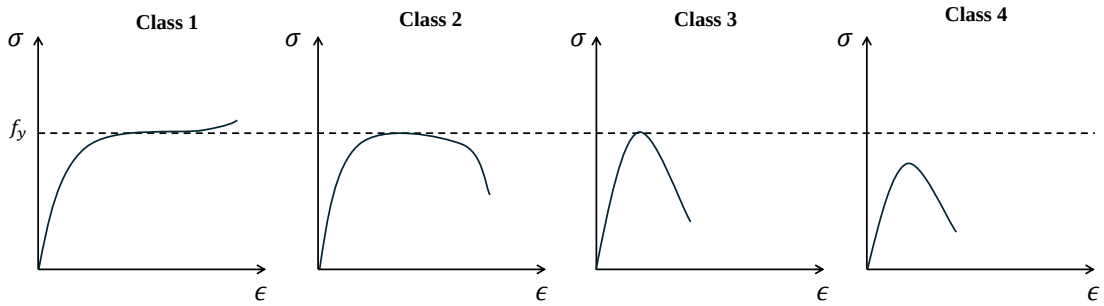

Figure 2.15: Stress strain relationship for different cross-section classes based on Al-Emrani (2023).

2.3 Structural stability

2.3.1 Orientation

Structural stability is a fundamental aspect of engineering design, determining whether a structure can sustain applied loads without experiencing sudden deformation or failure. Buckling, a key stability phenomenon, occurs when a structure under compressive loading experiences a loss of equilibrium, leading to a sudden change in its deformation mode. Various types of buckling exist, influenced by load duration, imperfections, and material behaviour, relevant theory will be presented in the following subsections.

2.3.2 Euler buckling

Classic Euler buckling theory can be used to determine when a column subjected to compression buckles. Euler buckling is a linear elastic buckling problem, sometimes referred to as a bifurcation problem, bifurcation is a point when a system undergoes qualitative changes in behaviour, in this case when a structure under load changes from one stable equilibrium to another, often leading to instability or buckling. For Euler buckling the following assumptions are made:

- The column is initially without any out-of-plane geometrical imperfections.
- An elastic material behaviour is assumed.
- No residual stresses or other internal stresses.
- Loading is applied centrically to the compressed member.
- The cross-section of the compressed member and its support conditions are such that only plane buckling in one direction is relevant.

The assumptions above implicate that the column will remain straight (i.e. no out of plane deformation) until the applied compressive load reaches a critical value denoted P_{cr}. Equation (2.16) can be used to analytically calculate the critical load for when the column will buckle. L_{cr} is the critical buckling length which depends on the boundary conditions (Al-Emrani, 2023).

$$P_{cr} = \frac{\pi^2 EI}{L_{cr}^2} \tag{2.16}$$

Important to note is that, in reality, the assumptions made for Euler buckling will never be entirely true for real structures, meaning that the critical buckling load will be lower depending on how much the assumptions are violated. However, in FE-analysis, where things can be modelled in a precise way, Equation (2.16) can be useful to verify if the results are reasonable.

2.3.3 Initial imperfections

As stated in Section 2.3.2, the assumptions made in Euler's buckling theory do not hold for real structures. One important factor to consider in real structures is the presence of initial imperfections, which can be classified into three main types: geometrical imperfections, material imperfections, and residual stresses.

Some geometrical imperfections will always exist and the imperfections can have

a huge impact on the response depending on the slenderness of the structure. An initial out-of-straightness combined with a compressive axial force will cause an additional moment, this moment will then cause a additional transversal deflection, which magnifies the moment and transversal deflection. Since the additional moments and deformations depend on the displaced shape, second-order effects are fundamentally non-linear, see Figure 2.16 for a visual example (Al-Emrani, 2023).

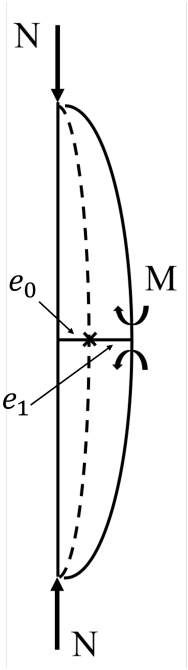

Figure 2.16: Strut with initial imperfection e_0 subjected to compressive axial forces N resulting in an additional moment M and additional transverse deflection e_1.

In Figure 2.17, it can be observed that for a perfect plate, there is a distinct point at which buckling occurs, resulting in a sudden change in the graph. For a plate with initial imperfections the transition is instead gradual. This occurs because the out-of-plane imperfection increases progressively as the compressive load increases, leading to a smoother transition at the bifurcation point rather than a sharp change. Additionally, it can be observed that while the critical buckling load is lower for a plate with initial imperfections, the ultimate capacity remains unaffected. This is explained by the steel's ability to redistribute forces to stiffer, unbuckled regions (Al-Emrani, 2023).

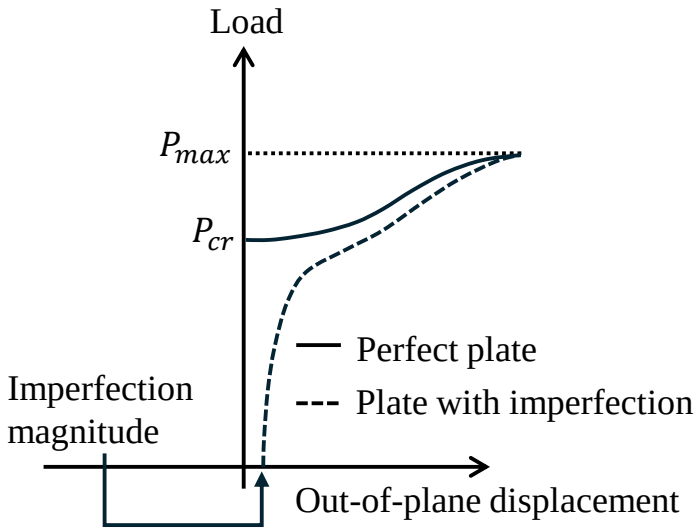

Figure 2.17: Response for an axially loaded plate with and without initial imperfection, where the distance in x-direction between the origin and the dotted line corresponds to the initial imperfection size, figure based on Al-Emrani (2023).

2.3.4 Slenderness

Slenderness is a key parameter in buckling analysis, as slender members are more susceptible to instability and loss of load-carrying capacity under compression. High slenderness ratios indicate a greater likelihood of elastic buckling, while lower slenderness ratios suggest that the member will fail due to material yielding before buckling occurs. The theoretical Euler curve and the buckling curve used in design is shown schematically in Figure 2.18. The reason for the difference between the two graphs is mainly residual stresses and initial imperfections, it can be noted that the largest difference between the curves is obtained for intermediate slenderness (Al-Emrani, 2023).

The relative slenderness, $\bar{\lambda}$, in Figure 2.18 is based on column buckling, however the concept is the same for other types of buckling problems, e.g. for plate buckling, $\bar{\lambda}_p = \sqrt{\frac{f_y}{\sigma_{cr}}}$ or for lateral torsional buckling $\bar{\lambda}_{LT} = \sqrt{\frac{M_{pl}}{M_{cr}}}$, i.e. the square root of a theoretical resistance divided by a theoretical buckling load.

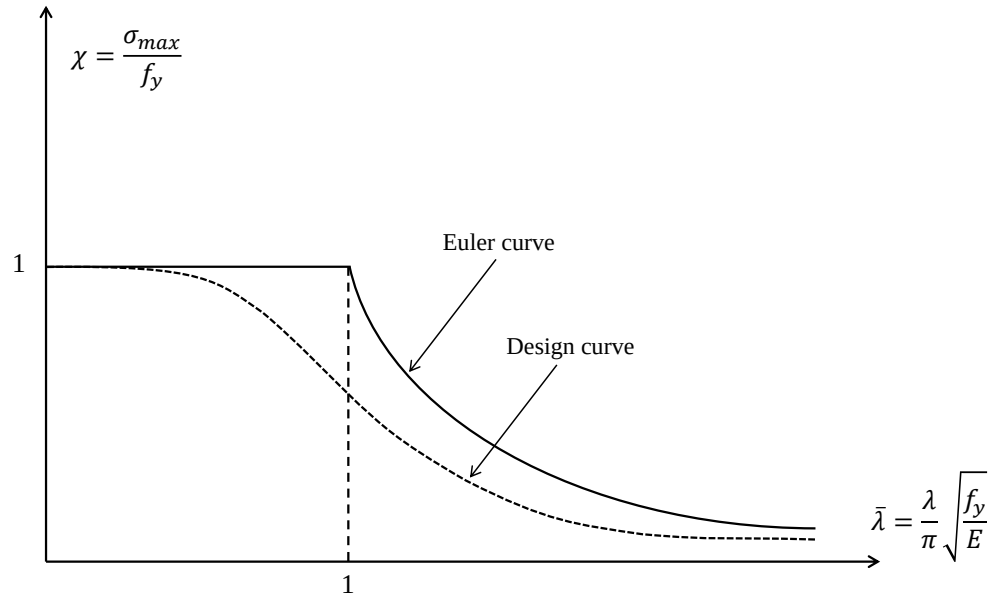

Figure 2.18: Relation between relative slenderness ratio and the buckling reduction factor for columns, figure based on Al-Emrani (2023).

2.3.5 Static plate buckling

According to Al-Emrani (2023), the critical buckling stress for an unstiffened plate, simply supported on each edge, can be derived based on the differential plate equation for an axially loaded plate. Assuming a buckling shape with one half-sine wave n in the transverse direction of the plate, the critical stress can be described by Equation (2.17).

$$\sigma_{cr} = k \cdot \frac{\pi^2 E}{12(1-v^2)\left(\frac{b}{t}\right)^2} \tag{2.17}$$

The equation for k is presented in Equation (2.18) and depends on the plate length a, width b, and the number of half-sine waves m in the longitudinal direction (loading direction), see Figure 2.19.

$$k = \left(\frac{m \cdot b}{a} + \frac{a}{m \cdot b}\right)^2 \tag{2.18}$$

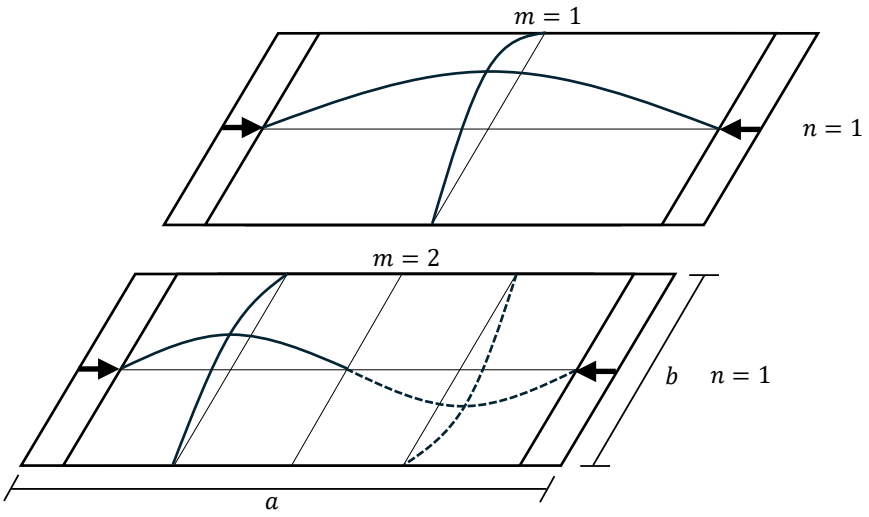

Figure 2.19: Illustration of variables in Equation 2.18.

The critical stress is thus dependant on the plate slenderness (b/t) and the loading conditions (simply supported edges, fixed edges e.t.c of which decides m) via the buckling coefficient k for the first buckling mode. To be noted is that initial imperfections are not considered in the derivation and will lead to a reduced buckling stress.

The critical axial buckling load P_{cr} can be calculated by multiplying the critical stress with the plate cross-sectional area A_{cs}, see equation (2.19).

$$P_{cr} = \sigma_{cr} \cdot A_{cs} = \sigma_{cr} \cdot b \cdot t \tag{2.19}$$

2.3.6 Post buckling behaviour of plates

When the load increases above the critical load the state of equilibrium is either stable or unstable. Stable means that an increasing load results in increasing deformation while unstable means that deformations increase for decreasing load, see Figure 2.20. The stable state is preferable and dictates a state of post buckling strength while the unstable state means that the structure cannot resist any more load and deforms freely.

There are, however, authors who claim that for the thin-walled structures with a stable post-buckling equilibrium path, dynamic buckling does not occur (Kubiak, 2013).

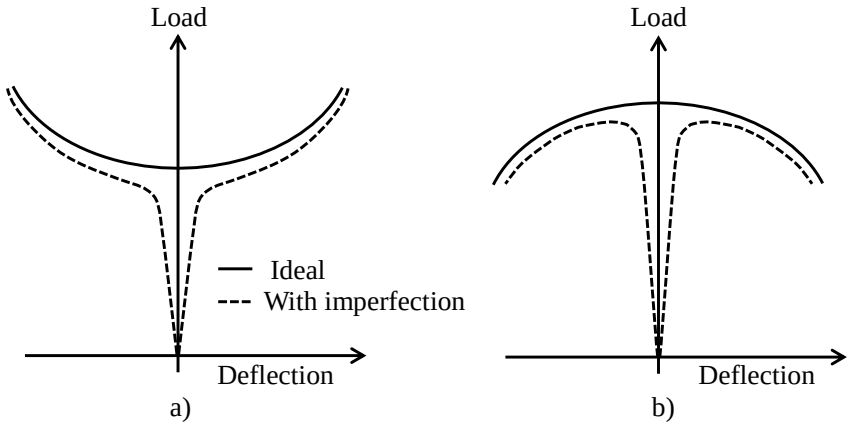

Figure 2.20: Stable state *a*) where deformation continuous to grow as the load is increased and unstable state *b*) where the load is decrease but deflection still continues to grow.

Plates are supported along at least three edges (Al-Emrani, 2023) meaning that if axially loaded the restrained edges will not be able to deform perpendicular to its plane. When the central part of the plate buckles, the stiffness is reduced in that area. The load is then shifted to the material along the restrained edges which still has a significant stiffness and a tension band that enables further loading evolves (Al-Emrani, 2023), see Figure 2.21. The post buckling state is thus stable with post critical reserve strength. The plate width where the remaining stiffness still exists is defined as the effective width b_{eff} and when the stress in the effective width exceeds the yield stress, failure occurs.

The ultimate load P_{max} due to post buckling strength can be calculated by multiplying the yield stress with the effective area, see Equation (2.20).

$$P_{max} = \sigma_y \cdot A_{eff} = \sigma_y \cdot b_{eff} \cdot t \tag{2.20}$$

The effective width according to SS EN 1993-1-5, 2005 is defined as in Equation (2.21).

$$b_{eff} = \rho \cdot b \tag{2.21}$$

Where the reduction factor ρ depends on the slenderness factor $\bar{\lambda}_p$, see Equation (2.22) and (2.23) respectively.

$$\rho = \frac{\bar{\lambda}_p - 0.22}{\bar{\lambda}_p^2} \tag{2.22}$$

$$\bar{\lambda}_p = \sqrt{\frac{f_y}{\sigma_{cr}}} \tag{2.23}$$

Note that Equation (2.22) only is true for the specific case when the plate is subjected to uniform compression, is simply supported on all four edges and can be seen as a internal compression part. For other cases see Eurocode 1993-1-5.

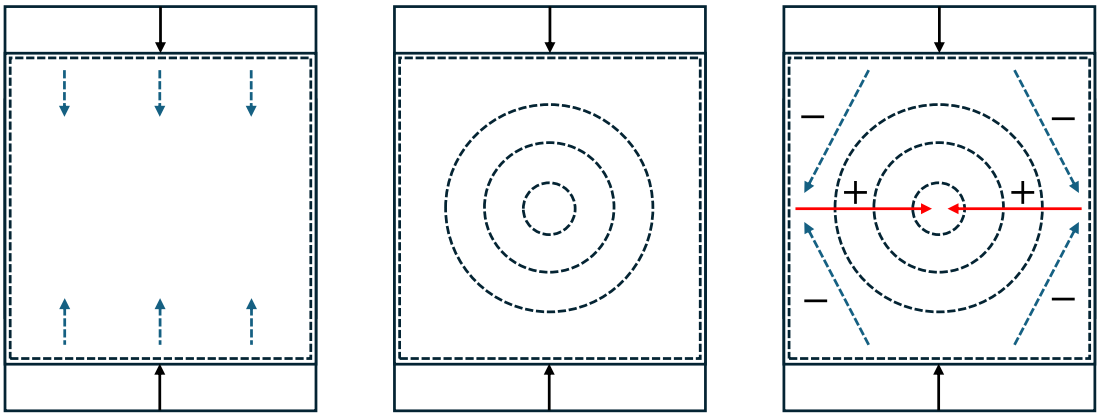

Figure 2.21: Force equilibrium caused by reduction of stiffness in plate centre due to buckling (black circles) leads to a strengthening tension field (positive arrows). Figure based on Al-Emrani (2023).

2.3.7 Dynamic buckling

Buckling can be divided into static and dynamic buckling depending on the load duration. If the loading is applied with a short duration similar to that of the period of natural vibration, the buckling is dynamic. If the load duration is longer, static buckling will occur. The main difference from static buckling apart from the load type is that dynamic buckling may result in an increase of the critical buckling load (Kubiak, 2013).

According to Kubiak (2013), different authors have formulated many different criteria to determine the critical load or failure load. The reason a criterion is needed to determine whether a structure has buckled is that the critical dynamic buckling load does not exhibit bifurcation behaviour (i.e., the transition is smooth). Therefore, it must be determined based on an assumed criterion.

Kowal-Michalska and Mania (2008) present 3 different dynamic buckling criterion's that are commonly used: the Volmir criterion, the Budiansky-Hutchinson criterion and Petry and Fahlbuschs criterion. These criteria can be used to predict if a structure will undergo dynamic buckling. Equation (2.24), where DLF is the dynamic load factor, is then formulated to describe the ratio between the dynamic critical buckling load and the static critical buckling load for a plate.

$$\mathrm{DLF} = \frac{N_{\mathrm{cr}}^{\mathrm{dyn}}}{N_{\mathrm{cr}}^{\mathrm{stat}}} \tag{2.24}$$

Kowal-Michalska and Mania (2008) states that numerous papers underline that dynamic buckling loads are not always higher than static ones, i.e. DLF in Equation (2.24) may be lower than 1. This is based on both experimental and numerical analysis, and the main influencing factors on the dynamic behaviour is initial imperfections and pulse intensity of the load, both factors heavily influence the dynamic buckling load. Low initial imperfection will result in a higher dynamic critical buckling load and large initial imperfection will result in a lower dynamic critical buckling load. This is the same behaviour that can be seen for

static loading. However, it seems that dynamic loading magnify the effect of initial imperfections indicating a stronger sensitivity to initial imperfections. In theory Kowal-Michalska and Mania (2008) states that the dynamic critical buckling load will tend to infinity for a "perfect" structure i.e., a structure with no initial imperfections.

2.4 Dynamic structural response

2.4.1 Orientation

The dynamic response of a structure depends on various factors such as loading conditions and material properties. Unlike static loading, dynamic loads, such as explosions, introduce additional complexities, including inertial effects and strain rate sensitivity. Understanding these factors is essential for accurately predicting structural behavior under dynamic conditions. This subsection provides an overview of key concepts relevant to dynamic structural response, laying the foundation for subsequent discussions on strain rate effects, dynamic increase factors and constitutive models.

2.4.2 Strain rate

Strain rate is the time derivative of the strain of a material, denoted $\dot{\epsilon}$ with the unit s^{-1}, see Equation 2.25.

$$\dot{\epsilon} = \epsilon/dt \tag{2.25}$$

A structure can be exposed to different strain rates depending on the loading situation (wind, snow, impact, explosion, etc). In Figure 2.1 the strain rate to which different types of loads correspond to is presented.

An aspect of viscous properties is the rate dependence that can be observed in the stress-strain relationship for certain materials. For metals, the rate dependence results in a increased stiffness and strength for higher loading rates. Typical behaviour for a rate-dependant steel material is shown in Figure 2.22 (Runesson and Larsson, 2024). An increased strain-rate results in increased strain hardening and ultimate load.

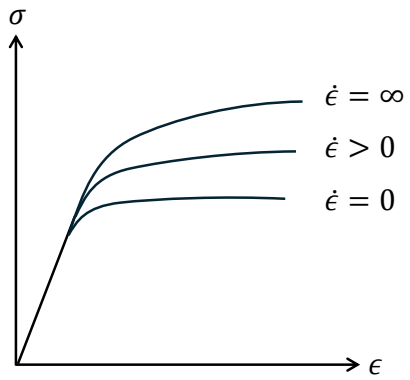

Figure 2.22: Schematic rate effect on stress-strain relation in steel.

2.4.3 Dynamic increase factor

To describe how the increased strength of steel under dynamic loading relates to the strength under static loading a dynamic increase factor is used, denoted DIF. According to Yang et al. (2022) three indices for the DIF in steel is commonly used:

- DIF_y: Defined as the ratio of dynamic yield strength to static yield strength:

$$DIF_y = \frac{f_{y,\text{dyn}}}{f_y}$$

- DIF_u: Defined as the ratio of dynamic ultimate strength to static ultimate strength:

$$DIF_u = \frac{f_{u,\text{dyn}}}{f_u}$$

- DIF_{avg}: Defined as the average of all DIF_i, where:

$$DIF_{avg} = \Sigma DIF_i \quad \text{and} \quad DIF_i = \frac{\sigma_{i,\text{dyn}}}{\sigma_i}$$

DIF_y is the most widely used index, but in some cases it can produce inaccurate results if applied as a stress amplification factor to the full quasi-static stress–strain curve. This is according to Yang et al. (2022) due to the following 3 reasons:

- When subjected to very high strain rates (impact/explosion), steel often deforms far beyond the yield point, (into the strain hardening range).
- Generally, the dynamic increment in $f_{y,dyn}$ is larger than for other points on the $\sigma - \epsilon$ curve, which will result in an overestimation of the predicted dynamic constitutive response.
- Measured DIF_y values reported in the literature, is sensitive to system errors associated with stress non-uniformity during the elastic stage and sensitive to some methods of defining $f_{y,dyn}$ if the steel does not have a defined yield plateau.

In the case with DIF_u, the predicted dynamic constitutive response using DIF_u will instead by underestimated. Because of this, it can be more appropriate to use DIF_{avg} if the DIF is applied as a stress amplification factor to the full quasi-static stress–strain curve (Yang et al., 2022). In the case with a steel section class 4, DIF_y is most probably the most representative factor.

2.4.4 Dynamic constitutive model

To be able to describe how stress is related to strain under dynamic loading, a dynamic constitutive model can be used. There are numerous models to describe the dynamic properties of steel, two that are implemented and ready to use in Abaqus are the Cowper-Symonds power function (C-S), see Equation (2.26) and the Johnson-Cook function (J-C), see Equation 2.27 (Yang et al., 2022).

$$\sigma_{dyn} = \left(1 + \left(\frac{\dot{\epsilon}}{D}\right)^{\frac{1}{p}}\right)\sigma_s \tag{2.26}$$

$$\sigma_{dyn} = \left(A + B \cdot \epsilon_p^n\right)(1 + C \cdot \ln \epsilon^*)(1 - T^{*m}) \tag{2.27}$$

Where:

$$\epsilon^* = \frac{\dot{\epsilon}}{\dot{\epsilon}_0} \tag{2.28}$$

$$T^* = \frac{T - T_r}{T_m - T_r} \tag{2.29}$$

D, p, A, B, C, m, and n are material constants. In Equation (2.26) D is representing the reference rate where yield stress begins to change significantly and p controls the degree of strain rate sensitivity. In Equation (2.27) A is the yield stress (at reference strain and temperature), B is the hardening modulus, n is the strain hardening exponent (defines the extent of strain hardening), C is the strain rate sensitivity (how much the yield stress increases with strain rate) and m is the thermal softening exponent (defines how temperature affects material strength). In some literature D and p in Equation (2.26) may be referred to as C and q.

In Table 2.3 some key differences are presented between the two models, note that the C-S model can be used for an arbitrary stress-strain relationship while the shape of the curve for the J-C model is controlled by 2.27, which might make it more suitable to use the C-S model in the case were a stress-strain relationship featuring a yield plateau is used.

Table 2.3: Comparison of Cowper-Symonds (C-S) and Johnson-Cook (J-C) material models

Feature	**Cowper-Symonds (C-S)**	**Johnson-Cook (J-C)**
Strain Rate Sensitivity	Power-law form	Logarithmic form
Strain Hardening	No	Yes
Thermal Softening	No	Yes
Computational Complexity	Low	High
Best for	Simple high-strain-rate cases	General dynamic problems

Proposed by Yang et al. (2022), inspired by the (C-S) model (i.e. Equation (2.26)) the constitutive dynamic model in Equation (2.30) can be used to describe the stress-strain relationship due to strain rate effects.

$$\sigma_{dyn} = \sigma_s(\epsilon) \cdot DIF_{avg}(\dot{\epsilon}, f_y) \tag{2.30}$$

Where:

$$DIF_{avg}(\dot{\epsilon}, f_y) = 1 + \left(\frac{\dot{\epsilon}}{D_{avg}}\right)^{\frac{1}{p_{avg}}} \tag{2.31}$$

$$D_{avg} = 1000\left(\frac{f_y}{235}\right)^6 \tag{2.32}$$

$$p_{avg} = 3\left(\frac{f_y}{235}\right)^{0.2} \tag{2.33}$$

$\sigma_s(\epsilon)$ is the constitutive model for static loading, which can be established either by physical testing or from an existing constitutive model. The strain in the dynamic stress-strain relationship may be assumed to be equal to the static strain.

In a similar manner DIF_y can be formulated, see Equation (2.34).

$$DIF_y(\dot{\epsilon}, f_y) = 1 + \left(\frac{\dot{\epsilon}}{D_y}\right)^{\frac{1}{p_y}} \tag{2.34}$$

Where:

$$D_y = 1000\left(\frac{f_y}{235}\right)^{3.8} \tag{2.35}$$

$$p_y = 5\left(\frac{f_y}{235}\right)^{-0.5} \tag{2.36}$$

2.5 Experimental and numerical results from previous studies

2.5.1 Orientation

This section presents the results from previous experimental and numerical studies relevant to the dynamic behavior of steel structures, with the aim of identifying key findings related to this thesis. The first study focuses on the experimental behavior of steel plates subjected to dynamic axial compressive loads, while the second study presents a numerical investigation into the performance of profiled steel barriers (CSM) under explosive loads. Note that these profiles are a have larger dimensions compared to "ordinary CSM" used as roof sheeting.

2.5.2 Study 1 - Steel plate subjected to axial compressive load

It is known that the strength characteristics of structural elements under dynamic loading can be different from the strength characteristics under a static or quasi-static loading situation.

According to the authors (Paik and Thayamballi, 2003a) there is a research gap related to the dynamic behaviour of plates, previous studies made on dynamically loaded steel structures are limited to either plates under lateral pressure or beams. Studies on the dynamic behaviour of thin walled steel structures, such as plates, subjected to dynamic in-plane loading are not seen (Paik and Thayamballi, 2003a). After a review of the studies available in the field of static and dynamic plastic behaviour of structures, it can be concluded that the there still is a lack of experimental studies made on the behaviour of in-plane dynamically loaded thin walled steel structures.

Therefore Paik and Thayamballi (2003a) conducted a experimental study with the aim to obtain data on the ultimate capacity of a plain steel plate subjected to dynamic compressive in-plane loads. They used one dimension for all specimens, steel plates with the dimension 500x500x1.6 mm, all specimens were made out of mild steel (steel with low carbon content, $\sigma_y = 251.8$ MPa). See Figure 2.23 for a

overview of the test set up. To investigate the dynamic effects they used different loading speeds in the range 0.05 - 400 mm/s, which corresponds to strain rates in the range $10^{-4} - 0.8$ 1/s. The test they performed were conducted until and after failure.

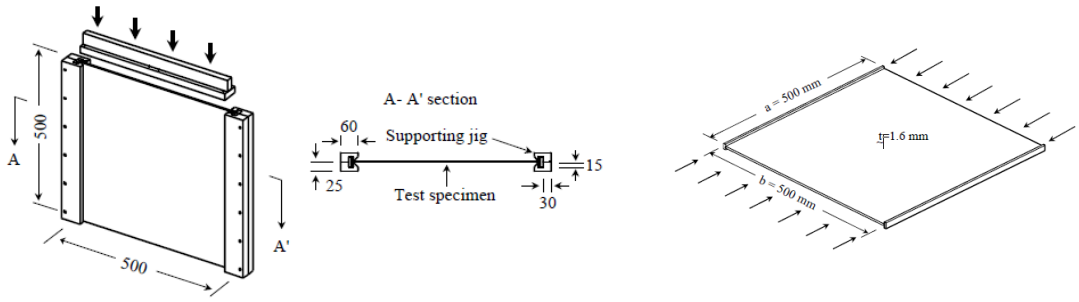

Figure 2.23: Test setup and geometry (Paik and Thayamballi, 2003a).

In Table 2.4 a summary of the test results is presented and in Figure 2.24 the load-displacement curve obtained from their experiments is shown (Paik and Thayamballi, 2003a). It can clearly be seen that the ultimate strength is increased when the load is applied with a higher speed. A slight increase in inclination of the curve can be seen, indicating a slight increase in stiffness. What also can be noted is that the in-plane displacement and lateral deflection increase when the loading speed increase at the ultimate limit state.

Table 2.4: Summary of the ultimate strength tests on steel plates under dynamic axial compressive loads obtained by the experiment conducted by Paik and Thayamballi (2003a).

Specimen	V_0 **(mm/s)**	$\dot{\epsilon}$ **[s^{-1}]**	$\frac{\sigma_{y,dyn}}{\sigma_y}$	$\frac{\sigma_{u,dyn}}{\sigma_u}$	$U_{u,dyn}$ **[mm]**	$\frac{U_{u,dyn}}{U_u}$	$\omega_{u,dyn}$ **[mm]**	$\frac{\omega_{u,dyn}}{\omega_u}$
USP-S	0.05	1.0×10^{-4}	0.20	1.0	0.63	1.0	1.37	1.0
USP-100	100	2.0×10^{-1}	0.25	1.23	1.07	1.70	2.06	1.50
USP-300	300	6.0×10^{-1}	0.28	1.35	1.23	1.95	2.41	1.76
USP-400	400	8.0×10^{-1}	0.29	1.44	1.27	2.02	2.60	1.89

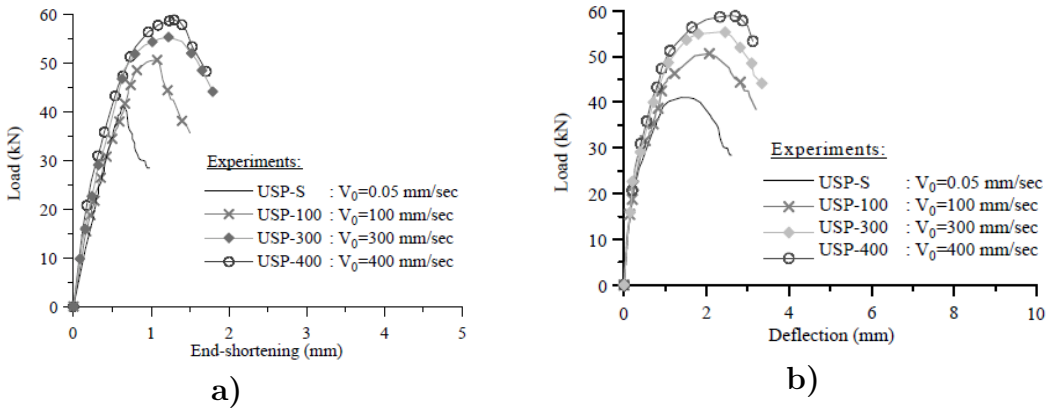

Figure 2.24: Response of the plate: a) In-plane end shortening, b) Lateral deflection (Paik and Thayamballi, 2003a).

From the results it can be concluded that an increase in ultimate strength is to be expected, however only one dimension of steel plate was used and all specimens had the same material properties. No sensitivity analysis was made regarding these properties. The cross-section class and the slenderness was not presented in the study. However, using expressions provided in Equation 2.23, it can be concluded that the cross-section is in class 4 and that λ is approximately 7, which is very slender.

2.5.3 Study 2 - Numerical assessment of explosion resistant profiled barriers

Bohb et al. (2004) presented a numerical study using the FE-software Abaqus, the purpose with the study was to investigate the response of profiled steel barriers subjected to explosions. They investigated three profiles of varying depths, and the static and dynamic response of the steel profiles were determined up to the ultimate capacity and after buckling had occurred.

In Table 2.5 the dimensions used in Bohb et al. (2004) study is presented and in Figure 2.25, the different parameters in Table 2.5 are explained. X/r refers to the global slenderness. The compressed flange in S1 is in CSC4, the compressed flange in S2 is in CSC2 and the compressed flange in S3 is in CSC1. No stiffening ripples were used in the top flange or along the web.

Table 2.5: Geometry of profiled barriers (mm) (Bohb et al., 2004).

Section	t	s	h	θ^0	l_1	l_2	l_3	L	X	X/r	l_1/t	l_3/t	s/l_3
S1	11	639.8	554	60.0	200	320	240	1280	6000	29.4	18.2	58.2	2.7
S2	9	256.1	200	51.3	160	160	160	800	4000	51.3	17.8	28.5	1.6
S3	2.5	60.2	45	48.4	62.5	40	45	250	2322	130.4	25.0	24.1	1.3

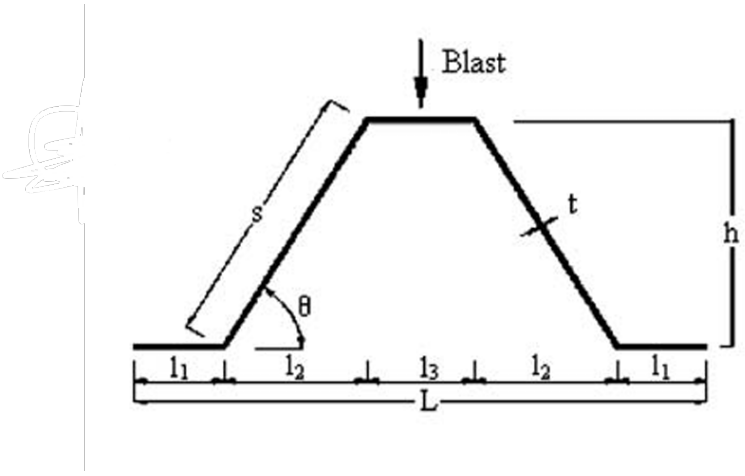

Figure 2.25: Typical profile, simply supported CSM strip and distributed load (Bohb et al., 2004).

In Figure 2.26 the static response is shown for the three different geometries, it can be seen that a deeper section will behave in a more brittle manner and that a more shallow section will have a very ductile behaviour (Bohb et al., 2004).

Figure 2.26 also summarizes the underlying structural problem that this thesis project aims to investigate. Geometry S1 is superior in terms of ultimate load-bearing capacity under static transverse loads; however, it has very low deformation capacity. This means it offers limited resistance to dynamic loads, as the ability to deform is an important parameter. S3, on the other hand, is very ductile but has a very low ultimate capacity. S2 might represent a good compromise between S1 and S3 if there is a risk of explosions or other dynamic loads. However, both S2 and S3 exhibit plastic deformation and may be suitable for dynamic load cases depending on the magnitude of the load.

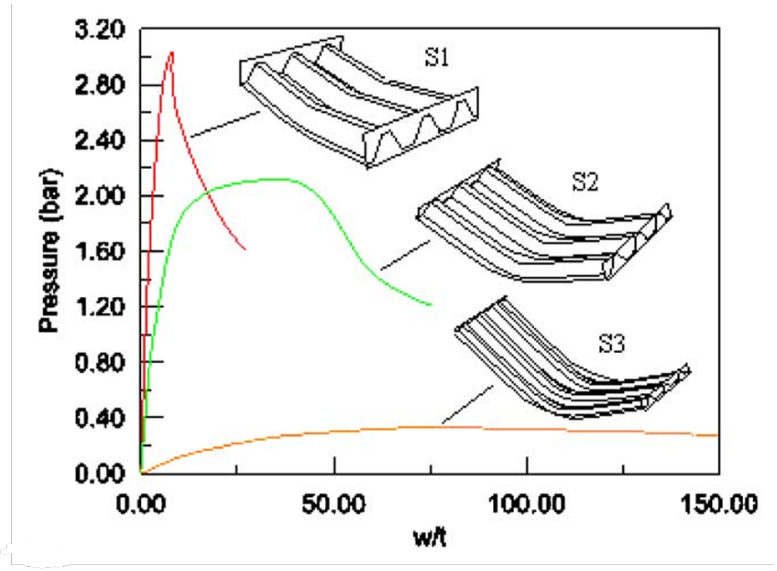

Figure 2.26: Static response for different geometries, simply supported and (Bohb et al., 2004).

After performing the numerical analysis Bohb et al. (2004) came up with some general recommendations for FE-modelling of a dynamically loaded CSM structure. At least three bays should be included in the model for most cases, they state the there is a increased sensitivity to the number of bays when the span is long compared to the width. A static non-linear analysis should be performed to check if the model behaves as expected before proceeding to the dynamic analysis. Special care should be directed to the imposed boundary conditions in the FE-model, correct modelling of the in-plane restraints can not be ignored, especially for deep sections, since buckling can be prevented due to membrane action otherwise. The assumption of a symmetry condition along the longitudinal axis of a outer bay can be used safely, since it will yield conservative results. The authors recommend that first order shell elements are used. A full corrugation should be modelled instead of a half with symmetry conditions in the middle if the post buckling behaviour is of interest since some asymmetric buckling modes cannot be captured with the symmetry boundary condition.

2.6 Reconnection of the theory to the CSM structure

The theory behind dynamic loading and the structural and material response for both static and dynamic loads have been explained in the previous sections. Returning to the main problem, it should now be more clear why dynamic loading of CSM is of interest.

The difference between static and dynamic loading was explained, highlighting the increased loading speed and magnitude of explosions, described as an impulse load. It was concluded that in order to withstand dynamic loads, energy absorption through deformation is crucial. Steel is ductile, but because of the geometrical properties of CSM, slenderness combined with high transverse stiffness means that elastic buckling will occur for high amplitude impulse loads before any major deformation is obtained. There are however strengthening effects of steel due to strain rate effects which will enhance both yield strength and post-buckling resistance, increasing overall energy absorption. Sufficient knowledge of the dynamic behaviour before, during and after buckling is thus important, highlighting the need for this study.

This can be exemplified as follows. The dynamic response of the CSM can be described by the SDOF system. By using the secant stiffness of the external load displacement the engineer can interpret the secant stiffness as the stiffness of the spring in the SDOF system and estimate the energy absorption.

Without prior knowledge of the dynamic buckling behaviour, the secant stiffness may be drawn below the critical buckling load as a conservative estimate. Depending on the post-buckling behaviour, increased energy absorption may be possible, leading to a larger energy absorption capacity than otherwise assumed. This is highlighted in Figure 2.27 where three different areas are drawn. Depending on the slope k, different energy absorption is obtained, see the three different sized areas marked. Note that the internal work (energy absorption) was described as the area under the internal force-displacement relation.

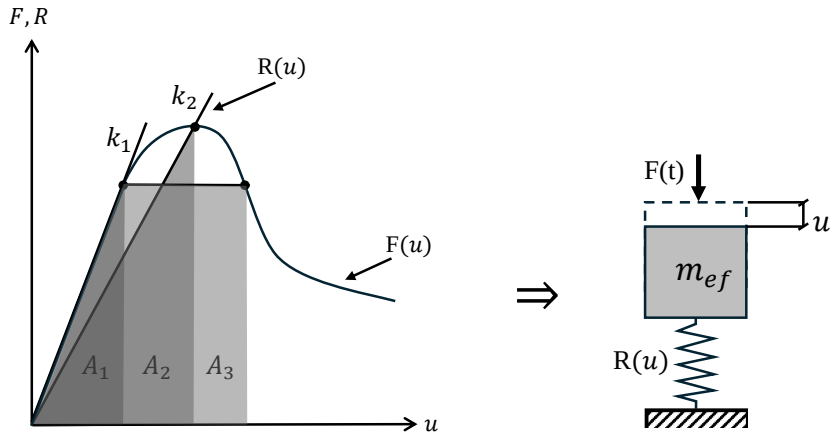

Figure 2.27: Load-displacement relation translated into stiffness in SDOF system.

3 Finite element method

3.1 Orientation

Nonlinearity increases the complexity in numerical analysis compared to linear analysis. Several factors need to be taken into consideration to provide accurate results. In order to make informed decisions in the numerical analysis theory regarding non-linear FEM, element types, loading methods, and convergence are presented in this chapter to act as a basis for decisions made during the numerical analysis.

3.2 Solving non-linear FE problems

Non-linearity in structural analysis can be broadly classified into two categories: geometric non-linearity and material non-linearity. Geometric non-linearity refers to structural behaviour where large deformations significantly influence stiffness and equilibrium conditions, often leading to phenomena such as buckling and large displacement responses. Material non-linearity, on the other hand, occurs when the force–displacement relationship deviates from linearity due to inherent material properties such as yielding or strain hardening.

Non-linear behaviour results in a force–displacement relationship that is no longer linear, meaning that the structure's stiffness changes as deformation progresses. Solving such problems requires an iterative approach, where the analysis is divided into load or time increments (steps), and the solution is updated within each step. The solution within each increment can be determined using an implicit method (Plos et al., 2021). Figure 3.1 illustrates a typical iterative solution scheme, In this scheme, the tangential stiffness matrix is created and decomposed at each iteration within a particular step.

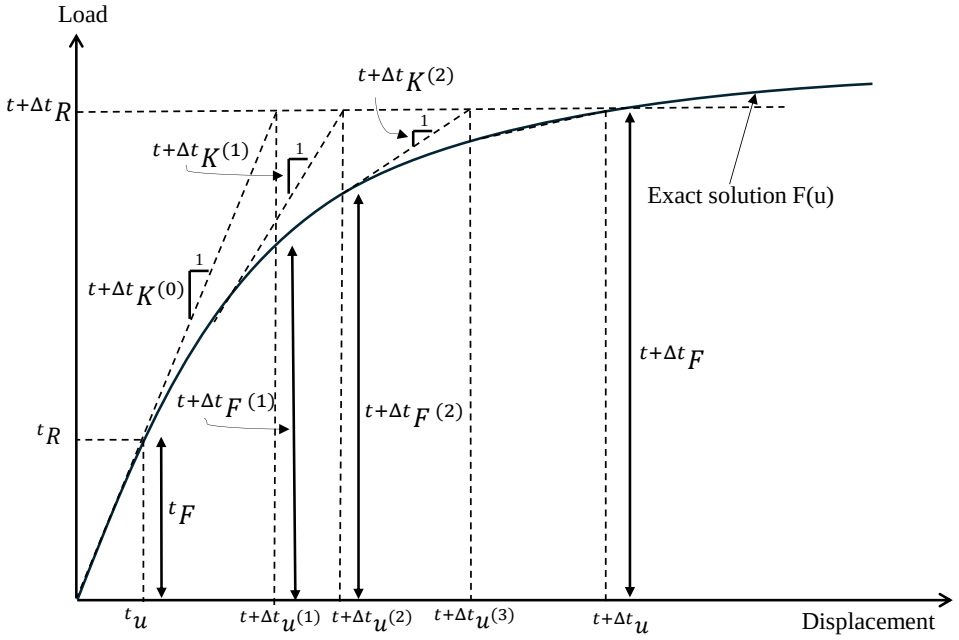

Figure 3.1: Iterative solution method: Newton-Raphson (NR) scheme.

The implicit method solves for the structural response by enforcing static or dynamic equilibrium at each time step. In each increment, either the applied load or the displacement is increased (see Section 3.3 for further details).

In addition to force equilibrium, convergence can also be evaluated using energy norms or displacement norms (Plos et al., 2021). While a smaller tolerance leads to higher accuracy, it may also require more iterations per time step. Conversely, a larger tolerance can improve convergence in challenging analyses. Notably, studies have shown that acceptable accuracy can still be achieved with relaxed tolerances (Plos et al., 2021). Implicit methods are suitable for both static and dynamic structural analyses.

In some cases, for example in highly non-linear problems, another method called explicit method may be used as an alternative to the implicit approach (Plos et al., 2021). The explicit method is based on dynamic equilibrium and does not require iteration, as all necessary information is obtained from the previous time step. This eliminates convergence issues. However, it requires very small time steps, which can significantly increase computational time. While the explicit method can be used for quasi-static problems, care must be taken to avoid errors introduced by small time steps. Therefore, it is generally more suitable for dynamic analyses, where small time steps need to be taken anyway, although it can be applied to static cases with appropriate strategies to reduce computational cost. The key difference between the implicit and explicit methods is that the implicit method requires solving for unknowns at the current time step using both current and previous information, which necessitates an iterative solution. In contrast, the explicit method computes the response directly using only information from the previous time step, thus avoiding iteration.

3.3 Load application

Load application refers to the method of applying the load to a structure within each time step. Three methods commonly used are load controlled, displacement controlled and the arc-length method (Plos et al., 2021), see Figure 3.2

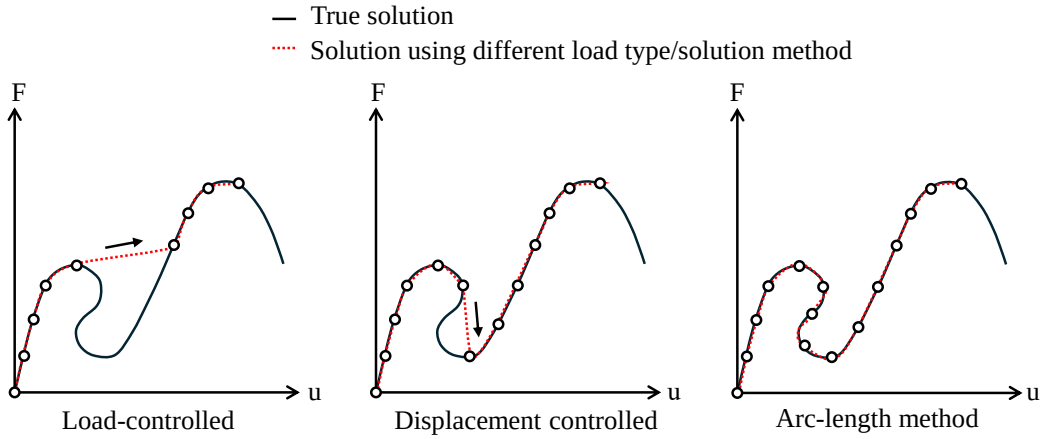

Figure 3.2: Schematic illustration of various concepts of load application (Plos et al., 2021).

Load controlled means that the load is applied as forces and moments. The load is applied step by step until the desired maximum load is applied. Featured in both linear and non-linear analysis.

For the displacement controlled approach, the load is instead applied stepwise as a displacement. The displacement may also be prescribed in terms of a velocity or acceleration.

In the arc length method both the displacements and loading increment is treated as unknowns, increasing the DOF by one. Introducing another unknown means that another equation also has to be introduced in the equilibrium equations, the arc-length equation (Memon and SU, 2004).

In non-linear FEM analysis the load-displacement response $F(u)$ is non linear, meaning that the choice of load application method is crucial to capture the true behaviour. Non-linear response such as buckling or snap-back means that no more load can be resisted by the structure but displacements continue to increase in the case of buckling or decrease in the case of snap back. The load controlled method fails to capture this response since the method is based on a load that is always increasing. The displacement controlled method is better suited for the buckling case since the prescribed displacement during each time step is increased, and the applied force is computed as a result of the displacement and will be able to decrease in the $F(u)$ plot. To capture the full snap back behaviour that features a decrease in both applied force and displacement, the displacement controlled method will not capture the displacement decrease. The arc-length method is then more accurate since the force and displacements are unknown, and the increment may be positive or negative (Plos et al., 2021).

3.4 Load application profile

In finite element analysis (FEA), particularly for dynamic or non-linear problems, the method of applying loads plays a crucial role in obtaining accurate and stable results. Various load application profiles are employed depending on the nature of the analysis and desired outcomes. The most common profiles include instantaneous loading, ramping up the load during several step increments, or cyclic loading.

Applying the full load instantaneously within one load step, which is easily implemented, can induce high-frequency oscillations or artificial numerical instabilities, particularly in dynamic analyses.

Ramping up the load gradually increases the load over a specified time period, which helps avoid sudden shock effects, improves numerical stability, and ensures better convergence in implicit methods. Additionally, for quasi-static analyses conducted via dynamic solvers, a slow ramping of the load minimizes inertia effects, allowing the system to better approximate static behaviour.

3.5 Element type

To model complex structures and their physical behaviour, different element types are available. They can be classified according to their family, element order and integration type.

The element family has several subcategories where continuum elements and structural elements are commonly used in stress-displacement problems. Both types support static and dynamic analyses.

Continuum elements are so-called volume elements used in both 1, 2 and 3D analyses. They are sufficient in contact analysis, plasticity, large deformation and multi-axial stress analysis (ABAQUS, 2006). These elements only feature translational DOFs and common shapes are triangles and squares in 2D and tetrahedrons and hexahedrals in 3D, see Figure 3.3.

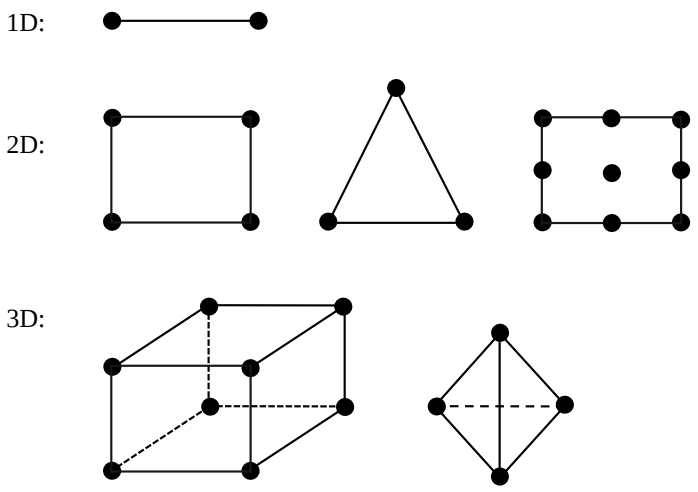

Figure 3.3: Continuum elements of various dimensions.

Structural elements are based on the deformation characteristics of certain structural elements such as trusses, beams or shells. Trusses, for example, only allow for axial displacement DOF, while beams account for rotation and translational DOF. Another subcategory of the structural elements is shells. Shell elements are used to discretize objects with small thickness compared to width or length. Shell elements, based on plate theory, enabling both bending and in-plane loading, are commonly used, see Figure 3.4 for examples of different kinds of structural elements.

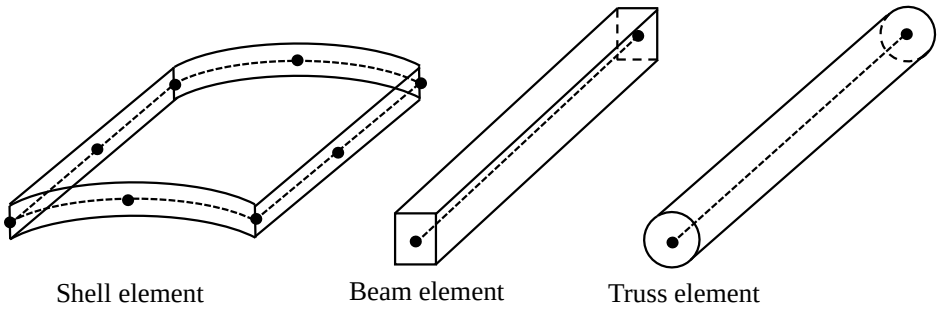

Figure 3.4: Different kinds of structural elements.

Element order refers to the number of nodes and the type of shape functions used within an element. The number of nodes indicates the points at which the DOF are evaluated. Most commonly elements are classified as either first-order (linear) or second-order (quadratic).

First-order elements have nodes only at the element corners, employing linear shape functions. They offer faster computation times but often require a highly refined mesh to achieve acceptable accuracy. Second-order elements include additional nodes along the element boundaries between corner nodes, utilizing quadratic shape functions. These elements enhance accuracy but result in longer computation times. The choice of element order affects both accuracy and computational efficiency. Numerical errors may arise depending on the element type and the nature of the analysis (ABAQUS, 2006).

Integration type refers to the numerical integration technique applied over finite elements to compute the stiffness matrix. Gaussian quadrature, a standard volume integration method, is commonly used in Abaqus. Two integration approaches are available when using Gauss integration, reduced and full integration. Both have their benefits and drawbacks.

Reduced Integration uses fewer integration points, resulting in faster computation but potentially reducing accuracy or introducing errors such as hour-glassing. Abaqus includes built-in functions to mitigate hour-glassing effects. Full Integration uses a higher number of integration points, improving accuracy but may cause issues such as shear locking and increases computational time. See Figure 3.5 for visual explanation of full vs. reduced Gauss integration.

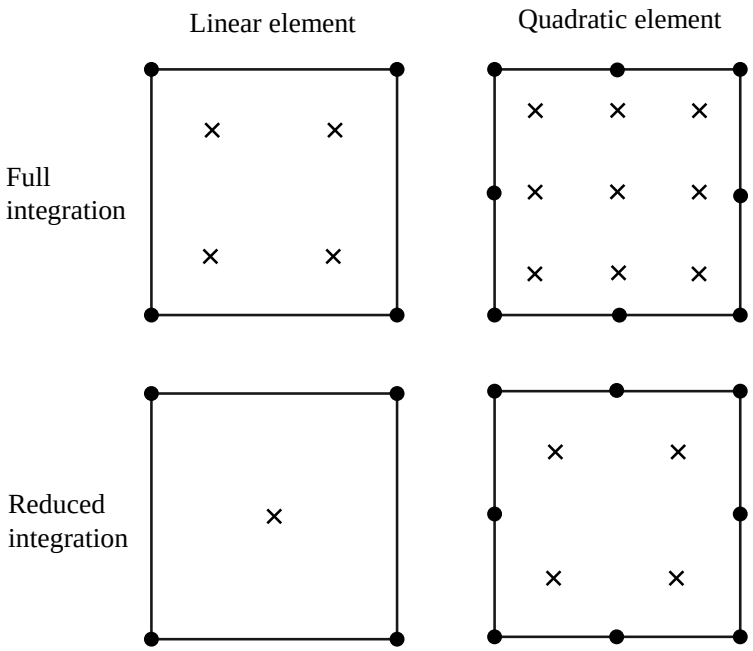

Figure 3.5: Reduced vs. full integration points for linear and quadratic elements using Gauss-integration.

Choosing the appropriate element and integration type is essential to balance accuracy, computational efficiency and avoiding numerical errors such as shear locking and hour-glassing effects (ABAQUS, 2006).

3.6 Mesh Convergence

A convergence study is essential in finite element analysis to ensure the accuracy and reliability of the numerical results. It involves systematically refining the mesh or adjusting other numerical parameters, such as element order or time step size, and observing how the solution approaches a stable value. Since FEA approximates continuous physical phenomena using discrete elements, very coarse meshes or improper element formulations can produce inaccurate results. A convergence study verifies that the solution is independent of the mesh density or other numerical parameters, ensuring that the obtained results accurately represent the underlying physical problem rather than numerical errors.

Increasing the number of elements increases the numerical accuracy but also the computational time. By conducting a convergence analysis the right amount of elements for convergence is obtained in balance with computational time and needed accuracy. Both static and dynamic buckling will be considered in this report. Kubiak (2013) suggests that one convergence analysis for each type of analysis should be conducted.

4 Methodology and pre-study of plate

4.1 Orientation

During out-of-plane bending of CSM, the top flange is the most critical with respect to buckling due to the compressive stresses being highest in that region. The compressed part of the CSM flange was initially simplified to a simple plate, see Figure 4.1. This choice was also motivated by the ease of experimental testing on such a structure in the future. The plate was modelled as an axially loaded plain steel plate, the effects of different parameters on the structural response were investigated in both static and dynamic cases. In this chapter, the modelling choices and the methodology used, are presented.

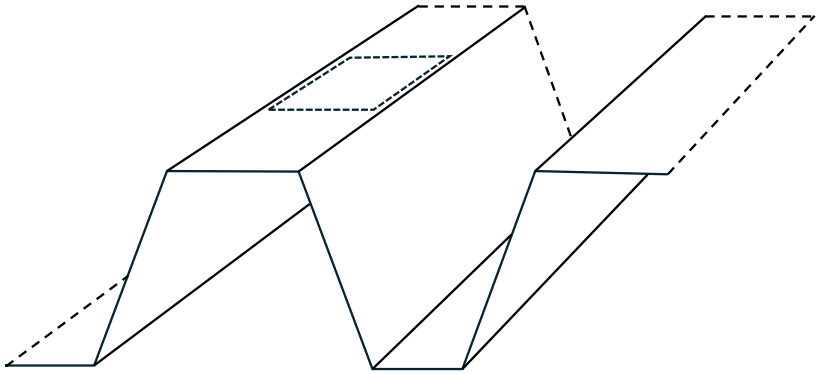

Figure 4.1: Visualization of the plate as a simplification of the top flange in a CSM section, see the dotted rectangle.

4.2 Selection of plate dimensions

Two main aspects were considered when selecting the plate dimensions. The first was practicality, the geometry must be compatible with testing equipment, Chalmers lab facilities was used as reference to allow for future experiments. The second was achieving a range of slenderness ratios, enabling the analysis of plates with varying slenderness to find different structural behaviour.

The dimensions of the plate were chosen to $b \times h = 100$ x 100 [mm]. A width of 100 mm is in line with the available test machine at Chalmers and since the height does not affect the critical buckling stress, see Equation (2.17), it was set to 100 mm to get a rectangular plate of reasonable size.

As seen in Figure 4.3, four thicknesses were chosen: a thickness of 1, 2, 3, and 4 mm, resulting in two geometries being in CSC4, one in CSC3, and one in CSC1. To support the choice of thickness, simple analytical calculations were made, see Appendix B. The slenderness λ_p was calculated in accordance with Equation (2.23), and the reduction factor ρ was calculated in accordance with Equation (2.22), with input parameters described in Section 2.3.5. The slenderness of the plate is presented in Figure 4.2 and the reduction factor vs. the plate thickness presented in Figure 4.3. In both figures, the circle represents what slenderness and reduction

factor the chosen thickness correspond to. The limits for each cross-section class was calculated in accordance with EN 1993-1-1, 2005.

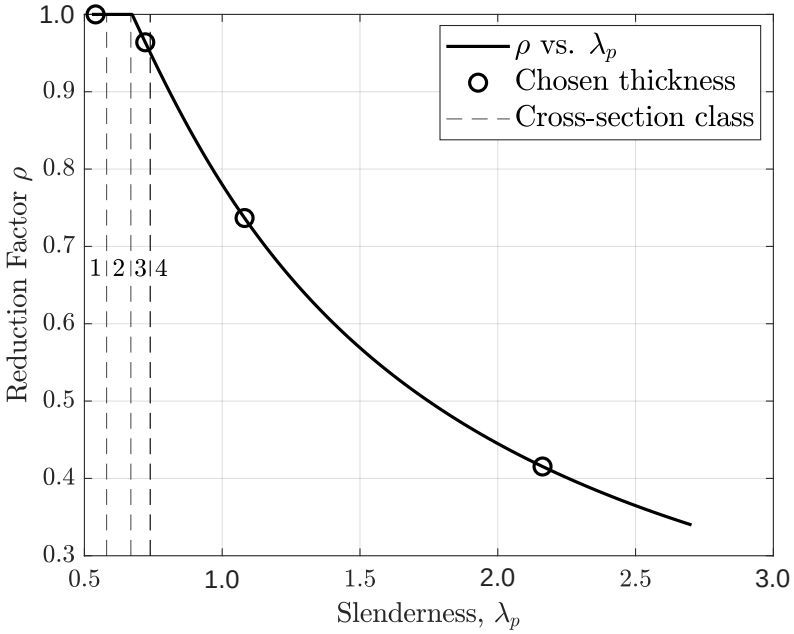

Figure 4.2: Reduction factor vs. slenderness.

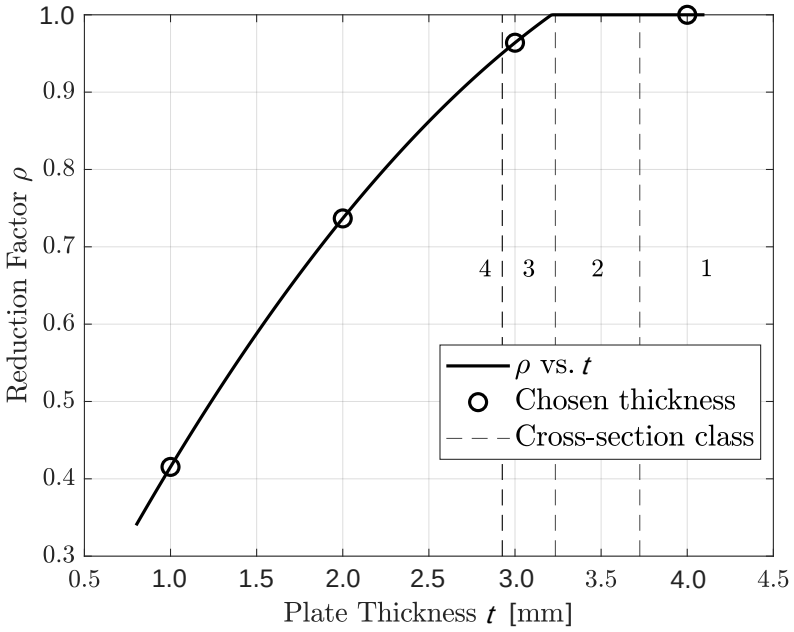

Figure 4.3: Reduction factor vs. thickness.

Regarding material strength, S355 steel with Young's modulus set 210 [GPa] was chosen since it is a commonly used steel quality. In Table 4.1, a summary of the results used to determine suitable thickness of the steel plate is presented. The expected critical buckling force, critical stress and the maximum load-carrying

capacity in the post-critical range are also presented. Note that the calculation is based on zero residual stresses or initial imperfections, while the CSC is based on the limits in Eurocode which considers imperfections and residual stresses. This explains the very high critical buckling force and stress, which are overestimated compared to a real plate. In this case the critical buckling force and stress are only used as validation of the Abaqus model.

Table 4.1: Summary of buckling parameters for different thicknesses t.

t **(mm)**	**CSC**	$\boldsymbol{\lambda}$	$\boldsymbol{\rho}$	$\boldsymbol{P}_{\text{cr}}$ [kN]	$\boldsymbol{\sigma}_{\text{cr}}$ [MPa]	$\boldsymbol{P}_{\text{max}}$ [kN]
1	4	2.16	0.42	7.59	75.9	16.4
2	4	1.08	0.74	60.7	304	65.6
3	3	0.78	0.96	205	683	148
4	1	0.54	1.00	486	1215	262

Table 4.2: Summary of mechanical properties for a steel plate with different thicknesses t.

t **(mm)**	$b \times h$ **[mm]**	$\boldsymbol{E}$ [GPa]	$\boldsymbol{f_y}$ [MPa]	$\boldsymbol{\nu}$	$\boldsymbol{\rho}$ [kg/m^3]	**Material**
1, 2, 3 and 4	100×100	210	355	0.3	7850	Steel

4.3 Choice of initial imperfections

To initiate plate buckling an imperfection shape was prescribed to the plate, several out-of-plane magnitudes were considered, see Table 4.3. In EN 1993-1-5 (2005) Annex C, it is stated that for a panel or sub-panel with short span a or b, the minimum of $a/200$ and $b/200$ is recommended to be used as initial imperfections, herein denoted e, which motivates the choice of $e = 0.5$ mm. An imperfection of $e = 0.01$, which can be considered to be negligible, was chosen to mimic the behaviour of a perfect plate. Note that the imperfection cannot explicitly be set to e = 0 since a second order analysis is run in Abaqus, if no eccentricity or horizontal force is initiating the second order effects, the reaction force in the load-deflection plot will be equal to F_y, meaning that the plate cross-section yields in compression even though the plate should buckle before reaching the yield stress.

Table 4.3: Relation between initial imperfection size e and relative size b/x.

e	0.01	0.1	0.25	0.5	1	2
Magnitude	$b/10000$	$b/1000$	$b/400$	$b/200$	$b/100$	$b/50$

4.4 Material model

The static stress-strain behaviour of various steel grades can be determined either through experimental material testing or by applying established constitutive models when test data is unavailable. In this study, hot-rolled steel was used, and the engineering stress-strain curve was derived using a bilinear model combined with non-linear hardening.

The model described by Equation (4.1) is proposed by Yun and Gardner (2017) and is based on data from over 500 experimental stress-strain curves on hot-rolled steels from the global literature.

$$f(\epsilon) = \begin{cases} E\,\epsilon, & \text{for } \epsilon \leq \epsilon_y \\ f_y, & \text{for } \epsilon_y < \epsilon \leq \epsilon_{sh} \\ f_y + (f_u - f_y)\left\{0.4\,\mu + \dfrac{2\,\mu}{[1 + 400\,\mu^5]^{1/5}}\right\}, & \text{for } \epsilon_{sh} < \epsilon \leq \epsilon_u \end{cases} \tag{4.1}$$

Where:

$$\mu = \frac{\epsilon - \epsilon_{sh}}{\epsilon_u - \epsilon_{sh}} \tag{4.2}$$

$$\epsilon_u = 0.6\left(1 - \frac{f_y}{f_u}\right), \quad \text{but } \epsilon_u \geq 0.06 \text{ for hot-rolled steels} \tag{4.3}$$

$$\epsilon_{sh} = 0.1\frac{f_y}{f_u} - 0.055, \quad \text{but } 0.015 \leq \epsilon_{sh} \leq 0.03 \tag{4.4}$$

In Figure 4.4 the stress-strain relationship obtained using Equation 4.1 is presented.

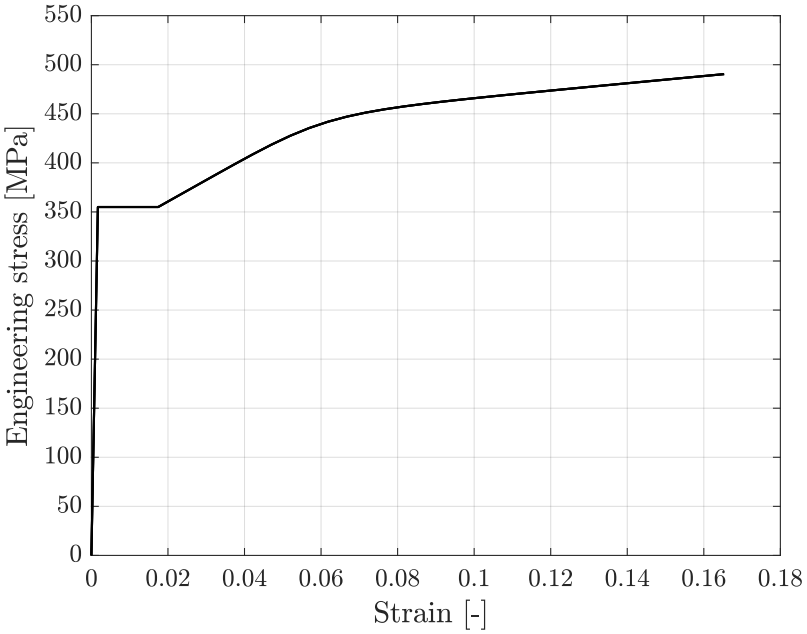

Figure 4.4: Material model for hot rolled steel using S355 grade steel, $f_y = 355$ MPa, $f_u = 490$ MPa, $E = 210$ GPa.

4.4.1 True stress and strain

Engineering stress and strain do not accurately capture the physical changes in geometry and must be converted into true stress and true strain. For steels,

engineering stress is determined through tensile tests performed on steel rods, during which load versus elongation is measured. Engineering stress is calculated as the applied force divided by the original cross-sectional area, while engineering strain is calculated as the measured elongation divided by the original length.

In reality, as the load increases, the cross-sectional area decreases, resulting in higher stress than indicated by engineering stress. Additionally, the reference length continuously increases between load steps, causing the true strain to be smaller than the engineering strain, which is based on the original length.

To compute the true stress and true strain, Equation (4.5) and (4.6) are commonly used (Faridmehr et al., 2014).

$$\sigma_{\text{true}} = \sigma_{\text{eng}}(1 + \epsilon_{\text{eng}}) \tag{4.5}$$

$$\epsilon_{\text{true}} = \ln(1 + \epsilon_{\text{eng}}) \tag{4.6}$$

In Abaqus, the elastic part of the material model is input via Young's modulus. The plastic part is implemented by inputting the true plastic stress-strain. The engineering stress-strain in Figure 4.4 was turned into true stress-strain using Equation (4.5) and (4.6), see Figure 4.5. The true plastic stress was obtained as the stress values from initiation of plastic deformation and forward while true plastic strain was obtained by subtracting the maximum true elastic strain from the true strain.

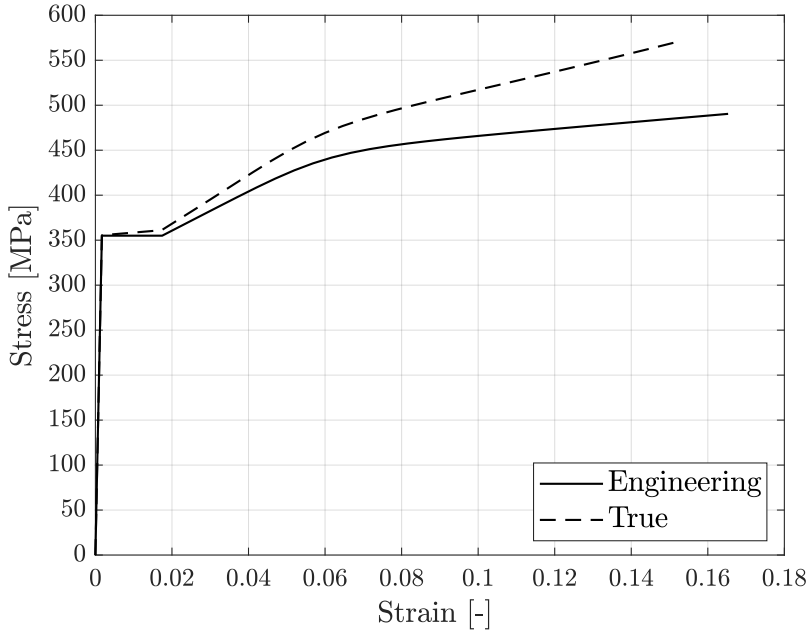

Figure 4.5: Engineering stress-strain vs. true stress-strain. The engineering version underestimates the relation during plastic deformation.

4.4.2 Variation of yield and ultimate strength

During very rapid loading it is expected that the material parameters f_y and f_u increase; to simulate this effect but without performing a dynamic analysis, one

can manually increase f_y and f_u.

In the static plate analysis four different material models were used. The different materials are denoted as material A, B, C and D, were material A is the original material that was presented in Section 4.4. Note that B, C and D are fictional materials, if their F_y and F_u were to be implemented in the same material model used to compute material A, they would look completely different. Instead they were made by interpolation, to get a distinct change in material behaviour.

The resulting stress-strain relationships for material A, B, C and D that is supposed to represent different strain rates are presented in Figure 4.6.

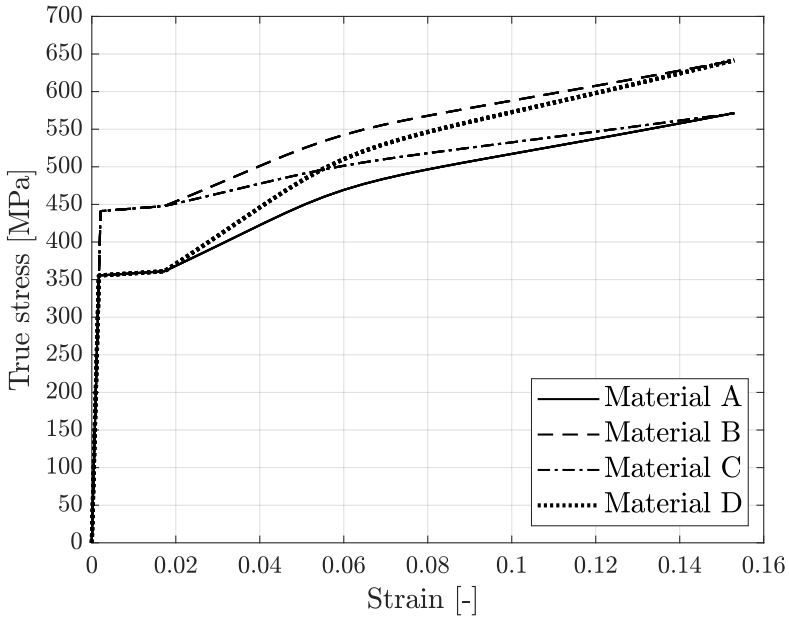

Figure 4.6: Stress-strain relationship to obtain fictional strain rate effect.

4.5 Geometry and element type

The plate was discretized using S4R shell elements (4-noded shell elements with reduced integration). Shell elements require significantly fewer degrees of freedom compared to solid elements, making the simulation computationally efficient while still capturing the essential structural behaviour. Shell elements are designed specifically for thin-walled structures, where one dimension (the thickness) is much smaller than the other two. Simply supported plates primarily experience bending and in-plane forces, both of which are efficiently captured using shell elements. Shell elements allow for buckling and post-buckling analyses without the need for excessive mesh refinement. They also support large deformation theory (by enabling Nlgeom in Abaqus), which is essential for studying plate instability and post-buckling behaviour.

The studied plate geometry is presented in Figure 4.7 with measurements in accordance with Section 4.2. Visually it appears as if the thickness is infinitely thin, which is not the case. A thickness is applied in the section module, mirrored around the midpoint line where the degrees of freedom are located.

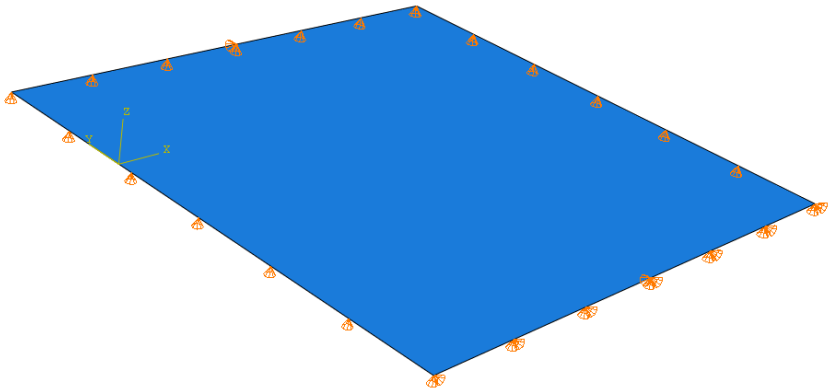

Figure 4.7: Geometry of the studied steel plate.

4.6 Boundary conditions

Two different boundary conditions were considered, referred to as case 1 and case 2, see Figure 4.8. Both cases are simply supported out-of-plane (z-direction) and restrained from moving in-plane (y-direction) at the unloaded edge. In case 1, the plate is allowed to contract and expand in the x-direction, a constraint is applied only in two nodes in the x-direction to prevent rigid body motion. In case 2, no contraction or expansion in the x-direction is allowed. The boundary conditions are further summarized in Table 4.4.

In reality, the plate boundary conditions lie somewhere between case 1 and 2. For a CSM section, the flange (here simplified to a plate) is supported by the webs. The webs will provide resistance in the x-direction to some extent but are likely not rigid enough to provide zero displacement, thus case 1 and 2 represent two extreme cases. Only case 1 is considered in the main analysis, however the effect of case 2 is briefly investigated.

Table 4.4: Boundary conditions for different cases.

Case	Side	Ux	Uy	Uz	URx	URz	URz
1	AB		•	•			
	CD (loaded edge)			•			
	AD and BC			•			
	Mid node of AB and CD	•	•	•			
2	AB		•	•			
	CD (loaded edge)			•			
	AD and BC	•		•			
	Mid node of AB	•	•	•			

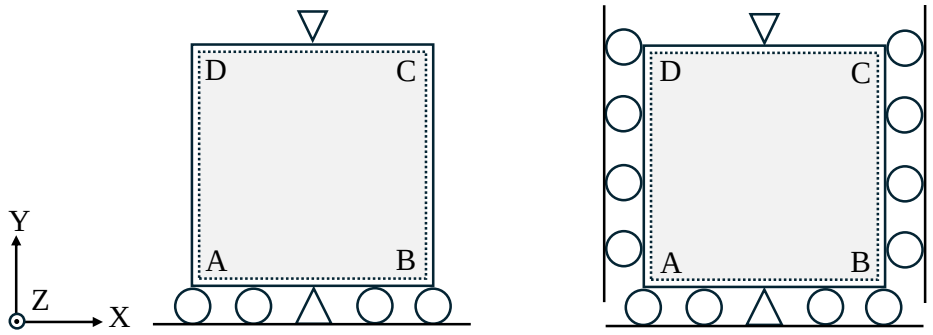

Figure 4.8: Boundary conditions, case 1 to the left, case 2 to the right.

4.7 Convergence study

As stated in Section 4.2, dimensions of $b \times h$=100×100 mm were chosen. To ensure adequate results, a convergence study was performed. In Table 4.5, the results of this are presented. The percentage change in the rightmost column was calculated as:

$$\left(\frac{\lambda_{\text{current,mesh}}}{\lambda_{\text{previous,mesh}}} - 1 \right) \times 100 \tag{4.7}$$

The study was conducted for the steel plate with a thickness of 1 mm, as a more slender plate is more sensitive to the mesh size. In Figure 4.9, the same results are visualized. Based on this, a mesh with 20×20 elements was selected.

An even number of elements was used for all mesh settings to ensure symmetry. An asymmetrical mesh might slightly affect the results since the maximum out-of-plane displacement will not occur exactly in the middle. Although a very fine mesh could resolve this issue, the goal was to achieve a relatively coarse mesh with fast computational time that still delivers converged results.

Table 4.5: Comparison of first eigenvalue for different mesh sizes with λ values rounded off to two decimals.

Elements	Total Elements	λ	Diff [%]
4x4	16	0.85	-
6x6	36	0.79	-5.96%
10x10	100	0.77	-3.08%
14x14	196	0.76	-0.90%
20x20	400	0.76	-0.54%
34x34	1156	0.76	-0.45%
50x50	2500	0.75	-0.21%

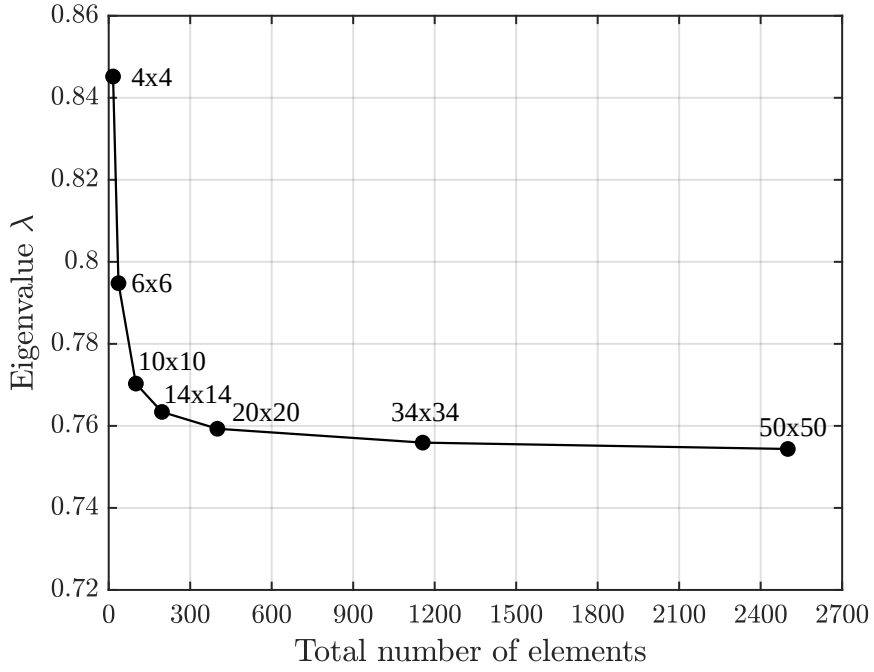

Figure 4.9: Buckling factor λ vs total number of elements.

4.8 Static analysis

A static non-linear buckling analysis was performed in Abaqus to investigate the structural response of thin-walled plates under in-plane compressive loading. The static analysis serves as a foundation for subsequent investigations, including the introduction of imperfections and comparison with analytical predictions.

The analysis consists of linear eigenvalue buckling analysis and non-linear post-buckling simulations. The linear buckling analysis provides the critical load which was used for validation of the model and the buckling mode shape was used as geometric imperfection shape in the non-linear simulations. A displacement-controlled approach is adopted for the non-linear analysis to capture post-buckling behaviour while ensuring numerical stability. Shell elements are employed due to their ability to accurately represent thin-walled structures. Different boundary conditions were tested to assess their influence on buckling behaviour.

4.8.1 Analysis steps

In the finite element analysis different steps are used to simulate various loading conditions and to capture different phenomena.

To determine the critical buckling load and imperfection shape, a linear eigenvalue buckling analysis was performed. The first buckling mode and its eigenvalue were used since that is the critical shape the plate will obtain. The resulting eigenvalue was multiplied with the resulting reaction force to obtain the critical load. For example if $\lambda = 0.7$ and the reaction force is 100 N/mm distributed over an edge with length 100 mm, then P_{cr} will be 7 kN. The buckling analysis uses a linear perturbation procedure through the Buckle step (small change in stiffness due to loading), utilizing the subspace iteration method, which is a numerical method that extracts the lowest (most critical) eigenvalues and their corresponding buck-

ling mode shapes.

For the non-linear static analyses, the Static general step was used, with the Nlgeom (Nl = nonlinear, geom = geometry) option enabled to account for geometric nonlinearity. Within this step, the displacement increment is adaptively adjusted to ensure sufficient data acquisition, enabling accurate and efficient capture of non-linear behaviour.

In the non-linear static analysis, an initial increment size of 0.0025 was used (which is a fraction of the total displacement i.e. the increment size in mm is 0.0025 $\times$ final displacement), with a maximum increment size of 0.0025 and a maximum of 10.000 increments. If convergence issues were encountered, both the initial and maximum increment sizes were reduced to 0.001. This adjustment was necessary for some imperfection amplitudes in the more slender plates studied.

The following list summarizes the implementation of Abaqus CAE across various steps that were used for the static analysis.

- **Step module:** Linear perturbation $\rightarrow$ Buckle $\rightarrow$ Eigensolver: Subspace
- **Step module:** General $\rightarrow$ Static, General

To save the imperfection shape, one has to add a text phrase in the keywords options of the linear buckling model. When the job is run, a .fil file containing the normalized deformation mode is saved with the same name as the job. The following was written under FIELD OUTPUT in keywords:

*NODE FILE, GLOBAL=YES, LAST MODE=1
U

The geometric imperfections are then introduced into the non-linear static buckling model by adding another line in the keywords option for the non-linear static buckling model. The following was written under STEP in keywords:

*IMPERFECTION, FILE=name of imperfection file, STEP=1
1, 0.01

Where on the second line, 1 refers to the buckling mode number, and 0.01 represents the magnitude of the initial imperfection, with the units consistent with those already implemented in the model. See Section 5.1.2 for the obtained shape. In this study, only the first mode shape was used to define the imperfections, as it is the most critical shape, however various imperfection amplitudes were tested.

4.8.2 Load application

A displacement-controlled approach was used, where the displacement was gradually increased linearly from 0 to 8 mm. Selecting an excessively large prescribed displacement can cause convergence issues toward the end of the analysis when significant deformations have occurred. This consideration motivated the choice of a limit of 8 mm.

To determine the force corresponding to the prescribed displacement, the reaction forces (RF2 in Abaqus) at the unloaded edge parallel to the loaded edge were summed, as shown in Equation 4.8.

$$F = \sum_{n} \text{RF2} \tag{4.8}$$

4.8.3 Displacement controlled vs. Load controlled

As stated in Section 3.3, various methods can be used to control the load. Before opting for the displacement-controlled loading, a shell edge load was applied.

This approach resulted in unexpected results. Given that the most critical imperfection shape (first buckling mode) is symmetric around the midpoint of the plate, see Figure 4.10 a), it was expected that buckling would initiate at the midpoint and the out-of-plane deflection would increase symmetrically around it.

When applying the force using shell edge load the expected behaviour was not observed. Instead, a fold emerged near the loaded edge. The post-buckling deformation shapes for the two loading methods are presented in Figure 4.10 b) and c).

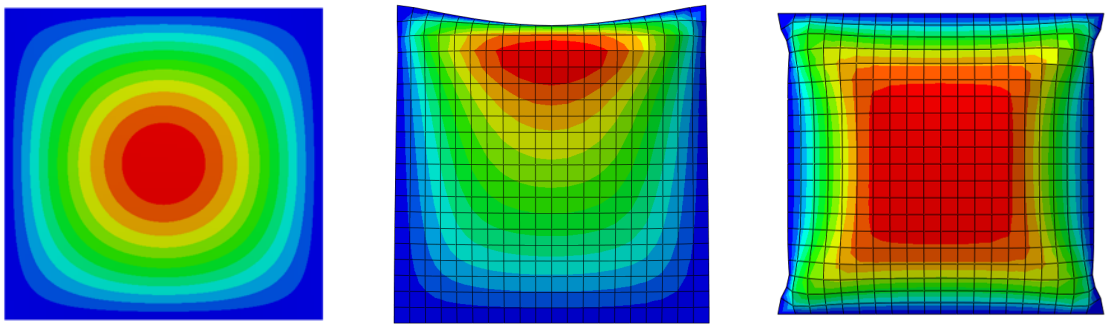

a) b) c)

Figure 4.10: a) Imperfection shape and Post-buckling deformation shape for: b) Load-controlled loading, c) Displacement-controlled loading.

Theoretically, displacement controlled loading should result in more symmetrical results since displacement boundary conditions are imposed on both the loaded edge and the opposite parallel edge. In contrast, load controlled loading is inherently asymmetrical due to the nature of the force application. However, the significant difference in post-buckling behaviour is unexpected, as the two approaches should theoretically produce similar results.

When the out-of-plane boundary conditions along the edges parallel to the loading direction are removed, allowing the plate to behave like a column, the method of loading appears to have no influence. This is likely because a simpler collapse mechanism occurs for a column compared to a plate, making the loading method less critical.

It was also observed that the same ultimate load is achieved regardless of the loading method. The discrepancy lies solely in the post-buckling behaviour, which is particularly important for this study.

4.9 Dynamic analysis

The dynamic analysis was conducted to investigate the structural response under increased loading rates. This analysis is the main focus of the thesis, and the results were compared to the static analysis to identify any differences.

The dynamic analysis was performed in two steps. In the first step, strain-rate effects were turned off to isolate the influence of dynamic effects on the structural response. In the second step, strain-rate effects were activated to represent the "real case," incorporating strain-rate effects and other dynamic phenomena. The analysis covers both the buckling and post-buckling phases. The same element type and boundary conditions were used as in the static case, and mesh discretization was consistent with that of the static analysis to enable a direct comparison of the results.

4.9.1 Analysis step and settings in the step module

Implicit analysis was used (see Section 3.2) in order to reduce computation time. The implicit analysis proved to be sensitive to increment size, resulting in two different solutions (post peak) depending on the chosen increment size, see Appendix A for further explanations. The two steps needed for the dynamic analysis are:

- **Step module:** Linear perturbation → Buckle → Eigensolver: Subspace (reused from the static analysis)
- **Step module:** General → Dynamic, Implicit

Automatic increment size generation: In Abaqus, during a dynamic implicit step, the automatic increment size generation is a part of ensuring numerical stability and efficiency. The time increment size is adapted throughout the simulation based on convergence behaviour, error estimates, and problem characteristics. In a dynamic implicit step in Abaqus, the following needs to be specified: total step time, initial increment size, minimum increment size, maximum increment size, and maximum number of increments (if automatic increment size generation is used).

The total step time depends on the desired total deformation and the velocity applied to the plate. For example, if a total in-plane deformation of 8 mm is required and a prescribed velocity of 0.01 mm/s is used, the total step time will be 800 seconds.

Regarding the initial increment size selection, an initial time increment, $\Delta t_{initial}$, is chosen; Abaqus uses this value to start the analysis. If the initial increment is too large and causes convergence issues, Abaqus will reduce it automatically.

The minimum increment size, Δt_{min}, prevents Abaqus from reducing increments too much.

The Maximum increment size, Δt_{max}, prevents Abaqus from taking excessively large increments that miss critical events.

The maximum number of increments dictates how many increments Abaqus is allowed to use in total before aborting the analysis.

Abaqus automatically adjusts the time increment size based on convergence be-

haviour, if convergence is difficult (many iterations or cutbacks), Abaqus reduces the increment. If convergence is smooth, Abaqus increases the increment. Abaqus monitors response quantities like displacement, velocity, and acceleration. If rapid changes occur, the increment is reduced to capture transient effects accurately.

In Table 4.6 the set-up used in the step settings is presented (if nothing else is specified), the settings are changed when the velocity is changed. Examples for two velocities are shown in the Table. For velocities below 10 mm/s the maximum increment is chosen so that:

(total step time) / 500 = Δt_{max}

and the minimum increment is chosen so that:

(ramp up time) / 10 = $\Delta t_{initial}$.

The load ramp-up time, where Abaqus's smooth step function is utilized (see Section 4.8.2), is set to 1/800 of the total time. For instance, if the total step time is 800 seconds, the ramp-up time will be 1 second.

Table 4.6: Settings used for different velocities

	0.01 mm/s	**1 mm/s**
Total Step Time [s]	800	8
Increment Sizes		
Initial	0.1	0.001
Minimum	1×10^{-6}	1×10^{-8}
Maximum	1.6	0.016
Maximum Number of Increments	2000	2000

For velocities higher than 10 mm/s Δt_{max} is chosen differently since more data points is needed to avoid the risk of missing important events in the force displacement curves, a Δt_{max} that yields in approximately 4000 data points is chosen instead.

4.9.2 Dynamic load application

A displacement controlled approach was used by prescribing a velocity to the nodes at the loaded edge. Load amplitude smooth-step was used to ramp up the the velocity since the loading speed cannot be applied full magnitude at once without an increased risk of introducing numerical errors. The full amplitude should however be reached before the peak load is reached since the behaviour at the peak load and post-buckling is of interest. If the maximum velocity is reached after the ultimate load, a different velocity and strain rate than intended is studied, hence it is of importance to choose a ramp up time that is suitable, it needs to be slow enough to avoid numerical errors but fast enough to reach its maximum amplitude before the ultimate load is reached.

Smooth-step interpolates a curve in-between two or more given points, see Figure 4.11. The vertical axis indicates the load multiplier, ranging from 0 to any magnitude. The horizontal axis indicates the step time.

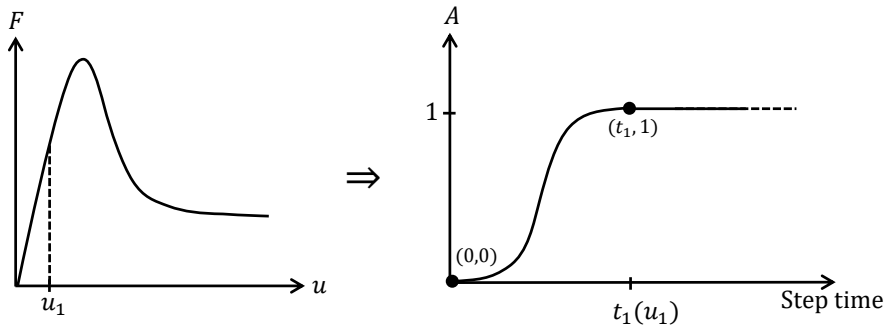

Figure 4.11: Full velocity amplitude (=1) reached around a displacement u_1 at step size t_1.

The point at t_1 indicates the time of which the multiplier equals 1 and has to be estimated. By using the prescribed velocity one can compute the time it takes to reach a certain displacement u_1 smaller than the displacement at the ultimate load.

The amount of time steps n, is computed by dividing the total desired prescribed displacement (in our case 8 mm) by the prescribed full velocity. t_1, the time it takes to reach u_1 is computed by dividing u_1 with the full velocity. By inserting the coordinates (0,0) and (t_1,1) in the smooth step amplitude settings, robust loading is obtained.

Velocity application in Abaqus is presented in Figure 4.12.

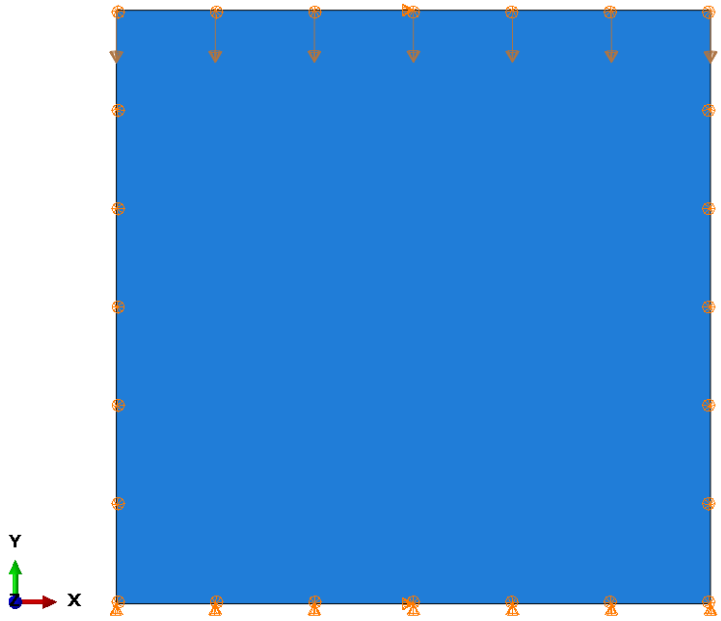

Figure 4.12: Velocity application on loaded edge.

4.9.3 Choice of loading speed

The loading in the dynamic analysis is applied by prescribing a velocity on the nodes of the loaded edge. The loading speeds were chosen based on the speed capacity of the experimental setup at Chalmers, with a maximum speed of around 200 mm/s. The lowest velocity was chosen to 0.1 mm/s to simulate static loading. Several other velocities were chosen within this interval to capture the behaviour for different strain rates. It should be noted that explosions may result in impulsive loads with significantly higher strain rates than those produced by these loading speeds. However, dynamic effects will still be captured regardless. See Table 4.7 for the chosen velocities. To go between velocity and strain rate, the velocity was simply divided by the plate height, see Equation 4.9 (the compressed edge displacement in comparison to the original height).

$$\dot{\epsilon} = \frac{v}{h} \tag{4.9}$$

Table 4.7: Chosen velocities and resulting strain rate.

Velocity [mm/s]	0.1	1.0	10	20	50	100	200
Strain rate [s^{-1}]	10^{-3}	10^{-2}	0.1	0.2	0.5	1.0	2.0

4.9.4 Choice of coefficients in dynamic constitutive model

To take into account the strain rate-dependent behaviour in the dynamic analysis, the Cowper-Symonds model described in Section 2.4.4 was chosen. Cowper-Symonds is implemented in Abaqus, named power law, see Equation 4.10 that can be rewritten into $R(\dot{\epsilon}) = DIF$, see Equation 4.11. Only the coefficients D and p are needed to implement the model in Abaqus.

$$\dot{\epsilon_{pl}} = D(R-1)^p \tag{4.10}$$

$$R = 1 + \left(\frac{\dot{\epsilon_{pl}}}{D}\right)^{\frac{1}{p}} = DIF \tag{4.11}$$

The values of D and p, as suggested by Yang et al. (2022) (see Section 2.4.4), are presented for S355 steel in Table 4.8. Additionally, the values provided by Paik and Thayamballi (2003b) for so-called mild steel and high-tensile steel are included in the same table. However, it is unclear which specific steels fall into these categories; S355 is likely somewhere in between.

Table 4.8: Suggested material parameters from different literature.

Source	D	p
Yield, Yang et al., 2022 (DIF_y)	4795	4.0
Average,Yang et al., 2022 (DIF_{avg})	11884	3.3
Mild steel, Paik and Thayamballi, 2003b	40.4	5.0
High tensile steel, Paik and Thayamballi, 2003b	3200	5.0
S355, Sargsyan and Sargsyan, 2024 (DIF_y)	1094	3.47

Increasing the values of D and p leads to reduced dynamic effects since DIF decreases. DIF is plotted for the tabulated values of these coefficients in Figure 4.13. Due to uncertainty in the suggested D and p values, a visual inspection of the graph was made and $D = 4795$ results in a slightly higher DIF than $D = 11884$. Therefore, the smaller D and p (4795 and 4.0) were chosen since dynamic effects become more prominent, which was more suitable for this study where the main goal is to study dynamic effects. The chosen velocities and the obtained dynamic increase factor is presented in Table 4.9.

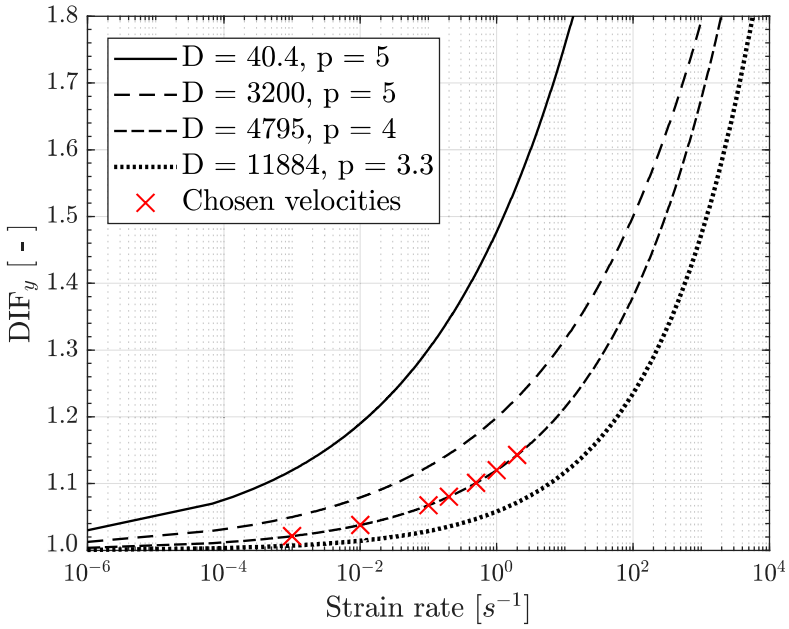

Figure 4.13: DIF calculated for chosen material coefficients in Table 4.8. Chosen velocities marked as red cross to indicate the obtained strain rate and dynamic increase factor.

Table 4.9: Resulting DIF for the chosen velocities.

Velocity [mm/s]	0.1	1.0	10	20	50	100	200
Strain rate [s^{-1}]	10^{-3}	10^{-2}	0.1	0.2	0.5	1.0	2.0
DIF$_y$ [-]	1.0214	1.04	1.07	1.08	1.10	1.12	1.14

5 Results of the plate study

5.1 Static analysis

5.1.1 Validation of static model

To verify the Abaqus model, a comparison was made between the analytical results obtained using Equation (2.19) and the critical buckling load determined from the linear static buckling analysis in Abaqus. The results show close alignment, indicating that the model setup is accurate.

Table 5.1: Comparison of analytical and numerical results for different thickness values.

t [mm]	P_{cr} **Analytical [kN]**	P_{cr} **Numerical linear [kN]**	**Difference [%]**
1	7.59	7.62	0.4%
2	60.7	60.5	-0.3%
3	205	202	-1.5%
4	486	474	-2.5%

5.1.2 Eigenvalue analysis

To determine the shape of the initial imperfection, an eigenvalue buckling analysis was performed. The first ten buckling mode shapes (in order) are shown in Figure 5.1, and the first mode was selected as the basis for the initial imperfection shape used in the subsequent analyses for the steel plates. In the figure, the out-of-plane displacement is shown. There is a large difference in eigenvalue depending on eigenmode; the first mode has $\lambda = 0.75$ and the last has $\lambda = 6.4$.

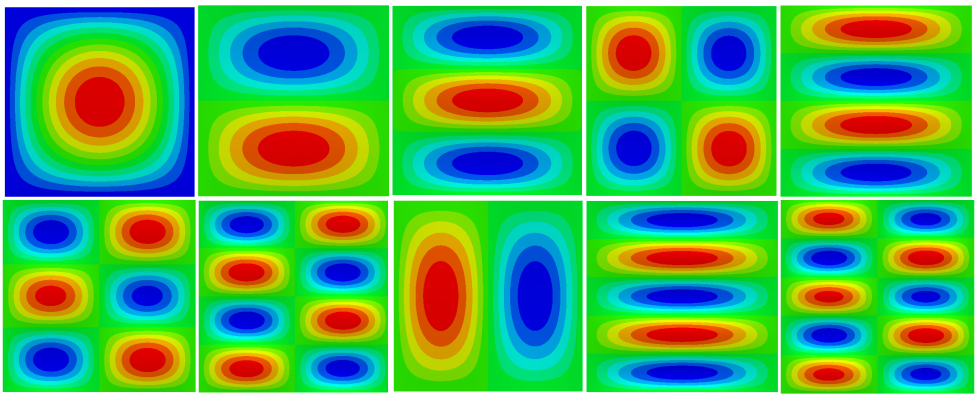

Figure 5.1: First 10 eigenmodes.

5.1.3 Effect of initial imperfections

To study the effect of initial imperfections, force-displacement plots were made for both in-plane and out-of-plane displacement. Since the load is displacement-controlled, the reaction force at the bottom of the plate represents the applied force that would be required to induce the same displacements. See Figure 5.2 for the nodes that data was extracted from. Several imperfection magnitudes were considered, See Section 4.3. The force-displacement plots are presented in Figure 5.3 to 5.10. The following notations are used in the plots:

- F_y - applied force that results in yielding of the cross-section if buckling is not critical.
- P_{cr} - critical buckling load for plate without initial imperfections.
- e - prescribed initial imperfection magnitude, unit millimetres (mm).

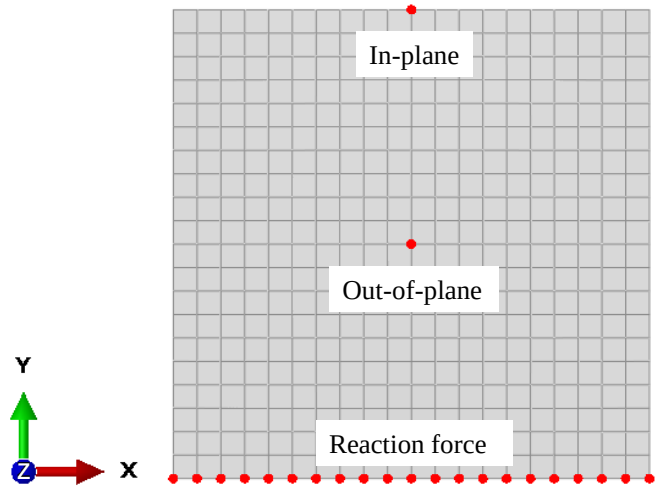

Figure 5.2: Clarification of which nodes data was extracted from.

The response for the 1 mm thick plate is presented in Figure 5.3 and 5.4. Looking at $e = 0.01$, the plate buckles close to the theoretical buckling load, as seen by the nick in the graph in Figure 5.4. Due to post-buckling strength, the load continues to increase before failure at around 16 kN. Following the peak load the force rapidly decreases but starts to converge, entering an area of post-peak strength, where displacements increase but the force is almost constant. As e increases the buckling point becomes less pronounced and the post-buckling strength is reduced.

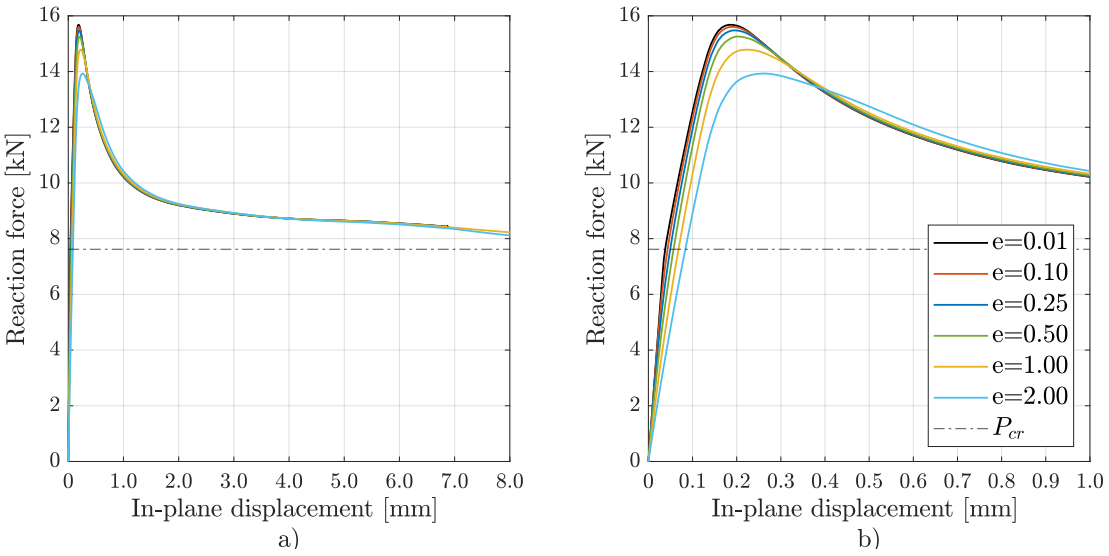

Figure 5.3: Force vs. In-plane displacement for a plate thickness of 1 mm. a) full graph, b) zoomed in on a range of 0-1 mm displacement.

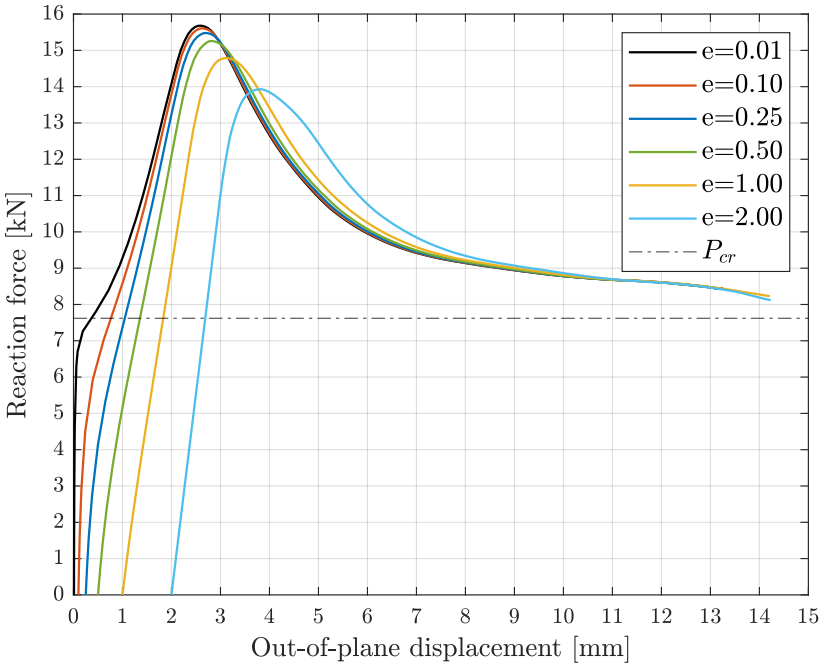

Figure 5.4: Force vs. Out-of-plane displacement for a plate thickness of 1 mm.

The response for the 2 mm thick plate is presented in Figure 5.5 and 5.6. P_{cr} is larger, closer to F_y. A similar behaviour as for 1 mm thickness is seen, except that the post-buckling strength increase is smaller. Looking at $e = 0.01$ in Figure 5.6, buckling is reached slightly below P_{cr}, followed by a small increase in strength until failure occurs at around 60 kN, that happens to coincide with P_{cr}.

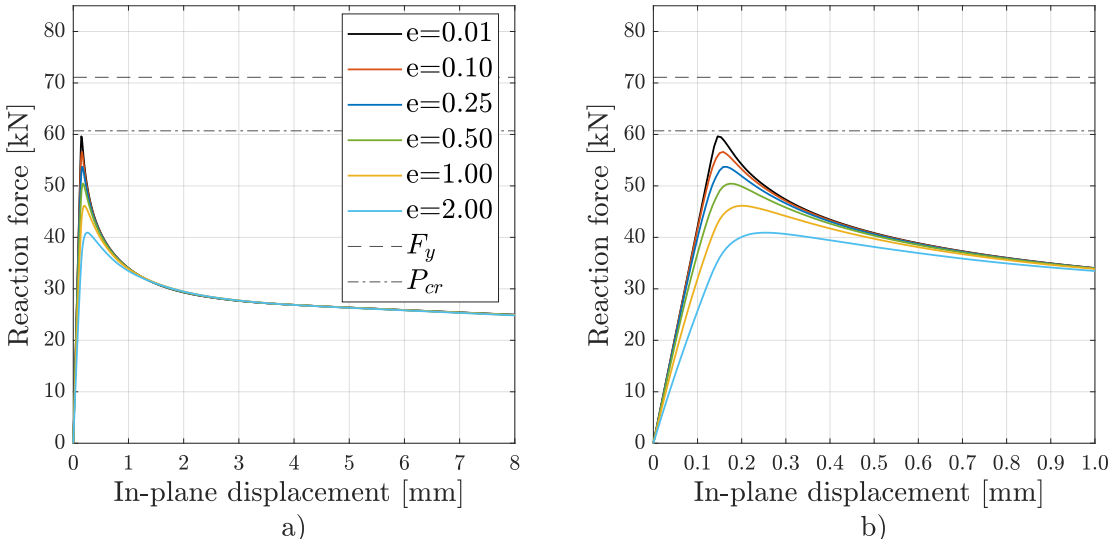

Figure 5.5: Force vs. In-plane displacement for a plate thickness of 2 mm. a) full graph, b) zoomed in on a range of 0-1 mm displacement.

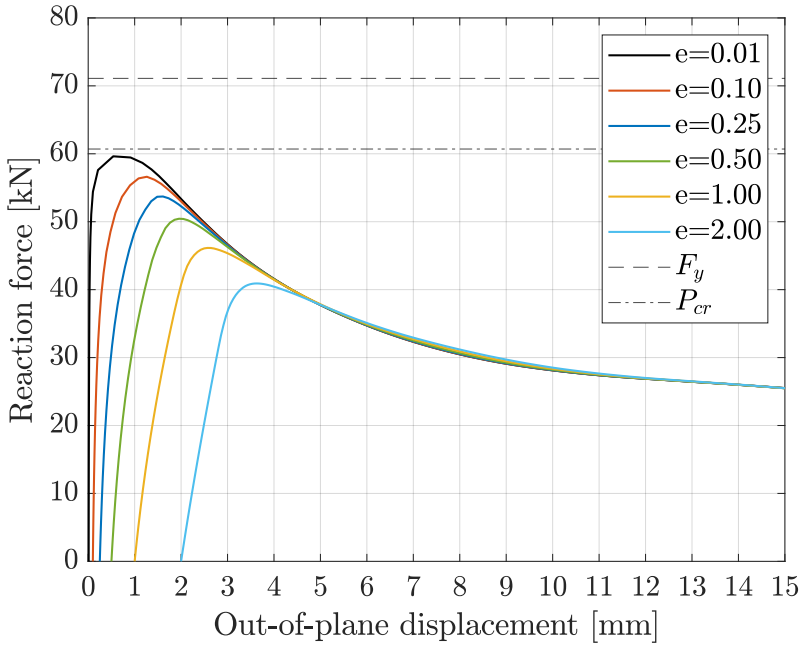

Figure 5.6: Force vs. Out-of-plane displacement for a plate thickness of 2 mm.

The response for the 3 mm thick plate is presented in Figure 5.7 and 5.8 and the 4 mm thick plate presented in Figure 5.9 and 5.10. P_{cr} is larger than F_y in both cases. Looking at the 4 mm thick plate, for smaller $e = 0.01, 0.10, 0.25$ no buckling occurs in the elastic range. The plate is elastic until the yield plateau is reached, initiating plastic deformation with strain hardening. The plate then suddenly fails due to buckling from second order effects introduced by the plastic deformation. The amount of plastic deformation before failure decreases with increased e. For larger $e = 0.5, 1.0, 2.0$ the yield plateau is not reached and the plate buckles for loads lower than F_y due to the imperfections. If $e = 0$ the resulting force displacement relation would resemble the material model e.g., no buckling and fails when f_u is reached. The described behaviour is less prominent for the 3 mm thick plate.

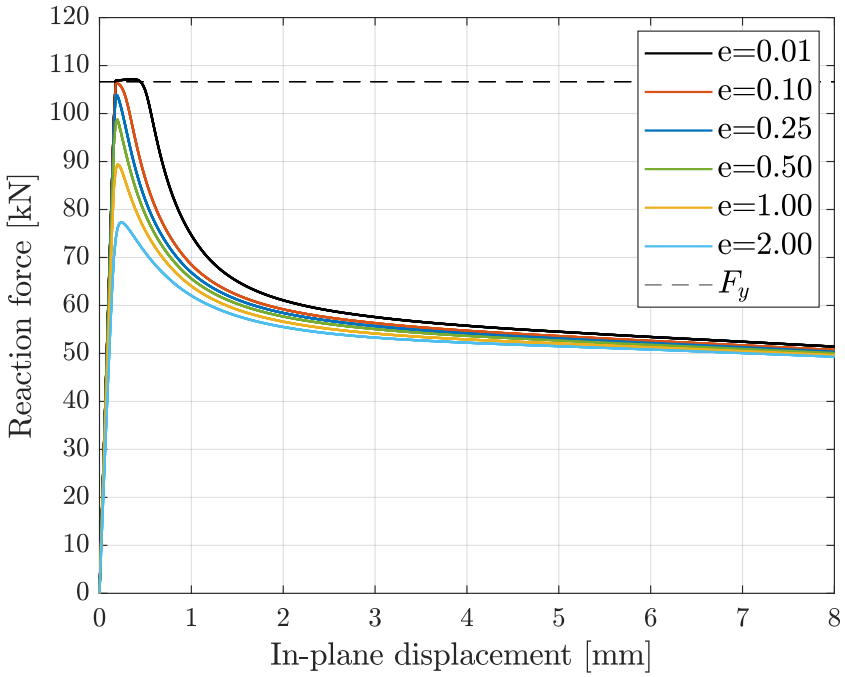

Figure 5.7: Force vs. In-plane displacement for a plate thickness of 3 mm.

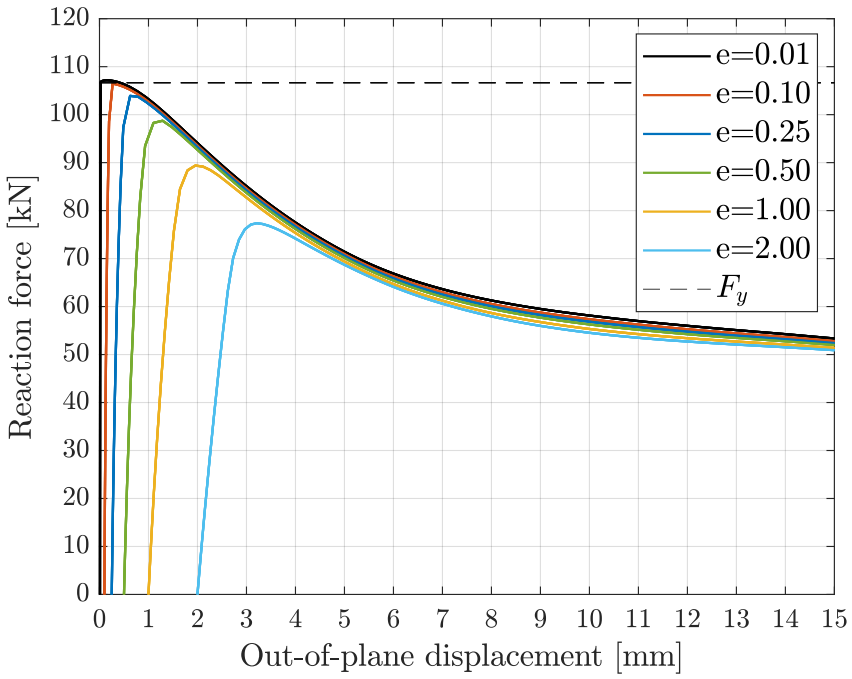

Figure 5.8: Force vs. Out-of-plane displacement for a plate thickness of 3 mm.

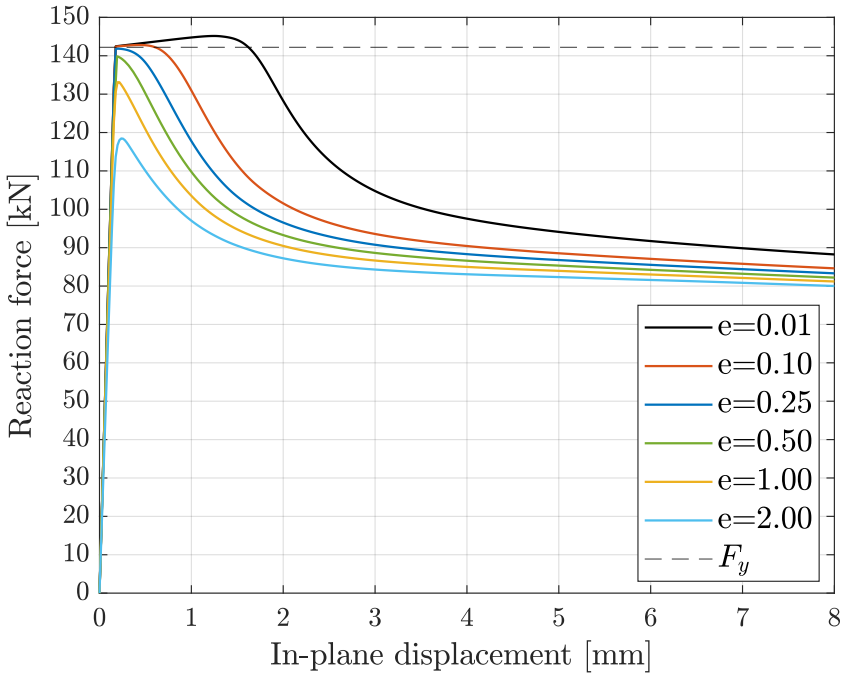

Figure 5.9: Force vs. In-plane displacement for a plate thickness of 4 mm.

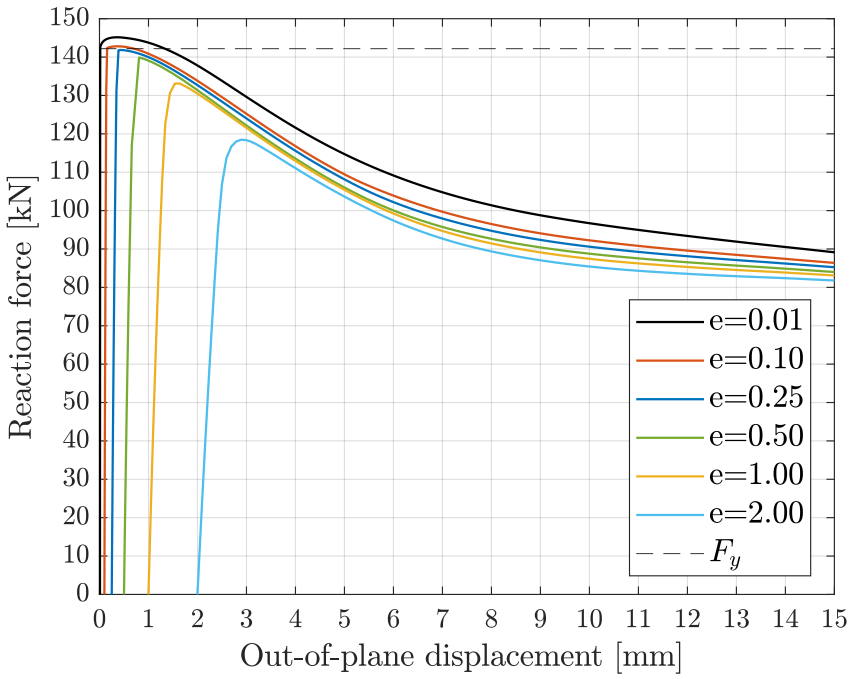

Figure 5.10: Force vs. Out-of-plane displacement for a plate thickness of 4 mm.

The deformation shape throughout the analysis for $t = 1$, 2, 3 and 4 mm with an imperfection e of 0.01 mm is presented in Figure 5.11 to 5.14. It can be seen that the prescribed initial imperfection mode is initiated and kept throughout the loading phase up until the peakload is reached for all thicknesses. After the ultimate load is reached, the deformation shape differs between the thicknesses.

For $t = 1$ mm, the out-of-plane displacement area is the largest, exhibiting a sharp-cornered square shape. As the thickness increases, the displaced area decreases and assumes a more oval shape. Additionally, the edges of the plate that are parallel to the load direction for $t = 1$ mm appear straight in comparison to the other thicknesses. This is due to the plate yielding near the corners, resulting in a pillow-like deformation shape.

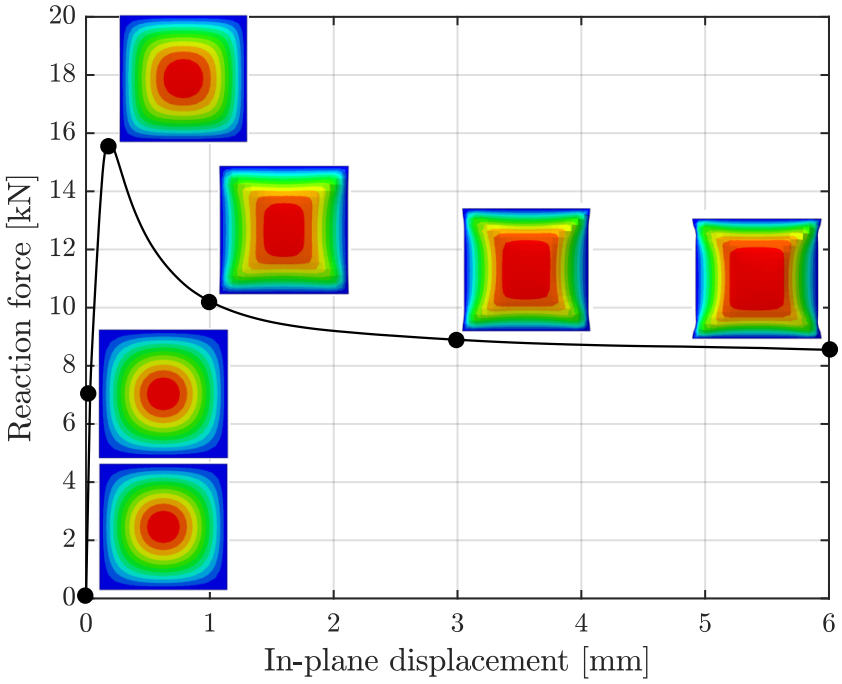

Figure 5.11: Force vs. In-plane displacement for a plate thickness of 1 mm. Plate out-of-plane deformation colormap, blue = 0, red = maximum.

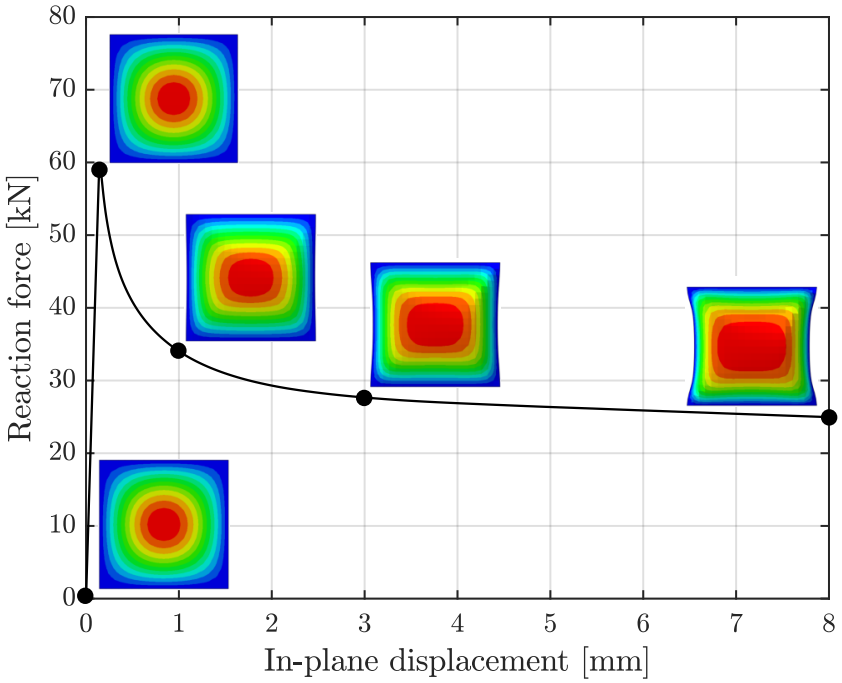

Figure 5.12: Force vs. In-plane displacement for a plate thickness of 2 mm. Plate out-of-plane deformation colormap, blue = 0, red = maximum.

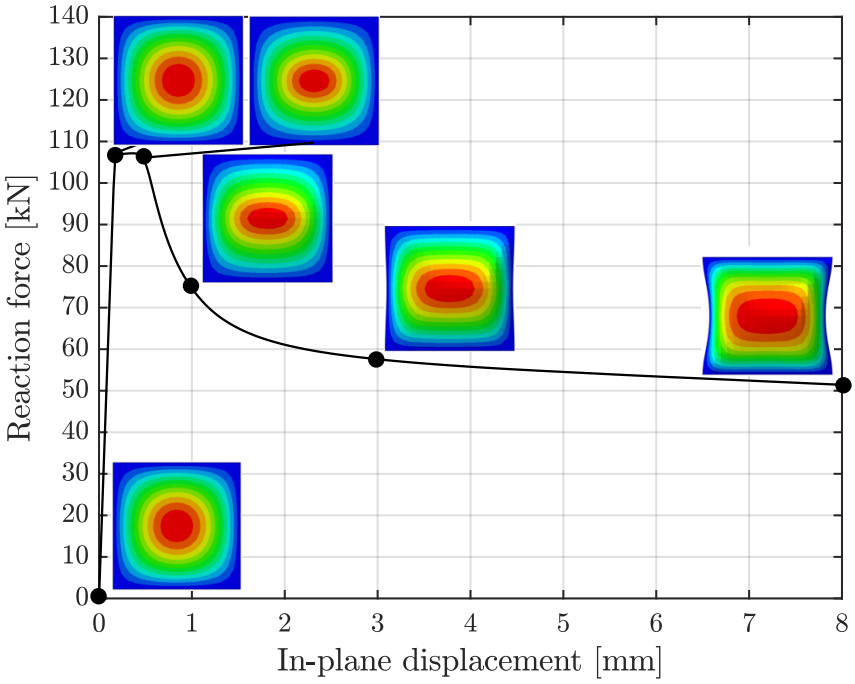

Figure 5.13: Force vs. In-plane displacement for a plate thickness of 3 mm. Plate out-of-plane deformation colormap, blue = 0, red = maximum.

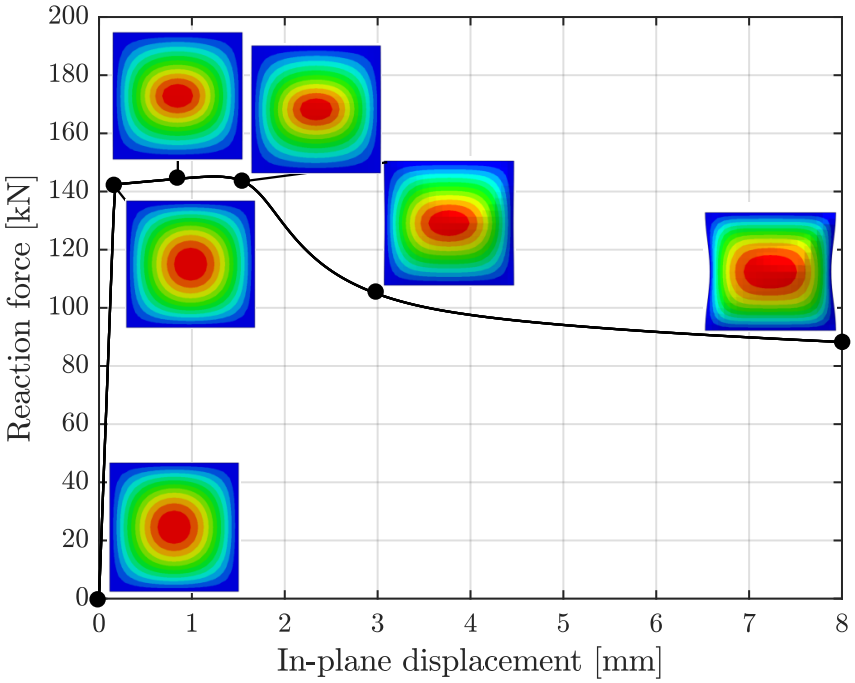

Figure 5.14: Force vs. In-plane displacement for a plate thickness of 4 mm. Plate out-of-plane deformation colormap, blue = 0, red = maximum.

5.1.4 Influence of boundary conditions

The influence of the two different sets of boundary conditions (see Section 4.6) on the structural response is presented in Figure 5.15. It shows that peak load is higher for case 2, where the edges parallel to the load are prevented from expanding or contracting.

In Figure 5.15 b) a reduction of the critical buckling load, P_{cr}, can be observed for case 2 compared to case 1. A sharp nick is also observed when the out-of-plane displacement is approximately 4.5 mm.

Note that it was not possible to use the displacement method when running the simulation for case 2, therefore the arc length method was used instead, but still with a prescribed displacement.

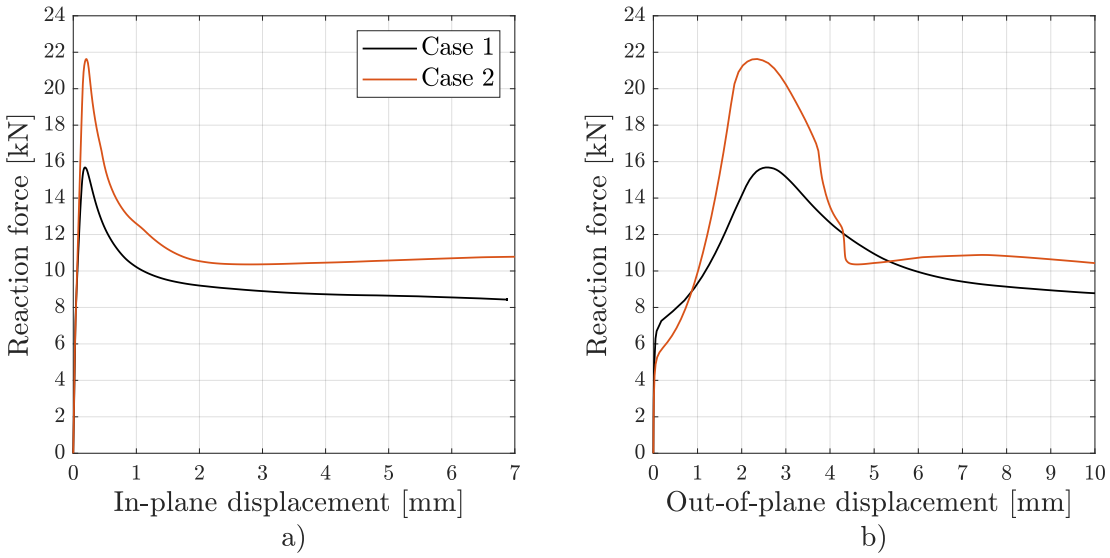

Figure 5.15: Force vs. In-plane displacement for a plate thickness of 1 mm and e = 0.01 mm. Two boundary cases considered according to Section 4.6.

5.1.5 Effect of changed material parameters

During rapid loading, the material properties f_y and f_u are expected to increase; see the discussion in Section 2.4.3. This sub-study aims to simulate the effects of high strain rates using a static analysis by manually adjusting the material model (stress-strain relationship). Four different material models are considered, labeled as Material A, B, C, and D, see Section 4.4.2.

Table 5.2 outlines the relationship between the modified materials' properties (f_y and f_u) and those of the original material. While the precise relationship should be determined from a strain rate study, an arbitrary relationship was chosen to assess whether altering the material properties affects the response. Material B is considered the most realistic of the modified materials (B, C, and D), as both the yield strength and ultimate strength are expected to increase during rapid loading. Materials C and D are designed to investigate whether the response is influenced by changes in both f_y and f_u or if only one of them plays a significant role.

Table 5.2: Relationship between material properties

Material	**A**	**B**	**C**	**D**
f_y [MPa]	355	440	440	355
f_u [MPa]	490	550	490	550
f_y [MPa]	355	$1.24f_y$	$1.24f_y$	$1.00f_y$
f_u [MPa]	490	$1.12f_u$	$1.00f_u$	$1.12f_u$

A initial imperfection of e = 0.5 mm was chosen for all the simulations since it corresponds to the recommendation in EN 1993-1-5 (2005), (b/200). The result is presented for the plates with thickness 1 mm and 4 mm, this choice was made too study the effect of slenderness when changing the material parameters.

The force-displacement relation for material A, B, C are presented in terms of in-plane and out-of-plane displacement in Figure 5.16.

Comparing the response for the original material A with material B, which features both an increase in f_y and f_u, the entire response is shifted upwards. An increase in post buckling strength is seen both when t = 1 mm and when t = 4 mm.

When t = 4 mm it can be observed that the increase in strength is proportional to the increase in f_y, i.e. $f_{y,B} = 1.24f_{y,A}$ and $P_{max,B} = 1.24P_{max,A}$. However, this is not case when t = 1 mm, when t = 1 mm the increase in capacity percentage wise is less than the increase in f_y percentage wise, i.e. $f_{y,B} < 1.24f_{y,A}$.

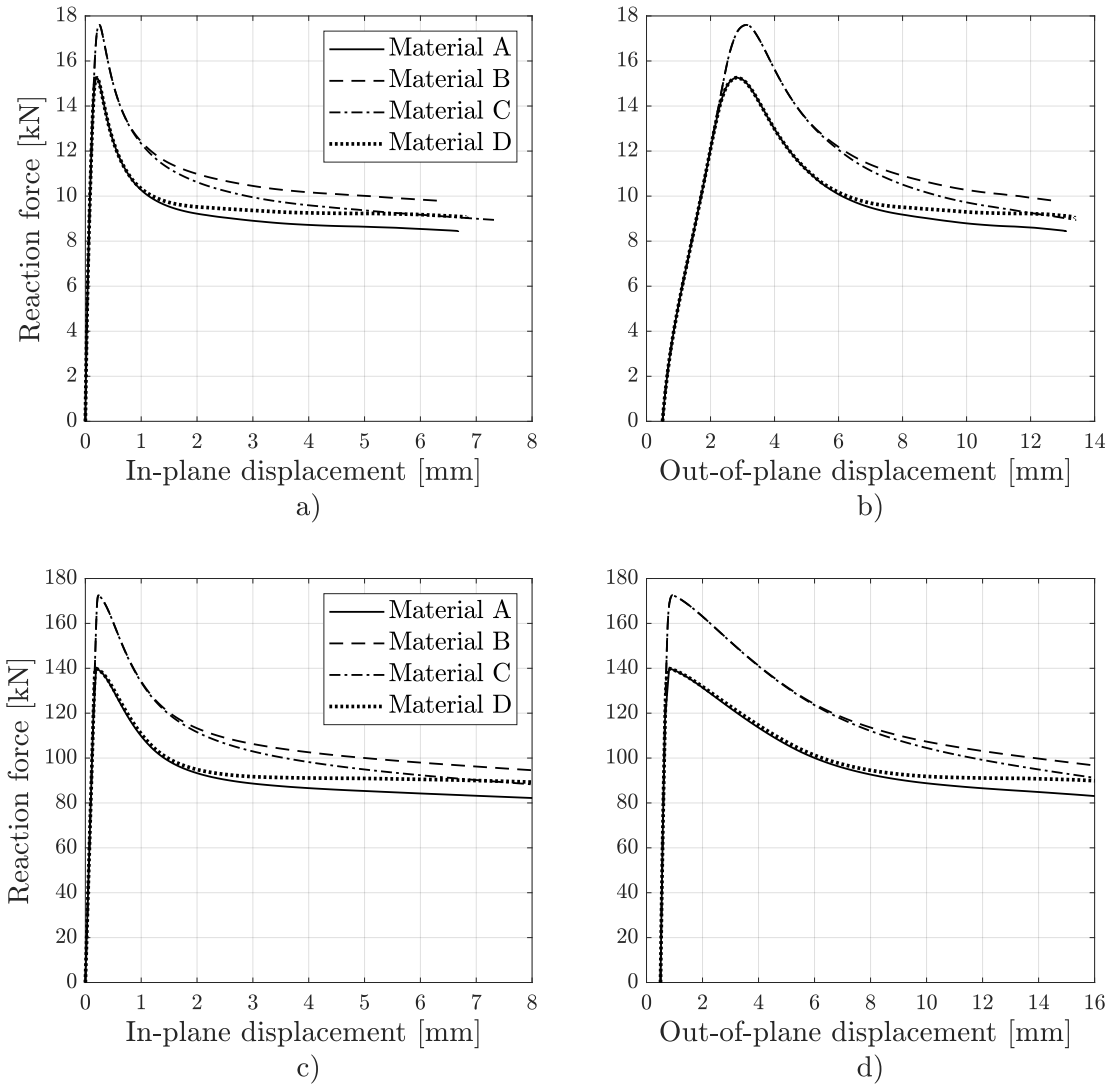

Figure 5.16: Force vs. displacement for a plate thickness of: a) and b) 1 mm, and c) and d) 4 mm for material A,B,C,D.

Studying Figure 5.16 b) it can be seen that changed material parameters have no influence on the critical buckling load, P_{cr}, this can be concluded since the curves are stacked on top of each other, this is logical since elastic buckling is expected for plates in cross-section class 1.

Upon examining Figure 5.16 a) to d) it can be concluded that up until when the maximum load is reached the response for material A is equal to the response for material D and the response for material B is equal to the response for material C. This means that f_u have no influence on the maximum load capacity for these combinations of geometry, thickness and initial imperfections. However, in the post-peak range when excessive deformation have taken place, increased f_u have an influence.

5.2 Studies on a plate with different dimensions

5.2.1 Orientation

Two sub-studies were conducted to investigate the effects of plate geometry on the response. In the first study, the plate height was increased to 100×200 mm. In the second study, the plate dimensions were increased to 200×200 mm. Theoretically, these modifications should not affect the critical buckling load nor the peak load (ultimate capacity). These studies aim to assess whether deviations from theoretical expectations occur when altering the plate geometry.

5.2.2 Rectangular plate, 100 x 200 mm

A static analysis was performed on the new plate geometry, the same analysis as in Section 5.1. The resulting response for both in-plane and out-of-plane displacement is presented in Figure 5.17.

The new plate geometry is seen in Figure 5.18 as well as the points from which the data is gathered. Since the height is doubled, during buckling the plate is simply divided into two equally sized 100x100 plates stacked on top of each other. The only difference is that the deformed shape is different, just as for the 100x100 plate, unexpected asymmetrical shapes were obtained depending on the settings used, see Figure 5.19 for 3 of the obtained deformation shapes.

It can be seen that both sub-plates align with the 100x100 plate in Figure 5.17 b). In Figure 5.17 a) they share the same shape and peak load, however the top sub-plate is shifted in terms of in-plane displacement. This is due to the fact that it is the top-edge that is displacement controlled. Due to similarities with the 100x100 mm plate, no dynamic analysis was conducted for this geometry.

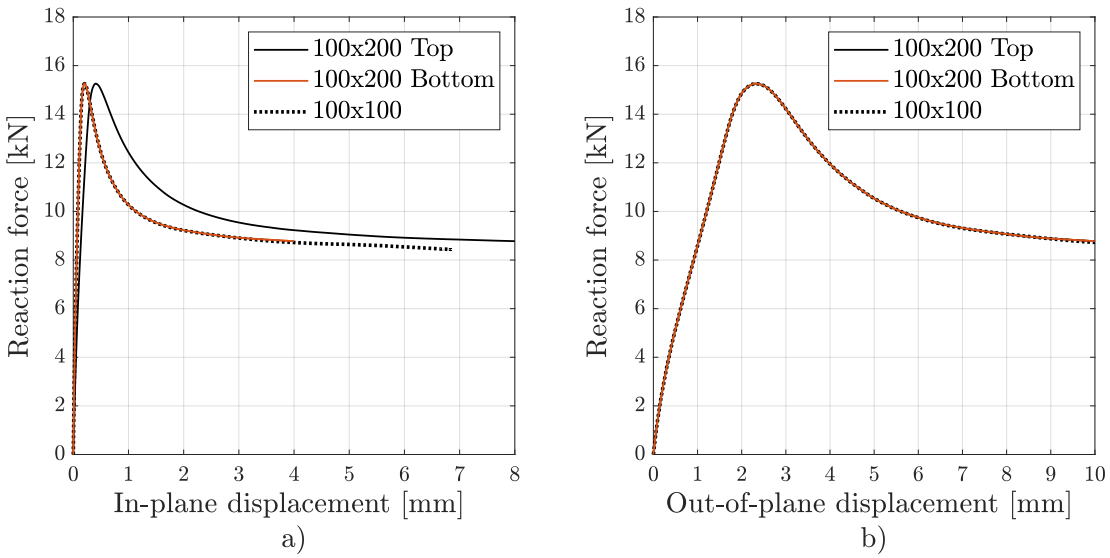

Figure 5.17: Force vs. Displacement for a plate thickness of 1 mm with dimensions 100x200 vs. 100x100 mm, initial imperfection 0.5 mm

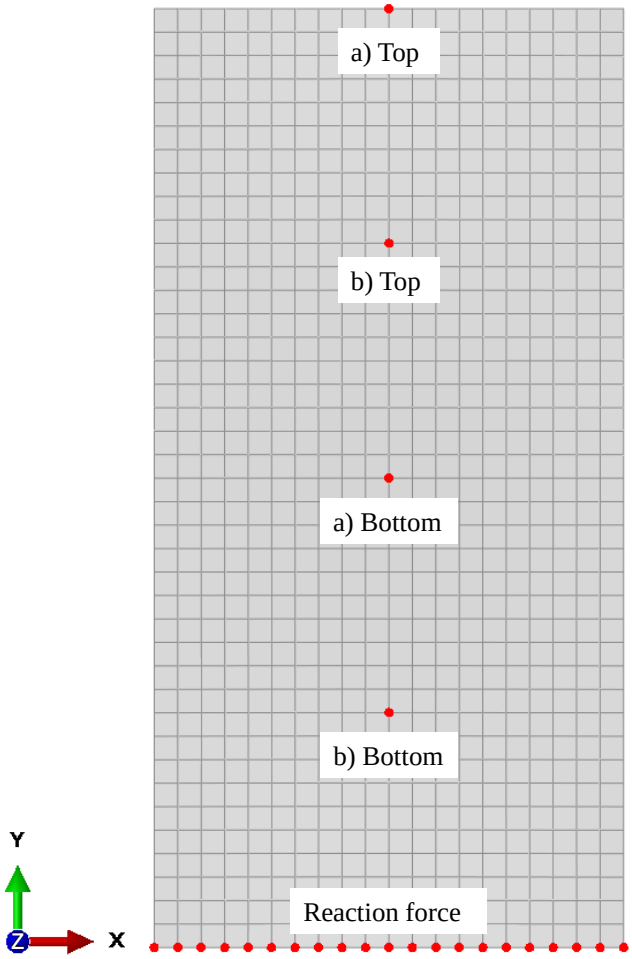

Figure 5.18: Geometry and clarification of which nodes data was extracted from, see Figure 5.17.

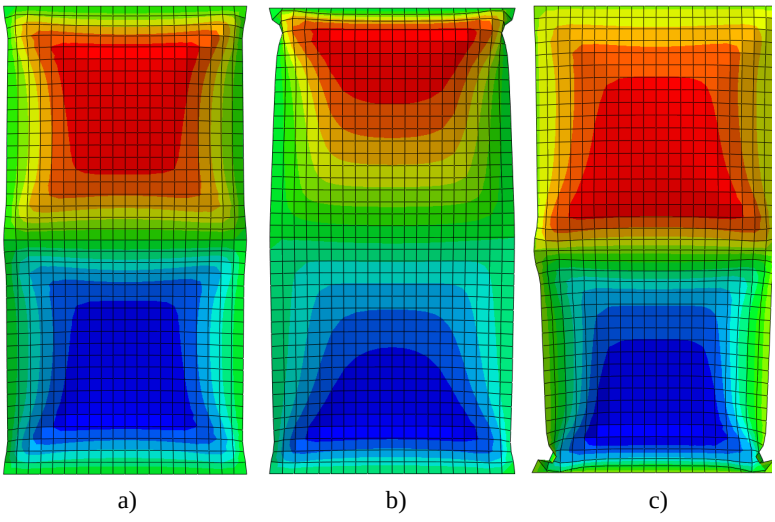

Figure 5.19: Obtained deformation modes for different increment settings, creases may develop at different position, a) symmetric deformation, b) crease at both top and bottom edge, b) crease at bottom edge and bottom of top sub-plate.

5.2.3 Square plate, 200 x 200 mm

A static analysis was performed on the new plate geometry, the same analysis as in Section 5.1. The resulting response for both in-plane and out-of-plane displacement is presented in Figure 5.20.

In order to compare the responses, the response for the 200x200 plate was normalized to the 100x100 response by dividing the reaction force by 4 since both the height and thickness were increased by a factor two to keep the same slenderness. It can be seen that the response of the plates is close up until the peak and start to diverge in the post-buckling range, which likely is explained by different mesh density. Due to similarities with the 100x100 mm plate, no dynamic analysis was conducted for this geometry either.

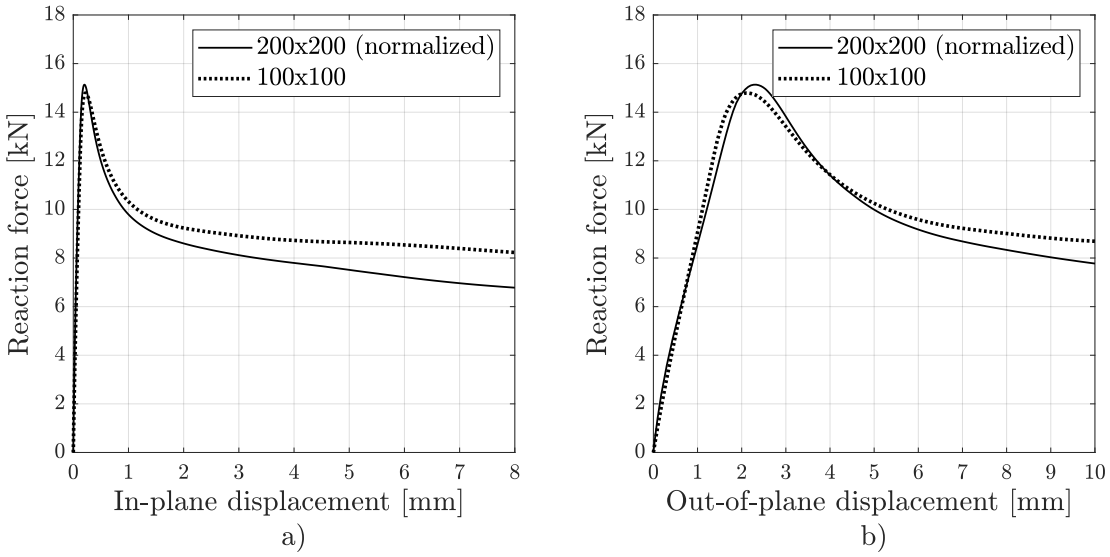

Figure 5.20: Force vs. Displacement for a plate thickness of 2 mm with dimensions 200 x 200 mm vs. a plate with plate thickness of 1 mm and dimensions 100 x 100 mm.

5.3 Dynamic Analysis

5.3.1 Validation of dynamic model

To ensure that the dynamic model behaves as expected it was validated by comparing the results of the dynamic analyses (with strain rate effects disabled) with the static analyses. If the loading speed is slow enough, the dynamic analysis should coincide with the static analysis. The loading speed was gradually decreased until no dynamic effects were observed and the dynamic and static analysis coincided. This was obtained for a loading speed of 0.01 mm/s. According to Yang et al. (2022) quasi-static loading corresponds to strain rates in the range 10^{-6} to 10^{-2} 1/s which for the chosen geometry corresponds to velocities between 0.0001 and 1 mm/s, further supporting the choice of loading speed.

The comparison between the dynamic model using the chosen loading speed and the static model is presented in Figure 5.21 and 5.22. Both implicit dynamic and explicit dynamic analysis were performed, with the same result obtained. Only the implicit results are presented in the figures.

It should be noted that in some cases when $t = 1$ mm, a second asymmetric deformation shape was obtained, especially at higher loading speeds. This was deduced as a numerical issue and not related to dynamic effects. In Figure 5.23 the two deformation shapes are presented. In Figure 5.23 b), the unsymmetrical shape has the buckle located close to the unloaded edge. Depending on the settings used in Abaqus, the buckle appears close to the loaded edge. When the deformation shape is non-symmetrical, it seems to be random if the maximum out-of-plane displacement appears closer to the loaded or unloaded edge. Figure 5.23 is just an example to illustrate that different deformation shapes are obtained, and should not be interpreted as that a certain deformation shape is associated with a certain velocity since more factors than the velocity affects the shape. For further explanation and investigation of the asymmetric mode see Appendix A.1.

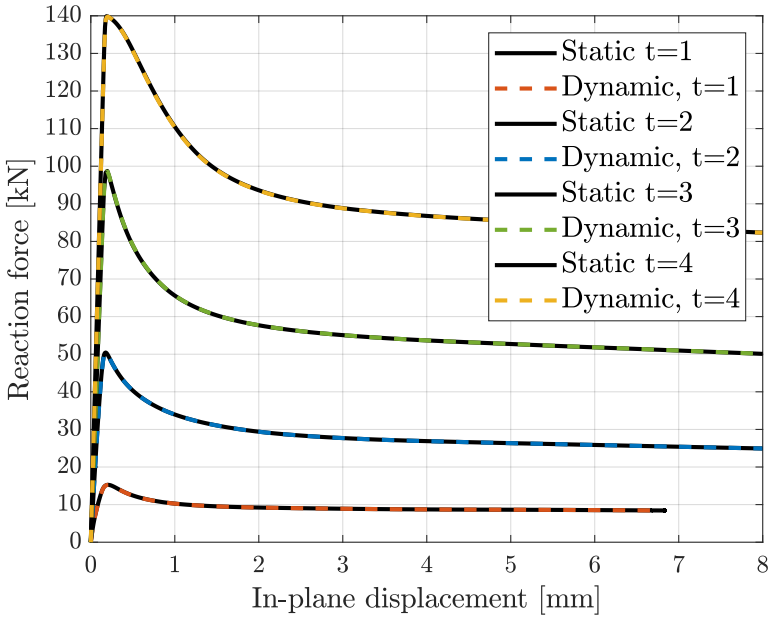

Figure 5.21: Comparison of dynamic and static models under slow loading conditions ($v = 0.01$mm/s) for all thicknesses, considering an initial imperfection of 0.5 mm.

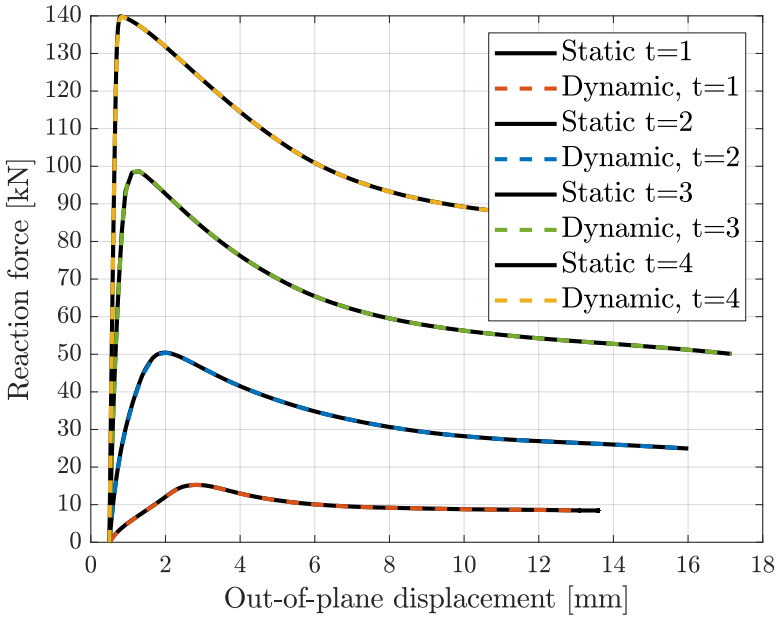

Figure 5.22: Comparison of dynamic and static models under slow loading conditions ($v = 0.01$mm/s) for all thicknesses, considering an initial imperfection of 0.5 mm.

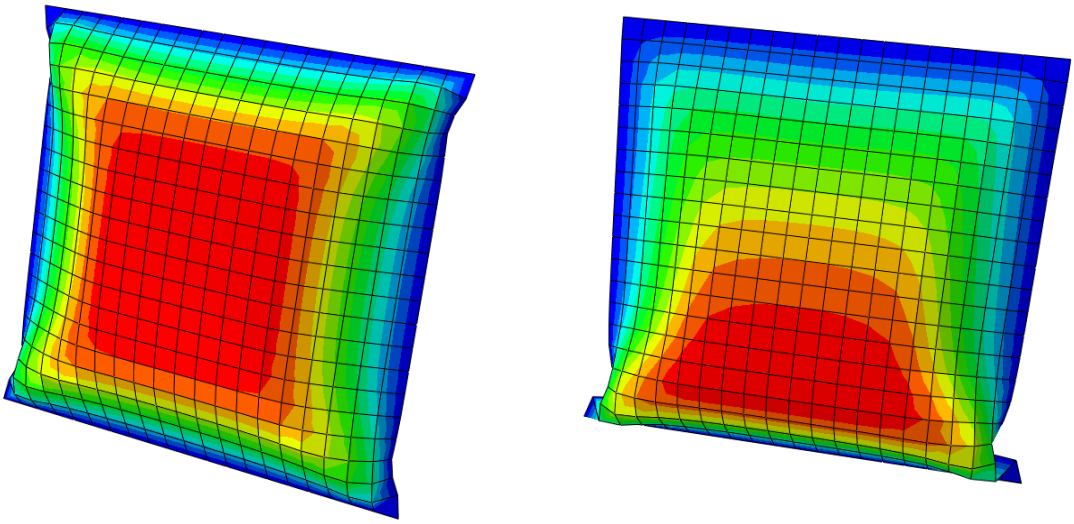

a) b)

Figure 5.23: Post buckling deformation shape example: a) Symmetric deformation when $v = 1$ mm/s, b) Unsymmetric deformation when $v = 10$ mm/s.

5.3.2 Response without strain rate effect activated

The response without consideration of strain rate effects, i.e. no rate dependence, was investigated. This is a fictitious case performed to make it possible to study what influence dynamic effects have on the structural response. The amplitude of the initial imperfection was set to 0.5 mm unless otherwise stated since it is in line with the recommendations in Eurocode.

As mentioned in Section 5.3.1 two deformation shapes were obtained for plate thickness 1 mm depending on the increment settings in Abaqus, the deformation shape obtained at the investigated velocities are presented in Table 5.3.

Table 5.3: Relation between velocity and deformation shape without strain rate effect considered for $t = 1$ mm.

Velocity [mm/s]	Deformation shape
0.1	Symmetric
1	Symmetric
10	Asymmetric
20	Asymmetric
50	Asymmetric
100	Asymmetric
200	Asymmetric

The response for $t = 1$ mm is presented in Figure 5.24, where the response for the lower velocities is presented in Figure 5.24 a) and b). Looking at Figure 5.24 b) almost no dynamic effects are obtained for velocities up to 10 mm/s, however small oscillations appear at a velocity of 20 mm/s. The fact that the lines for $v =$ 10 mm/s and higher values deviate from and do not follow and oscillate around the line for $v = 0.1$ mm/s at around 0.3 mm in-plane displacement is due to different deformation shapes after global buckling.

The response for higher velocities is presented in Figure 5.24 c) and d). Large dynamic effects can be seen as increased oscillation amplitude, however, the effect decreases drastically after approximately 1 mm of in-plane displacement. P_{cr} (and F_y for larger thickness) is indicated for reference, obtained for the static case, with infinitesimal imperfection.

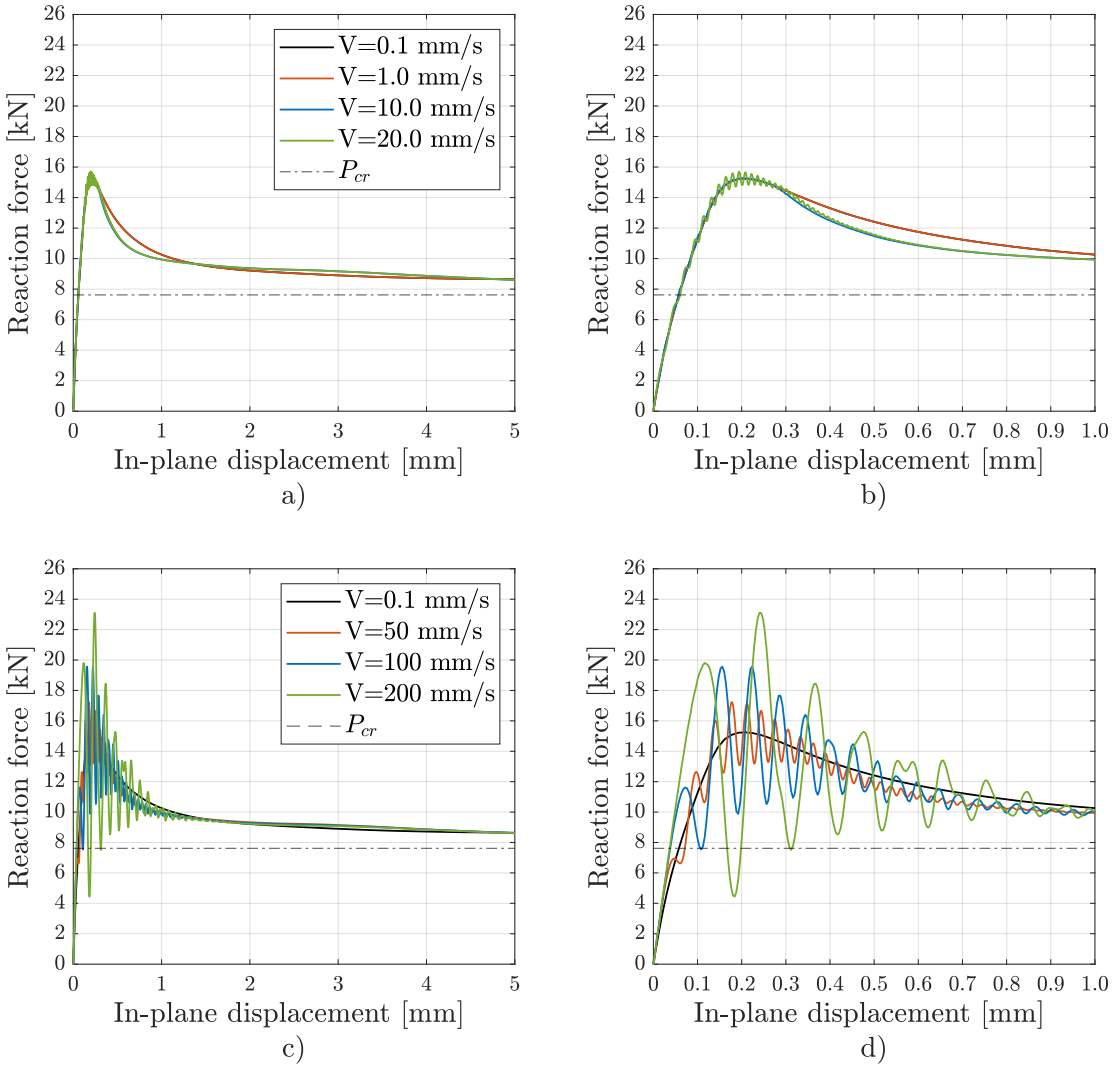

Figure 5.24: Force vs. In-plane displacement for plate thickness 1 mm. a) and b) feature lower velocities, c) and d) higher velocities. Full graph in left column, zoomed in on 0-1 mm in the right column.

The oscillations are further visualized in Figure 5.25. As the velocity-controlled edge is displaced in-plane, see the white dot, the middle section of the plate deflects out-of-plane, as shown by the solid line. Simultaneously, the plate oscillates back a small part of the previous deflection and then back up again due to both the loading and the oscillation, see the black arrows. These oscillations explain the fluctuations in the reaction force. Since the loaded edge is displacement-controlled and constrained to move only in one in-plane direction, it cannot move backward. When the plate moves upwards out-of-plane, it reduces the in-plane stiffness, reducing the reaction force. Conversely, when it oscillates back down, the in-plane stiffness increases, causing an increase in reaction force, as the loaded edge cannot retreat. The oscillations are initiated by the high loading speed, as a dynamic effect.

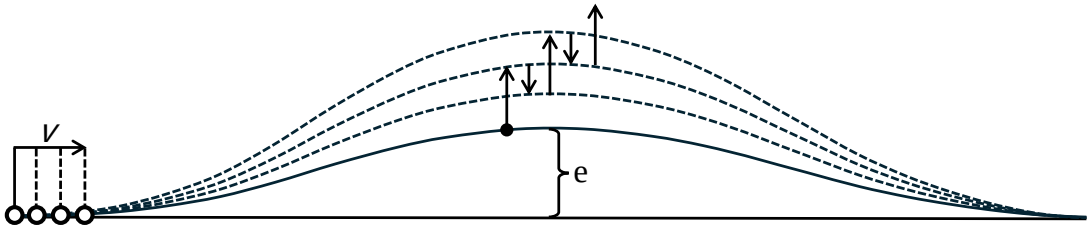

Figure 5.25: Visualization of obtained out-of-plane oscillation of plate mid-point for a plate with initial imperfection e and loading speed v.

The response for $t = 2$ mm is presented in Figure 5.26. No dynamic effects can be seen for the lower velocities in plot a) and b). Dynamic effects can be seen for the higher velocities in plot c) and d) (except for the reference case $v = 0.1$ mm/s) with smaller oscillation amplitude compared to $t = 1$ mm. The deformation shape is symmetric for all velocities.

To be noted is that P_{cr} is larger than the peak value of the reaction force. This is due to the choice of imperfection amplitude, if the amplitude would be infinitely small value the peak would be above the horizontal line for P_{cr}.

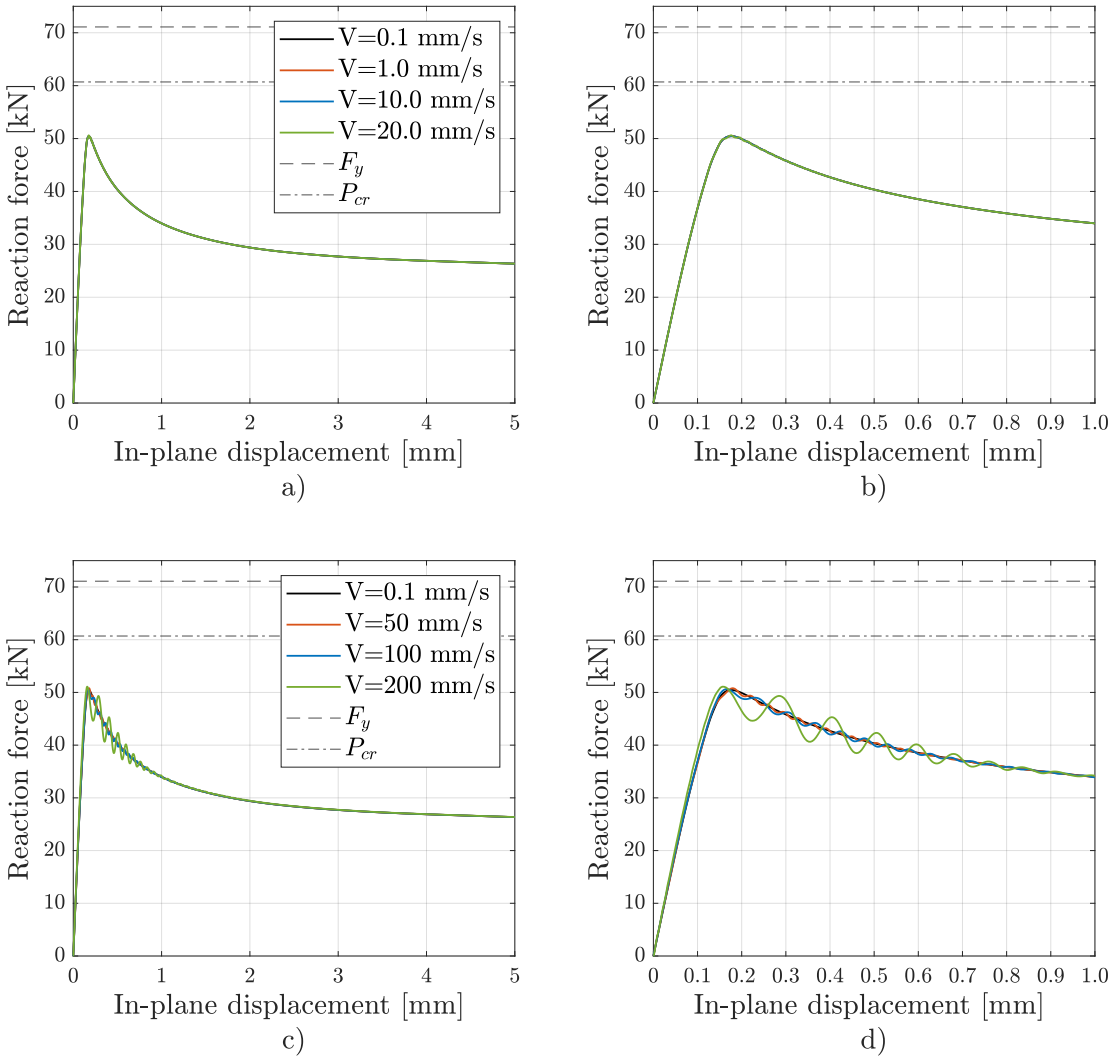

Figure 5.26: Force vs. In-plane displacement for plate thickness 2 mm. a) and b) feature lower velocities, c) and d) higher velocities. Full graph in left column, zoomed in on 0-1 mm in the right column.

The response for $t = 3$ mm is presented in Figure 5.27. No dynamic effects can be seen for the lower velocities in plot a) and b). Dynamic effects can be seen for the higher velocities in plot c) and d), with smaller oscillation amplitude compared to t = 2 mm. The deformation shape is symmetric for all velocities.

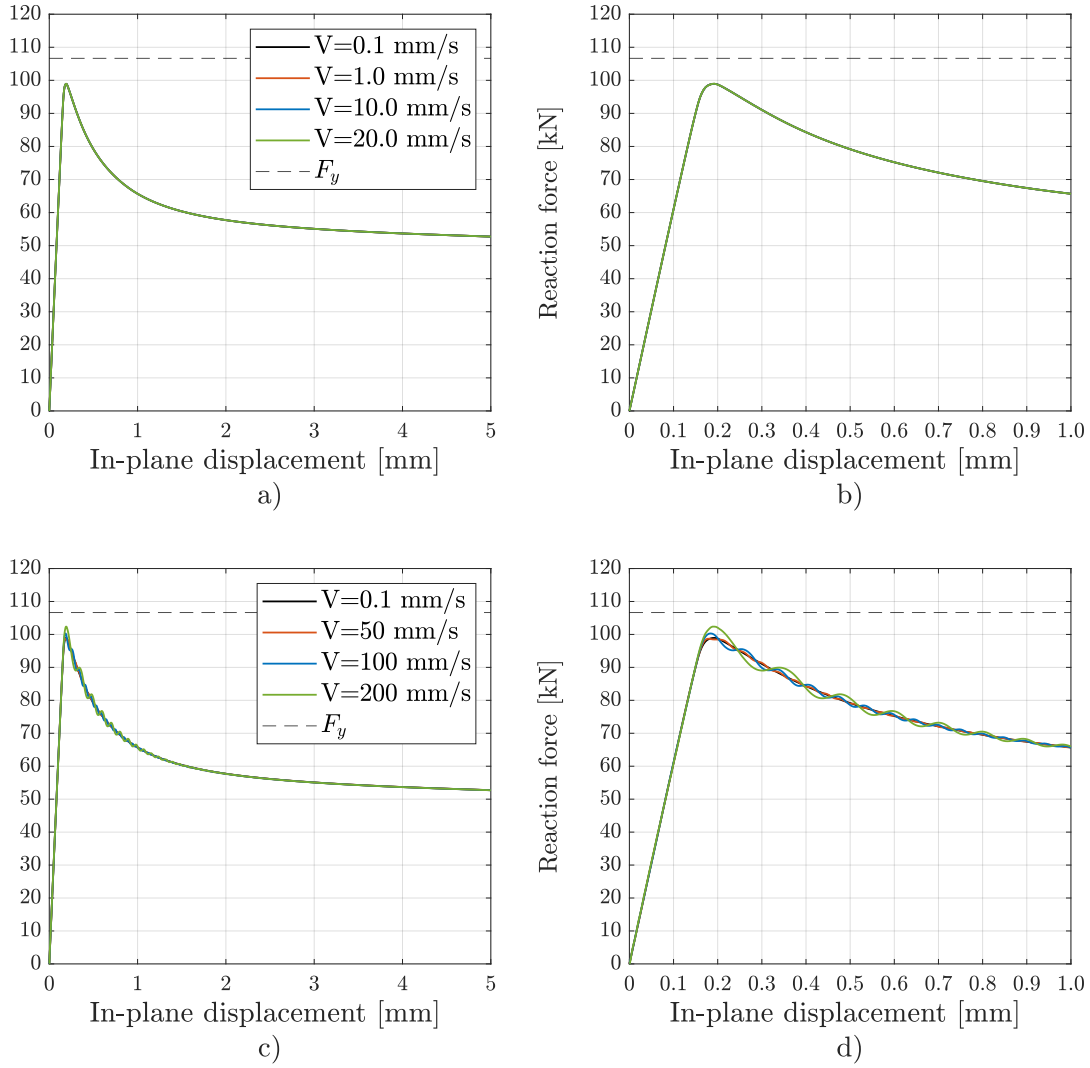

Figure 5.27: Force vs. In-plane displacement for plate thickness 3 mm. a) and b) feature lower velocities, c) and d) higher velocities. Full graph in left column, zoomed in on 0-1 mm in the right column.

The response for the out-of-plane displacement is presented in Figure 5.28 for $t = 1$ mm. It can be seen that as the velocity increases, the stiffness increase, see especially Figure 5.28 d).

Overall the result is similar to the response of the in-plane displacement. A difference is that not only the reaction force oscillates, but also the out-of-plane displacement oscillates in the measured point, see Figure 5.25, causing the displacement to decrease and increase before and after the peak load is reached, leading to the oscillation peaks being tilted slightly to the left.

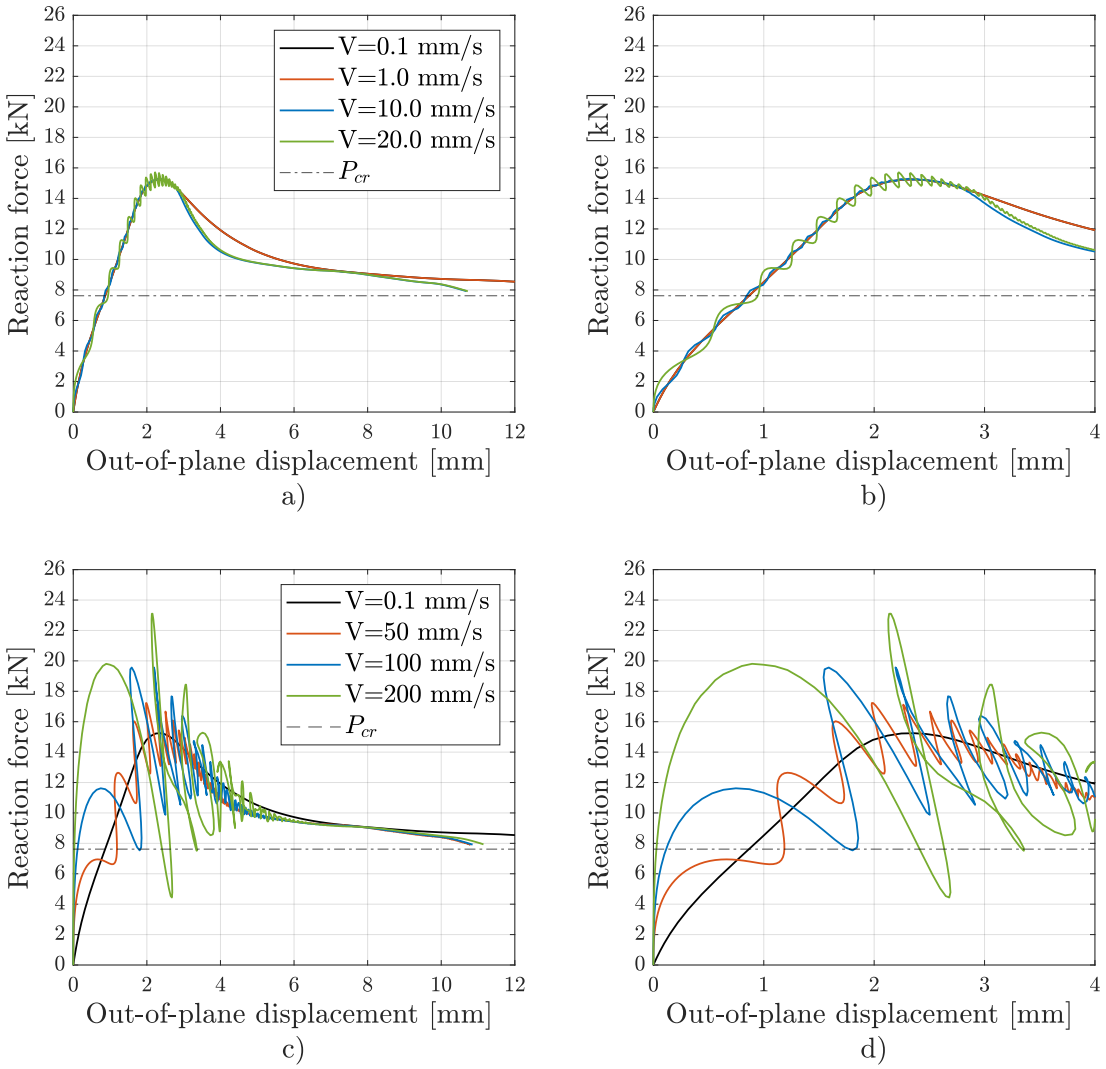

Figure 5.28: Force vs. Out-of-plane displacement for plate thickness 1 mm. a) and b) feature lower velocities, c) and d) higher velocities. Full graph in left column, zoomed in on the first 4 mm in the right column.

5.3.3 Influence of strain rate

The influence of strain-rate effects during dynamic loading was investigated to represent the real case, see Section 4.9.4 for details on how this was implemented in Abaqus.

It should be noted that when activating strain rate effects the two deformation modes appear for different velocities than for the case without strain rate effects, see Section 5.3.2. The new observations are presented in Table 5.4.

Table 5.4: Relation between velocity and deformation shape when strain rate effect is considered when $t = 1$ mm.

Velocity [mm/s]	**Deformation shape**
0.1	Asymmetric
1	Asymmetric
10	Asymmetric
20	Symmetric
50	Symmetric
100	Symmetric
200	Symmetric

In Figures 5.29 to 5.31 the same type of plots as in Section 5.3.2 are presented with strain rate effects activated.

For the chosen geometric and material parameters, in combination with the studied velocities, only a small change in response can be seen when the strain rate effect is activated, however, it is large enough to be significant.

It can be seen that the lines are no longer stacked on top of each other but are instead shifted upwards, indicating a capacity increase. This is observed for all velocities, and the shift increases for larger velocities. Note that no adjustment of f_y has been made so that the same value is obtained in a dynamic analysis with slow loading speed and a static analysis, meaning that a very small strain rate effect is present, even for very slow loading speeds.

This is further exemplified in Figure 5.32 where the response with and without strain rate effects for $t = 1$ mm and $v = 10$ and 100 mm/s is plotted. It is seen that the dynamic effect is unchanged, the force oscillations have the same shape and amplitude, however strain rate effects shifts the line upwards.

The observed response can be seen as the combination of changed material properties, see Section 5.1.5 and dynamic effects, see Section 5.3.2, but with a relationship between the static and dynamic yield strength that follows the power law presented in 4.9.4.

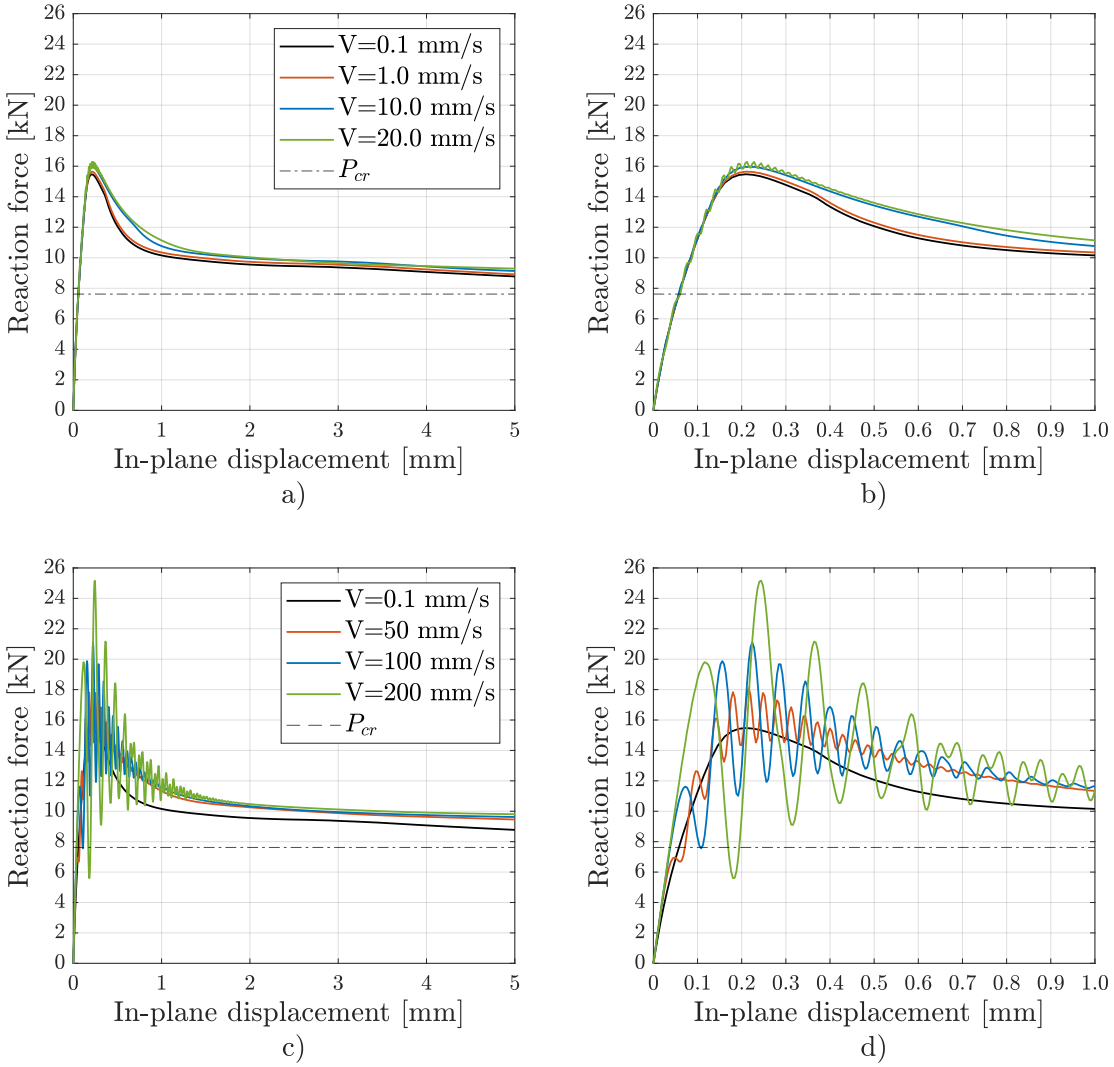

Figure 5.29: Force vs. In-plane displacement for plate thickness 1 mm with strain-rate effects considered. a) and b) feature lower velocities, c) and d) higher velocities. Full graph in left column, zoomed in on 0-1 mm in the right column.

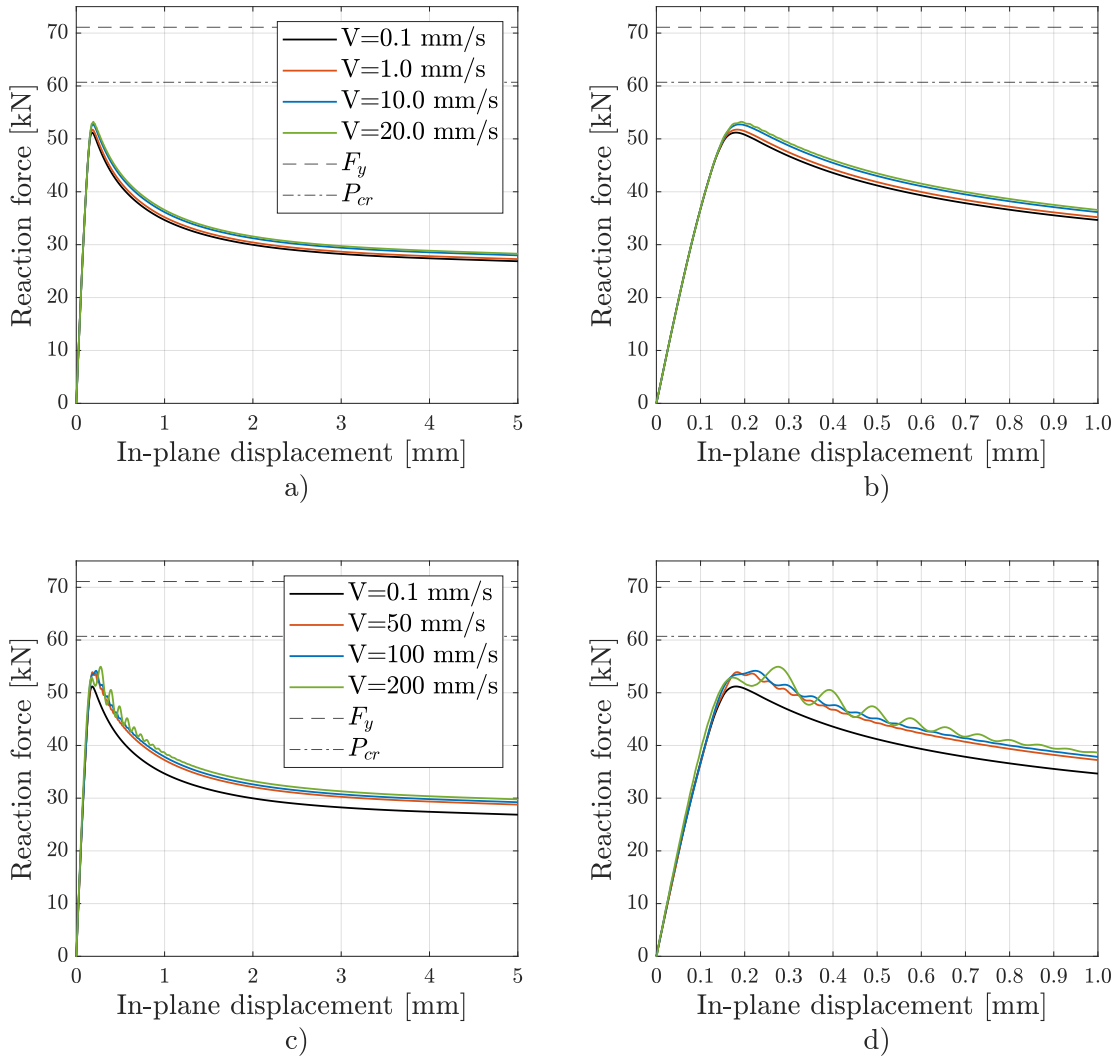

Figure 5.30: Force vs. In-plane displacement for plate thickness 2 mm with strain-rate effects considered. a) and b) feature lower velocities, c) and d) higher velocities. Full graph in left column, zoomed in on 0-1 mm in the right column.

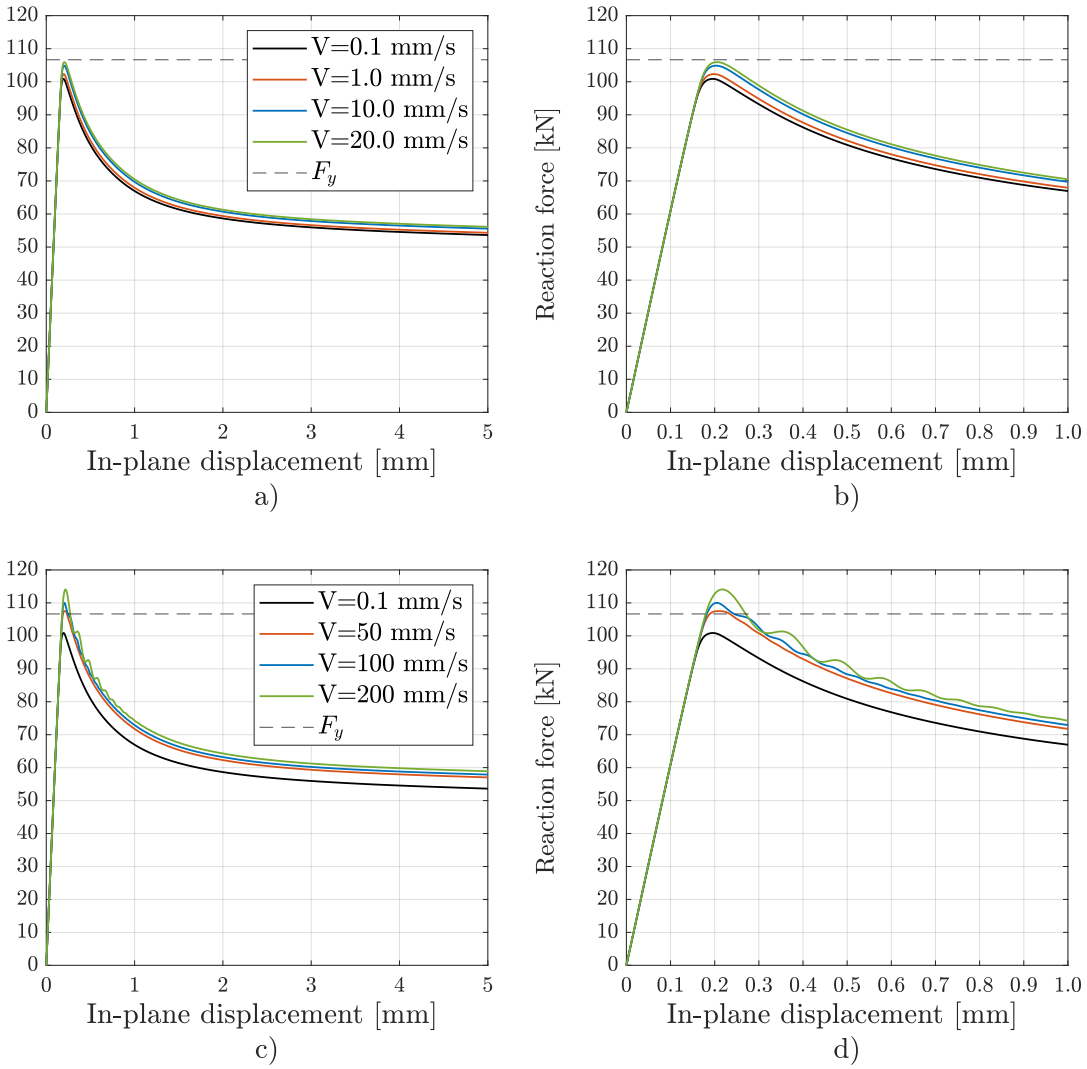

Figure 5.31: Force vs. In-plane displacement for plate thickness 3 mm with strain-rate effects considered. a) and b) feature lower velocities, c) and d) higher velocities. Full graph in left column, zoomed in on 0-1 mm in the right column.

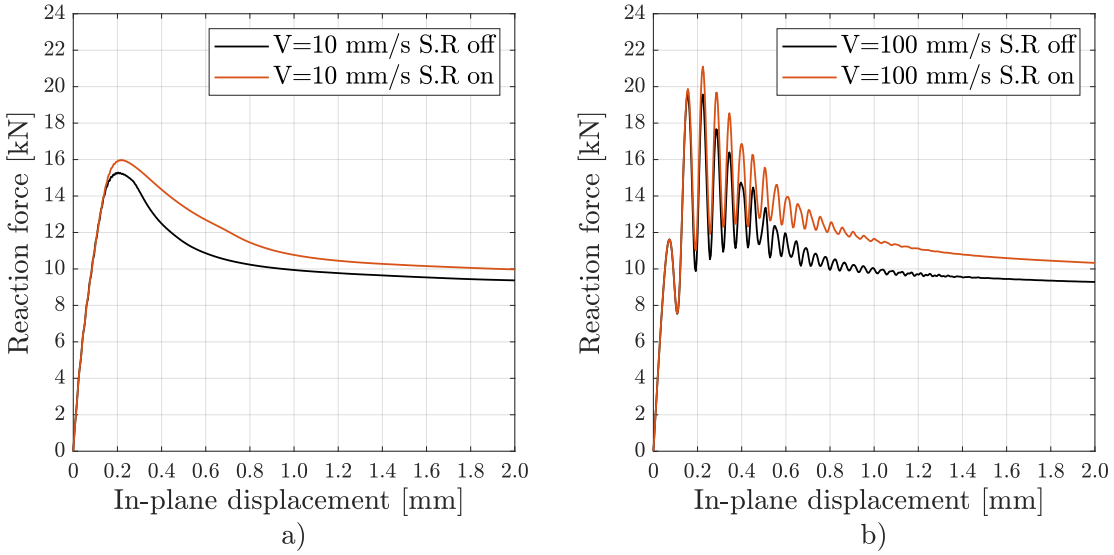

Figure 5.32: Force vs. In-plane displacement for plate thickness 1 mm with and without strain-rate effects considered. Note that the deformation shape is asymmetric for all lines except the black line in plot b).

5.3.4 Effect of initial imperfection

The effect of initial imperfection amplitude on the dynamic response was investigated by using different imperfection amplitudes for a velocity of 50 mm/s, corresponding to strain rate $\dot{\epsilon} = 0.5$, without any strain rate effects considered. The result is presented in Figure 5.33 for the in-plane displacement. It is observed that initial imperfections have a large influence on the oscillation amplitude. Small imperfections, see Figure 5.33 b), result in larger amplitudes, while larger imperfections, see Figure 5.33 d) result in smaller amplitudes.

In Figure 5.33 a) and c) it also shown that the imperfection amplitude has no effect on when dynamic effects decrease, they all end at around the same place, independent of initial imperfection. Looking at Figure 5.33 d) however, it can be seen that the oscillations are initiated at smaller displacements for the larger imperfections, whereas in Figure 5.33 b) the oscillations are not initiated until larger displacements have been reached.

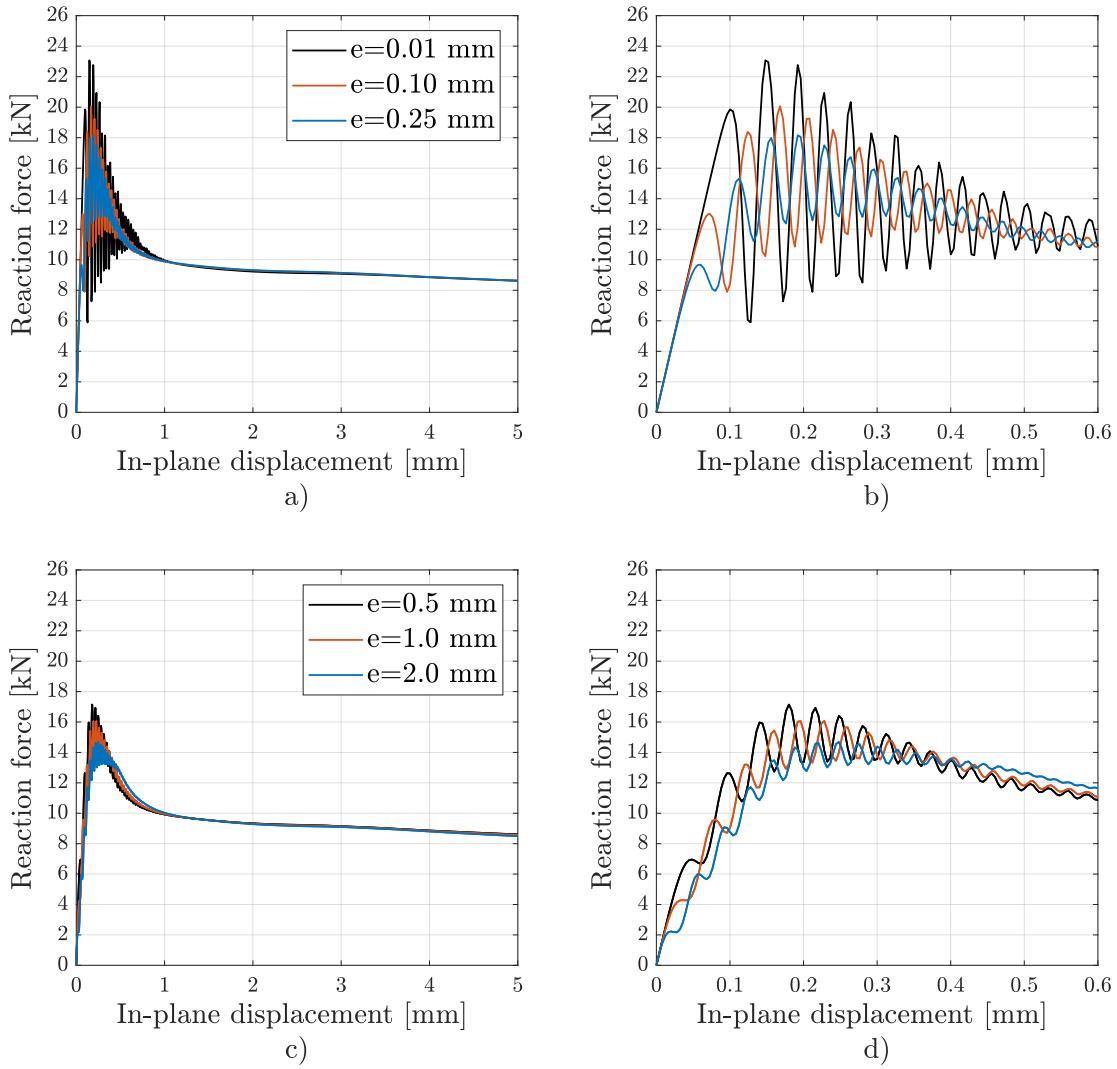

Figure 5.33: Force vs. In-plane displacement for plate thickness 1 mm. a) and b) feature smaller imperfections, c) and d) larger imperfections. Full graph in left column, zoomed in on 0 - 0.6 mm in the right column.

5.3.5 Comparisons to the static case

To assess the magnitude of the dynamic effects, the results from the dynamic analysis of the plate is compared to the static case. Since there is no clear definition of a dynamic buckling load, it is more appropriate to compare the peak load (ultimate capacity). For thicker plates, it is possible to compare P_{cr}, as it coincides with the peak load, indicating that the plate has reached its maximum capacity upon buckling. However, to maintain consistency across all thicknesses, the peak load is used throughout.

In Tables 5.6, 5.9, and 5.12 rate dependence is disabled, while in Tables 5.7, 5.10, and 5.13 rate dependence is enabled. In all tables P_{max} refers to the peak load.

Table 5.5: General Parameters for both rate-dependent and rate-independent cases, relevant for Table 5.6 and 5.7.

Parameter	Value
t	1 mm
e	0.5 mm
$P_{\text{max, static}}$	15.26 kN

Table 5.6: Results when rate dependence is not considered ($t = 1\,\text{mm}$).

$\boldsymbol{v}$ [mm/s]	$\dot{\boldsymbol{\epsilon}}$ [1/s]	$\boldsymbol{P}_{\text{max}}$ [kN]	$\boldsymbol{P}_{\text{max}}/\boldsymbol{P}_{\text{max, static}}$ [-]
0.1	0.001	15.24	1.00
1	0.01	15.24	1.00
10	0.1	15.29	1.00
20	0.2	15.60	1.02
50	0.5	17.23	1.13
100	1	19.57	1.28
200	2	23.10	1.51

Table 5.7: Results when rate dependence is considered ($t = 1\,\text{mm}$).

$\boldsymbol{v}$ [mm/s]	$\dot{\boldsymbol{\epsilon}}$ [1/s]	$\boldsymbol{P}_{\text{max}}$ [kN]	$\boldsymbol{P}_{\text{max}}/\boldsymbol{P}_{\text{max, static}}$ [-]
0.1	0.001	15.47	1.01
1	0.01	15.65	1.03
10	0.1	15.98	1.05
20	0.2	16.29	1.07
50	0.5	18.11	1.19
100	1	21.10	1.38
200	2	25.16	1.65

Table 5.8: General Parameters for both rate-dependent and rate-independent cases, relevant for Tables 5.9 and 5.10.

Parameter	Value
t	2 mm
e	0.5 mm
$P_{\text{max, static}}$	50.44 kN

Table 5.9: Results when rate dependence is not considered ($t = 2\,\text{mm}$).

$\boldsymbol{v}$ [mm/s]	$\dot{\boldsymbol{\epsilon}}$ [1/s]	$\boldsymbol{P}_{\text{max}}$ [kN]	$\boldsymbol{P}_{\text{max}}/\boldsymbol{P}_{\text{max, static}}$ [-]
0.1	0.001	50.45	1.00
1	0.01	50.45	1.00
10	0.1	50.45	1.00
20	0.2	50.63	1.00
50	0.5	50.81	1.01
100	1	50.73	1.01
200	2	51.09	1.01

Table 5.10: Results when rate dependence is considered ($t = 2\,\text{mm}$).

$\boldsymbol{v}$ [mm/s]	$\dot{\boldsymbol{\epsilon}}$ [1/s]	$\boldsymbol{P}_{\text{max}}$ [kN]	$\boldsymbol{P}_{\text{max}}/\boldsymbol{P}_{\text{max, static}}$ [-]
0.1	0.001	51.19	1.01
1	0.01	51.75	1.03
10	0.1	52.73	1.05
20	0.2	53.23	1.06
50	0.5	53.91	1.07
100	1	54.17	1.07
200	2	54.94	1.09

Table 5.11: General Parameters for both rate-dependent and rate-independent cases, relevant for Tables 5.12 and 5.13.

Parameter	**Value**
t	3 mm
e	0.5 mm
$P_{\text{max, static}}$	98.94 kN

Table 5.12: Results when rate dependence is not considered ($t = 3\,\text{mm}$).

$\boldsymbol{v}$ [mm/s]	$\dot{\boldsymbol{\epsilon}}$ [1/s]	$\boldsymbol{P}_{\text{max}}$ [kN]	$\boldsymbol{P}_{\text{max}}/\boldsymbol{P}_{\text{max, static}}$ [-]
0.1	0.001	98.94	1.00
1	0.01	98.95	1.00
10	0.1	98.95	1.00
20	0.2	98.98	1.00
50	0.5	98.70	1.00
100	1	100.31	1.01
200	2	102.37	1.03

Table 5.13: Results when rate dependence is considered ($t = 3\,\text{mm}$).

$\boldsymbol{v}$ [mm/s]	$\dot{\boldsymbol{\epsilon}}$ [1/s]	$\boldsymbol{P}_{\text{max}}$ [kN]	$\boldsymbol{P}_{\text{max}}/\boldsymbol{P}_{\text{max, static}}$ [-]
0.1	0.001	100.87	1.02
1	0.01	102.32	1.03
10	0.1	104.86	1.06
20	0.2	105.92	1.07
50	0.5	107.51	1.09
100	1	110.01	1.11
200	2	114.09	1.15

6 Methodology and pre-study of CSM

6.1 Orientation

To investigate the correlation between the plate and the CSM section, an entire CSM section was also modelled and investigated. This section outlines the methodology used for modelling and analysing the CSM. To ensure consistency and facilitate direct comparison with the steel plate model, the same material model was applied to the CSM. This approach is justified by the objective of maintaining comparable conditions, as the steel plate is intended to represent the compressed part of the CSM flange (see Sections 4.4 and 4.4.1 for details on the material model). The overall analysis procedure for the CSM structure closely follows that of the steel plate. The primary distinction, aside from the geometric differences, lies in the load application. For the static analysis, a pressure load was applied to the horizontal segments of the CSM (see Section 6.7.1), while the dynamic analysis involved an explosion load (see Section 6.7.2). The recommendations presented in Section 2.5.3 are followed when making modelling decisions.

6.2 Geometry and element type

The load carrying CSM roofing product T130-75L-930 (insulated roof) from the reseller RUUKKI was used as reference, see Ruukki Sverige AB (2025). The CSM sheets come in segments with three top-flanges (corrugations) of which are then assembled together to cover larger areas, see Figure 6.1 and the cross-sectional measurements in Figure 6.2. As can be seen in both figures, there are longitudinal ripples along the sheet. The ripples stiffen the CSM, but was in the present study disregarded to reduce complexity, this was motivated by the study performed being a principle study and the goal was not to investigate the exact capacity of a certain product.

Figures 6.3 and 6.4 show the geometry used in Abaqus for the CSM model. As with the plate model, shell elements of type S4R were employed. The length of the CSM strip was set to 6000 mm, and three different thicknesses were analysed: 0.7 mm, 1.05 mm, and 1.4 mm. The 0.7 mm thickness and 6000 mm length are based on Ruukki's specifications (see Appendix C), while the other thicknesses were chosen as scaled variations: 1.05 mm equals 0.7 mm $\times$ 1.5, and 1.4 mm equals 0.7 mm $\times$ 2.

The reason for the tension flange being cut in half at the ends in Abaqus was that symmetry boundary conditions were used along the two longitudinal edges, meaning that the actual width of all tension flanges is 75 mm even though only 37.5 mm is modelled.

In reality, some overlap between tension flanges is needed to mount multiple segments of sheets; this was disregarded since only a negligible influence is expected if a larger thickness is modeled locally at the locations for the overlap.

Figure 6.1: CSM from RUUKKI.

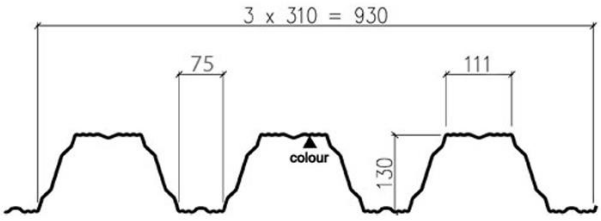

Figure 6.2: RUUKKI cross-section for specific product.

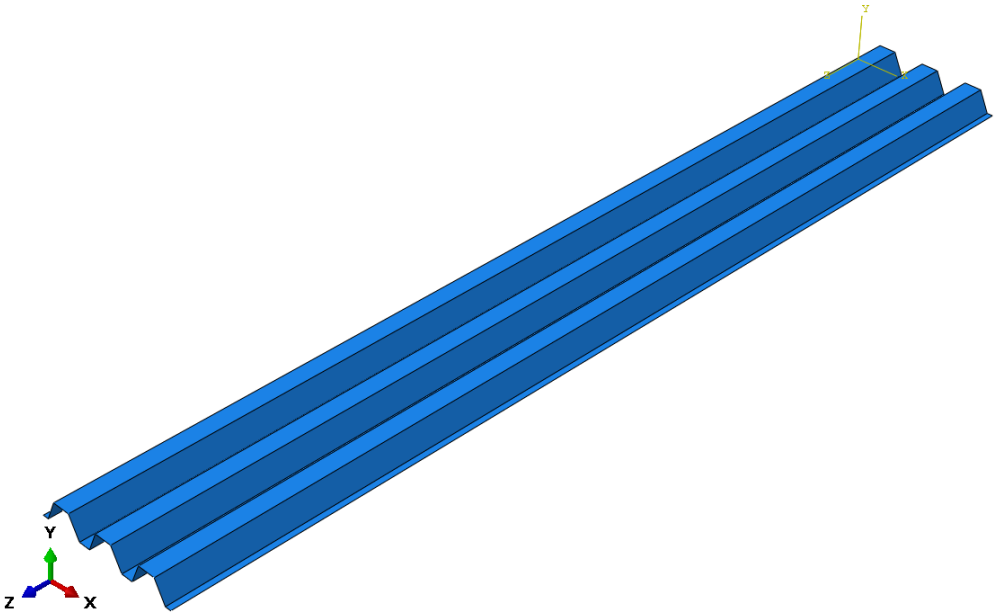

Figure 6.3: Geometry in Abaqus.

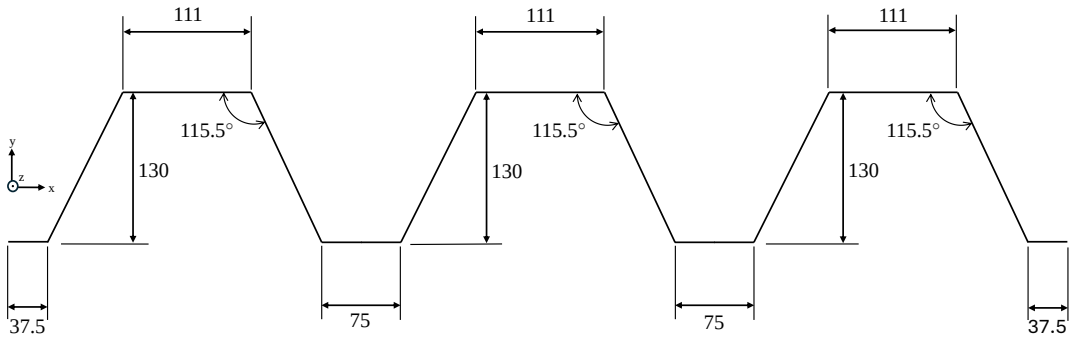

Figure 6.4: Simplified cross-section, unit mm.

6.3 Initial imperfections

During the static analysis, difficulties were encountered in capturing the post-buckling behaviour. According to Eurocode guidelines, an initial geometric imperfection of $b/200$ should be applied, where b is the width of the compressed flange, in this case, $b = 111$ mm, resulting in an imperfection magnitude of approximately 0.55 mm. However, with this value, the analysis struggled to progress into the post-buckling regime. By increasing the imperfection amplitude, Abaqus was better able to reach and maintain convergence beyond the peak load, where equilibrium paths become unstable. As a result, an imperfection magnitude of

$e = 3$ mm was selected to facilitate convergence and guide the solution toward the post-buckling path. In the dynamic simulations, this issue was not observed. Nevertheless, to ensure consistency across all simulations, an imperfection magnitude of $e = 3$ mm was also applied (unless otherwise stated). For a comparison of dynamic responses using different imperfection amplitudes, see Section 7.3.9, which further supports that the chosen amplitude has limited influence on the overall results in this study.

6.4 Boundary conditions

6.4.1 Base conditions

The influence of different boundary conditions was investigated, with the primary case being a simply supported configuration. Symmetry boundary conditions were applied along both longitudinal edges in the x-direction, as shown in Figure 6.5, representing an infinitely wide sheet of connected segments.

The CSM base condition was simply supported, with an in-plane restraint at the transversal edges in the x-direction positioned at the centre of a bottom bay, representing the location of fasteners where the CSM would be attached to a supporting beam, see Figure 6.6. Apart from the simply supported case additional cases were also examined, including a configuration with full restraint at both transversal edges (pinned-pinned). For a more realistic simulation, a case with partial restraint was also studied, as described in Section 6.4.2.

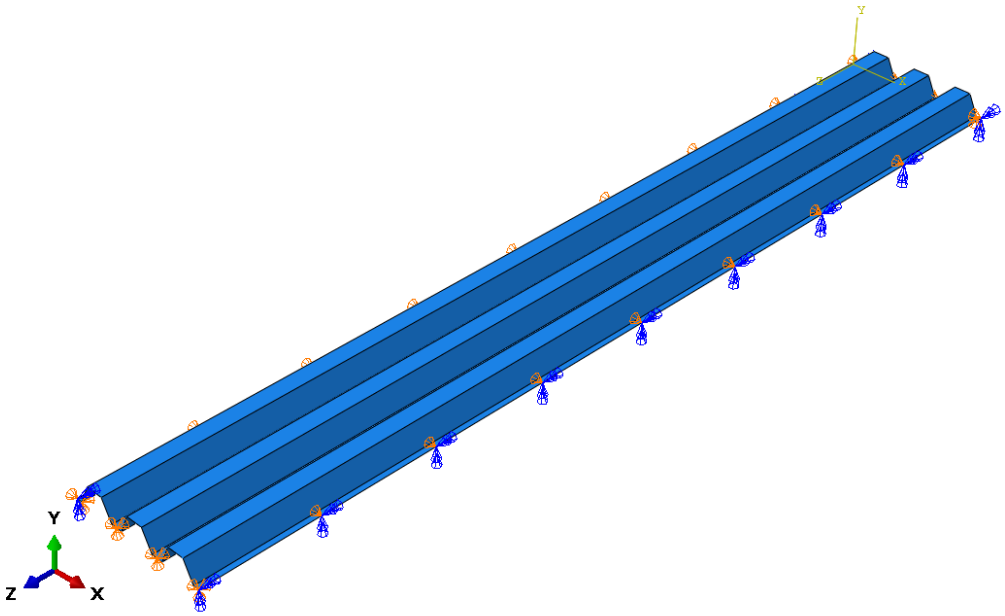

Figure 6.5: Boundary conditions along longitudinal edges, simply supported case, considered as base condition.

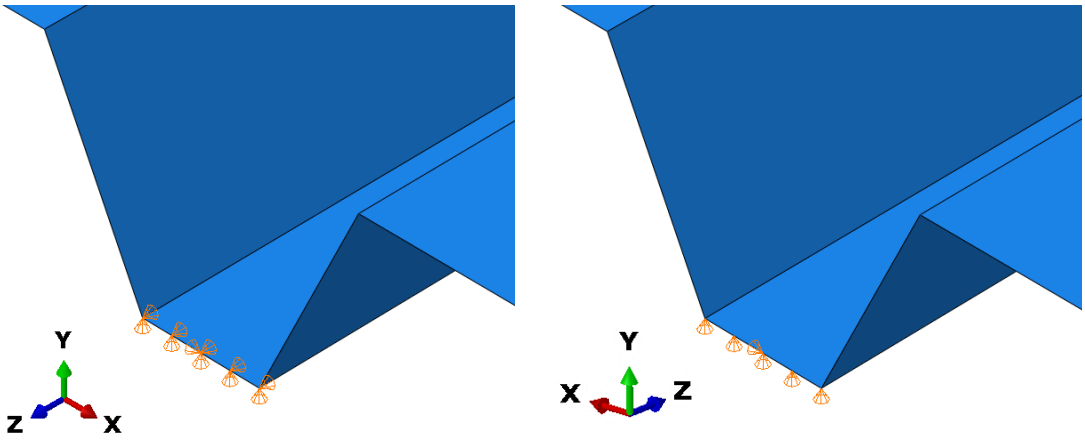

Figure 6.6: Boundary conditions at the transversal edges, simply supported.

6.4.2 Partial restraint using spring elements

In reality, the CSM is fastened to the roof beams along the supported edges, suggesting a boundary condition closer to pinned-pinned rather than simply supported. The connection introduces additional potential failure modes, such as fastener fracture or localized plastic deformation of the steel due to increased stress concentrations at the fastener-hole edges as the fastener transfers the load.

The fasteners were assumed to resist failure, thereby shifting the focus of the analysis to potential plastic deformation in the steel. To model this behaviour non-linear springs were implemented. The springs were only allowed to elongate at the critical load corresponding to potential failure modes (edge breakout / edge failure), as defined by the Eurocode. The non-linear spring behaviour corresponding to Eurocode is denoted K_1 and presented in Table 6.1 and visualized in Figure 6.7. Two other fictional spring behaviour were also investigated. K_2 represents a fictional increase in spring stiffness, see Table 6.1 and K_0 represent a case with almost no stiffness in one end and infinitely stiff springs in the other to validate the springs against the simply supported case, see Table 6.2. The calculations and assumptions used to determine the spring stiffness K_1 are provided in Appendix F. Failure may be defined as when the spring displacement is equal to the bolt-to-edge distance, see Figure 6.8.

The number of springs was determined based on the imperfection file. Initially, assigning a single spring to the node corresponding to a bolt location resulted in a distorted imperfection shape, with deformation concentrated near the edges adjacent to the spring. This configuration proved insufficient to support buckling behaviour at the mid-section. To mitigate this, springs were instead distributed across every node along the supported edge, which produced an imperfection mode more consistent with that observed in previous simulations. As a result, the total spring stiffness was preserved by dividing the computed critical force stiffness equally among the springs associated with each bolt hole. Even though this is not an entirely correct description of reality, it should have no major influence on the results

Table 6.1: Force and Displacement for K_1 and K_2.

K_1		K_2	
Force [N]	**Disp [mm]**	**Force [N]**	**Disp [mm]**
-1000	-100	-2000	-100
-937	-0.1	-1874	-0.1
0	0	0	0
937	0.1	1874	0.1
1000	100	2000	100

Table 6.2: Force and Displacement for K_0.

K_0			
Pinned edge		**Free edge**	
Force [N]	**Disp [mm]**	**Force [N]**	**Disp [mm]**
-101000	-100	-0.0000101	-100
-100000	-0.1	-0.0000100	-0.1
0	0	0	0
100000	0.1	0.0000100	0.1
101000	100	0.0000101	100

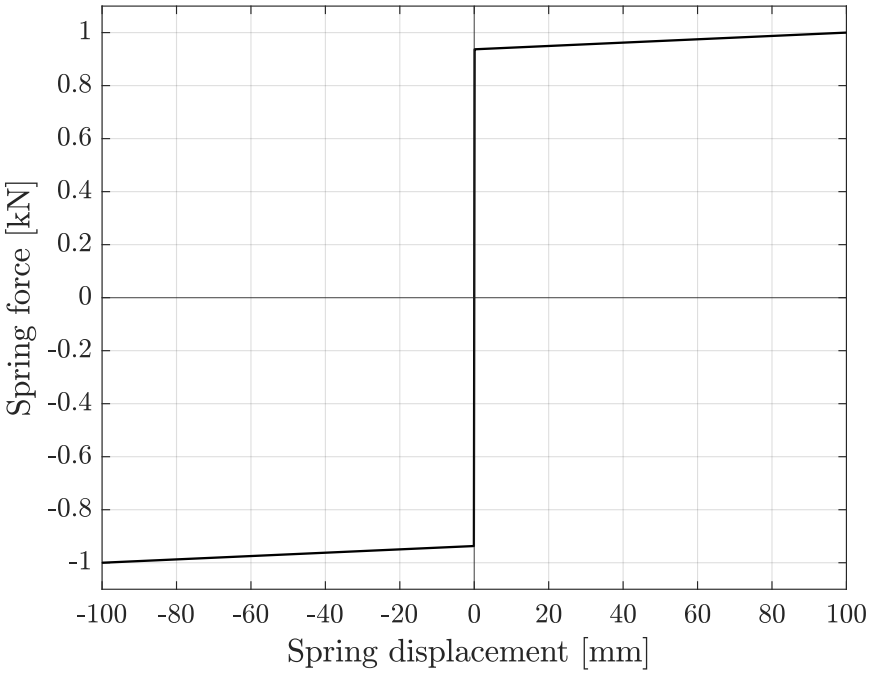

Figure 6.7: Non-linear spring behaviour K_1 used to model plastic failure at the bolt hole edge. The spring allows infinitesimal displacement until the critical load is reached and may then displace freely to simulate plasticity in the steel.

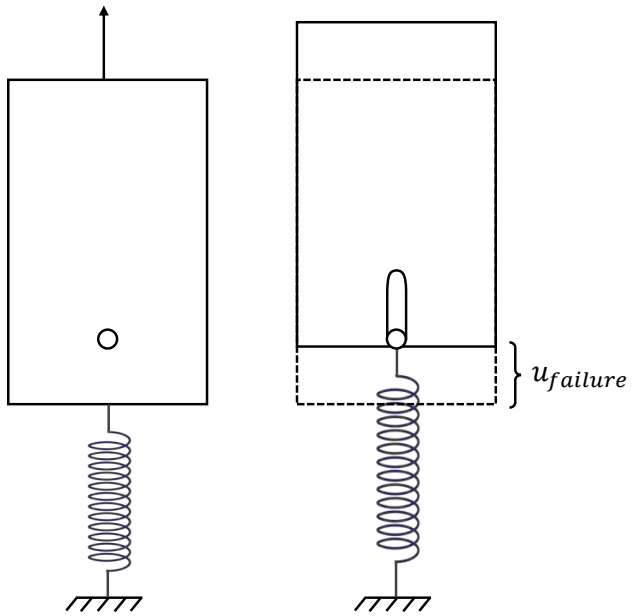

Figure 6.8: Failure assumed when the displacement of the springs is equal to the bolt-to-edge distance, since that is the limit of the plastic deformation.

6.5 Fictional density when modelling the CSM

As shown in Table 4.2, the typical density of steel is 7850 kg/m^3. When modelling the CSM structure this density results in a relatively low weight. For example, with a thickness of 0.7 mm, the mass is approximately 8.3 kg/m^2. However, the mass of the structure significantly influences the results of dynamic simulations. In reality, the actual weight would be higher due to additional components such as insulation and attachments mounted on the CSM.

To address this in Abaqus, one simplified approach is to artificially increase the density to achieve a more realistic total mass. For instance, increasing the density by a factor of 20 yields a mass of approximately 166 kg/m^2, and a factor of 40 results in 332 kg/m^2. It is important to note that if the sheet thickness or geometry is changed, the scaling factor must be adjusted accordingly to maintain the desired overall mass. Three different masses was chosen to find their influence on the results, the masses and density used in Abaqus is presented in Table 6.3.

Table 6.3: Total masses kept constant for the three thicknesses, resulting in different densities used in Abaqus.

Mass $[kg/m^2]$	**Density** $[kg/m^3]$		
930 mm	t **= 0.7 mm**	t **= 1.05 mm**	t **= 1.40 mm**
84	78571	52381	39286
166	157143	104762	78571
332	314286	209524	157143

Note that the chosen method for adjusting the mass, by artificially increasing the material density, affects the P-wave speed, as shown in Equation 6.1. While the

wave propagation behaviour in the full CSM structure is more complex and would require a more detailed expression, the key takeaway is that increasing the density leads to a reduction in c_p. However, this effect is considered negligible for the purposes of this study.

$$c_p = \sqrt{\frac{E}{\rho}} \tag{6.1}$$

6.6 Analysis steps

As with the steel plate, a buckling analysis step is required. In this case, the Lanczos method was used instead of the subspace method, as Lanczos allows for the exclusion of negative eigenvalues—an important feature when dealing with potential instability. Since snap-back behaviour may occur in the post-buckling regime, the arc-length method (Static, Riks) was employed in the static analyses to ensure accurate tracing of the equilibrium path beyond the critical point. For the dynamic simulations, both the implicit and explicit solution methods were utilized; when comparing the results obtained from the implicit and explicit solution methods, they resulted in very similar results, see Section 7.3.3. In the list below the solution steps used in the analysis of the CSM is summarized.

- **Step module:** Linear perturbation → Buckle → Eigensolver: Lanczos (used before both steps below)
- **Step module:** General → Static, Riks
- **Step module:** General → Dynamic, Implicit
- **Step module:** General → Dynamic, Explicit

To apply the imperfection shape, the same procedure as used for the plate was followed, with a slight modification to allow for the combination of multiple buckling modes in some analyses. Specifically, in the *BUCKLE step of the input file, the following keyword lines were inserted before the *END STEP command:

*NODE FILE, GLOBAL=YES, LASTMODE=600
U

And the geometric imperfections were then introduced into the non-linear static buckling model and dynamic models by adding another line in the keywords option for the non-linear static buckling model. The following input was provided under STEP in keywords:

*IMPERFECTION, FILE=name of imperfection file, STEP=1
1, 0.5
553, 0.5

In cases where only the first imperfection shape was of interest, the exact same procedure as for the plate was used.

6.7 Load application

6.7.1 Static pressure load

For both the buckling analysis, used to generate the imperfection shape, and the non-linear static analysis, a static pressure load was applied. In the buckling analysis, a reference pressure of 1 kPa was used, while the non-linear static analysis employed a load of 4 kPa. As a simplification, the pressure was applied only to the horizontal surfaces (i.e., the top and bottom flanges), excluding the diagonal webs, as illustrated in Figure 6.9 and 6.10. This influences the total load, the load is expressed as a pressure distributed over the full area, but only a part of the area is loaded, meaning that one needs to scale up the load in Abaqus accordingly to take this into account. Note that the exact magnitude of the applied load is not critical in either the buckling analysis or the non-linear static analysis. In the buckling analysis, the eigenvalue simply scales with the reference load, and in the non-linear static analysis, the arc-length method was used, allowing the applied load to vary through a load proportionality factor (LPF).

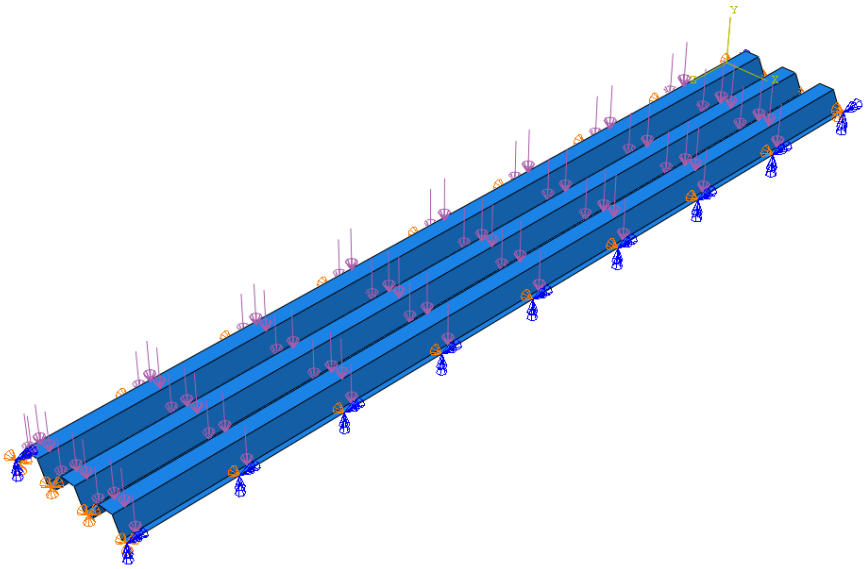

Figure 6.9: Static load application in Abaqus.

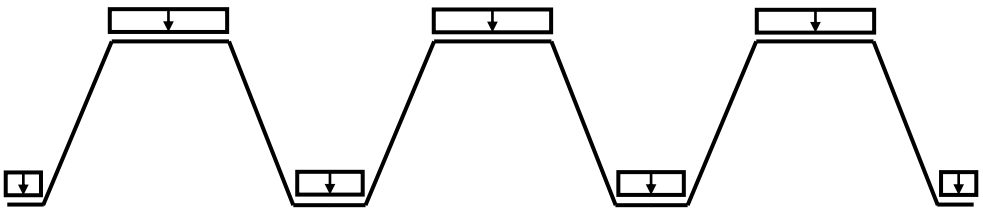

Figure 6.10: Static load application, pressure only applied to the horizontal surfaces.

6.7.2 Dynamic pressure load

A dynamic investigation was conducted by prescribing the load as a pressure-time relation, describing the positive part of the overpressure created by the explosion, see Section 2.1.2. The applied load amplitudes are visualized in Figure 6.11 and further presented in Table 6.4. The load is characterized by a sudden increase in pressure that is reduced to zero within a time frame of milliseconds. The three different amplitudes result in the same impulse.

The pressure amplitudes and their corresponding time intervals were determined in consultation with the thesis supervisor. Load 2 represents the dynamic load resulting from an unreflected incident shock wave generated by the detonation of 100 kg of TNT near the ground, at a distance of 25 meters from the roof.

The pressure was assumed to act over the full width of the corrugated sheet metal when creating the load amplitudes, however, in Abaqus the load was applied only on the horizontal surfaces (558 mm). As a result, the pressures listed in Table 6.4 were scaled by a factor of 1/0.6 to account for this difference in application area (horizontal width / total width, where the total width is 930 mm). The values input into Abaqus were thus obtained by dividing the tabulated pressures by 0.6.

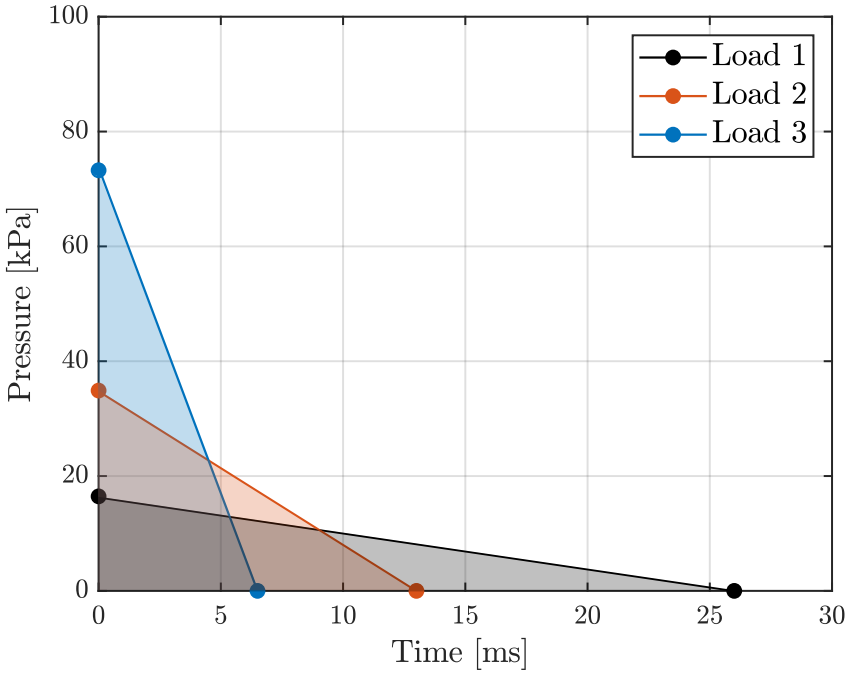

Figure 6.11: Dynamic load application.

Table 6.4: Pressure-time relations that results in the same impulse (area under the graph).

Load	Time [s]	Pressure [kPa]	Impulse [Pas]
Load 1	0	18.5	240
	0.026	0	
Load 2	0	36.9	240
	0.013	0	
Load 3	0	73.8	240
	0.0065	0	

6.8 Mesh and convergence study

A convergence study was carried out on the mesh size and mesh layout. The results from the eigenvalue analysis are presented in Table 6.5. It was observed that the number of elements in the compressed flange plays a significant role. When the number of elements in the compressed flange remains constant but the total number of elements increases, the eigenvalue changes very little. However, as the mesh is refined specifically in the compressed flange, a gradual decrease in the buckling value was observed.

Figure 6.12 shows a zoomed-in view of the force–displacement relationship for mesh configurations with 4, 6, 8, 12, and 16 elements in the compressed flange. For cases with 9 or more elements in the compressed flange, problems to reach convergence was observed, typically stalling at what most probably was the peak value of F and failing to proceed into the post-peak range. Based on the results presented in Table 6.5 and Figure 6.12, an element size of 14 mm — corresponding to 8 elements in the compressed flange was selected.

The final mesh layout is presented in Figure 6.13, the mesh is structured and has elements of uniform size.

Table 6.5: Convergence study for different element sizes.

Element size [mm]	No. of elements [-]	λ	$\Delta\lambda$ [%]	Elements in compressed flange
30	9600	0.76	–	4
27.5	10464	0.76	-0.08	4
25	14400	0.76	0.08	4
22.5	16821	0.72	-5.07	5
20	21600	0.70	-2.63	6
17.5	26574	0.70	0.02	6
16.25	32103	0.69	-1.57	7
15	39600	0.69	0.01	7
14	43758	0.68	-1.04	8
11.75	59787	0.68	-0.69	9
11	68670	0.67	-0.49	10
10	84600	0.67	-0.37	11
9	104052	0.67	-0.27	12
8.5	116490	0.67	-0.24	13
7	174828	0.66	-0.40	16

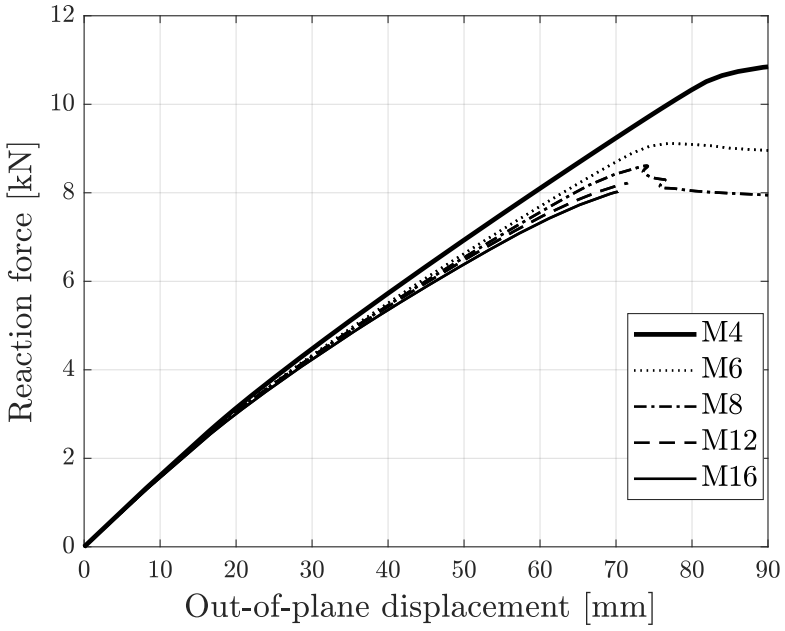

Figure 6.12: Zoomed in plot on reaction force vs displacement for different meshes. $t = 0.7$ mm, $e = 3$ mm. M is the number of elements in the compressed flange.

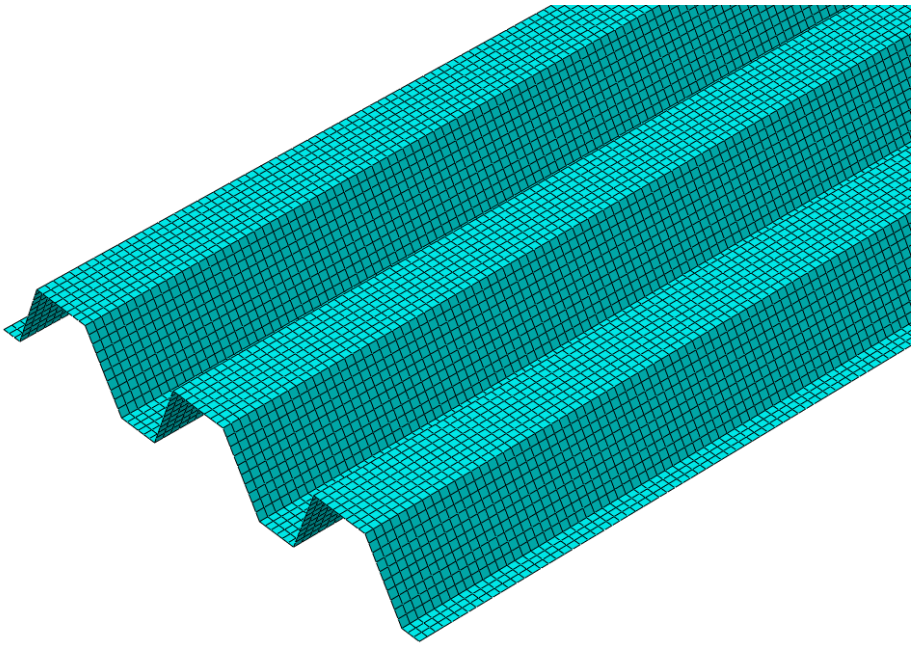

Figure 6.13: Mesh layout.

7 Results of the CSM study

7.1 Eigenvalue analysis

To obtain the shape of the initial imperfections used in the subsequent analyses, a linear buckling analysis was performed. The first eigenmode is shown in Figure 7.1, while the shapes of the first ten eigenmodes are presented in Figure 7.2. It can be observed that all ten modes correspond to local buckling patterns involving only parts of the CSM structure. This trend continues for at least the first 50 eigenmodes, which was the number specified in the analysis. The magnitude of the eigenvalue was relatively constant for the first ten eigenmodes, if $t = 0.7$ mm and a load of 1 kPa is applied to all horizontal surfaces, λ was in the range 0.68153 - 0.69556 for the first ten eigenmodes.

Note that the output displayed from Abaqus in the figures is "U, Magnitude", which is explained in Equation (7.1)

$$U_{\text{mag}} = \sqrt{U_1^2 + U_2^2 + U_3^2} \tag{7.1}$$

Where 1,2 and 3 corresponds to x-, y- and z-direction.

The first mode is the mode that is the most critical one and therefore is the one used for the shape of the initial imperfections in subsequent analyses unless otherwise stated.

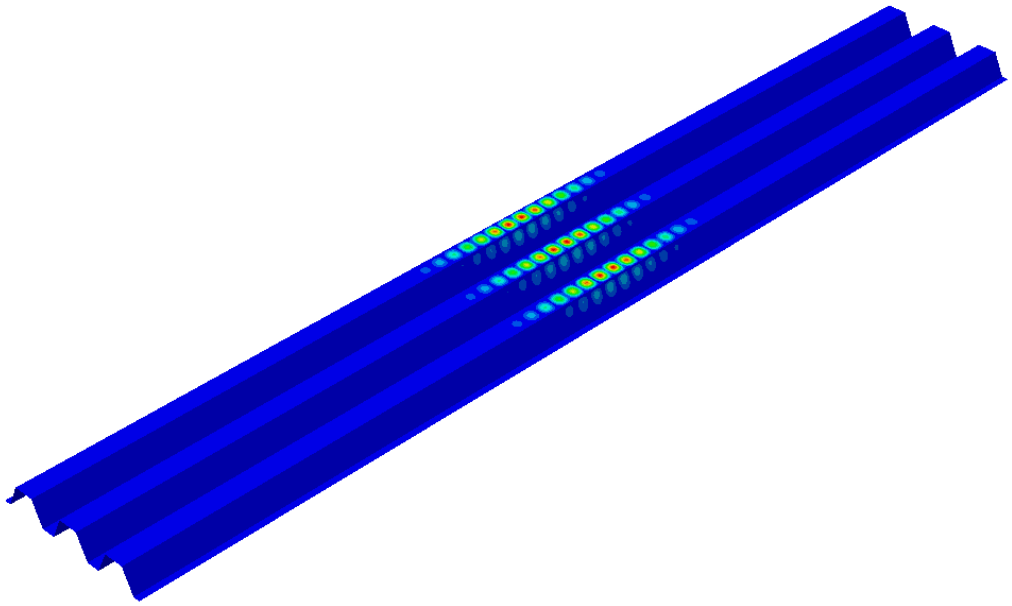

Figure 7.1: First eigenmode.

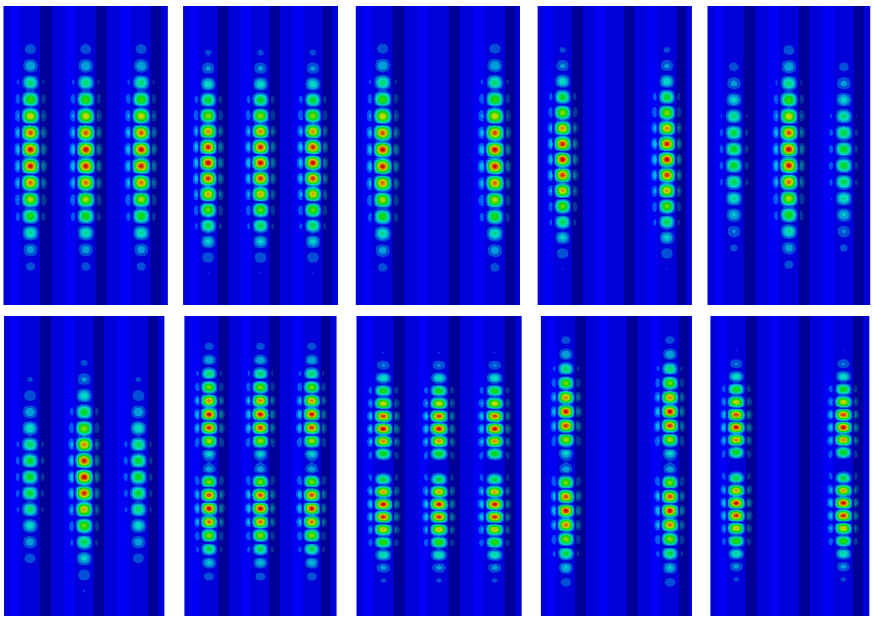

Figure 7.2: First 10 eigenmodes.

7.2 Static

7.2.1 Hand calculation of expected maximum capacity

An analytical calculation based on the expressions in EN 1993-1-5 and EN 1993-1-3 was carried out to determine the maximum load-carrying capacity for three different plate thicknesses. The results are presented in Tables 7.1 and 7.2, with detailed calculation steps provided in Appendix G. In parallel, finite element (FE) simulations were conducted in Abaqus to obtain the corresponding numerical capacities.

As discussed in Section 6.3, challenges were encountered in capturing the post-buckling behaviour when small initial imperfections were applied. To address this, an imperfection amplitude of 3 mm was used in general simulations to facilitate convergence beyond the peak load. However, for the capacity comparison shown here, where only the peak load is of interest and post-buckling response is not relevant, an imperfection amplitude of $b/200$ was applied in the FE models to align with the assumptions made in the Eurocode formulations. Note that it is uncertain whether the peak was reached, since the load-displacement curve did not reach the post-buckling range; however, it is believed that the maximum value is reached since, due to the nature of how convergence problems are encountered and reduced step sizes are automatically used.

From Table 7.1, it can be observed that the discrepancy between analytical and numerical results is somewhat larger than expected, and notably, the relative difference varies significantly with the thickness. The smallest deviation is observed for $t = 1.4$ mm. Inspection of the Mathcad calculation reveals that, at this thickness, almost the entire web area is effectively utilized. In contrast, for $t = 1.05$ mm and $t = 0.7$ mm, only a small portion of the web contributes due to susceptibility to local buckling.

Further investigation of the first eigenmode (see Figure 7.1) shows that the initial imperfection amplitude in the web is very small. This contrasts with the Eurocode approach, which uses the effective width concept for both the flange and web simultaneously. To better capture the web's contribution, a combined imperfection shape was constructed using mode 1 and a higher mode (mode 553), in which web buckling is prominent (see Figure 7.3). The resulting FE capacities are summarized in Table 7.2. It can be seen that this combined mode approach yields results that are more consistent with the analytical predictions, and the discrepancy falls within an acceptable range.

Table 7.1: Comparison of numerical and analytical capacity at different thicknesses when using the first modeshape as initial imperfection.

t [mm]	Numerical capacity [kN]	Analytical capacity [kN]	Difference [%]
0.7	9.2	8.0	13.4
1.05	17.8	16.5	7.5
1.4	28.8	27.6	4.1

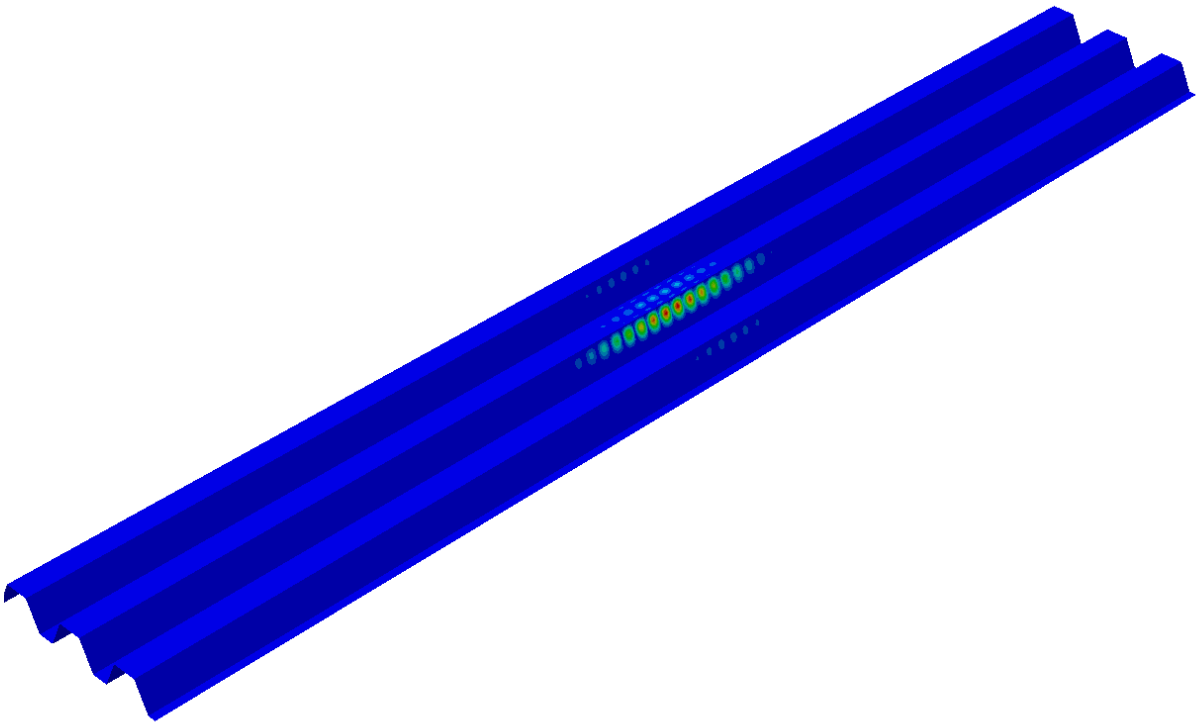

Figure 7.3: Eigenmode when only the middle webs buckle.

Table 7.2: Comparison of numerical and analytical capacity at different thicknesses when combining the first mode and the mode in Figure 7.3.

t [mm]	Numerical capacity [kN]	Analytical capacity [kN]	Difference [%]
0.7	7.6	8.0	-4.2
1.05	17.1	16.5	3.7
1.4	27.3	27.6	-1.2

In Figure 7.4, 7.5 and 7.6 the results from a hand calculation are compared to those obtained from the finite element analysis in Abaqus. Note that an initial imperfection with a magnitude of 3 mm was introduced in the FE model to trigger and explore the post-buckling response, and only the first eigenmode was used to produce Figure 7.4 to 7.6 and should not be confused with "Numerical capacity" in Table 7.2. As a result, the red curve representing the analytical prediction slightly overestimates the peak load observed in the FE simulation.

Two stiffness values are also included in the figure: one based on the full cross-section and one on the effective cross-section. This distinction is important because, in the absence of detailed knowledge about post-buckling behaviour, the maximum capacity and associated stiffness are typically used to estimate dynamic capacity. However, it can be observed that relying solely on these simplified parameters leads to a conservative prediction. The FE results show a significantly larger area under the load–displacement curve representing energy absorption, highlighting the contribution of the post-buckling phase, which is neglected in the simplified hand calculation, see Appendix H for the calculation of the stiffness. k is the stiffness if the full cross-section is utilized and k_{eff} is the stiffness of the most critical cross-section (effective widths in accordance with Eurocode). It can in the figures be seen that for all thickness k_{eff} coincide with peak even tough it is based on only the most critical cross-section and the deflection depends on the stiffness along the whole CSM strip.

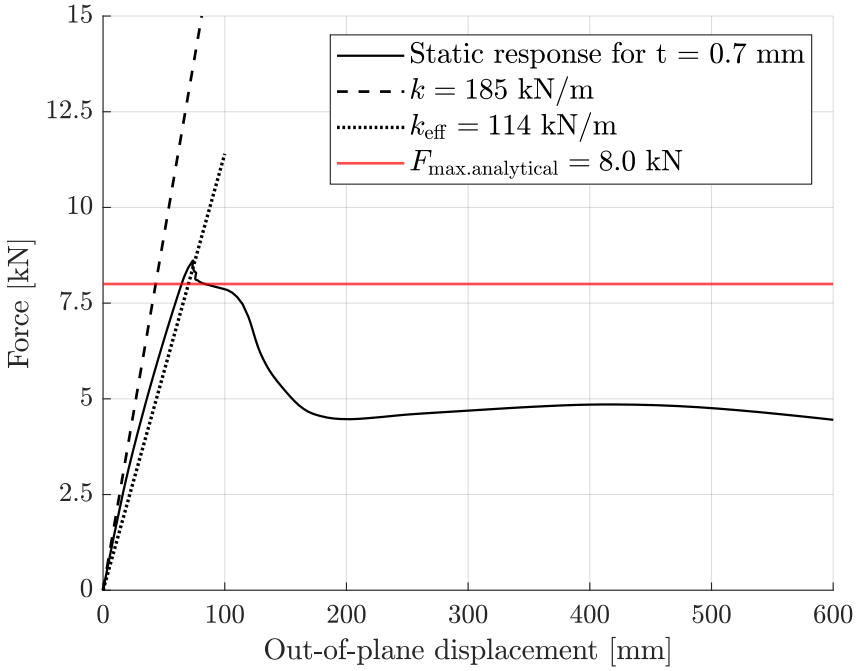

Figure 7.4: Static response for $t = 0.7$ mm compared with the analytical capacity.

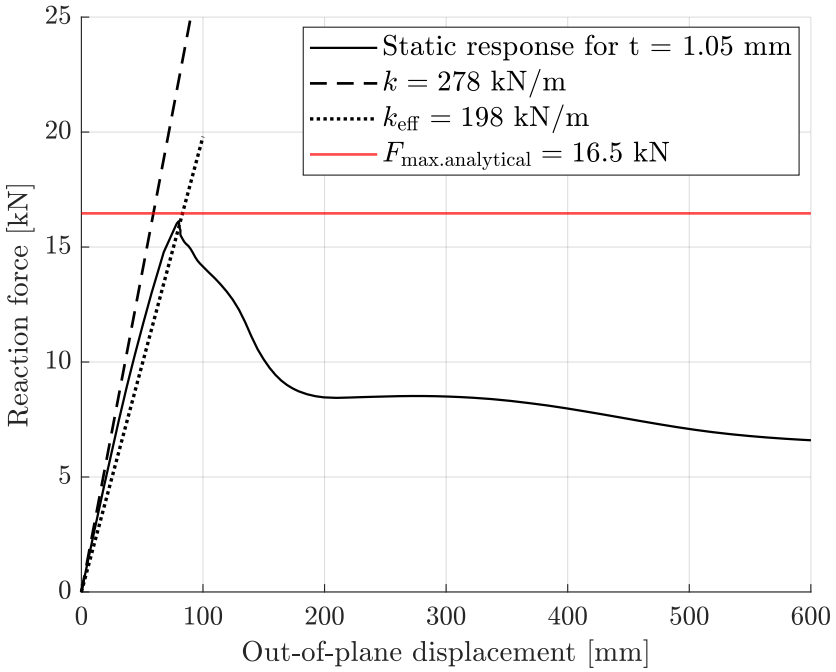

Figure 7.5: Static response for $t = 1.05$ mm compared with the analytical capacity.

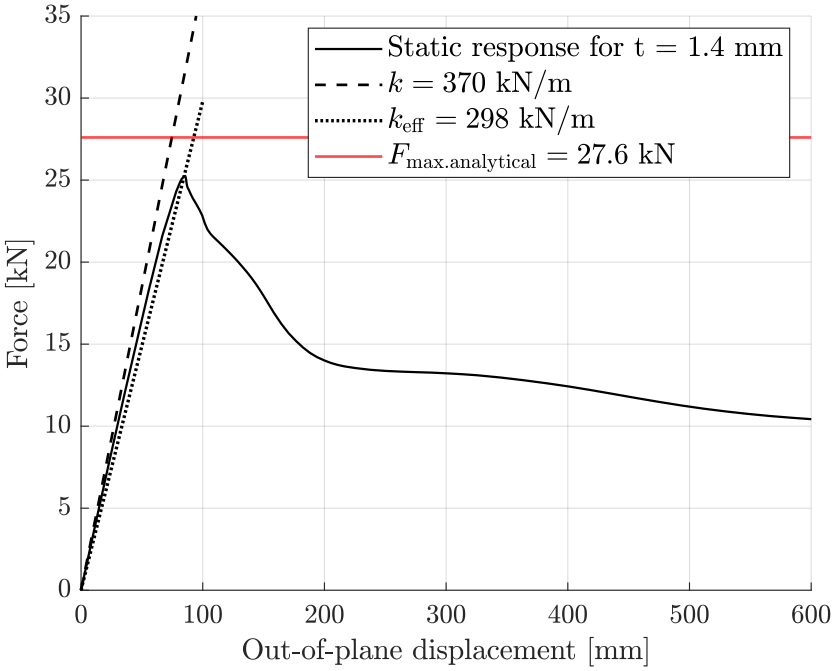

Figure 7.6: Static response for $t = 1.4$ mm compared with the analytical capacity.

7.2.2 Static behaviour

The static response for t = 1.05, under simply supported conditions, is presented in Figure 7.7. The response is governed by buckling of the top flanges at the critical load and yielding of the cross-section leading to failure at the peak load, indicated by point D. After the peak load, a sudden drop in force occurs, which then stabilizes as the displacement increases, reaching a residual capacity of about 8 kN until point H is reached. The buckled shape at a displacement of 500 mm as well as the stress distribution is shown in Figure 7.8. The end at the rolling support has moved closer to the middle of the loaded CSM strip as the displacement increases.

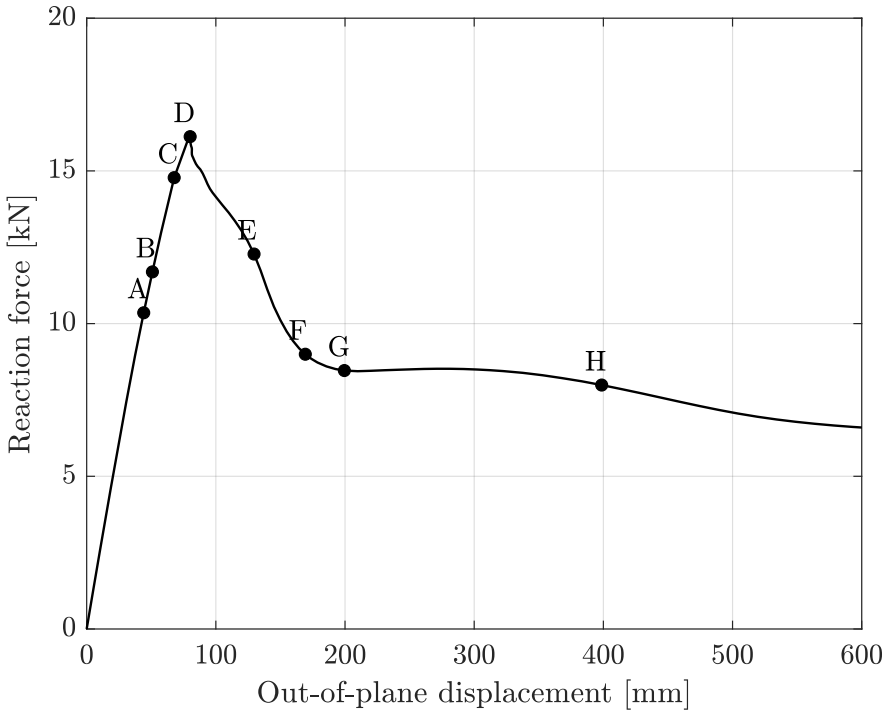

Figure 7.7: Static response for $t = 1.05$ mm. Black dots indicate selected points used for visualization of the response in subsequent figures.

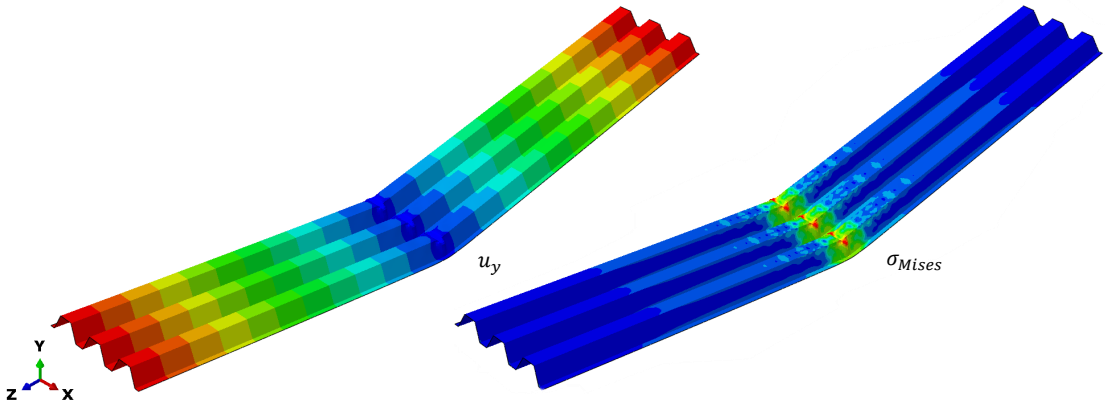

Figure 7.8: Static deflection and stress distribution for the simply supported CSM strip at 500 mm out-of-plane displacement in the mid node.

The cross-sectional deformation at the center of the buckle is presented in Figure 7.9 for some of the points in Figure 7.7. It can be observed that, up to the point of failure, only local elastic buckling occurs in the web and flange at point B. After failure, the deformation increases rapidly due to the onset of plastic deformation. Note that the initial imperfections are not visible in the plot due to how data was extracted.

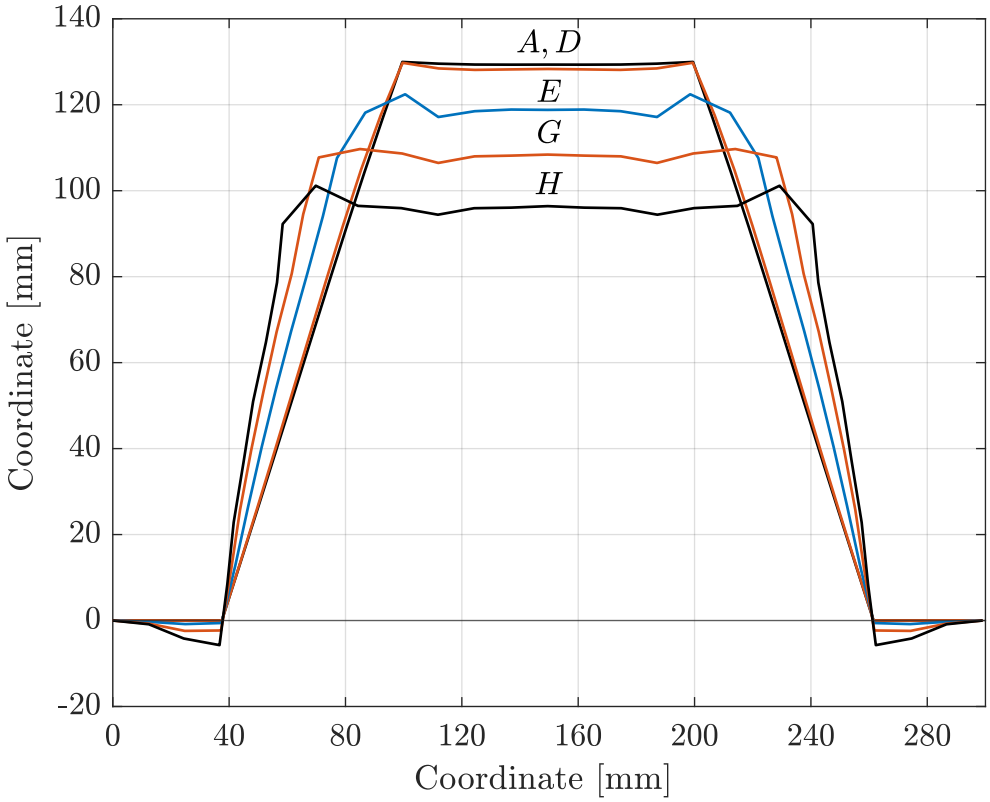

Figure 7.9: Cross-sectional response for the points in Figure 7.7.

The cross-sectional response is further illustrated in Figure 7.10. For a cross-section without initial imperfections, the undeformed state appears as shown in Figure 7.10 a), where the material above the neutral axis is in compression. As the applied load approaches the critical value, local buckling occurs in the compressive zone, reducing the load-carrying area to an effective section, as illustrated in Figure 7.10 b). As the load increases, compressive stresses in the effective area rise until yielding occurs, leading to a loss of stability and cross-sectional failure, as shown in Figure 7.10 c).

Due to the large imperfections, there is no clear distinction between the transition from Figure 7.10 a) to Figure 7.10b); in other words, no distinct bifurcation point is observed.

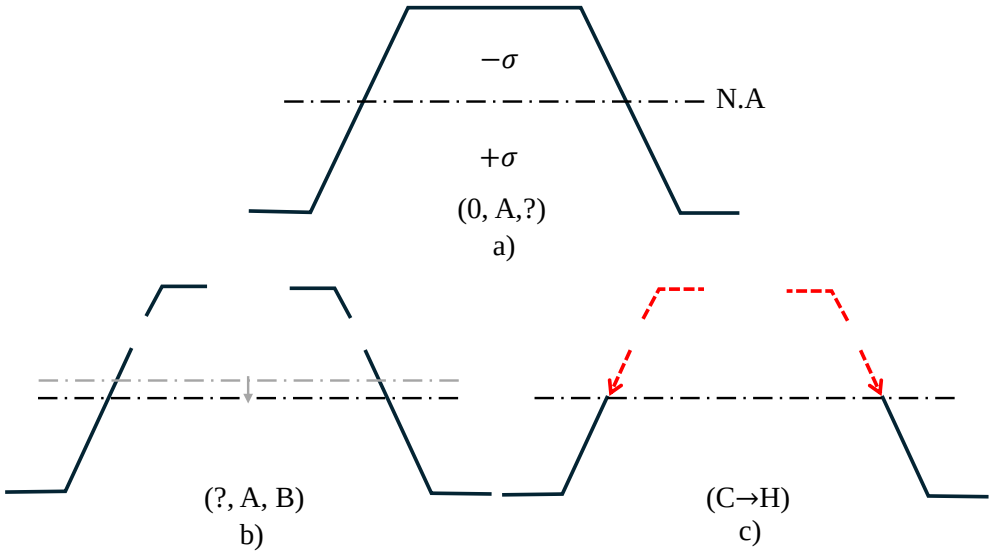

Figure 7.10: Cross-sectional response during buckling and failure. a) Unbuckled state without any imperfections b) Local buckling at top flange and part of web in compression, c) cross-section yields (red line), complete failure.

The corresponding plastic strain distribution at key points is presented in Figure 7.11. It can be seen that plastic strains (indicated by red elements) begin to develop in the flange corners, at the location of the effective area. This occurs near the peak load and the plastic deformation increase as the cross-section fails and folds in the mid-span region.

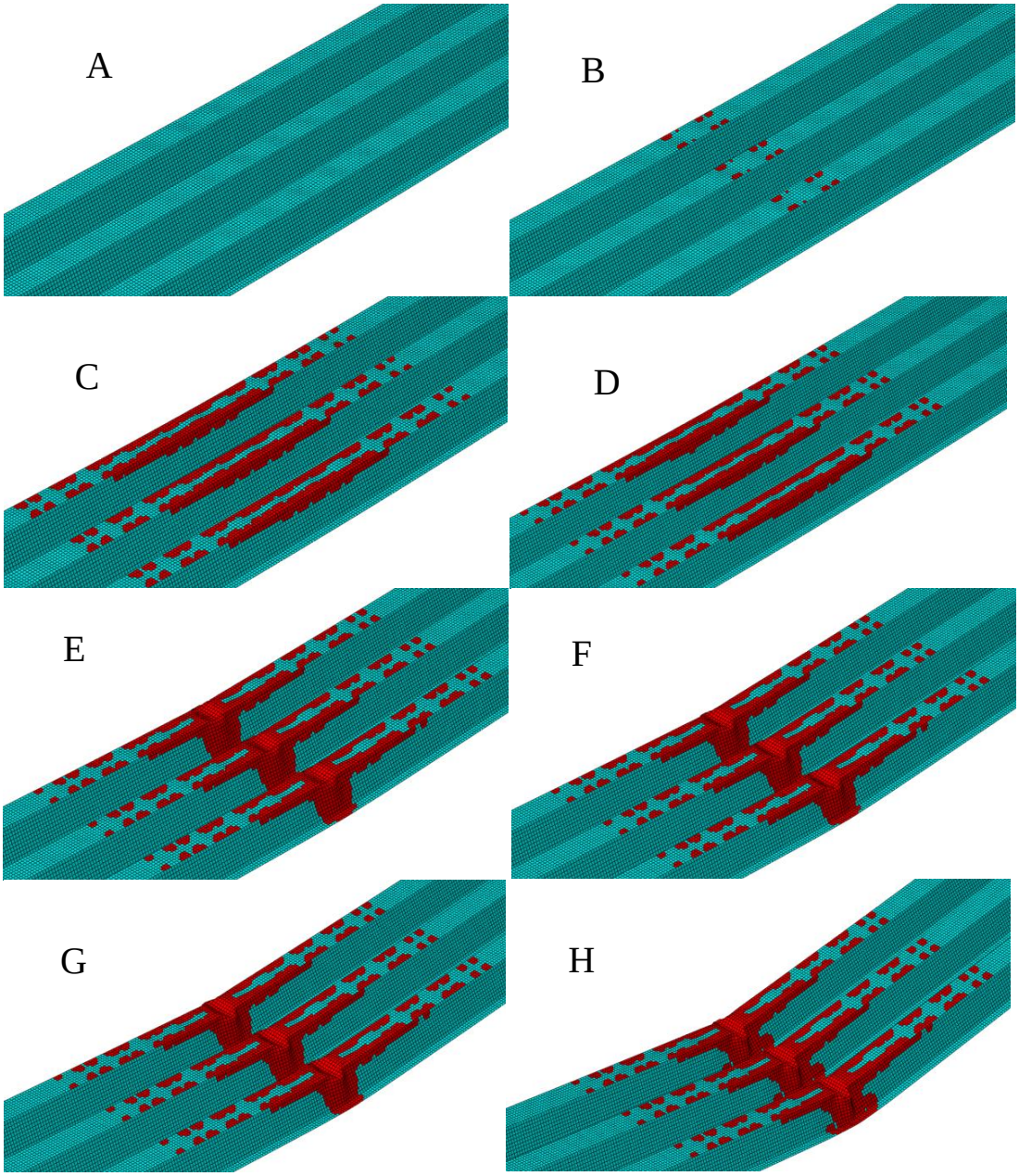

Figure 7.11: Plastic strain (red) for the points in Figure 7.7.

To clarify the structural response at failure, a zoomed-in section of Figure 7.7 is shown in Figure 7.12, and the corresponding plastic strain distributions at selected points are presented in Figure 7.13. For the collapse mechanism to fully develop, yielding must occur across the buckle. The figures reveal that yielding does not occur simultaneously in the top flanges, which explains the observed irregularities (shifts) in the load-displacement plot in Figure 7.12.

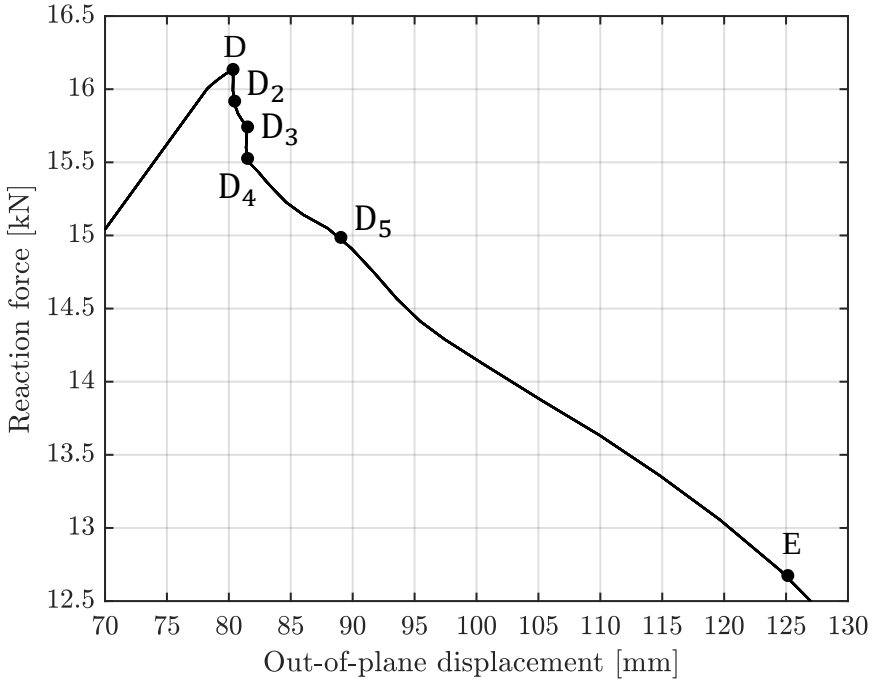

Figure 7.12: Figure 7.7 zoomed in between point D and E.

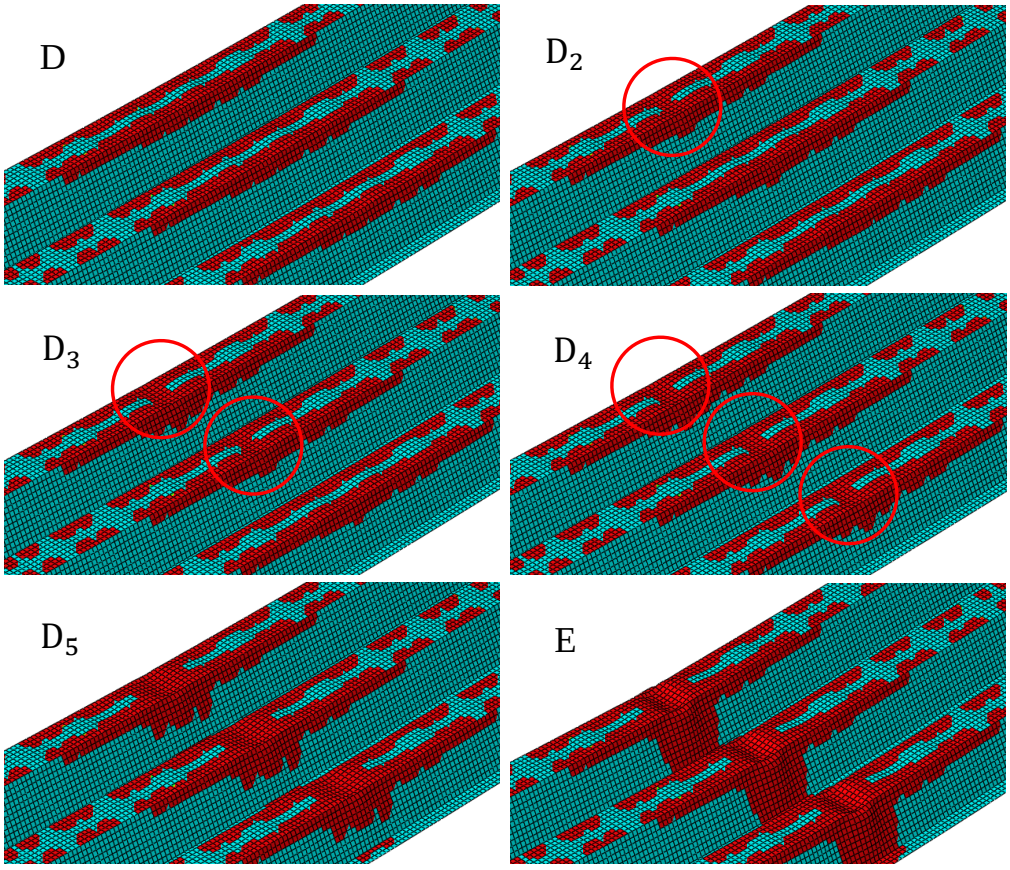

Figure 7.13: Plastic strain at the points indicated in Figure 7.12. Red circles mark when each buckle has fully yielded across.

7.2.3 Boundary conditions

Two different sets of boundary conditions were considered for the base case. The force-displacement response for a simply supported section is presented in Figure 7.14 a) and the response for a section with both ends pinned in Figure 7.14 b) for thicknesses 0.7, 1.05, and 1.4 mm. The response of the simply supported section resembles that of the plate: elastic deformation followed by collapse due to buckling (peak load) and then a decreasing post-peak strength. In contrast, the pinned-pinned condition exhibits a smaller peak load but increasing post-peak strength due to catenary action, see Section 2.1.11, indicating that the segment is capable of carrying additional load after global buckling. Note that when using the pinned-pinned boundary conditions for $t = 0.70$ mm, convergence issues were encountered and the analysis was terminated.

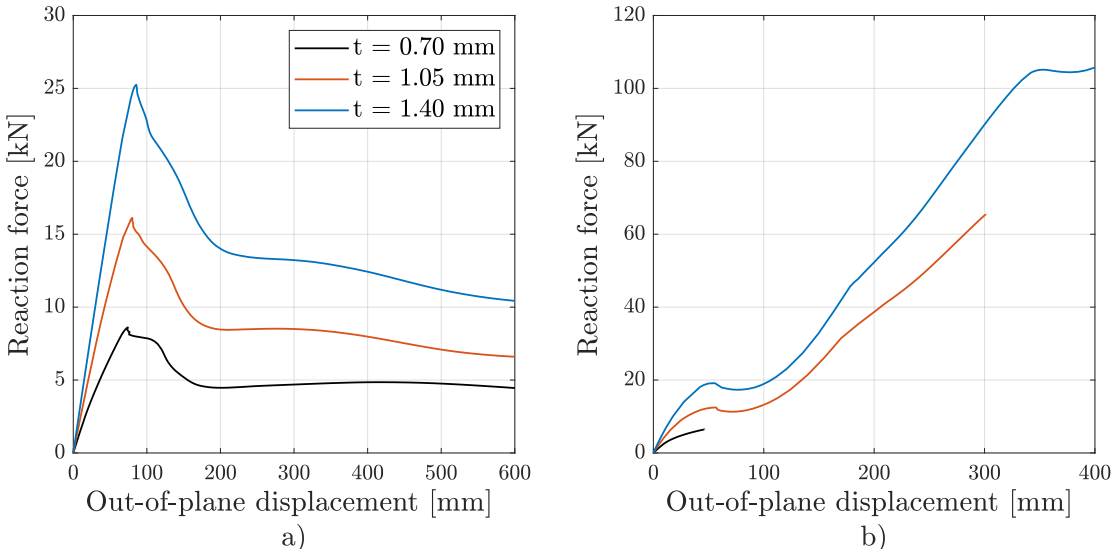

Figure 7.14: Force-displacement response for different steel thicknesses, a) simply supported (SS), b) pinned-pinned (PP).

The response for the partially restrained condition using springs is presented in Figure 7.15, for t = 1.05 mm and the three different spring stiffnesses, along with the results for the simply supported and pinned-pinned segments. It can be seen that for K_0 the response is identical to that of the simply supported case, verifying that the springs work as intended. For K_1 and K_2 the response with springs lies between the two base cases. As the stiffness of the springs increases (K_2), the response approaches that of the pinned condition, which essentially represents a case with infinitely stiff springs. After the first peak, the response initially follows the same trend as the pinned case, with increasing reaction force. However, it then suddenly diverges, creating a second peak. This marks the point at which the springs begin to deform freely, that is when the springs are yielding, indicating the onset of local plate failure around the fasteners. The sharp shifts right after the first peak load for K_1 and K_2 are the same phenomenon as shown in Figure 7.13.

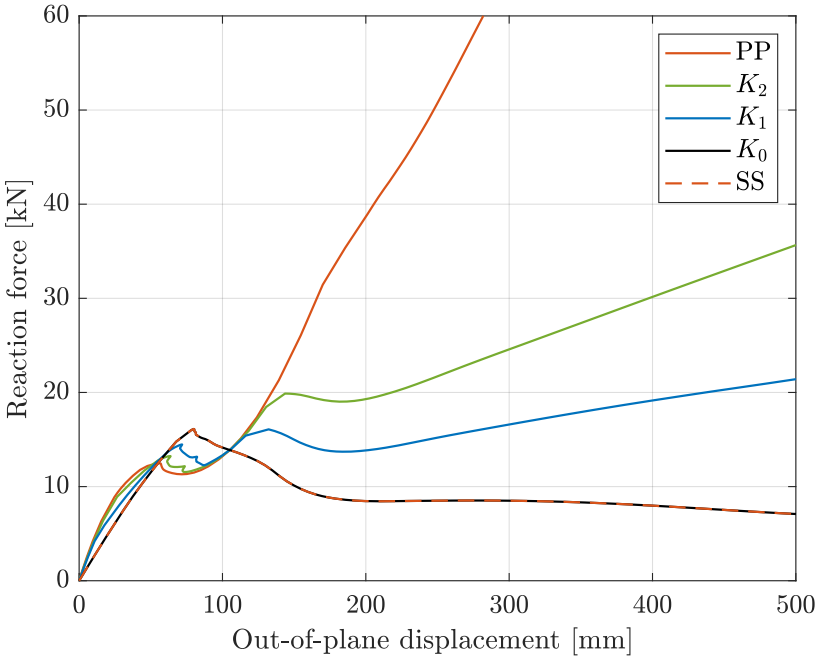

Figure 7.15: Influence of springs to simulate local failure in steel around fasteners for $t = 1.05$ mm.

7.3 Dynamic

7.3.1 Orientation

The results from the dynamic analyses are presented in this section. Various parameters are altered to investigate their influence on the structural response, specifically the out-of-plane displacement over time. Since the structure is no longer a simple plate the reaction force versus displacement is no longer a reliable response metric, as the reaction force may lag behind the actual deformation, see Section 2.1.4. The reference case used throughout is a CSM section with a plate thickness of 1.05 mm, a mass of 166 kg/m^2 and subjected to load amplitude 2, see Figure 6.11, with strain rate effects turned on and simply supported boundary condition. Note that in both the static and dynamic analysis the self weight is not modelled, i.e. $g = 0\ m/s^2$ and no damping is considered.

7.3.2 Hand calculation of expected maximum deflection based on static response

A step-by-step simplified analytical calculation is included in Appendix E, and the resulting comparison is presented in Table 7.3. The results from Abaqus are taken from the case where load 3 is applied and when the strain rate effect is not activated, meaning that $\gamma_I = 1.00$ and $DIF = 1.00$. A good correlation can be observed in the Table, except for the case when $t = 0.7$ mm, where a difference of 30 percent can be observed, the cause of the inconsistency was not found. However, a check for the simpler case assuming linear-elastic material behaviour and only small deformation was made, in that case a difference of 4 percent was obtained, indicating a good correlation and that no obvious error was made since the same Abaqus model was used.

Several simplifications is made during the hand calculations, for instance, the entire CSM structure was simplified to a single-degree-of-freedom (SDOF) system to facilitate the calculations, whereas the actual system is significantly more complex. Also note that κ_{mF} assuming plastic response was used, see Appendix E, depending on mass and thickness of the CSM strip it might be more correct to use κ_{mF} assuming elastic response. The displacement is taken from only the exact midpoint of the of the top mid flange, which isn't necessarily the point where maximum deflection occurs, see for example Figure 7.27, note that in Figure 7.27 strain rate effect is activated in Abaqus. For more details of the assumptions made, including support conditions and dynamic effects, see Appendix E.

Table 7.3: Comparison of u_{SDOF} and u_{FEM} results for varying thickness and mass values.

	u_{SDOF} [mm]		u_{FEM} [mm]		**Difference [%]**	
m [**kg/m²**]	**166**	**332**	**166**	**332**	**166**	**332**
$t = 0.7$ mm	210	113	297	126	-30%	-11%
$t = 1.05$ mm	130	80	135	80	-4%	0%
$t = 1.4$ mm	100	65	95	63	5%	3%

7.3.3 Explicit vs. Implicit

Both implicit and explicit solvers were used in the dynamic analyses. The explicit solver proved to be significantly more time-efficient compared to the implicit one. To justify the use of different solvers, results from two representative cases are presented in Figure 7.16, demonstrating that they produce comparable outcomes. As shown, both solvers yield nearly identical results, with minor differences observed in the pinned–pinned case after the point of maximum displacement. However, this discrepancy is considered negligible, as the overall response is consistent, and the maximum displacement is the primary focus in the dynamic analysis.

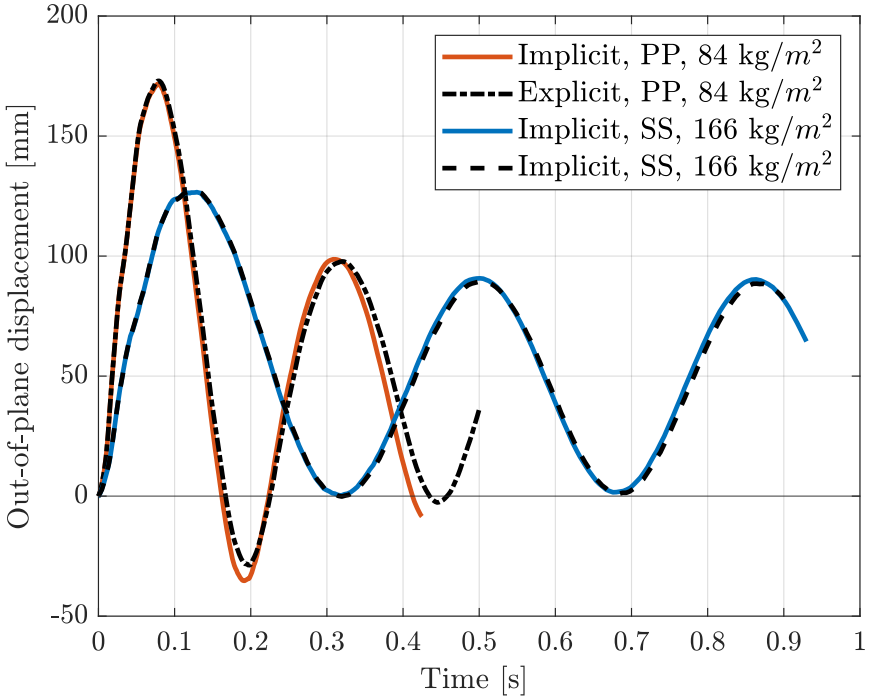

Figure 7.16: Dynamic response using implicit vs. explicit solver for two different boundary conditions and mass combinations. Thickness 1.05 mm, load 2, strain rate effects enabled.

7.3.4 Dynamic response

The dynamic response over the first 5 seconds is shown in Figure 7.17. The full load is applied instantaneously and reduced to zero within 13 milliseconds. However, the maximum deflection does not occur until approximately 110 milliseconds after the load has been removed, indicating a delayed structural response. After reaching peak displacement, the CSM section exhibits oscillatory behaviour. Note that displacements in the loading direction are defined as positive. It is also worth noting that the fact the curve's response appears to teach a displacement of approximately zero is coincidental; for different cross-section thicknesses or mass values, the oscillation may occur around a different baseline level.

The response is further illustrated in Figure 7.18, which shows the longitudinal out-of-plane displacement. When oscillating back upwards, the region between the edges and the midpoint appears to deflect more (red vs. green), whereas at the bottom of the oscillation, the midpoint shows the largest deflection (blue).

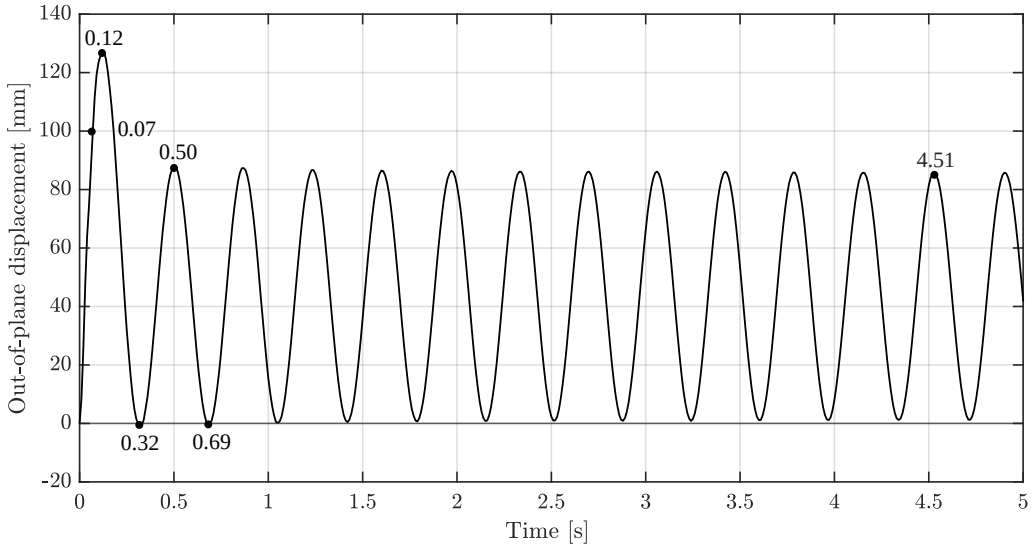

Figure 7.17: Dynamic response for $t = 1.05$ mm, $m = 166$ kg/m^2 and load 2 with strain rate effects enabled. Black dots indicate selected time steps used for visualization of the response in subsequent figures.

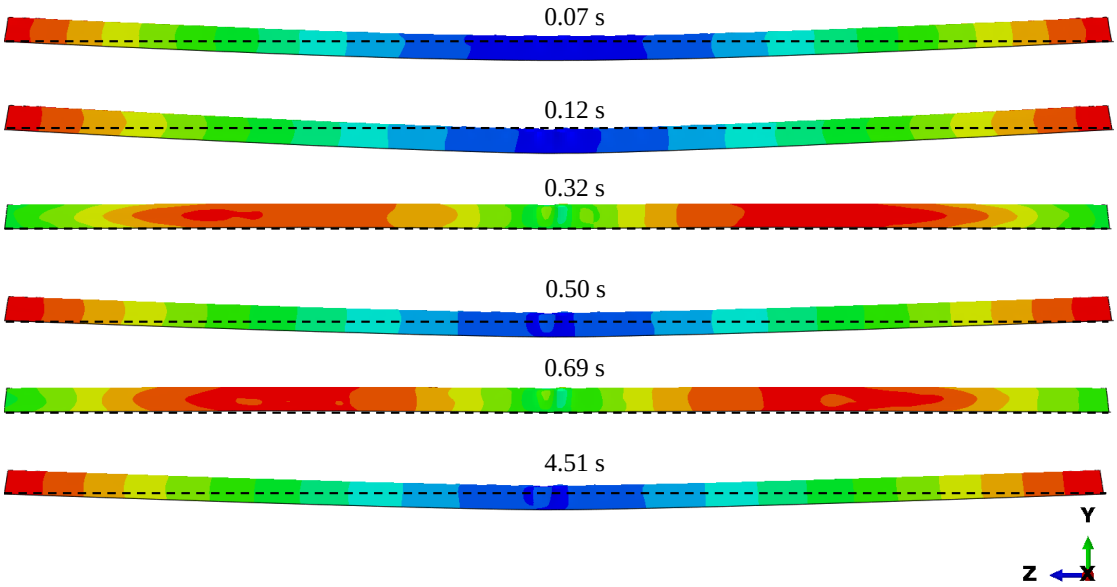

Figure 7.18: Out-of-plane displacement for time steps in Figure 7.17. Dotted line indicates the undeformed position.

The out-of-plane displacement and stress distribution is seen in Figure 7.19. The displacement pattern resembles that of the static case, however the stress distribution is no longer static or gradually varying. Instead, stress waves propagate dynamically between the supports and the midspan in the direction of the arrows, resulting in the patchy appearance. These stress fluctuations are governed by the material's wave speed and do not move dependently of the beam oscillations.

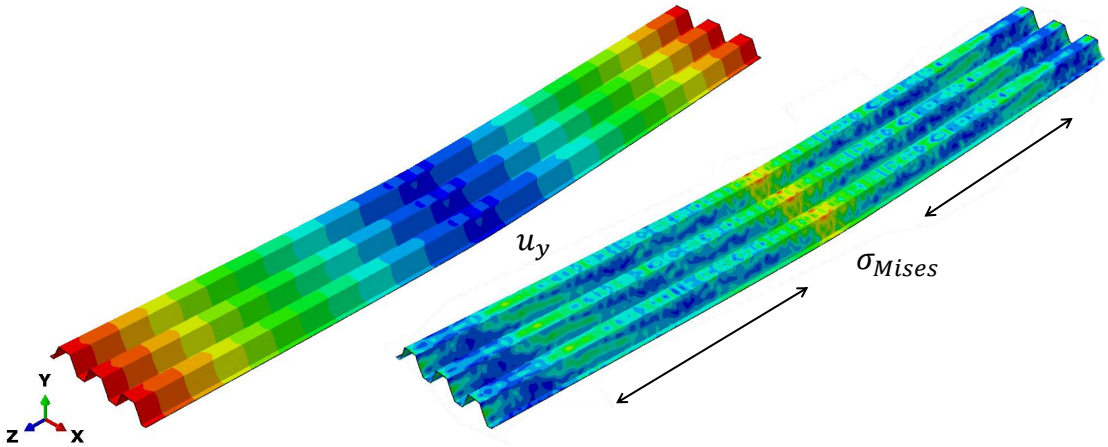

Figure 7.19: Displacement in the dynamic case for the simply supported CSM strip and still-picture of the stress distribution.

The middle part of the CSM affected by buckling is presented for several time steps in Figure 7.20. The upper flanges buckle at around 70 milliseconds, obtaining plastic deformation. The plastic deformation is irreversible and kept throughout the oscillations.

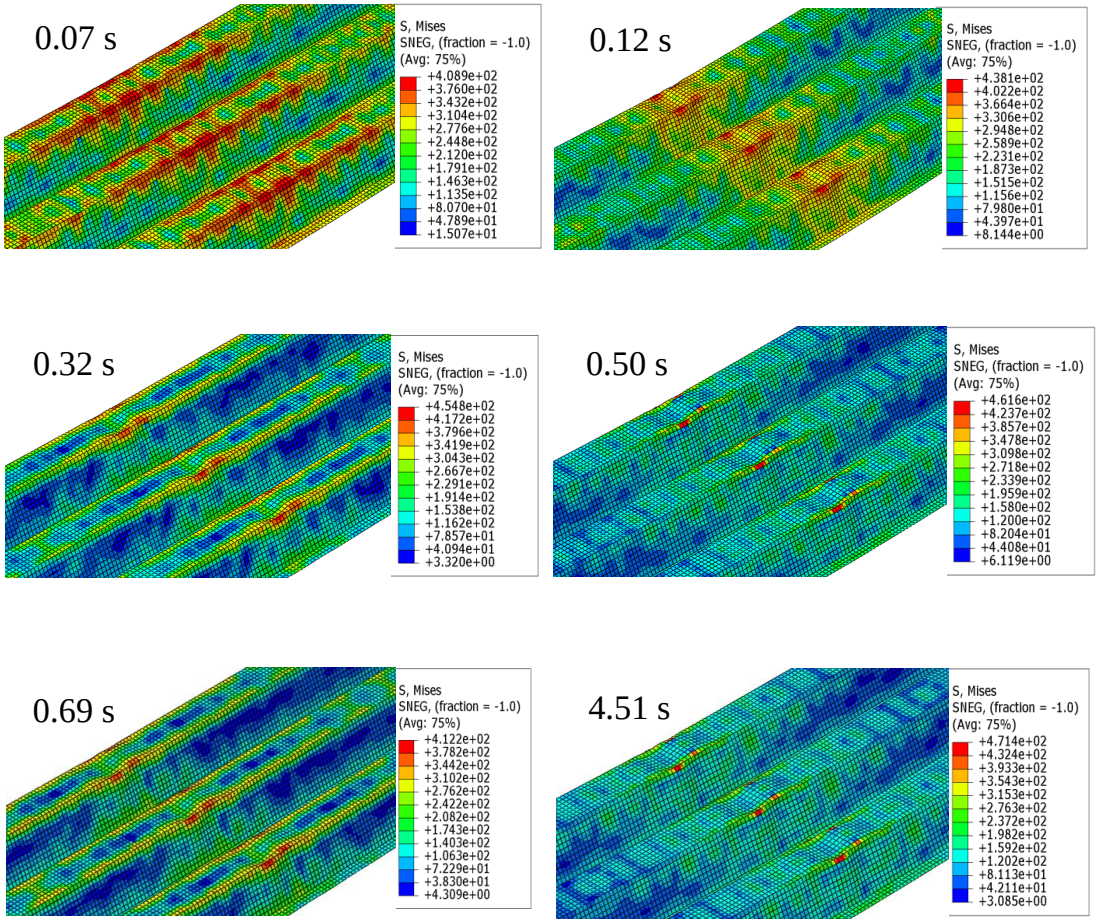

Figure 7.20: Von Mises stress plot of the buckled area for time steps in Figure 7.17.

The longitudinal out-of-plane displacement during the initial 20 ms is presented in Figure 7.21. The load is zero after 13 ms. It can be seen that the section displaces evenly during the first 5 ms. During 7 to 15 ms there is a small delay in the middle part of the section, causing it to displace less than the edges until it catches up after 20 ms. The edges displace since the displacement is measured at the top flange; only the bottom flange resting on the supporting beams is prohibited from moving. The Figure highlights the difference between the deformation shape for a static case where the response for the first 15 ms is completely different to the response for a static case where one would expect a parabolic shape, like that obtained after 20 ms in Figure 7.21.

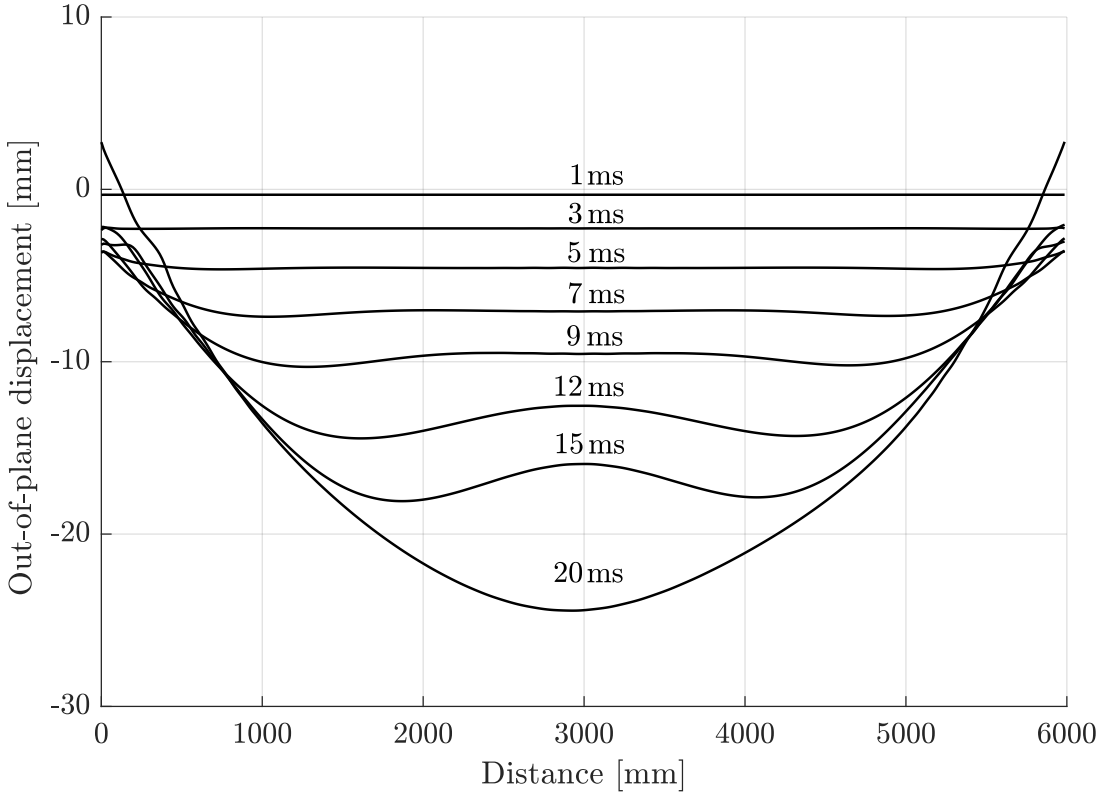

Figure 7.21: Initial longitudinal displacement for load 2 during the first 20 milliseconds.

The plastic strain is presented in Figure 7.22 for the time steps in Figure 7.23. A much larger area has obtained plastic strains in the dynamic case compared to the static case in Figure 7.11.

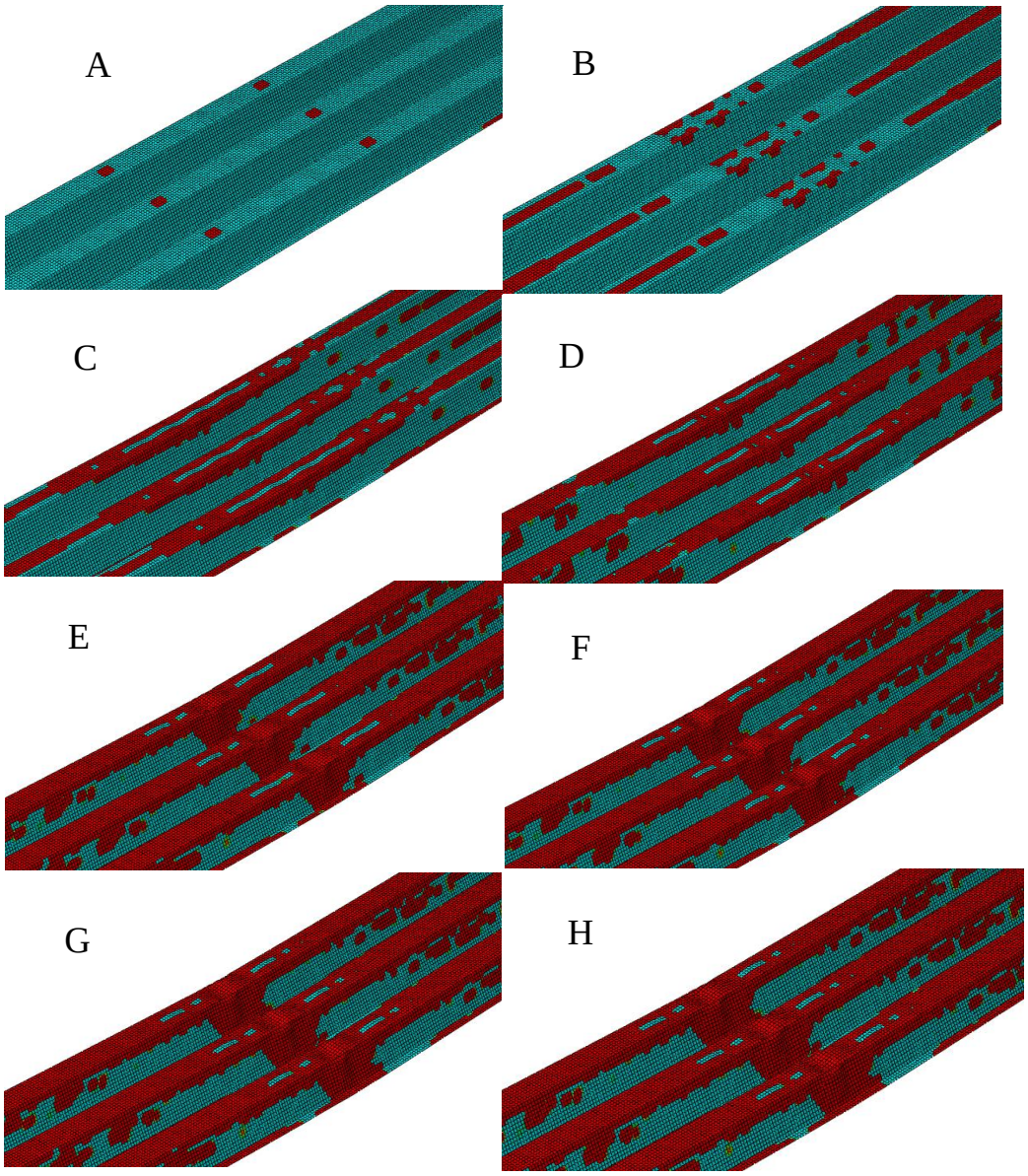

Figure 7.22: Plastic strain distribution (red) after dynamic loading for the time steps in Figure 7.23.

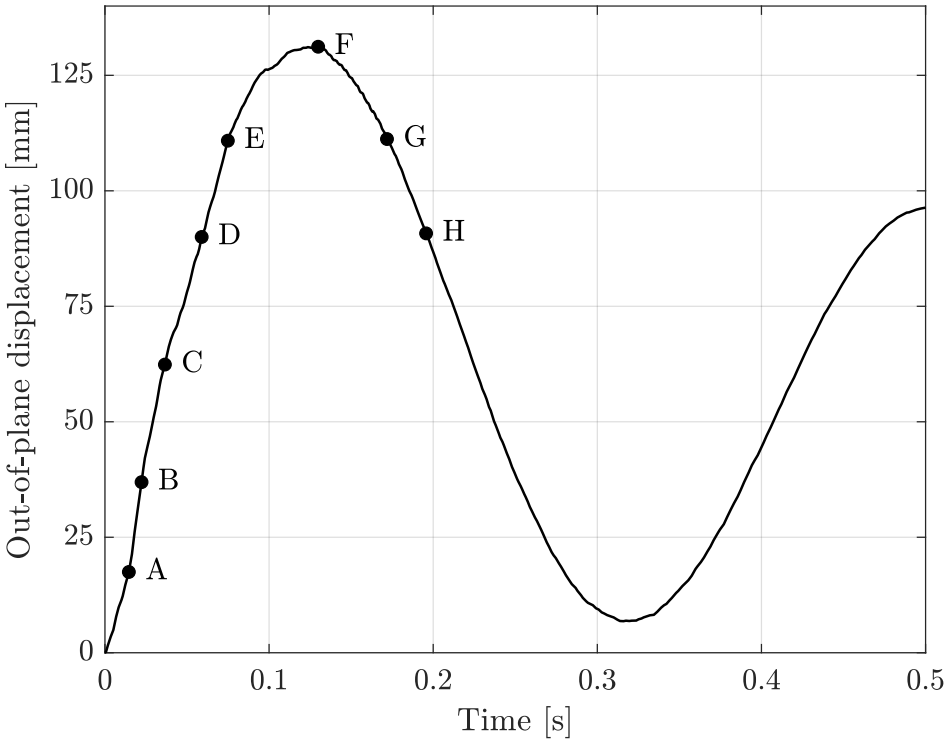

Figure 7.23: Dynamic response for $t = 1.05$ mm, $m = 166$ kg/m^2 and strain rate effects enabled.

7.3.5 Strain rate

The influence of strain rate effects is presented in Figure 7.24 for thicknesses t = 0.7, 1.05, and 1.4 mm. Accounting for strain rate effects reduces the out-of-plane displacement and increases the frequency of the oscillations.

The corresponding changes in initial maximum deflection are summarized in Table 7.4. As the thickness increases, the influence of strain rate effects becomes less pronounced.

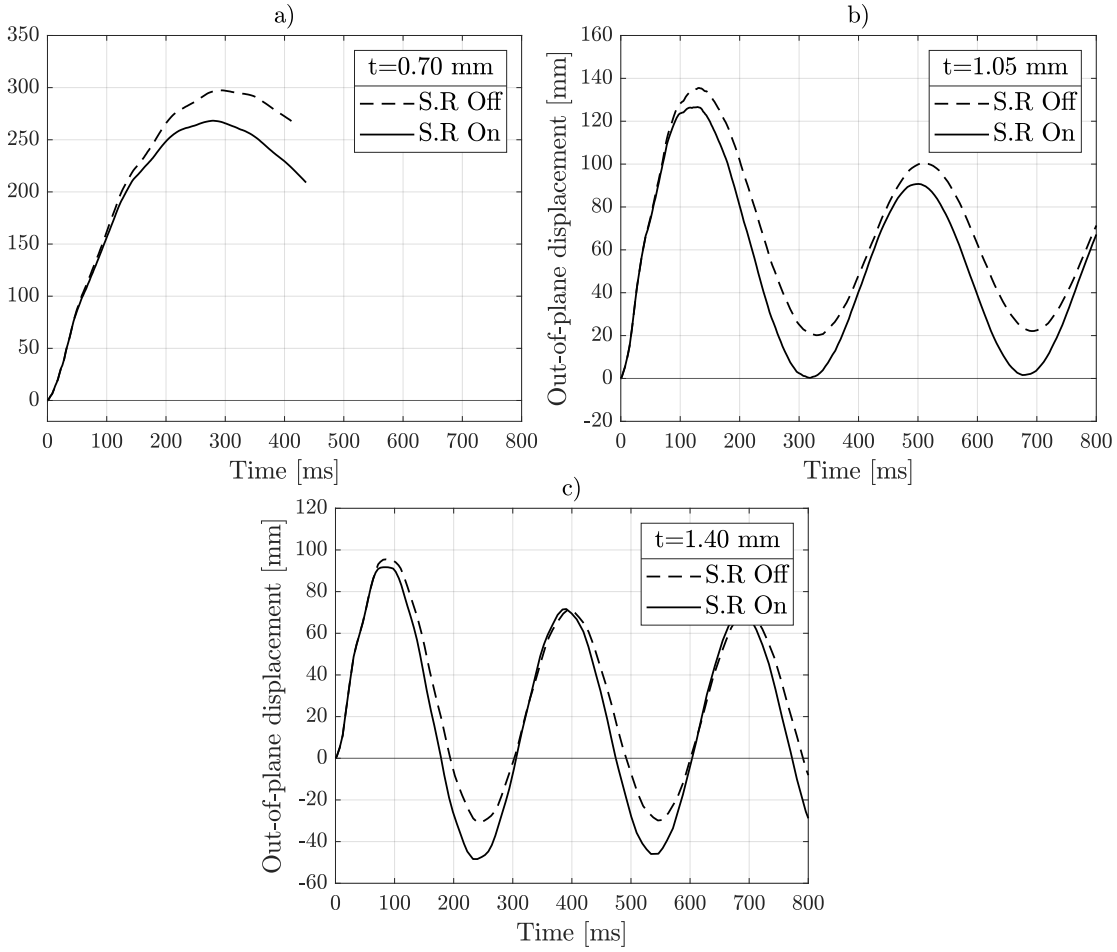

Figure 7.24: Influence of strain rate on the out of plane displacement for different thicknesses of the CSM, m = 166 kg/m^2 and load 2.

Table 7.4: Change of initial maximum displacement due to strain rate effects.

t [mm]	S.R Off	S.R On	diff [%]
0.70	297	268	-9.8
1.05	136	127	-6.6
1.40	95	92	-3.9

7.3.6 Influence of load amplitude

As described in Section 6.7.2, three different dynamic pressure loads were investigated, referred to as load 1, 2, and 3. Load 1 has the smallest amplitude and load 3 the largest, while the impulse density remains the same across all three loads.

Figure 7.25 illustrates the structural response of the CSM with a thickness of $t = 1.05$ mm. A noticeable difference in the peak amplitude of out-of-plane displacement is observed between the application of load 1 and load 2, while the difference between load 2 and load 3 is minimal. This variation becomes more pronounced when the mass per unit area is $m = 166$ kg/m^2 compared to when $m = 332$ kg/m^2.

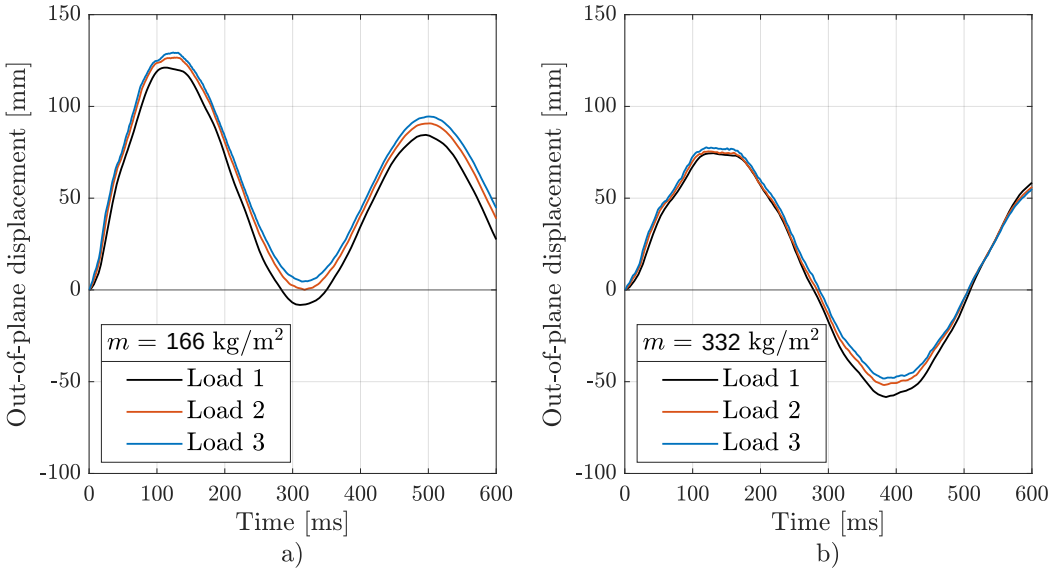

Figure 7.25: Comparison of the response for different load amplitude with the same impulse density for $t = 1.05$ mm: a) $m = 166$ kg/m^2 and b) $m = 332$ kg/m^2, load 2, strain rate effects enabled.

7.3.7 Slenderness

The influence of slenderness is presented in Figure 7.26 for thicknesses $t = 0.7$, 1.05, and 1.4 mm. Reducing the slenderness, i.e increasing the thickness, results in smaller displacements and reduced oscillation frequency. Negative oscillation amplitude is observed for $t = 1.4$ mm.

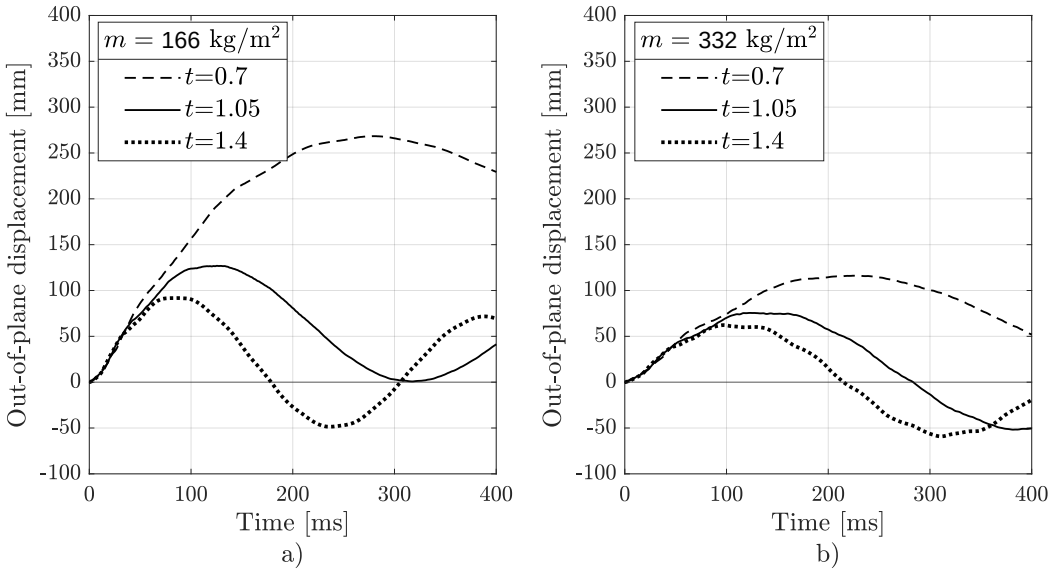

Figure 7.26: Comparison of the response for different thicknesses of the CSM: a) $m = 166$ kg/m^2 and b) $m = 332$ kg/m^2, load 2, strain rate effects enabled.

Figure 7.27 shows the longitudinal out-of-plane displacement along the top corrugation for five time increments. The final increment in each case corresponds to the point of maximum deflection for the respective thickness. It can be observed that as the thickness decreases, the deformation shape transitions from a smooth, parabolic profile to a sharper, more V-shaped form, likely due a more distinct hinge in the middle of the CSM strip caused by the buckling that take place there.

The appearance of a wavy pattern in the deformation is influenced by the shape and magnitude of the initial imperfections. A lower imperfection magnitude results in less pronounced waviness, indicating a reduced sensitivity to local geometric irregularities.

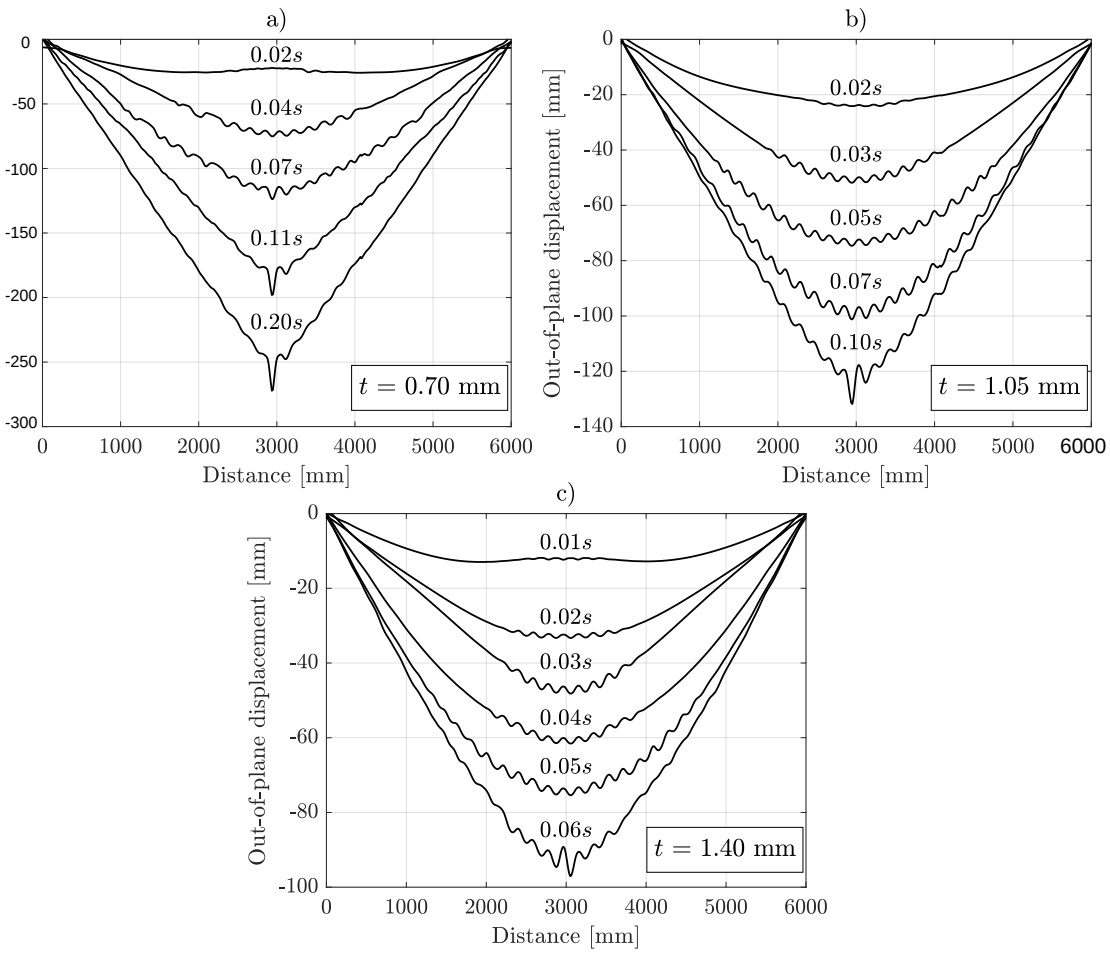

Figure 7.27: Longitudinal displacement for: a) $t = 0.70$ mm, b) $t = 1.05$ mm, c) $t = 1.40$ mm, with $m = 166$ kg/m^2, load 2 and strain rate effects enabled.

7.3.8 Influence of mass

Figure 7.28 shows the out-of-plane displacement over time for mass 84, 166, and 332 kg/m^2. As the mass increases, the displacement decreases, indicating greater resistance to motion. The oscillation frequency remains nearly unchanged between the 84 and 166 kg/m^2 cases but is noticeably lower for the 332 kg/m^2 case. This figure clearly demonstrates the significant influence of mass on the system's dynamic response. Specifically, as the mass of the structure increases, the energy transferred into the body decreases, and thus less deflection is needed to dissipate the energy, see Equation (2.1).

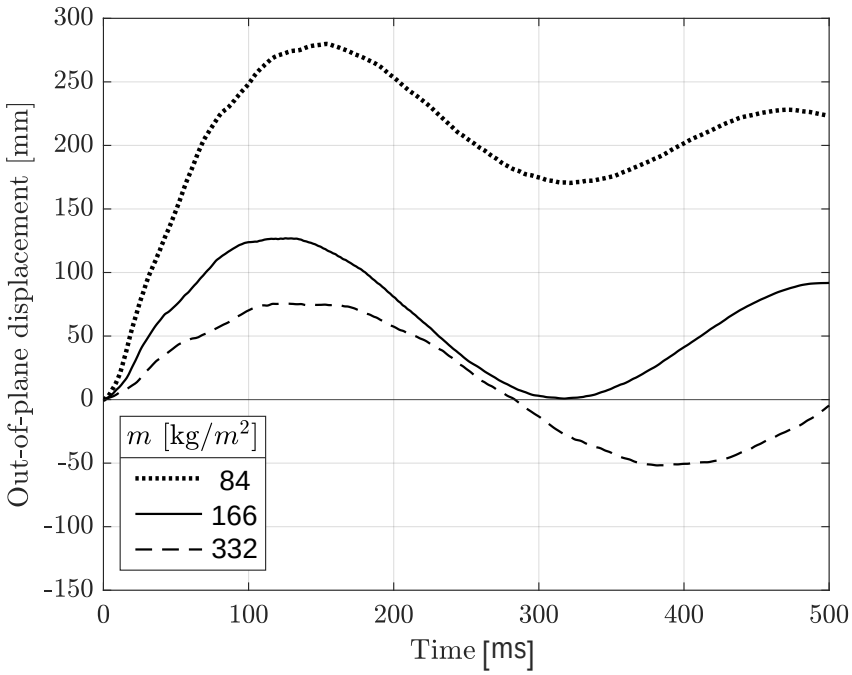

Figure 7.28: Comparison of the response for different masses, $t = 1.05$ mm, load 2, strain rate effects enabled.

7.3.9 Initial imperfections

Figure 7.29 presents the out-of-plane displacement over time for initial imperfections of 0.5, 1, 2, and 3 mm. As the imperfection increases, both the maximum deflection and the amplitude of positive oscillations increase, while the amplitude of negative oscillations decreases. This behaviour supports the decision to adopt 3 mm as the magnitude of the initial imperfection. Despite being approximately six times larger than the value recommended in the Eurocode, no significant change in the dynamic response is observed. This is acceptable in the context of this study, which focuses on overall behaviour rather than precise magnitudes.

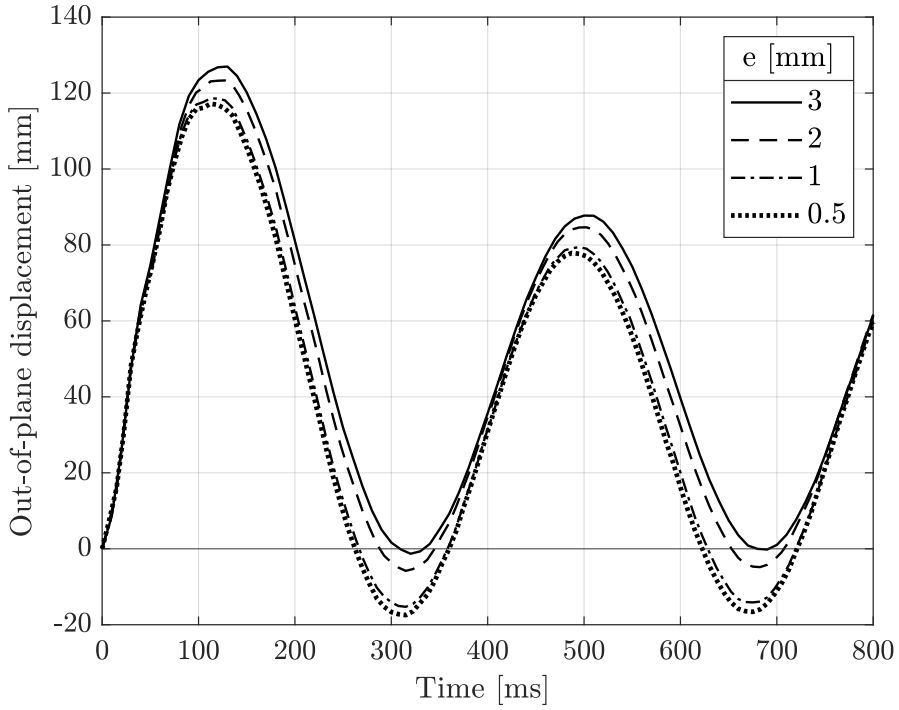

Figure 7.29: Comparison of the response for different initial imperfections, $t = 1.05$ mm, $m = 166$ kg/m^2, load 2 and strain rate effects enabled.

7.3.10 Boundary conditions

The out-of-plane displacement over time is presented in Figure 7.30 for a mass of 55 kg/m^2 and thickness 1.05 mm. The mass was reduced to ensure that the springs would yield, as increasing the mass leads to reduced displacement (see Section 7.3.8). With larger masses, the displacement becomes too small for the springs to engage significantly, making their positive contribution to energy absorption negligible. Since the area under the force-displacement curve remains nearly constant for small displacements—regardless of boundary conditions—catenary action plays a minor role unless the displacement exceeds approximately 120 mm (see Figure 7.15).

Among the tested boundary conditions, the simply supported case exhibits the largest maximum displacement but shows less oscillatory behavior compared to the spring-supported configurations. The spring boundary models were validated against the simply supported case using stiffness K_0, showing good agreement in terms of dynamic response.

As spring stiffness increases, the maximum displacement decreases, with the lowest values observed in the pinned-pinned configuration. The K_1 springs begin to yield at approximately 129 mm, while the K_2 springs yield at around 139 mm. The earlier yielding of K_1 allows displacement to accumulate sooner, resulting in a higher peak displacement.

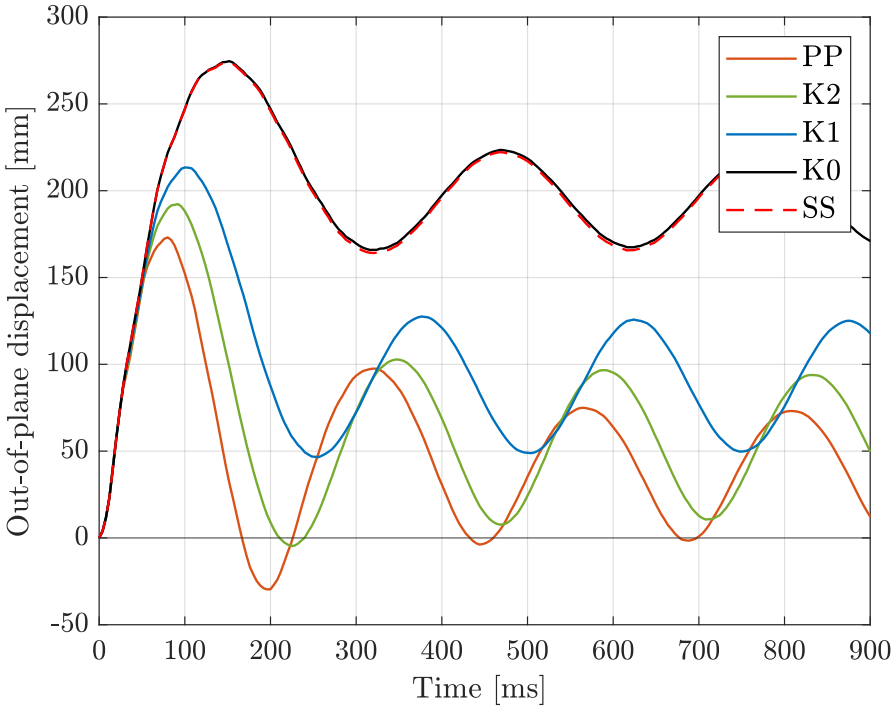

Figure 7.30: Comparison of the response for different boundary conditions, $t = 1.05$ mm, $m = 84$ kg/m^2, load 2 and strain rate effects enabled.

7.4 Comparison static vs dynamic

The distribution of plastic strain for the points in Figure 7.31 is presented in Figure 7.32 , each number corresponds to a specific displacement, meaning that point 1 has the same displacement in the static and dynamic case.

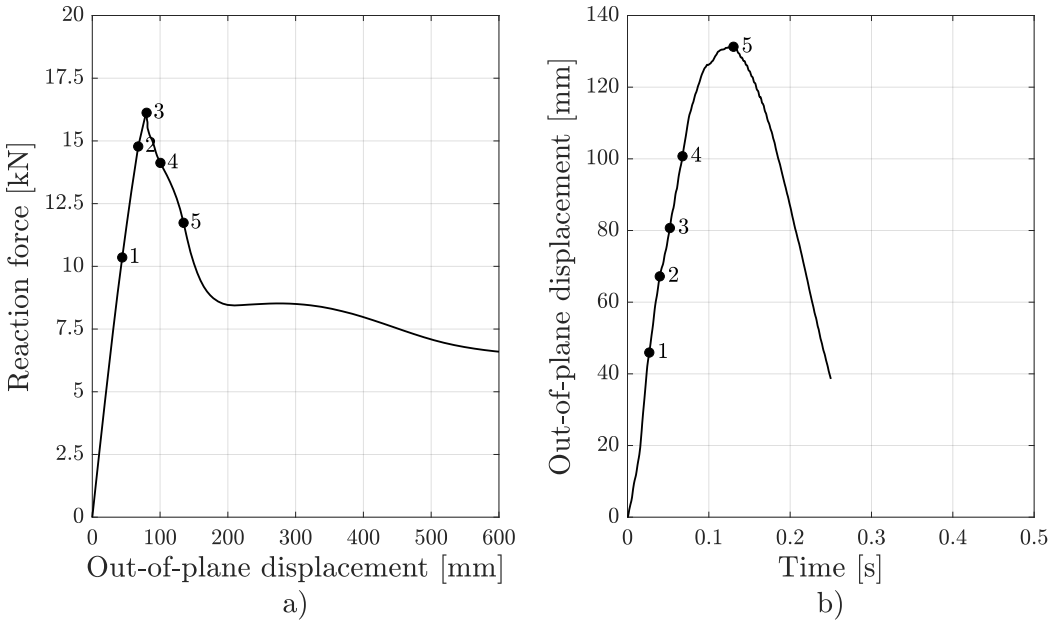

Figure 7.31: Points where the plastic strain in Figure 7.32 is evaluated. The points correspond to the same displacements in the static and dynamic cases. Thickness 1.05 mm, mass 166 kg/m^2, load amplitude 2 and strain rate effects enabled in the dynamic case.

The red regions in Figure 7.32 indicate areas of plastic strain. The evolution from Point 1 to Point 5 shows an increase in both the intensity and spread of plastic deformation. In the static case, as loading progresses, these bands become more prominent and wider, with strain localization becoming more severe by Point 4 and 5. While in the dynamic case, plastic strain appears earlier and with greater intensity than in the static case at the same displacement points.

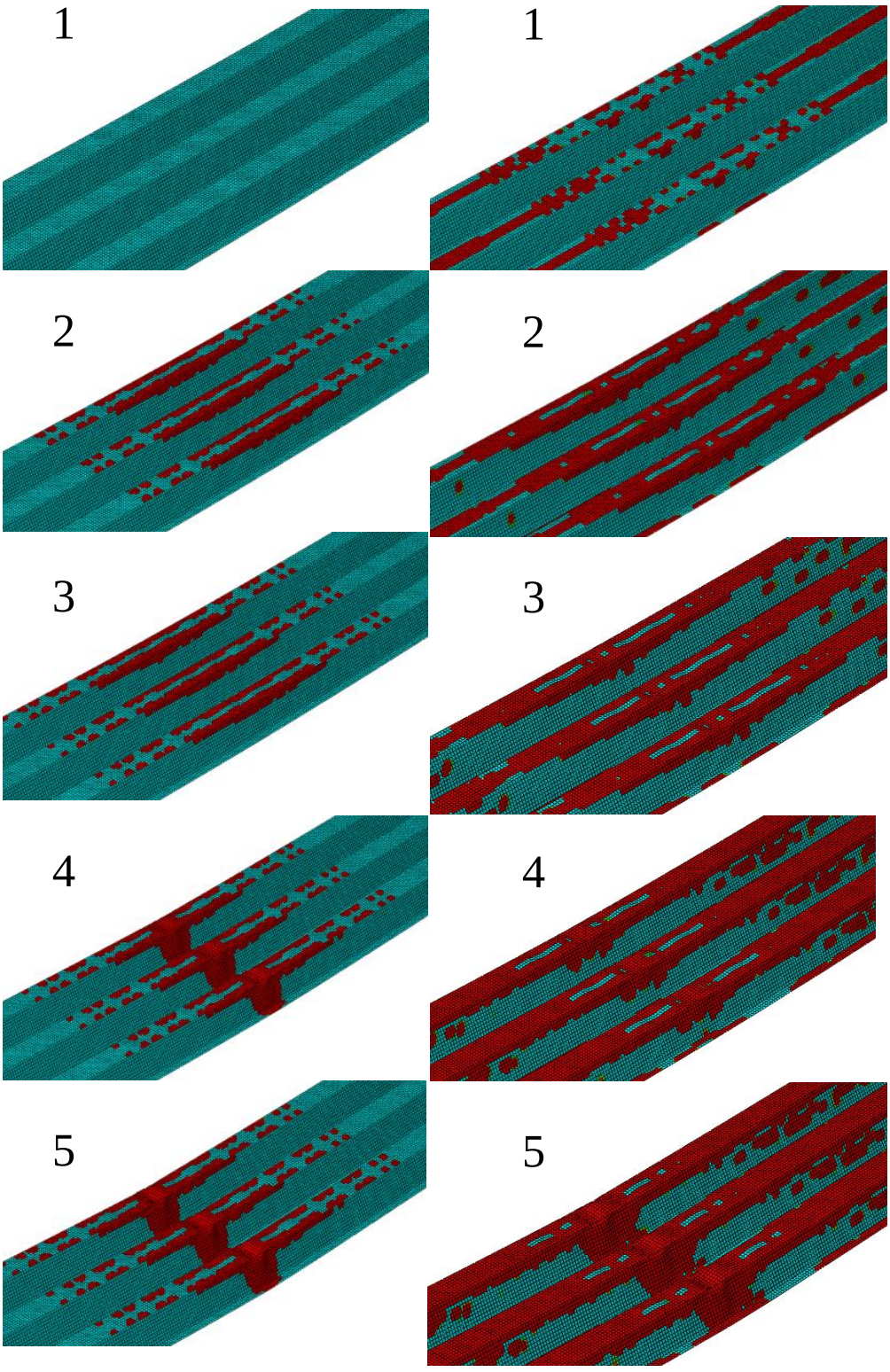

Figure 7.32: Distribution of plastic strain (red), static case to the left, dynamic case to the right, at the same out-of-plane displacement for the points in Figure 7.31.

8 Final remarks

8.1 General

The aim of this Master's thesis has been to improve the understanding of the structural response of thin-walled steel structures subjected to static and dynamic loading through numerical investigations of a 100 x 100 mm plain steel plate and a Corrugated Sheet Metal (CSM) section with three corrugations. The study focused on varying key parameters, such as slenderness, initial imperfections, boundary conditions, and loading rate, to evaluate their influence on the structural response, particularly in the post-buckling and post-peak regimes. Overall, the objectives of the thesis have been successfully achieved.

Considerable effort was devoted to identifying relevant and well-documented experimental studies on steel plates subjected to both static and dynamic in-plane compressive loading and CSM sections exposed to static and dynamic transverse loads. However, such studies proved difficult to find, especially those that capture the residual post-peak response. Most analyses or experiments tend to terminate shortly after the peak load is reached, as this is typically the primary focus of investigation.

8.2 Discussion plate response

Four different plate thicknesses, corresponding to four slenderness ratios and three different cross-section classes where studied. The imperfection magnitude was varied while keeping the imperfection shape constant. Considering the static response, it was concluded that large imperfections significantly reduce the peak load (ultimate capacity). This means the theoretical assumption that peak load remains constant regardless of imperfections holds only for amplitudes within Eurocode recommendations (e.g., l/200, corresponding to 0.5 mm in this case). In the FE analyses, imperfections of up to l/33 (3 mm) was assumed. While such values may not be realistic under normal conditions, in cases of physical damage or pre-existing defects, their influence on capacity reduction could be significant.

Boundary conditions were shown to substantially influence the structural response, not only reducing the critical buckling load, but more notably increasing the peak load.

As discussed in Sections 5.2.2 and 5.2.3, the geometry affects the response as expected. Plate height does not influence the peak load, and plate size is not critical as long as slenderness is held constant and the response is normalized.

Slenderness was found to significantly affect the dynamic response. In this study, thickness was varied to alter slenderness. Higher slenderness led to more pronounced dynamic oscillations under the same strain rate. Conversely, as slenderness decreased, higher strain rates were required to induce dynamic inertia effects, i.e. dynamic sensitivity increases markedly with slenderness.

A reduced imperfection magnitude increased both critical and post-buckling strength. This effect is particularly noticeable under dynamic loading, where small imperfections delay instability, enabling the plate to carry higher loads and endure larger

deformations. Compared to the static case, the dynamic response is more sensitive to initial imperfection magnitude (see Figures 5.3 and 5.33). Notably, under dynamic loading, there is no distinct point of local buckling initiation, especially when imperfections are small. In contrast, under static loading, the onset of local buckling is more clearly defined.

When comparing the plate response to typical force–displacement behaviour of columns (see Sargsyan and Sargsyan (2024)), both similarities and differences were found. The response is more similar to columns when the plate is in CSC1–CSC3, but differs significantly in CSC4. While column stiffness, whether defined by Young's modulus or secant stiffness, remains largely unaffected by strain rate, slender plates (e.g., 1 mm thickness) showed a notable increase in stiffness under dynamic loading. Less slender plates behaved more like columns with minimal strain rate sensitivity. Additionally, both columns and plates exhibit increased dynamic effects when geometric imperfections are reduced, particularly for slender specimens. Another observed difference is that the studied plates retained a clear residual strength after peak load compared to typical columns.

The appearance of two failure modes observed in the FE analyses was attributed to numerical artefacts. While they did not substantially influence the results, they may cause confusion in interpreting plots and require clarification, see Appendix A.

8.3 Discussion CSM response

Three different CSM thicknesses (0.7, 1.05, 1.4 mm), corresponding to three slenderness ratios were studied. All fall within CSC4 classification for both the compressed flange and the web, though the case with $t = 1.4$ mm is close to the CSC3 limit. The structural response at various thicknesses was similar, increased thickness raised the peak and post-peak loads. However, the post-peak drop became more abrupt as thickness, and thus the peak load, increased.

Hand calculations were performed both to validate the Abaqus results and to highlight key differences between simplified analytical methods and finite element simulations, particularly in the post-buckling regime. The Eurocode based calculations showed good agreement with the finite element simulations in the static case. An effective stiffness was also estimated based on the most critical cross-section. For the studied thicknesses, this effective stiffness closely matched the secant stiffness at the peak load. If this observation holds true for other geometries, using effective stiffness may offer a simple and practical method for estimating the secant stiffness corresponding to peak resistance.

Different boundary conditions were modelled in the static case: simply supported, pinned-pinned, and partially restrained (via non-linear springs). The pinned-pinned case exhibited a lower first local peak than the simply supported one, but a subsequent increase in strength due to catenary action, limited by local failure at fastener holes (springs). In contrast, the simply supported case showed an almost constant post-peak strength. While greater energy absorption is expected for the pinned-pinned case, it is limited by failure at the fasteners, which is difficult to simulate accurately. The possibility of accounting for even a limited catenary effect from the CSM strips 'normal' fasteners could contribute significantly to its

overall energy absorption capacity.

Dynamic analysis included three pressure magnitudes: a reference (Load 2), a doubled peak amplitude (Load 3), and a halved peak amplitude (Load 1), all with constant impulse. Differences between Load 1 and Loads 2 and 3 were minor, and almost no difference was observed between Loads 2 and 3, see Figure 7.25. Higher mass led to smaller variations in displacement–time response. This indicates that within the studied amplitude range, the load magnitude has negligible effect on peak displacement.

Strain rate dependence was modelled using the Cowper–Symonds law, in the same way as for the steel plate. Displacement decreased with increasing strain rate, especially for CSM sections with smaller thickness, a trend also observed in the plain steel plate.

The effect of mass was also examined. Increasing mass reduced displacement, this is due to reduced applied energy. It is worth noting, for $t = 0.7$ mm, the full load-bearing capacity may be fully consumed by dead loads alone when the mass reaches 332 kg/m^2. In Abaqus, this self-weight was not explicitly modelled (i.e., no distributed load of 3.32 kN/m^2 was applied). Therefore, the simulations more accurately reflect wall behaviour when subjected to the chosen dynamic loads, not that of a roof, which would be subjected to transverse loading.

In the static FE analyses, convergence problems were encountered when small initial imperfections were used, thus hindered reaching the post-peak regime. However, this was not an issue under dynamic loading using the explicit solution procedure, which allowed a more detailed investigation of imperfection effects. As expected, larger imperfections led to greater maximum deflections, though the structural response showed limited sensitivity to imperfection magnitude within the studied range.

8.4 Conclusions

The structural response of an axially loaded plate under static and dynamic loading was investigated numerically using the finite element method. Based on the results for the considered plate geometry and assumptions made, the following conclusions can be made:

1. The main difference between static and dynamic loading is the occurrence of dynamic effects, oscillations due to inertia effects and strain rate effects in the steel material.
2. The results indicate a notable post-peak residual strength, stabilizing at approximately 50–60 percent of the peak load under static loading conditions. This residual strength appeared at all studied plate thicknesses. The same trend was observed under dynamic loading; once the dynamic oscillations ended, the same level of residual strength as in the static case was reached. However, when strain rate effects were considered, the residual strength was somewhat increased.
3. The sensitivity to dynamic loading increases markedly with slenderness, when the slenderness increase the dynamic oscillations increase for the same strain rate. Additionally increased strain rate increases stiffness, critical

buckling load and post-buckling strength. Potentially increasing the energy absorption capacity.

4. The choice of boundary conditions for the plate edges is of great importance since both peak load and residual strength are affected.
5. There is a larger sensitivity to imperfection amplitude during dynamic loading compared to static loading, in the dynamic case a smaller imperfection leads to larger oscillation amplitude. During dynamic loading a larger difference in peak load depending on imperfection magnitude can be observed compared to the static case.

To provide deeper insight into the dynamic response of thin-walled steel structures, a full CSM section was also investigated. Instead of displacement controlled axial loading, an out-of-plane impulse load approximately corresponding to that of an incident shock wave generated by a detonation of 100 kg TNT on the ground at a distance of 25 m to the CSM strip, was applied. Based on this analysis, the following conclusions can be drawn:

1. The results indicate that there is a notable post-peak residual strength similar to the plate, after the peak load is reached a drop can be seen due to buckling, however at some unknown load level the response start to stabilize.
2. For the studied thicknesses, the post-peak strength drop becomes more pronounced as the thickness increases in the simply supported case, manifested by both a faster and larger drop after the peak load is reached.
3. The results indicates that an effective stiffness calculated based on the most critical cross-section may be used as a simple way to estimate a secant stiffness that coincides with the peak load. However, more geometries needs to be studied to make sure it is applicable for geometries other than the ones studied in this thesis.
4. An in-plane restraint can drastically improve the capacity during dynamic loading due to catenary effects if the load is large enough to trigger post-peak behaviour.

8.5 Further studies

This thesis has only focused on non-linear numerical analysis using the finite element method. It would thus be valuable to validate the numerical findings through experiments on similar structures, in a first stage on simple steel plates, but secondly also on a CSM structure.

It would be of particular interest to validate the findings of the post-peak capacity. Determining the load level at which this residual strength stabilises would be highly valuable in dynamic loading due to explosions considering energy absorption. Such knowledge could contribute to more efficient utilisation of material capacity in simplified design calculations, allowing engineers to estimate the ultimate capacity and determine in advance the load level at which the structure transitions into a stable post-peak regime. This was not the primary objective of this thesis, and further studies with a larger sample size are required to draw any quantitative conclusions.

9 References

ABAQUS, I. (2006). *Abaqus online documentation: Version 6.6-1* [Retrieved from Dassault Systèmes Simulia Corp.]. https://classes.engineering.wustl.edu/2009/spring/mase5513/abaqus/docs/v6.6/books/usb/default.htm?startat=pt06ch21s01abo21.html

Al-Emrani, M. (2023). *Steel structures*. Department of Architecture; Civil Engineering.

Al-Emrani, M., Engström, B., Johansson, M., & Johansson, P. (2019). *Bärande konstruktioner – del 1* [Kompendium för kurser i bärande konstruktioner vid Chalmers tekniska högskola]. Institutionen för arkitektur och samhällsbyggnadsteknik, Chalmers tekniska högskola.

Bohb, J., Louca, L., & Choo, Y. (2004). Numerical assessment of explosion resistant profiled barriers. *Marine Structures*, *17*, 139–160.

EN 1993-1-1. (2005). *Eurocode 3 — design of steel structures — part 1-5: Plated structural elements* (tech. rep. No. EN 1993-1-1:2006) (Retrieved February 4, 2025). CEN (Comité Européen de Normalisation). Brussels, Belgium. https://www.sis.se/produkter/byggnadsmaterial-och-byggnader/byggnadsindustrin/tekniska-aspekter/ss-en-1993-1-52006a22019/

EN 1993-1-5. (2005). *Eurocode 3 — design of steel structures — part 1-5: Plated structural elements* (tech. rep. No. EN 1993-1-5:2006) (Retrieved February 4, 2025). CEN (Comité Européen de Normalisation). Brussels, Belgium. https://www.sis.se/produkter/byggnadsmaterial-och-byggnader/byggnadsindustrin/tekniska-aspekter/ss-en-1993-1-52006a22019/

European Commission. (2017). Guidelines and recommendations for integrating specific profiled steel sheets in the eurocodes (grispe): Final report.

Faridmehr, I., Osman, M. H., Adnan, A. B., Nejad, A. F., Hodjati, R., & Azimi, M. (2014). Correlation between engineering stress-strain and true stress-strain curve [Accessed: 2025-02-10]. *American Journal of Civil Engineering and Architecture*, *2*(1), 53–59. https://doi.org/10.12691/ajcea-2-1-6

Gerard, R. B. F., & Larsson, N. (2023). *Buckling of a steel plate subjected to axial compression loading of various load rates* [Master's Thesis]. Chalmers University of Technology [Examensarbete ACEX30].

Harry, O. A., & Lu, Y. (2019). Simplified theoretical model for prediction of catenary action incorporating strength degradation in axially restrained beams. *Engineering Structures*, *191*, 219–228. https://doi.org/10.1016/j.engstruct.2019.04.043

Johansson, M., & Laine, L. (2012a). Bebyggelsens motståndsförmåga mot extrem dynamisk belastning del 1: Last av luftstötvåg [https://www.example.com/documenthttps://www.msb.se/siteassets/dokument/amnesomraden/krisberedskap-och-civilt-forsvar/befolkningsskydd/skyddsrum/bebyggelsens-motstandsformaga/last-av-luftstotvag.pdf].

Johansson, M., & Laine, L. (2012b). Bebyggelsens motståndsförmåga mot extrem dynamisk belastning del 3: Kapacitet hos byggnader [https://www.msb.se/siteassets/dokument/amnesomraden/krisberedskap-och-civilt-forsvar/befolkningsskydd/skyddsrum/bebyggelsens-motstandsformaga/kapacitet-hos-byggnader.pdf].

Kowal-Michalska, K., & Mania, R. J. (2008). Some aspects of dynamic buckling of plates under in-plane pulse loading. *Mechanics and Mechanical Engineering*, *12*(2), 135–146.

Kubiak, T. (2013). Static and dynamic buckling of thin-walled plate structures. *Journal of Constructional Steel Research*.

Memon, B.-A., & SU, X.-z. (2004). Arc-length technique for nonlinear finite element analysis [ISSN 1009-3095, Document code: A, CLC number: TU31, Received July 30, 2003; revision accepted Sept. 11, 2003]. *Journal of Zhejiang University SCIENCE*, *5*(5), 618–628. http://www.zju.edu.cn/jzus

Paik, J. K., & Thayamballi, A. K. (2003a). An experimental investigation on the dynamic ultimate compressive strength of ship plating. *International Journal of Impact Engineering*, *28*(7), 803–811.

Paik, J. K., & Thayamballi, A. K. (2003b). *Ultimate limit state design of steel-plated structures*. John Wiley & Sons Ltd.

Plos, M., Johansson, M., Zandi, K., & Jiangpeng, S. (2021). *Recommendations for assessment of reinforced concrete slabs: Enhanced structural analysis with the finite element method* (tech. rep. No. ACE 2021:3) (Retrieved February 4, 2025). Chalmers University of Technology. Göteborg, Sweden. https://research.chalmers.se/publication/524987

Runesson, K., & Larsson, R. (2024). *Constitutive modeling of engineering materials - theory and computation: The primer* [Unpublished lecture notes]. Lecture Notes, Department of Industrial; Materials Science, Chalmers University of Technology.

Ruukki Sverige AB. (2025). Bärande profilerad takplåt [Accessed May 8, 2025]. https://www.ruukki.com/swe/building-envelope/produkter/roof-structure/load-bearing-sheets?TabfiltersB2B=1tabfilter#b%c3%a4rande-takpl%c3%a5t

Sargsyan, H., & Sargsyan, N. (2024). *Structural response in thin-walled steel structures subjected to compressive axial dynamic loading* [Master's Thesis]. Chalmers University of Technology [Master's Thesis in the Master's Program Structural Engineering and Building Technology].

Yang, X., Yang, H., Gardner, L., & Wang, Y. (2022). A continuous dynamic constitutive model for normal- and high-strength structural steels. *Journal of Constructional Steel Research*. https://doi.org/10.1016/j.jcsr.2022.107254

Yang, X., Yang, H., Lai, Z., & Zhang, S. (2020). Dynamic tensile behavior of s690 high-strength structural steel at intermediate strain rates. *Journal of Constructional Steel Research*, *168*, 105961. https://doi.org/10.1016/j.jcsr.2020.105961

Yun, X., & Gardner, L. (2017). Stress-strain curves for hot-rolled steels. *Journal of Constructional Steel Research*. https://doi.org/10.1016/j.jcsr.2017.01.024

Appendix A

A.1 Difficulties with validating the dynamic plate analysis

Significant difficulties in validating the dynamic plate analysis arose. Initially, the results from the static analysis and the dynamic analysis were identical up to and including P_{max}. However, after the maximum load capacity was reached, different deformation modes emerged, which affected the response $R(u)$. The problem only arose for $t = 1$ mm.

The static analysis resulted in a symmetric deformation shape, and the dynamic analysis resulted in an symmetric or unsymmetrical deformation shape depending on the settings used and prescribed velocity in Abaqus. Since the static analysis consistently produced symmetric results without any errors when using the displacement controlled approach, symmetric results were also expected for the dynamic analysis since the same model was used. Both explicit and implicit methods were used, however no differences were observed, therefore the dynamic implicit solution step was exclusively utilized.

Great efforts were put in to find the cause of the discrepancy. See Figure A.1 for the comparison between the response when a symmetric deformation shape is formed vs an nonsymmetric shape, also see Figure A.2 for the deformed shape (out-of-plane displacement) at different positions along the curve. It can be noted that even though the curves merge at an in-plane displacement of 5 mm, the deformed shape is still inconsistent.

The difference in terms of settings in Abaqus is presented in Table A.1, it can be seen that only the maximum increment size varies.

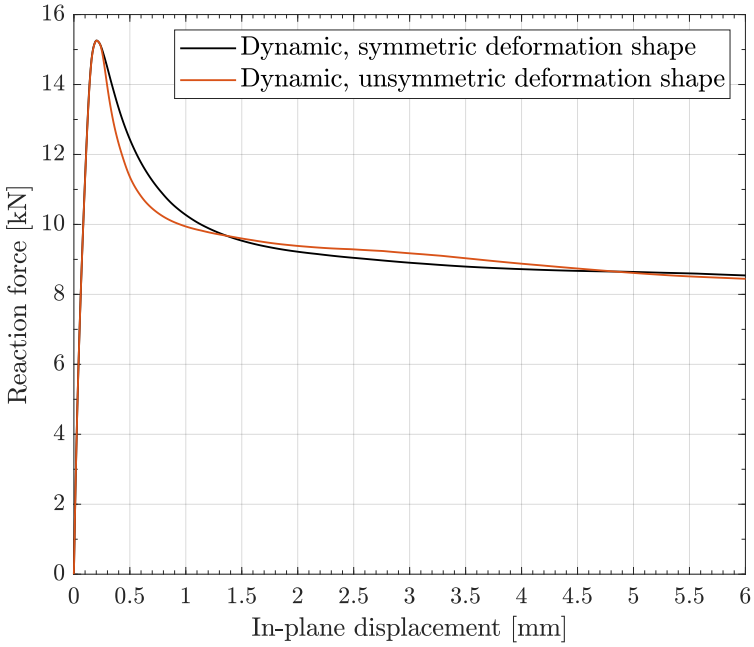

Figure A.1: Comparison of response for different deformation shapes, $t = 1$ mm, $v = 0.01$ mm/s and $e = 0.5$ mm.

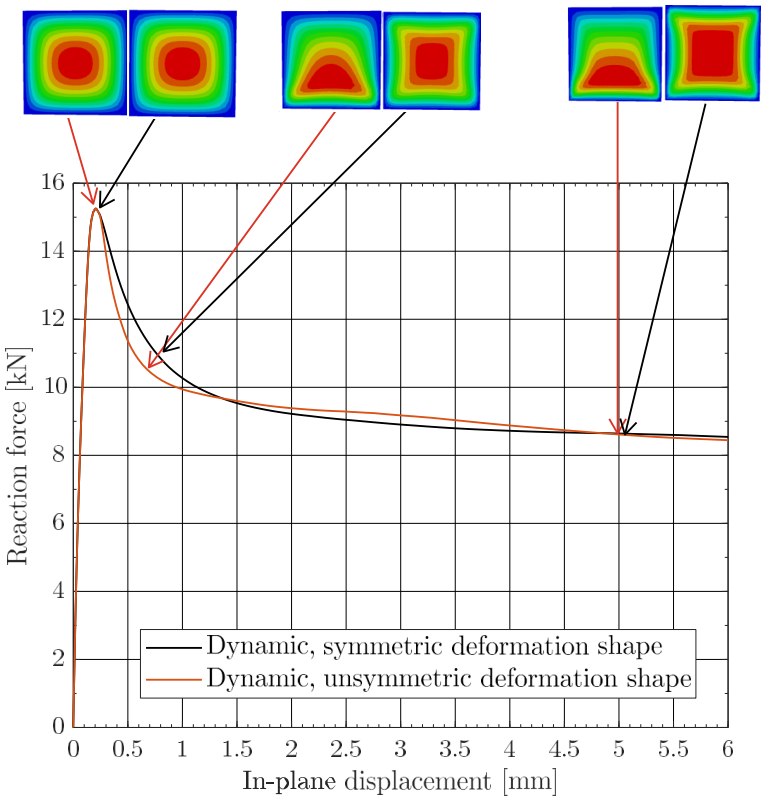

Figure A.2: Comparison of out-of-plane displacement (small colour plots of the plate) at different position along the force-displacement curve for $t = 1$ mm, $v = 0.01$ mm/s and $e = 0.5$ mm.

Table A.1: Settings used to produce Figure A.1.

	Symmetric deformation	**Asymmetric deformation**
Velocity [mm/s]	0.01	0.01
Total step time [s]	800	800
Increment size		
Initial	0.1	0.1
Minimum	1×10^{-6}	1×10^{-6}
Maximum	1.6	0.9
Maximum number of increments	2000	2000

A.2 Numerical problem or physical problem

A.2.1 Orientation

Uncertainty about whether the two deformation shapes presented in Section A.1 is due to a numerical error or related to the post-buckling behaviour of dynamically loaded plates, extensive tests were performed to investigate the observation. The investigations carried out and their findings are presented in Subsections A.2.3 to A.2.10.

A.2.2 Slenderness of the plate

Four different slendernesses were investigated, different slendernesses were achieved by changing the thickness of the plate.

The problem with inconsistent deformation shapes was only present for $t = 1$ mm, which is the most slender plate studied. When $t = 2$, 3, and 4 mm, results from the dynamic analysis for the lowest velocity matched the results from the static analysis without any sensitivity to the increment size, in addition only the symmetric deformation shape was observed for all velocities. Only the slender plate with a thickness of 1 mm was thus studied further since the other thicknesses produced satisfactory results.

In Section 5.1.3 it was found that only the plate with a thickness of 1 mm had significant post critical buckling strength. When t = 2 mm a small post buckling strength (almost negligible) could be seen and when t = 3 and 4 mm no post critical buckling strength could be seen.

Therefore a study on a plate with a thickness of 1.5 mm was made to see if the same problems occur for $t = 1.5$ mm as for $t = 1$ mm. In Figure A.3 the force-displacement relationship when $t = 1.5$ mm is presented, it is clear that the plate has a post critical buckling strength since it buckles approximately at 24 kN and carries load until the ultimate capacity is reached at 33 kN.

The two different deformation shapes appear also for $t = 1.5$ mm, see Figure A.4. This indicates that the symmetry issue is only prevalent for slender plates. This sub-study also excludes the possibility that the problem is connected to the thickness $t = 1$ mm only.

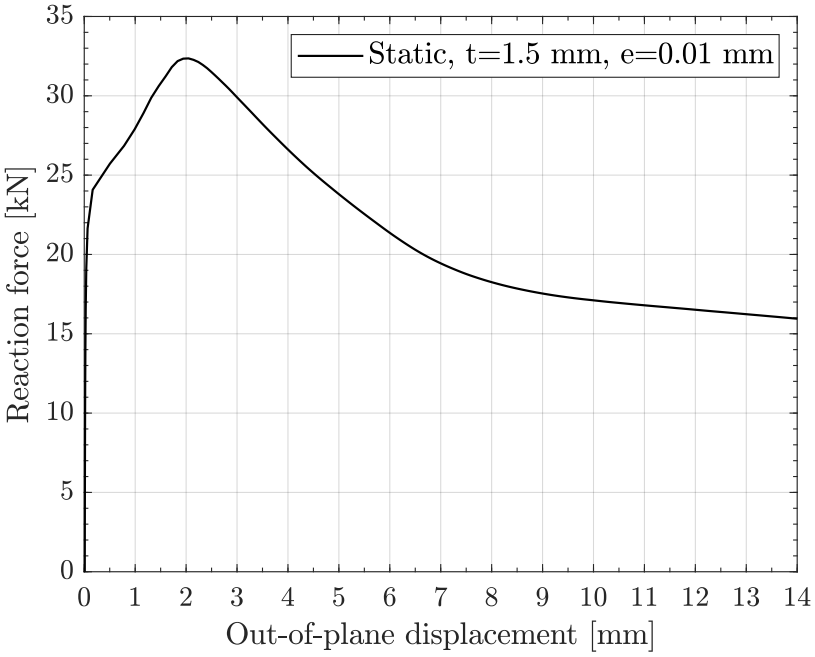

Figure A.3: Force-displacement relation for plate thickness 1.5 mm.

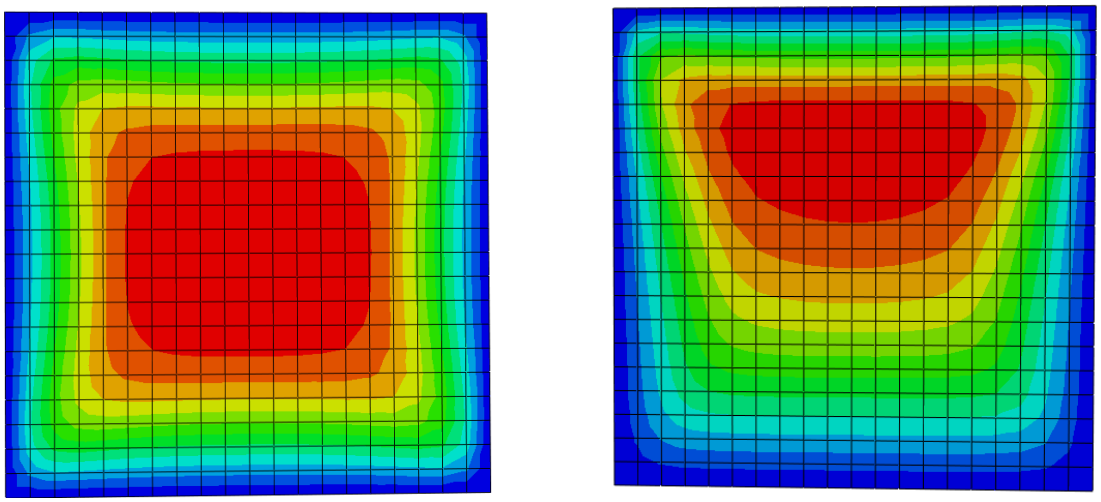

a) b)

Figure A.4: Post buckling deformation shape: a) Symmetric deformation for the static case, b) Unsymmetrical deformation for the dynamic case.

A.2.3 Increment size

As presented in Section 4.9.1 a maximum increment, Δt_{max}, can be specified when using the automatic increment size in Abaqus. During the process of finding a suitable increment size to achieve a sufficient number of data points when post processing the data, a sensitivity towards the choice of Δt_{max} was discovered.

The settings held constant for all simulations in this sub-study are presented in Table A.2. Table A.3 presents whether the deformation shape after buckling is symmetric or non-symmetric, it is also presented how long the simulation was ran in terms of in-plane displacement.

If the maximum in-plane displacement is equal to 8 it means that the full analysis is performed, if it is less than 8 mm it means that the analysis gets stuck, taking smaller and smaller steps until the simulation is aborted, either due to the allowed maximum number of total increment is exceeded or due to the increment size needed is smaller than the specified minimum increment Δt_{min}. To specify a very small Δt_{min} or a very large allowed total number of increment does not effect the results, it only allows the simulation to run longer, this was however negligible.

Table A.2: Simulation settings.

Parameter	**Value**	**Unit**
Initial imperfection	0.5	mm
Velocity	0.01	mm/s
Total step time	800	s
Initial increment	0.1	-
Minimum increment	1×10^{-9}	-

In Table A.3 the result for 10 different choices of Δt_{max} is presented and it can be observed that a non-symmetrical deformation shape is obtained 2 out of 8 times. What can be noted is that no pattern can be seen, at least for this sample size. Between Δt_{max} and the deformation shape, it seems to be random. It is worth noting that when an unsymmetrical deformation shape is obtained, Abaqus has no troubles with running the full analysis and Δt_{max} is utilized for a majority of the increments, while for a symmetric deformation shape the analysis at some point obtains convergence errors and gets stuck.

It is not at the point where the analysis gets stuck that a non-symmetrical deformation shape is formed, if a non-symmetrical deformation shape is formed it is formed shortly after the ultimate load, which is approximately at $u = 0.2$-0.3 mm depending on thickness of the plate and initial imperfections, see Figure A.1. Based on the results in Table A.3 the occurrence of two different deformation shapes seems to be a numerical issue rather than a modelling error.

Table A.3: maximum increment size and symmetry correlation.

Max increment [-]	0.8	0.9	0.95	1.0	1.05	1.1	1.15	1.2	1.5	3
Max in-plane displacement [mm]	1.91	8	6.56	6.71	1.99	8	6.65	6.56	6.58	6.64
Symmetrical deformation	yes	no	yes	yes	yes	no	yes	yes	yes	yes

A.2.4 Velocity ramp up

An investigation was made to see if velocity ramp-up time effects the deformation shape. In Table A.4 the settings that are constant for all simulations in this sub-study is presented and in Table A.5 and A.6 the result is presented. The initial increment was set to one tenth of the ramp-up time to make sure that Abaqus does not take to big jumps and the velocity is ramped up smoothly.

The maximum ramp up time of 10 seconds was chosen so that the full amplitude of the velocity is reached before the peak value of the force in the force displacement curve for this specific plate and its associated parameters (thickness, imperfections etc) is reached, to make sure that the correct speed is actually studied.

What can be seen is that the ramp-up time affects the deformation shape; however, no pattern of how it affects the shape can be seen. It seems random if the deformation shape is symmetric or non-symmetrical when different ramp up times are used.

Table A.4: Simulation settings.

Parameter	**Value**	**Unit**
Initial imperfection	0.5	mm
Velocity	0.01	mm/s
Total step time	800	s
Minimum increment	1×10^{-6}	-

Table A.5: Deformation shape for different ramp up times when $\Delta t_{max} = 1.6$.

Ramp up time [s]	10	1	0.1	0.01	0.001
Initial increment size	1	0.1	0.01	0.001	0.0001
Maximum increment size	1.6	1.6	1.6	1.6	1.6
Symmetrical deformation	yes	yes	yes	no	yes

Table A.6: Deformation shape for different ramp up times when $\Delta t_{max} = 1.1$

Ramp up time [s]	10	1	0.1	0.01	0.001
Initial increment size	1	0.1	0.01	0.001	0.0001
Maximum increment size	1.1	1.1	1.1	1.1	1.1
Symmetrical deformation	yes	no	no	no	no

A.2.5 Mesh size

The mesh was refined to deduce any mesh discretization dependence. The resulting force-displacement relation for several mesh sizes are presented in Figure A.5, all of which resulted in symmetric deformation. It can be seen that the influence of mesh size is neglectable up to the ultimate load but past the ultimate load some difference is observed. It was found that refining the mesh reduced increment sensitivity, meaning that the analysis could be completed and obtain symmetric shape for several increment settings. The unsymmetrical shape, though, remains for some increment settings. The convergence analysis indicates that a coarser mesh should have been used, see Table A.7 indicating that 50x50 elements is appropriate. The dynamic effects were however possible to distinguish even at such coarse mesh as 20x20 elements, thus no effort was done to re-run the analyses.

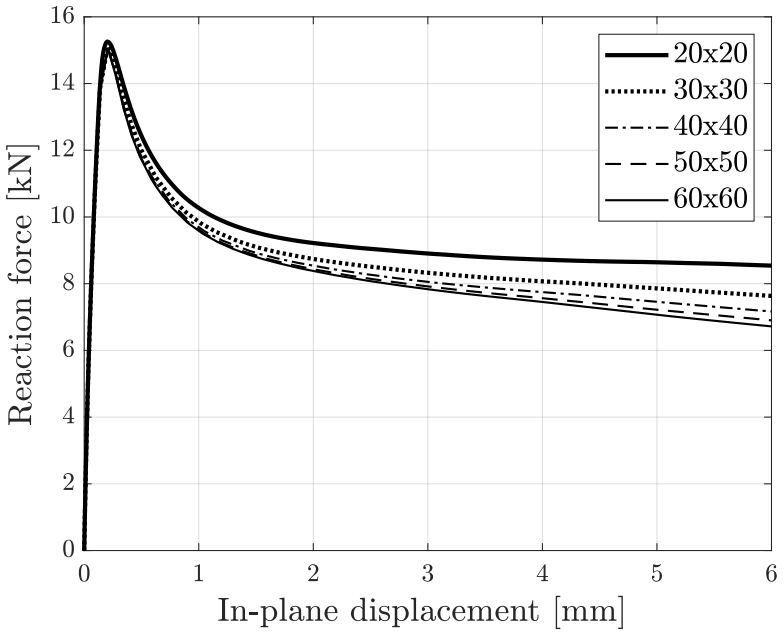

Figure A.5: Force-displacement relation for different mesh size, elements along the plate width and height (width x height).

Table A.7: Reaction force at 4 mm in-plane displacement for different mesh size. Change decreases as the mesh gets finer, convergence at around 50x50 elements since 2% is commonly allowed.

Elements	**RF** [kN]	**change** [%]
20x20	8.70	
30x30	8.08	-7.13
40x40	7.75	-4.08
50x50	7.60	-1.94
60x60	7.45	-1.97

A.2.6 Mesh shape

The mesh layout was considered a possible cause. The mesh was made unsymmetrical by using quad-dominated - free - advancing font, see Figure A.6. No effects were observed, results remained the same as for the structured mesh. Another variant was tested in which the midpoint of the partitioned edges AD and BC, was shifted upward and downward. This resulted in, when observed for a certain increment setting, that the unsymmetrical shape shifted in the direction of the shifted midpoint. An attempt of shifting the midpoints in different directions was made to counteract the shift, however the shape instead shifted to the top.

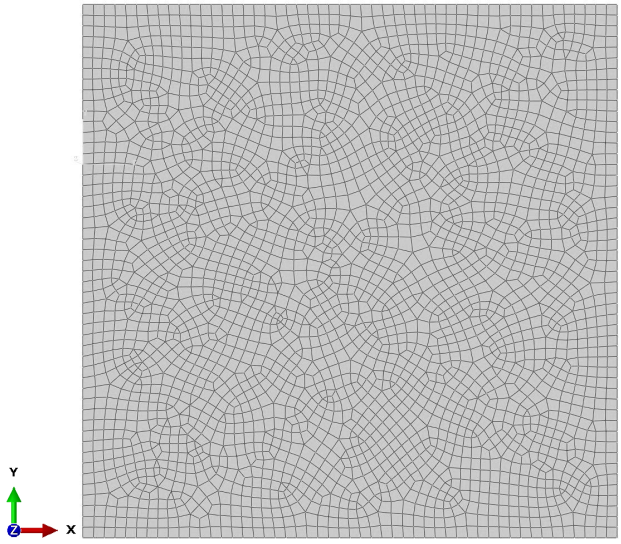

Figure A.6: Unsymmetrical mesh.

A.2.7 Load

The load application was investigated to deduce if the unsymmetrical loading was the cause of the two possible solutions. The load was applied also at the bottom edge, without any restraints in y-direction since the two loads cancel out the net displacement and prevent rigid body motion, see Figure A.7. No effects were observed and thus this alternative was left out.

Another loading variant was also tested, by prescribing the deflection on a reference point, rigidly connected to the edge. No effects were observed.

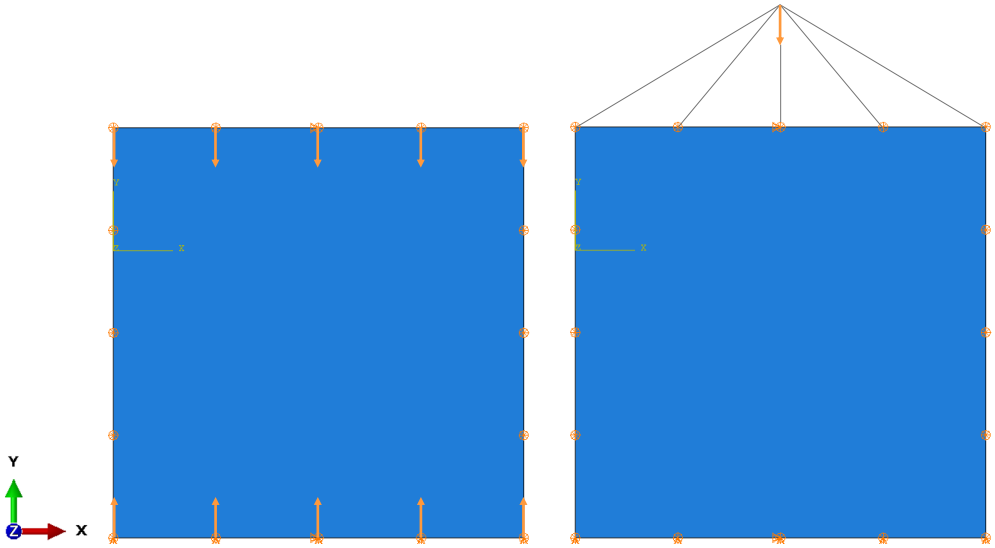

Figure A.7: Two different load applications, top and bottom (left) and load prescribed in reference point connected to nodes at top edge (right).

A.2.8 Convergence tolerance

The convergence tolerance for the implicit step was decreased to force the solver to find a more accurate solution. The hypotesis were that the standard settings were too loose, and by decreasing the tolerance the solver is forced to check for a closer solution. No effects were observed.

A.2.9 Imperfection amplitude

Different imperfection magnitudes e were considered in order to force the plate into a symmetric shape. A range of magnitudes between 0.01 mm to 20 mm was tested. Hypothetically, if the initial imperfection is large enough the deformation would become symmetric since it is forced into the symmetric shape of the initial imperfection, see Table A.9 for the results and Table A.8 for the settings used.

Although a symmetric deformation shape was obtained for all velocities when $e = 20$ mm, we would not say that the hypothesis is true, since 20 mm corresponds to L/5 which is very large, we expected a smaller imperfection to effect the result. The "no" highlighted in red in the last row deviates from the rest of the results, it is strange that the deformed shape goes from a symmetric shape for lower values of the imperfection amplitude and then to a non-symmetric for $e = 2$ mm and then back to symmetric when e is increased further.

Table A.8: Simulation settings for different velocities.

Parameter	**10 mm/s**	**5 mm/s**	**1 mm/s**
Ramp up time [s]	1×10^{-3}	5×10^{-3}	1×10^{-2}
Initial time increment	1×10^{-4}	5×10^{-4}	1×10^{-3}
Minimum time increment	1×10^{-8}	5×10^{-8}	1×10^{-7}
Maximum time increment	1.6×10^{-3}	0.0032	1.6×10^{-2}
Total step time [s]	0.8	1.6	8

Table A.9: Effect of imperfection amplitude on deformation symmetry.

Imperfection amplitude [mm]	0.01	0.1	0.5	1	2	4	10	20
L/X	10000	1000	200	100	50	25	10	5
Symmetrical deformation (10 mm/s)	no	no	no	no	no	no	no	yes
Symmetrical deformation (5 mm/s)	no	no	no	no	no	no	no	yes
Symmetrical deformation (1 mm/s)	yes	yes	yes	yes	no	yes	yes	yes

A.2.10 Strain rate effect

The effects of strain rate was investigated by enabling strain rate effects through the power law, trying two different loading speeds. For $v = 100$ mm/s, without strain rate effects, the deformation is unsymmetric. With strain rate effects considered, the deformation becomes symmetric (a bit distorted). For $v = 0.01$ mm/s, without strain rate effects, the initial state is symmetric but becomes unsymmetrical with strain rate effects turned on.

If instead the maximum incrementation is decreased to 0.9 (from 1.6), considering $v = 0.01$ mm/s, the deformation is unsymmetrical independently of strain rate

effects , different behaviour from the previous increment setting. The behaviour for $v = 100$ mm/s is however the same as for the previous increment settings.

See Table A.10 for summarized observations.

Table A.10: Effect of strain rate and incremental settings on deformation shape.

v [**mm/s**]	100	100	0.01	0.01	0.01	0.01	100	100
S.R	on	off	on	off	on	off	on	off
Max time inc.	10^{-3}	10^{-3}	0.9	0.9	1.6	1.6	$1.6 \cdot 10^{-3}$	$1.6 \cdot 10^{-3}$
Symmetric def.	Yes	No	No	No	No	Yes	Yes	No

The result for $v = 100$mm/s is intuitively realistic for both increment settings, implying that an increase in strength due to strain rate effects cancels out the unsymmetrical shift (happens in the plastic region after utlimate strength is reached). The result for $v = 0.01$ mm/s is however contradictory in-between the two settings, making it difficult to establish any conclusions.

A.3 Concluding remarks

An extensive investigation was conducted to determine whether a modelling error had occurred, what factors influence the deformation shape, and whether there are any solutions to the issue where certain combinations of settings in Abaqus led to unexpected, unsymmetrical deformation shapes.

It is unlikely that a modelling error was made, as satisfactory results can be obtained. However, the issue lies in the inability to consistently reproduce the same deformation shape across different prescribed velocities.

If the unsymmetrical deformation shape only appeared at high velocities the conclusion may have been that the unsymmetrical deformation shape is associated with dynamic effects, however the problem arose for all velocities but to varying extent, it is harder (maybe impossible for some velocities) to produce the symmetrical results at higher velocities.

Almost everything that was investigated related to the inconsistency with the deformation shape had some influence on whether the deformation turned out to be symmetric on nonsymmetric, for example a refined mesh decreased the sensitivity towards the choice increment size. However no general solution to the problem was found. Although this investigation identified factors that facilitated obtaining the same symmetric deformation shape as in the static case, particularly at lower velocities (< 1 mm/s), the issue persists at higher velocities, except when strain rate effects are included

The cause of the inconsistency could be numerical noise, small round-off errors in the solver can push the solution toward one path or the other. On the other hand it can not be fully ruled out that the asymmetric deformation shape is a valid correct solution, both deformation shapes might be equally realistic, the uncertainties thus remain unsolved.

Appendix B

Plots to motivate the choice of thickness

```
clear
clc
addpath('C:\Users\timlu\OneDrive\Desktop\Examensarbete\fonts');

%Plate properties
h = 200/1000; % Height (m)
b = 100/1000; % Width (m)

%Material properties
fy = 355e6;  % Yield strength (Pa)
E = 210e9;   % Young's modulus (Pa)
v = 0.3;     % Poisson's ratio

%Plate is simply supported along all four edges
a = h;       % Plate length
k = 4;       % Buckling coefficient

%
epsilon = sqrt(235e6 / fy);
c = b; % Plate width for classification

%
t_values = 0.8e-3:0.00001:4.1e-3;

rho_values = zeros(size(t_values));
lambda_p_values = zeros(size(t_values));
sigma_cr_values = zeros(size(t_values));
sigma_max_values = zeros(size(t_values));

%Iteration over thickness values
for i = 1:length(t_values)
    t = t_values(i);
    I = b * t^3 / 12; % Moment of inertia

    % Critical Buckling Load
    sigma_cr = k*((pi^2*E)/(12*(1-v^2)*(b/t)^2));   %[Pa]
    Pcr = sigma_cr*t;                               %[N/m]

    %Classification (EN 1993-1-1 Table 5.2)
    Beta = c / t;

    C1 = 33 * epsilon;
    C2 = 38 * epsilon;
    C3 = 42 * epsilon;
    C4 = 42 * epsilon; % Class 4 limit

    %Slenderness Calculation (EN 1993-1-5 Table 4.1)
    b_bar = b;
    gaffel = 1;  % Assume uniform compression
    k_sigma = 4; % Internal compression element
```

```
    lambda_p = sqrt(fy/sigma_cr);

    % Apply the new condition for #
    if lambda_p < 0.673
        rho = 1; % Fully effective cross-section
    else
        %rho = 1/lambda_p;
        rho = (lambda_p - 0.055 * (3 + gaffel)) / lambda_p^2;
        rho = max(rho, 0); % Ensure non-negative values
    end
    %Maximum Load
    Pmax = 1.9 * sqrt(E * fy) * t^2;                                %[N]
    sigma_max = Pmax / (b * t);                                     %[Pa]

    % Store results
    fy = fy;
    rho_values(i) = rho;
    lambda_p_values(i) = lambda_p;
    sigma_max_values(i) = sigma_max;
    sigma_cr_values(i) = sigma_cr;
    fy_values(i) = fy;

end

% Define points to highlight (t = 1, 2, 3, 4 mm)
highlight_t = [1, 2, 3, 4]; % t values in mm

% Initialize arrays for rho and lambda_p corresponding
% to t = 1, 2, 3, 4 mm
highlight_rho = zeros(size(highlight_t));
highlight_lambda_p = zeros(size(highlight_t));

% Calculate corresponding rho and lambda_p values for t = 1, 2, 3, 4 mm
for i = 1:length(highlight_t)
    t_mm = highlight_t(i) / 1000; % Convert mm to meters
    index = find(t_values >= t_mm, 1); % Find the closest index for t

    highlight_rho(i) = rho_values(index);
    highlight_lambda_p(i) = lambda_p_values(index);
end


% Define classification limits for width-to-thickness ratio (b/t)
C1 = 33 * epsilon; % Class 1 limit
C2 = 38 * epsilon; % Class 2 limit
C3 = 42 * epsilon; % Class 3 limit
C4 = 42 * epsilon; % Class 4 limit (same as C3)

% Convert classification limits into thickness values
t_C1 = b / C1;
t_C2 = b / C2;
t_C3 = b / C3;
t_C4 = b / C4;
```

```
% Recalculate sigma_cr for each classification thickness
sigma_cr_C1 = k * (pi^2 * E) / (12 * (1 - v^2)) * (t_C1 / b)^2;
sigma_cr_C2 = k * (pi^2 * E) / (12 * (1 - v^2)) * (t_C2 / b)^2;
sigma_cr_C3 = k * (pi^2 * E) / (12 * (1 - v^2)) * (t_C3 / b)^2;
sigma_cr_C4 = k * (pi^2 * E) / (12 * (1 - v^2)) * (t_C4 / b)^2;

% Recalculate slenderness limits based on corrected sigma_cr
lambda_C1 = sqrt(fy / sigma_cr_C1);
lambda_C2 = sqrt(fy / sigma_cr_C2);
lambda_C3 = sqrt(fy / sigma_cr_C3);
lambda_C4 = sqrt(fy / sigma_cr_C4);

figure(1)
plot(t_values * 1000, rho_values, 'k', 'LineWidth', 1.5);
hold on;
plot(highlight_t, highlight_rho, 'ko', 'MarkerSize', 8, 'LineWidth', 1.5);


t_C1 = t_C1*1000;
t_C2 = t_C2*1000;
t_C3 = t_C3*1000;
t_C4 = t_C4*1000;

% Add vertical lines at lambda_C1, lambda_C2, lambda_C3, lambda_C4
xline(t_C1, '--k');
xline(t_C2, '--k');
xline(t_C3, '--k');
xline(t_C4, '--k');

% Add horizontal labels at each vertical line using the 'text' function
text((4.5-(4.5-t_C1)/2), 0.67, '1', 'Interpreter', 'latex','FontSize', ...
    12, 'HorizontalAlignment', 'center', 'VerticalAlignment', 'middle');

text(t_C2-(t_C2-t_C1)/2, 0.65, '2', 'Interpreter', 'latex','FontSize', ...
    12, 'HorizontalAlignment', 'center', 'VerticalAlignment', 'bottom');

text((t_C3-t_C2)/2+t_C2, 0.65, '3', 'Interpreter', 'latex', 'FontSize', ...
    12, 'HorizontalAlignment', 'center', 'VerticalAlignment', 'bottom');

text(t_C3 - 0.1, 0.65, '4', 'Interpreter', 'latex','FontSize', 12, ...
    'HorizontalAlignment', 'center', 'VerticalAlignment', 'bottom');

xlabel('Plate Thickness t (mm)', 'Interpreter', 'latex');
ylabel('Reduction Factor $\rho$', 'Interpreter', 'latex');
title('Reduction Factor $\rho$ vs. Plate Thickness', 'Interpreter', ...
    'latex');
grid on;
legend('$\rho$ vs. t', 'Chosen thickness',  'Cross section class', ...
    'Location', 'best',  'Interpreter', 'latex','FontSize', 14);
hold off;

ax = gca
ax.TickLabelInterpreter = 'latex';
```

```
ax.FontSize=12


figure(2)
plot(lambda_p_values, rho_values, 'k', 'LineWidth', 1.5);
hold on;
plot(highlight_lambda_p, highlight_rho, 'ko', 'MarkerSize', 8, ...
    'LineWidth', 1.5); % Highlight points



% Add vertical lines at lambda_C1, lambda_C2, lambda_C3, lambda_C4
xline(lambda_C1, '--k');
xline(lambda_C2, '--k');
xline(lambda_C3, '--k');
xline(lambda_C4, '--k');

% Add horizontal labels at each vertical line using the 'text' function
text((lambda_C1-0.5)/2+0.5, 0.67, '1', 'Interpreter', 'latex', ...
    'FontSize', 12, 'HorizontalAlignment', 'center', ...
    'VerticalAlignment', 'middle');

text((lambda_C2-lambda_C1)/2+lambda_C1, 0.65, '2', 'Interpreter', ...
    'latex','FontSize', 12, 'HorizontalAlignment', 'center', ...
    'VerticalAlignment', 'bottom');

text((lambda_C3-lambda_C2)/2+lambda_C2, 0.65, '3', 'Interpreter', ...
    'latex', 'FontSize', 12, 'HorizontalAlignment', 'center', ...
    'VerticalAlignment', 'bottom');

text(lambda_C3 + 0.04, 0.65, '4', 'Interpreter', 'latex','FontSize', ...
    12, 'HorizontalAlignment', 'center', 'VerticalAlignment', 'bottom');

xlabel('Slenderness, $\lambda_p$', 'Interpreter', 'latex');
ylabel('Reduction Factor $\rho$','Interpreter', 'latex');
grid on;
legend('$\rho$ vs. $\lambda_p$', 'Chosen thickness', ...
    'Cross section class','Location', 'best', ...
    'Interpreter', 'latex','FontSize', 14);
hold off;

ax = gca


ax.TickLabelInterpreter = 'latex';
ax.FontSize=12

figure(3)
plot(t_values * 1000, sigma_cr_values/1e6, 'b', 'LineWidth', 1.5);
hold on;
plot(t_values * 1000, sigma_max_values/1e6, 'b--', 'LineWidth', 1.5);
plot(t_values*1000,fy_values/1e6,'r','LineWidth', 1.5)
xlabel('Plate Thickness t [mm]', 'FontName', 'Serif');
ylabel('Stress [MPa]', 'FontName', 'Serif');
```

```
grid on;
legend('Critical Stress (\sigma_{cr})', ...
    'Maximum Stress (\sigma_{max})','Yield Stress (f_{y})', ...
    'Location', 'best', 'FontName', 'Serif');

hold off
figure(4)
plot(lambda_p_values, sigma_cr_values/1e6, 'b', 'LineWidth', 1.5);
hold on;
plot(lambda_p_values, sigma_max_values/1e6, 'b--', 'LineWidth', 1.5);
plot(lambda_p_values,fy_values/1e6,'r','LineWidth', 1.5)
xlabel('Slenderness', 'FontName', 'Serif');
ylabel('Stress [MPa]', 'FontName', 'Serif');
grid on;
legend('Critical Stress (\sigma_{cr})', ...
    'Maximum Stress (\sigma_{max})','Yield Stress (f_{y})', ...
    'Location', 'best', 'FontName', 'Serif');

set(gca,'Fontname', 'Serif')
```

```
ax =

  Axes (Reduction Factor $\rho$ vs. Plate Thickness) with properties:

            XLim: [0.5000 4.5000]
            YLim: [0.3000 1]
          XScale: 'linear'
          YScale: 'linear'
    GridLineStyle: '-'
         Position: [0.1300 0.1100 0.7750 0.8150]
            Units: 'normalized'

  Use GET to show all properties


ax =

  Axes (Reduction Factor $\rho$ vs. Plate Thickness) with properties:

            XLim: [0.5000 4.5000]
            YLim: [0.3000 1]
          XScale: 'linear'
          YScale: 'linear'
    GridLineStyle: '-'
         Position: [0.1300 0.1136 0.7750 0.8114]
            Units: 'normalized'

  Use GET to show all properties


ax =

  Axes with properties:
```

```
            XLim: [0.5000 3]
            YLim: [0.3000 1]
          XScale: 'linear'
          YScale: 'linear'
    GridLineStyle: '-'
         Position: [0.1300 0.1100 0.7750 0.8150]
            Units: 'normalized'

  Use GET to show all properties


ax =

  Axes with properties:

            XLim: [0.5000 3]
            YLim: [0.3000 1]
          XScale: 'linear'
          YScale: 'linear'
    GridLineStyle: '-'
         Position: [0.1300 0.1136 0.7750 0.8114]
            Units: 'normalized'

  Use GET to show all properties
```

Published with MATLAB® R2022a

Appendix C

T130-75L-930 Isolerat tak

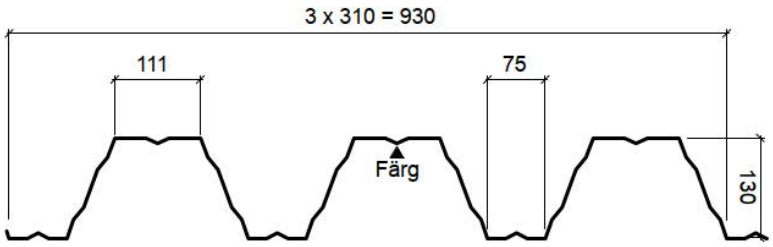

TVÄRSNITTSDATA

Tabell 1

ALLMÄNT		Plåttjocklek, nominell	t	mm	0,70	0,80	0,90	1,00	1,20	1,50
		Plåttjocklek vid beräkning	t_{ber}	mm	0,66	0,76	0,86	0,96	1,16	1,46
		Sträckgräns	f_{ty}	N/mm^2	350	350	350	350	350	350
		Massa	m	kg/m	8,24	9,42	10,60	11,78	14,13	17,66
		Egentyngd	G_{pl}	kN/m^2	0,09	0,10	0,11	0,13	0,15	0,19
TRANSVERSALLAST	**Smal fläns tryckt**	Upplagsreaktion för l_s=100 mm	$R_{sw.Rd}$	kN/m	18,60	24,60	31,60	39,80	60,00	96,90
		Moment	$M_{s,Rd}$	kNm/m	10,88	13,27	15,48	17,69	23,47	33,60
		Tröghetsmoment	I_{sef}	mm^4/mm	2487	2863	3239	3616	4368	5496
	Bred fläns tryckt	Upplagsreaktion för l_s=100 mm	$R_{bw.Rd}$	kN/m	20,70	28,20	36,30	44,70	63,50	96,90
		Moment	$M_{b,Rd}$	kNm/m	9,11	11,40	13,80	16,28	21,10	26,87
		Tröghetsmoment	I_{sef}	mm^4/mm	2314	2731	3156	3584	4368	5496
SKIVDATA	**Skjuvbuckling**	Livbuckling	$V_{w,Rd}$	kN/m	30,4	44,8	63,1	85,5	142,4	219,3
		Flänsbuckling	$V_{f,Rd}$	kN/m	44,6	66,0	93,0	120,9	172,8	267,2
		Globalbuckling	$V_{g,Rd} \cdot L^2$	kN/m	768	950	1143	1348	1790	2527
	Ändstöd	Böjning profilhörn	$V_{r,Rd}$	kN/m	9,6	11,9	14,3	16,8	22,4	31,6
		Upplagsreaktion av skivkraft	R_v/V		1,06	1,06	1,06	1,06	1,06	1,06
		Dragkraft i fästdon	F_{c2}/V		0,165	0,165	0,165	0,165	0,165	0,165

SNABBDIMENSIONERING - Tvåfacksplåt i säkerhetsklass 2

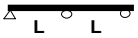

Tabell 2

Snözon	Maximal spännvidd L för olika tjocklekar t, upplagsbredder l_s och snözoner s_k											
s_k	t=0,70		t=0,80		t=0,90		t=1,00		t=1,20		t=1,50	
kN/m^2	l_s=100	l_s=200	l_s=100	l_s=200	l_s=100	l_s=200	l_s=100	l_s=200	l_s=100	l_s=200	l_s=100	l_s=200
1	6,2	6,8	7,2	7,8	8,1	8,6	8,8	9,3	9,6	9,6	9,6	9,6
1,5	5,1	5,7	6,0	6,6	6,8	7,3	7,5	7,9	8,9	9,3	9,6	9,6
2	4,4	4,9	5,2	5,7	5,9	6,4	6,5	7,0	7,8	8,3	9,6	9,6
2,5	3,9	4,4	4,6	5,1	5,3	5,7	5,8	6,3	7,0	7,5	8,7	9,2
3	3,5	4,0	4,2	4,7	4,8	5,2	5,3	5,8	6,4	6,8	8,0	8,2
4	2,9	3,4	3,5	4,0	4,0	4,5	4,5	5,0	5,5	5,9	6,9	7,3

FÖRKLARINGAR

Snabbdimensionering enligt tabell 2 gäller i säkerhetsklass 2 för egentyngd G_k = 0,3, formfaktor för snö μ=0,85 och ett vind-hastighetstryck på q_k = 0,7 med c_{pep} =0,5. För säkerhetsklass 3 kan spännvidderna reduceras med 7%.

Dimensioneringsvärden beror av byggnadens säkerhetsklass. Takplåt utsatt för transversallast och som inte har stabiliserande funktion dimensioneras i normalt säkerhetsklass 2.

Plåt som stabiliserar stommen genom skivverkan dimensioneras för denna del av lasten som stommen, normalt säkerhetsklass 3 och för samtidig transversallast i säkerhetsklass enligt ovan.

Nedböjningen är kontrollerad för L/200. Beakta känslighet i anslutande detaljer

För andra förutsättningar använd Ruukkis dimensionerings-program Poimu

Minimiinfästning:

Ändupplag	2 skruvar i varje profilbotten
Mellanupplag, ändöverlapp	1 skruv i varje profilbotten
Sidöverlapp	Max c/c 500mm

Vid skivverkan erfordras normalt fler infästningar

GÅBARHET

Tabell 3

Tjocklek	Rekommenderad max spännvidd	
	Enfack	Flerfack
0,70	6,6	7,8
0,80	7,4	8,6
0,90	7,8	9,0
1,00	8,0	9,0
1,20	8,2	9,0
1,50	8,4	9,0

T130-75L-930 Innertak

MAXIMALA BELASTNINGAR i kN/m²

Tabell 4

Upplags-fall	Tjock-lek mm	Last-Fall	Begränsningar	Spännvidder L (m) 5,1	5,4	5,7	6,0	6,3	6,6	6,9	7,2	7,5	7,8	8,1	8,4
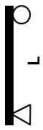	**0,70**	1	Moment	2,80	2,50	2,24	2,02	1,84	1,67	1,53	1,41	1,30	1,20	1,11	1,03
		3	Nedböjning	1,41	1,19	1,01	0,86	0,75	0,65	0,57	0,50	0,44	0,39	0,35	0,31
		2	Vindsug	3,35	2,98	2,68	2,42	2,19	2,00	1,83	1,68	1,55	1,43	1,33	1,23
	0,80	1	Moment	3,51	3,13	2,81	2,53	2,30	2,09	1,92	1,76	1,62	1,50	1,39	1,29
		3	Nedböjning	1,66	1,40	1,19	1,02	0,88	0,77	0,67	0,59	0,52	0,46	0,41	0,37
		2	Vindsug	4,08	3,64	3,27	2,95	2,67	2,44	2,23	2,05	1,89	1,74	1,62	1,50
	0,90	1	Moment	4,24	3,79	3,40	3,07	2,78	2,53	2,32	2,13	1,96	1,81	1,68	1,56
		3	Nedböjning	1,92	1,62	1,37	1,18	1,02	0,89	0,77	0,68	0,60	0,54	0,48	0,43
		2	Vindsug	4,76	4,25	3,81	3,44	3,12	2,84	2,60	2,39	2,20	2,04	1,89	1,76
	1,00	1	Moment	5,01	4,47	4,01	3,62	3,28	2,99	2,74	2,51	2,32	2,14	1,99	1,85
		3	Nedböjning	2,18	1,84	1,56	1,34	1,16	1,01	0,88	0,77	0,69	0,61	0,54	0,49
		2	Vindsug	5,44	4,85	4,36	3,93	3,57	3,25	2,97	2,73	2,52	2,33	2,16	2,01
	1,20	1	Moment	6,49	5,79	5,20	4,69	4,25	3,88	3,55	3,26	3,00	2,77	2,57	2,39
		3	Nedböjning	2,66	2,24	1,90	1,63	1,41	1,23	1,07	0,94	0,83	0,74	0,66	0,59
		2	Vindsug	7,22	6,44	5,78	5,22	4,73	4,31	3,94	3,62	3,34	3,09	2,86	2,66
	1,50	1	Moment	8,26	7,37	6,62	5,97	5,42	4,93	4,52	4,15	3,82	3,53	3,28	3,05
		3	Nedböjning	3,34	2,81	2,39	2,05	1,77	1,54	1,35	1,19	1,05	0,93	0,83	0,75
		2	Vindsug	10,33	9,22	8,27	7,47	6,77	6,17	5,65	5,19	4,78	4,42	4,10	3,81
	**0,70**	1	Upplag 100	2,32	2,13	1,96	1,81	1,68	1,56	1,46	1,36	1,28	1,20	1,13	1,06
		1	Upplag 200	2,73	2,50	2,29	2,10	1,94	1,80	1,67	1,56	1,45	1,36	1,28	1,20
		3	Nedböjning	3,60	3,04	2,58	2,21	1,91	1,66	1,46	1,28	1,13	1,01	0,90	0,81
		2	Vindsug	2,80	2,50	2,24	2,02	1,84	1,67	1,53	1,41	1,30	1,20	1,11	1,03
	0,80	1	Upplag 100	3,00	2,74	2,52	2,33	2,15	2,00	1,86	1,74	1,63	1,53	1,44	1,35
		1	Upplag 200	3,50	3,19	2,92	2,68	2,47	2,28	2,12	1,97	1,84	1,72	1,61	1,51
		3	Nedböjning	4,22	3,55	3,02	2,59	2,24	1,95	1,70	1,50	1,33	1,18	1,05	0,94
		2	Vindsug	3,51	3,13	2,81	2,53	2,30	2,09	1,92	1,76	1,62	1,50	1,39	1,29
	0,90	1	Upplag 100	3,66	3,35	3,08	2,83	2,62	2,43	2,26	2,11	1,97	1,85	1,74	1,63
		1	Upplag 200	4,25	3,87	3,53	3,24	2,98	2,76	2,56	2,38	2,21	2,07	1,94	1,82
		3	Nedböjning	4,84	4,08	3,47	2,97	2,57	2,23	1,95	1,72	1,52	1,35	1,21	1,08
		2	Vindsug	4,24	3,79	3,40	3,07	2,78	2,53	2,32	2,13	1,96	1,81	1,68	1,56
	1,00	1	Upplag 100	4,33	3,96	3,63	3,34	3,09	2,86	2,66	2,48	2,31	2,17	2,03	1,91
		1	Upplag 200	5,00	4,54	4,15	3,80	3,50	3,23	2,99	2,78	2,59	2,42	2,26	2,12
		3	Nedböjning	5,46	4,60	3,91	3,36	2,90	2,52	2,21	1,94	1,72	1,53	1,36	1,22
		2	Vindsug	5,01	4,47	4,01	3,62	3,28	2,99	2,74	2,51	2,32	2,14	1,99	1,85
	1,20	1	Upplag 100	5,92	5,40	4,95	4,56	4,20	3,89	3,62	3,37	3,14	2,94	2,76	2,59
		1	Upplag 200	6,80	6,17	5,63	5,16	4,74	4,37	4,05	3,76	3,50	3,26	3,05	2,86
		3	Nedböjning	6,64	5,59	4,75	4,08	3,52	3,06	2,68	2,36	2,09	1,86	1,66	1,49
		2	Vindsug	6,49	5,79	5,20	4,69	4,25	3,88	3,55	3,26	3,00	2,77	2,57	2,39
	1,50	1	Upplag 100	8,71	7,94	7,27	6,68	6,16	5,70	5,29	4,93	4,60	4,30	4,03	3,79
		1	Upplag 200	9,94	9,02	8,22	7,52	6,91	6,37	5,89	5,47	5,09	4,74	4,43	4,15
		3	Nedböjning	8,35	7,04	5,98	5,13	4,43	3,85	3,37	2,97	2,63	2,33	2,08	1,87
		2	Vindsug	8,26	7,37	6,62	5,97	5,42	4,93	4,52	4,15	3,82	3,53	3,28	3,05

FÖRKLARINGAR

Alla data är baserade på Eurocode och EKS10. Plåten kontrolleras för följande lastfall:

Brottgränstillstånd:

Lastfall 1 - Egentyngd, snö som huvudlast och vindlast

$$Q_{u1} = \gamma_d \cdot 0,89 \cdot 1,35 \cdot G_k + \gamma_d \cdot 1,5 \cdot \mu \cdot s_k + \psi_0 \cdot \gamma_d \cdot 1,5 \cdot c_{pep} \cdot q_p$$

Lastfall 2 - Vindsug som huvudlast och egentyngd

$$Q_{u2} = \gamma_d \cdot 1,5 \cdot c_{pes} \cdot q_p - 1,0 \cdot G_k$$

Bruksgränstillstånd:

Lastfall 3 - Egentyngd, snö som huvudlast och vindlast

$$Q_n = G_k + \psi_1 \cdot \mu \cdot s_k$$

Nedböjningen kontrolleras för L/200

där

- G_k Egentyngd
- μ Formfaktor for snölast
- s_k Karakteristisk snölast
- c_{pep} Formfaktor for vind, tryck
- c_{pes} Formfaktor for vind, sug
- q_p Karakteristiskt hastighetstryck
- ψ_0 Faktor för kombinationsvärde - vind ψ_0=0,3
- ψ_1 Faktor för frekvent värde för variabel last
  - ψ_1= 0,3 för snözon s_k = 1,0 -1,5
  - ψ_1= 0,4 för snözon s_k = 2,0 - 2,5
  - ψ_1= 0,6 för snözon s_k = 3,0 - 6,0
- γ_d Partialkoefficient med hänsyn till säkerhetsklass
  - γ_d = 0,83 för säkerhetsklass 1
  - γ_d = 0,91 för säkerhetsklass 2
  - γ_d = 1,00 för säkerhetsklass 3

Appendix D

Table D.1: Material model data points used in Abaqus

Yield stress [MPa]	Plastic strain [-]
355.5	0
361.09	0.016
399.86	0.030
460.21	0.054
489.40	0.072
513.60	0.094
535.77	0.117
557.9	0.139
571.49	0.151

Appendix E

Explosion load - CSM

Load 3

$P := 73.8\ kPa$

$i := 240\ Pa \cdot s$

$b := 558\ mm$ width were the load is applied

$b_{tot} := 930\ mm$ total width of the CSM strip

$L := 6000\ mm$

$A := b \cdot L = 3.348\ m^2$

$A_{tot} := b_{tot} \cdot L = 5.58\ m^2$

$\gamma_b := \frac{b}{b_{tot}} = 0.6$

$P_{FE} := \frac{P}{\gamma_b} = 123\ kPa$

$i_{FE} := \frac{i}{\gamma_b} = 400\ Pa \cdot s$

Distributed mass and total mass

$m'_{b1} := 166\ \frac{kg}{m^2}$ $\quad m_{b1} := m'_{b1} \cdot A_{tot} = 926.28\ kg$

$m'_{b2} := 332\ \frac{kg}{m^2}$ $\quad m_{b2} := m'_{b2} \cdot A_{tot} = \left(1.853 \cdot 10^3\right)\ kg$

$\kappa_{mF} := 0.667$ (Simply supported, plastic case, see table below)

	Jämnt utbredd last			
	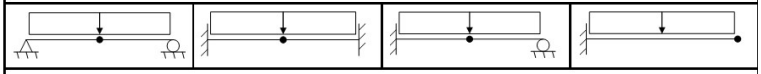			
	Utböjningskurva elastiskt fall			
κ_m	0,504	0,406	0,483	0,257
κ_F	0,640	0,533	0,600	0,400
κ_{mF}	0,787	0,762	0,805	0,642
	Utböjningskurva plastiskt fall			
κ_m	0,333	0,333	0,333	0,333
κ_F	0,500	0,500	0,500	0,500
κ_{mF}	0,667	0,667	0,667	0,667

Momentum

$I := i \cdot A_{tot} = \left(1.339 \cdot 10^3\right)\ \boldsymbol{N \cdot s}$

Effective mass

$m_{ef1} := m_{b1} \cdot \kappa_{mF} = 617.829\ \boldsymbol{kg}$

$m_{ef2} := m_{b2} \cdot \kappa_{mF} = \left(1.236 \cdot 10^3\right)\ \boldsymbol{kg}$

Exterior work

$W_{E1} := \frac{I^2}{2 \cdot m_{ef1}} = \left(1.451 \cdot 10^3\right)\ \boldsymbol{J}$

$W_{E2} := \frac{I^2}{2 \cdot m_{ef2}} = 725.709\ \boldsymbol{J}$

Static response:

$R_{max\_t0.7} := 9.4\ \boldsymbol{kN}$

$R_{max\_t1.05} := 16.8\ \boldsymbol{kN}$ (See graph below)

$R_{max\_t1.4} := 26\ \boldsymbol{kN}$

$q_1 := \frac{R_{max\_t0.7}}{A_{tot}} = 1.685\ \boldsymbol{kPa}$

$q_2 := \frac{R_{max\_t1.05}}{A_{tot}} = 3.011\ \boldsymbol{kPa}$

$q_3 := \frac{R_{max\_t1.4}}{A_{tot}} = 4.659\ \boldsymbol{kPa}$

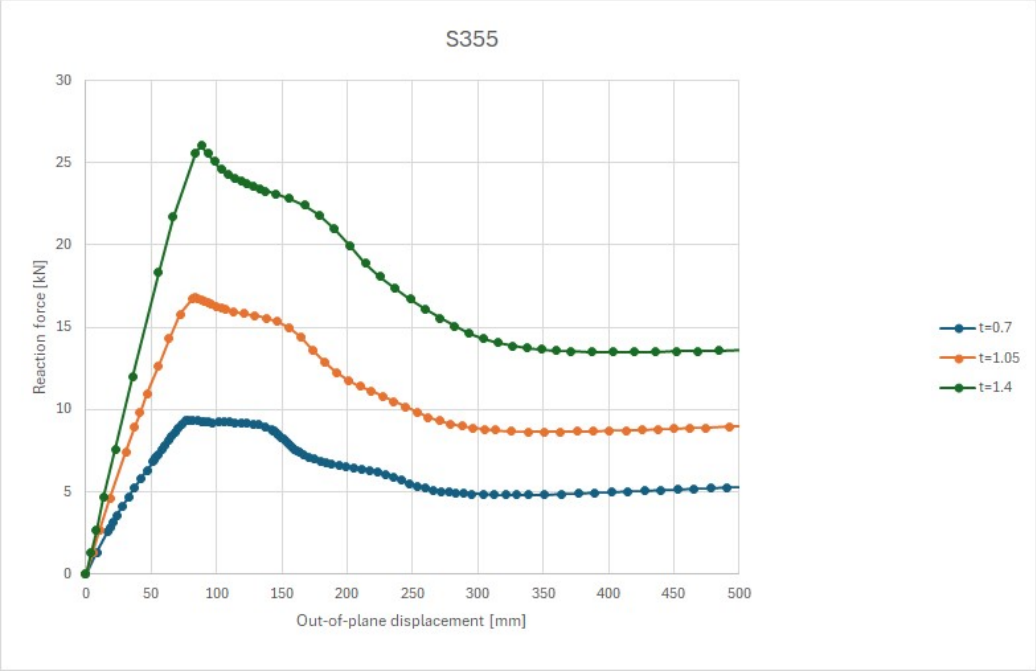

$\frac{P}{q_1} = 43.809$

$\frac{P}{q_2} = 24.512$ $\gamma_i := 1.0$

$\frac{P}{q_3} = 15.839$

W_E = W_I

$W_{I.1} := W_{E1} = \left(1.451 \cdot 10^3\right)\ \boldsymbol{J}$ approx. 1500 kJ

$W_{I.mod2} := W_{E2} = 725.709\ \boldsymbol{J}$ approx. 725 kJ

--> Compare with area under static load - deflection curve

--> It is calculated how large deflection (w in a excel table which is used to plot the graphs above) is needed to get a area, that is the same magnitude as WI.1 and WI.2 for the three different thicknesses
and 2 different masses

--> Expected maximal out-of-plane displacement:

t = 0.7, m = 332 kg/m^2 --> 112.5 mm
t = 0.7, m = 166 kg/m^2 --> 210 mm

t = 1.05, m = 332 kg/m^2 --> 80 mm
t = 1.05, m = 166 kg/m^2 --> 130 mm

t = 1.4, m = 332 kg/m^2 --> 65 mm
t = 1.4, m = 166 kg/m^2 --> 100 mm

Appendix F

Input data

Hole diameter $d_0 := 5.5\ mm$

Screw diameter $d := 5.0\ mm$

Screw distance to free edge $e_1 := 37.5\ mm$

Screw distance to web $e_2 := 37.5\ mm$

Plate thickness $t := 1.05\ mm$

Steel tensile capacity $f_u := 500\ MPa$

Springs per fastener $n := 7$

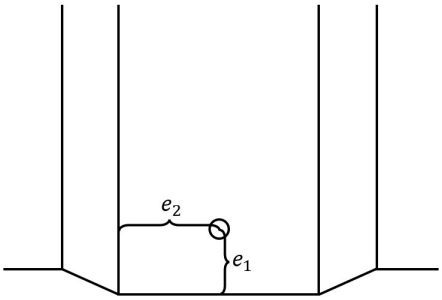

Capacity (Eurocode, one screw)

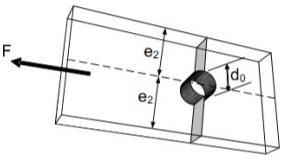

Tensile failure $F_t := \left(2.8 \cdot \frac{e_2}{d} - 1.7\right) \cdot f_u \cdot d \cdot t = 50.663\ kN$

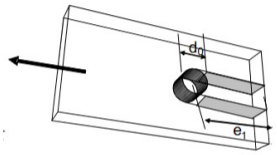

Shear failure $F_s := 2.5 \cdot \left(\frac{e_1}{3 \cdot d_0}\right) \cdot f_u \cdot d \cdot t = 14.915\ kN$

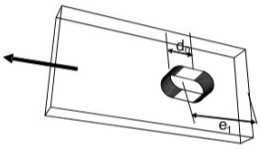

Elongation $F_e := 2.5 \cdot f_u \cdot d \cdot t = 6.563\ kN$

Actual force in spring

Mid springs $F_{mid} := \frac{min\left(F_t, F_s, F_e\right)}{n} = 937.5\ N$

Edge springs at symmetry line $F_{edge} := \frac{F_{mid}}{2} = 468.75\ N$

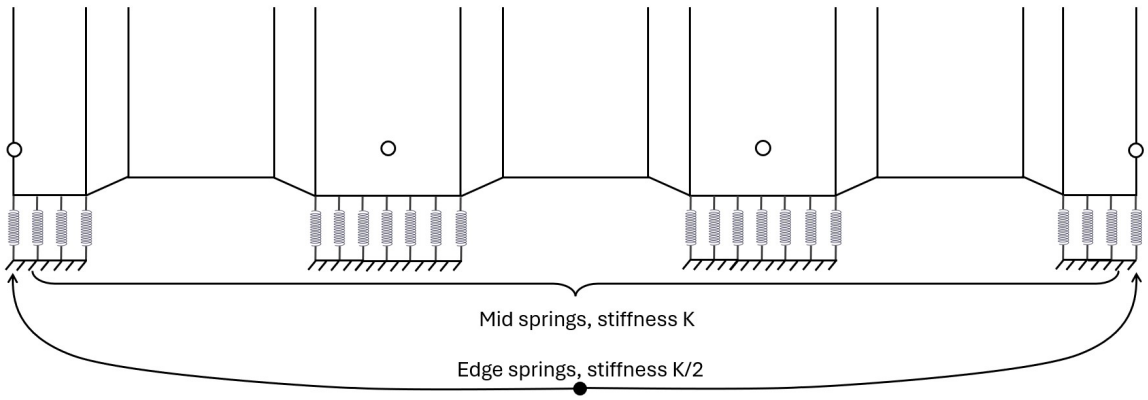

Appendix G

Hand calculation - static capacity CSM

Calculation of Loadbearing capacity of CSM strip with 3 corrugations and length 6 m with the following thicknesses:
- t1 = 0.7 mm
- t2 = 1.05 mm
- t3 = 1.4 mm

$\theta := 64.5 \cdot \frac{\pi}{180}$

$L := 6\ m$

$t_1 := 0.7\ mm$

$t_2 := 1.05\ mm$

$t_3 := 1.4\ mm$

$t := t_3$ Change to desired thickness

$\gamma_{M0} := 1.0$

$f_y := 355\ MPa$

$f_{yb} := 355\ MPa$

$E := 210000\ MPa$

Cross-section:

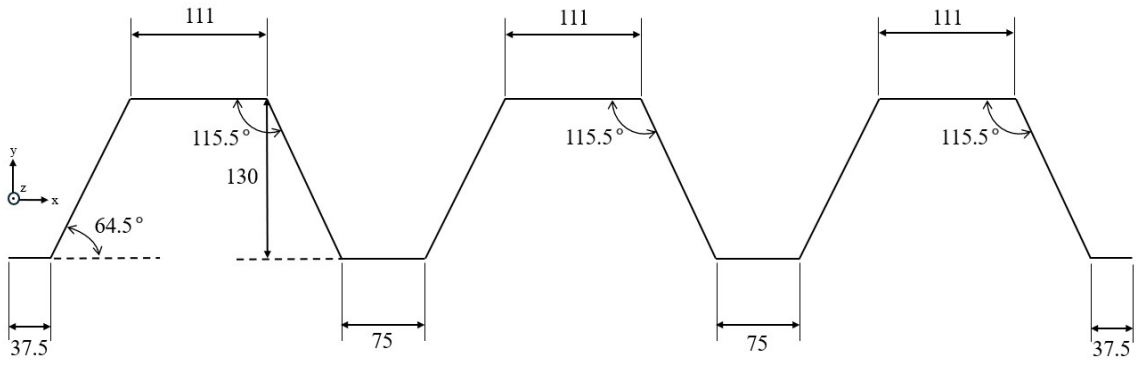

Effective width compressed part of the web
**1993-1-3 chapter 7*

$$s_{eff.0} := 0.76 \cdot t \cdot \sqrt{\frac{E}{\frac{f_{yb}}{\gamma_{M0}}}} \qquad (7.53)$$

$h_c := 59\ mm$
$h_t := 71\ mm$
(AutoCAD, (reasonable since we have more mass at the top 111 > 75))

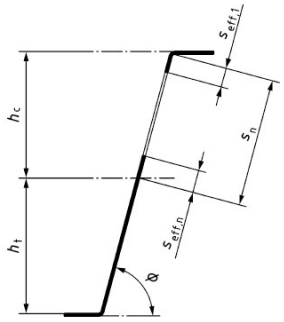

(a) without stiffener

$s_{eff.1} := s_{eff.0} = 25.878\ mm \qquad (7.54)$

$s_{eff.n} := 1.5 \cdot s_{eff.0} = 38.818\ mm \qquad (7.59)$

$$s_n := \frac{h_c}{\sin(\theta)} = 65.368\ mm$$

$s_{eff.1} + s_{eff.n} = 64.696\ mm$ < Sn, ok! (if not, see 7.60 and 7.61)

Effective width compression flange:
**1993-1-5 chapter 4*

$b := 111\ mm$

$$\varepsilon := \sqrt{\frac{235 \cdot MPa}{f_y}} = 0.814$$

$\psi := 1$

$k_\sigma := 4$ (Table 4.1)

$$\lambda_p := \frac{\frac{b}{t}}{28.4 \cdot \varepsilon \cdot \sqrt{k_\sigma}} = 1.716$$

$$\rho := \frac{\lambda_p - 0.055 \cdot (3 + \psi)}{{\lambda_p}^2} = 0.508 \qquad (4.2)$$

$b_{eff} := b \cdot \rho = 56.402\ mm$ (Table 4.1)

$b_{eff.1} := b_{eff} \cdot 0.5 = 28.201\ mm$

$b_{eff.2} := b_{eff} \cdot 0.5 = 28.201\ mm$

Effective cross-section for one corrugation:

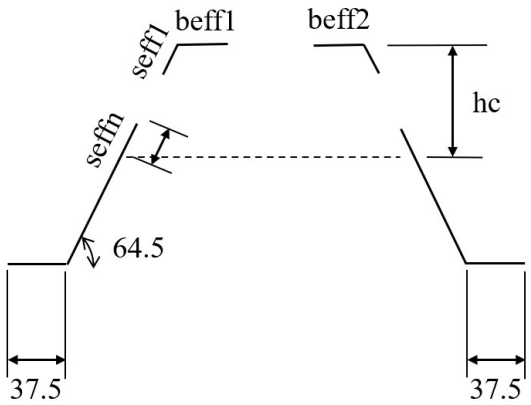

Sectional constants:

$$z_{TP.eff} := \frac{\begin{aligned} & b_{eff.1}\cdot t\cdot\frac{t}{2}+b_{eff.2}\cdot t\cdot\frac{t}{2}+2\cdot 37.5\ mm\cdot t\cdot\left(\left(130\ mm\right)+\frac{t}{2}\right) \\ & +2\cdot s_{eff.1}\cdot t\cdot\left(\sin\left(\theta\right)\cdot\frac{s_{eff.1}}{2}+\frac{t}{2}\right)+2\cdot s_{eff.n}\cdot t\cdot\left(\left(s_n-\frac{s_{eff.n}}{2}\right)\cdot\sin\left(\theta\right)+\frac{t}{2}\right) \\ & +2\cdot\left(\frac{130\ mm}{\sin\left(\theta\right)}-s_n\right)\cdot t\cdot\left(s_n\cdot\sin\left(\theta\right)+\frac{\left(\frac{130\ mm}{\sin\left(\theta\right)}-s_n\right)}{2}\cdot\sin\left(\theta\right)+\frac{t}{2}\right) \end{aligned}}{\begin{aligned} & b_{eff.1}\cdot t+b_{eff.2}\cdot t+2\cdot 37.5\ mm\cdot t \\ & +2\cdot s_{eff.1}\cdot t \\ & +2\cdot s_{eff.n}\cdot t+2\cdot\left(\frac{130\ mm}{\sin\left(\theta\right)}-s_n\right)\cdot t \end{aligned}} = 68.724\ mm$$

$$z_{TP.eff.top} := z_{TP.eff} = 68.724\ mm$$

$$z_{TP.eff.bottom} := 130\ mm - z_{TP.eff} + t = 62.676\ mm$$

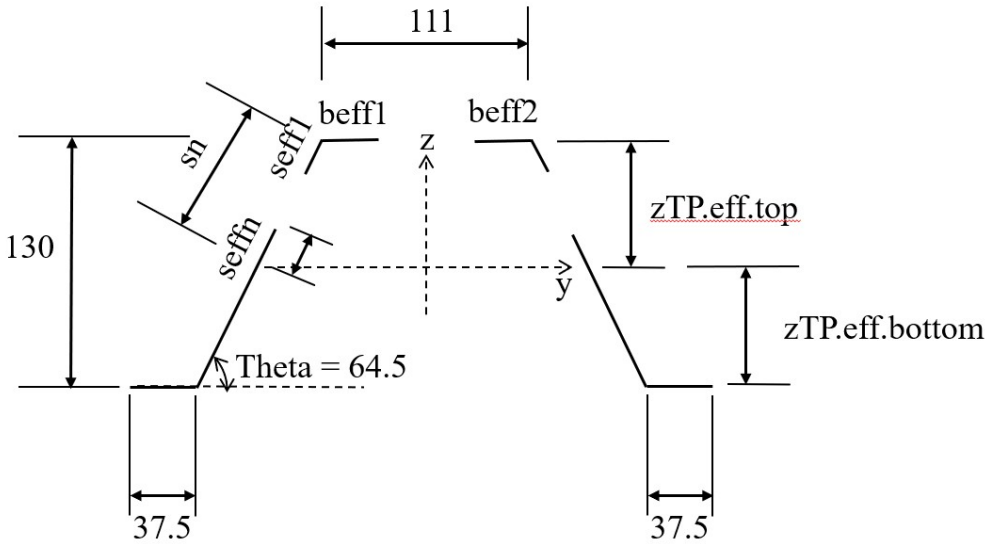

contribution around weak axis is disregarded since t <<< length

$$I_{bottom.flange} := 37.5\ mm \cdot t \cdot \left(z_{TP.eff.bottom} - \frac{t}{2}\right)^2 = \left(2.017 \cdot 10^5\right)\ mm^4$$

$$I_{beff} := \left(b_{eff.1} + b_{eff.2}\right) \cdot t \cdot \left(z_{TP.eff.top} - \frac{t}{2}\right)^2 = \left(3.654 \cdot 10^5\right)\ mm^4$$

2D rotation matrix:

(needed since the webs are rotated with respect to the global coordinate system, (only for illustrational purposes, not actual variables))

$$R := \begin{bmatrix} \cos(\theta) & -\sin(\theta) \\ \sin(\theta) & \cos(\theta) \end{bmatrix} \quad \text{-->} \quad \begin{bmatrix} I_{yy} & -I_{yz} \\ I_{zy} & I_{zz} \end{bmatrix} := R \cdot I_{local} \cdot R^T \quad \text{-->} \quad I_{yy} := I_{zz.local} \cdot \sin(\theta)^2$$

Explanation of notation on this and the next page:

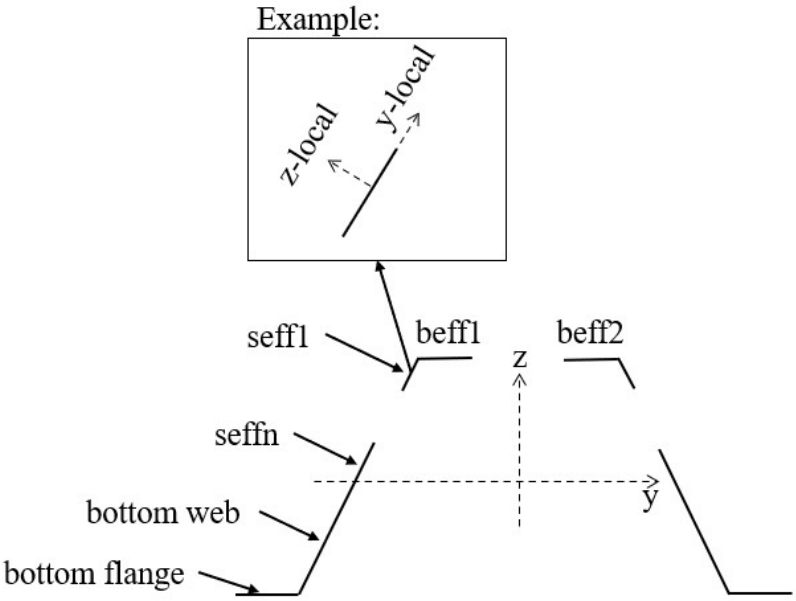

$$I_{bottom.web.local.z} := \frac{\left(\frac{130\ mm}{\sin(\theta)} - s_n\right)^3 \cdot t}{12}$$

$$I_{bottom.web.global.y} := I_{bottom.web.local.z} \cdot \sin(\theta)^2 \hookleft + \left(\frac{130\ mm}{\sin(\theta)} - s_n\right) \cdot t \cdot \left(z_{TP.eff.bottom} - \left(\frac{\left(\frac{130\ mm}{\sin(\theta)} - s_n\right)}{2} \cdot \sin(\theta)\right) - \frac{t}{2}\right)^2$$

$$I_{seff.1.local.z} := \frac{s_{eff.1}{}^3 \cdot t}{12} = \left(2.022 \cdot 10^3\right)\ mm^4$$

$$I_{seff.1.global.y} := I_{seff.1.local.z} \cdot \sin(\theta)^2 \hookleft + s_{eff.1} \cdot t \cdot \left(z_{TP.eff.top} - \frac{s_{eff.1}}{2} \cdot \sin(\theta) - \frac{t}{2}\right)^2 = \left(1.167 \cdot 10^5\right)\ mm^4$$

$$I_{seff.n.local.z} := \frac{s_{eff.n}{}^3 \cdot t}{12} = \left(6.824 \cdot 10^3\right)\ mm^4$$

$$I_{seff.n.global.y} := I_{seff.n.local.z} \cdot \sin(\theta)^2 \hookleft + s_{eff.n} \cdot t \cdot \left(z_{TP.eff.top} - \left(s_n - \frac{s_{eff.n}}{2}\right) \cdot \sin(\theta) - \frac{t}{2}\right)^2 = \left(4.384 \cdot 10^4\right)\ mm^4$$

$$I_{eff.y} := I_{bottom.flange} \cdot 2 + I_{beff} + I_{bottom.web.global.y} \cdot 2 + I_{seff.1.global.y} \cdot 2 + I_{seff.n.global.y} \cdot 2 \hookleft = \left(1.337 \cdot 10^6\right)\ mm^4$$

$$W_{eff.t} := \frac{I_{eff.y}}{z_{TP.eff.bottom}} = \left(2.133 \cdot 10^4\right)\ mm^3$$

$$W_{eff.c} := \frac{I_{eff.y}}{z_{TP.eff.top}} = \left(1.945 \cdot 10^4\right)\ mm^3$$

$W_{eff} := 3 \cdot min\left(W_{eff.t}, W_{eff.c}\right)$ (x3 since we have modelled 3 corrugations in Abaqus)

$$M_{c.Rd} := W_{eff} \cdot \frac{f_{yb}}{\gamma_{M0}} = 20.714\ kN \cdot m$$ (8.10), Weff < Wel since CSC4

$$q := 8 \cdot \frac{M_{c.Rd}}{L^2} = 4.603 \ \frac{1}{m} \cdot kN$$

$$F_{tot} := q \cdot L = 27.618 \ kN$$

FEM: *(F is the total reaction force of the CSM on both sides, and e = 0.5 is used as amplitude for the initial imperfections which is approx. b/200)*
- t = 0.7 mm: F = 9.2 kN
- t = 1.05 mm: F = 17.8 kN
- t = 1.4 mm: F = 28.8 kN

Analytical:
- t = 0.7 mm: F = 7.972 kN
- t = 1.05 mm: F = 16.465 kN
- t = 1.4 mm: F = 27.618 kN

FEM with combination of 2 modes:
- t = 0.7 mm: F = 7.6 kN (unclear if the peak is reached)
- t = 1.05 mm: F = 17.1 kN
- t = 1.4mm: F = 27.3 kN

Difference when only first mode:
- t = 0.7 mm: 13.35%
- t = 1.05 mm: 7.50%
- t = 1.4 mm: 4.10%

Difference when using and combining 2 modes:
- t = 0.7 mm: -4.2%
- t = 1.05 mm: 3.7%
- t = 1.4 mm: -1.16%

Appendix H

Hand calculation - stiffness of CSM

$\theta := 64.5 \cdot \frac{\pi}{180}$

$L := 6\ m$

$t_1 := 0.7\ mm$

$t_2 := 1.05\ mm$

$t_3 := 1.4\ mm$

$t := t_3$ Change to desired thickness

$\gamma_{M0} := 1.0$

$f_y := 355\ MPa$

$f_{yb} := 355\ MPa$

$E := 210000\ MPa$

$b_{top.flange} := 111\ mm$

$b_{bottom.flange} := 37.5\ mm$

$l_{web} := \frac{130\ mm}{\sin(\theta)} = 144.031\ mm$

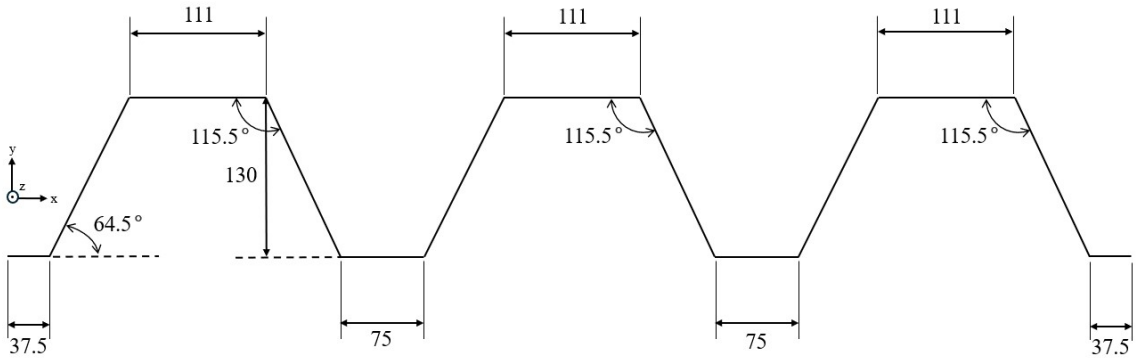

Stiffness <u>without</u> area reduction

Sectional constants:

$z_{TP.top} := 59\ mm + \frac{t}{2}$

$z_{TP.bottom} := 71\ mm + \frac{t}{2}$

$I_{bottom.flange} := b_{bottom.flange} \cdot t \cdot \left(z_{TP.bottom} - \frac{t}{2}\right)^2 = \left(2.647 \cdot 10^5\right)\ mm^4$

$I_{top.flange} := b_{top.flange} \cdot t \cdot \left(z_{TP.top} - \frac{t}{2}\right)^2 = \left(5.409 \cdot 10^5\right)\ mm^4$

$I_{web.local} := \frac{t \cdot {l_{web}}^3}{12}$

$I_{web.global} := I_{web.local} \cdot \sin(\theta)^2 + l_{web} \cdot t \cdot \left(\frac{(130\ mm + t)}{2} - z_{TP.top}\right)^2 = \left(2.912 \cdot 10^5\right)\ mm^4$

$I_{tot} := 3 \cdot \left(2 \cdot I_{bottom.flange} + I_{top.flange} + 2 \cdot I_{web.global}\right) = \left(4.958 \cdot 10^6\right)\ mm^4$

Stiffness <u>with</u> area reduction ("effective stiffness")

$z_{TP.eff.top} := 68.724\ mm$

$z_{TP.eff.bottom} := 62.676\ mm$

$\varepsilon := \sqrt{\frac{235 \cdot MPa}{f_y}} = 0.814 \qquad \psi := 1 \qquad k_\sigma := 4$

$\lambda_p := \frac{\frac{b_{top.flange}}{t}}{28.4 \cdot \varepsilon \cdot \sqrt{k_\sigma}} = 1.716$

$\rho := \frac{\lambda_p - 0.055 \cdot (3 + \psi)}{{\lambda_p}^2} = 0.508$

$b_{eff} := b_{top.flange} \cdot \rho = 56.402\ mm$

$b_{eff.1} := b_{eff} \cdot 0.5 = 28.201\ mm$

$b_{eff.2} := b_{eff} \cdot 0.5 = 28.201\ mm$

$$s_{eff.0} := 0.76 \cdot t \cdot \sqrt{\frac{E}{\frac{f_{yb}}{\gamma_{M0}}}}$$

$$s_{eff.1} := s_{eff.0} = 25.878\ mm$$

$$s_{eff.n} := 1.5 \cdot s_{eff.0} = 38.818\ mm$$

$$s_{eff.1} + s_{eff.n} = 64.696\ mm \qquad s_n := \frac{z_{TP.top}}{\sin(\theta)} = 66.143\ mm$$

$$I_{eff.bottom.flange} := 37.5\ mm \cdot t \cdot \left(z_{TP.eff.bottom} - \frac{t}{2}\right)^2 = \left(2.017 \cdot 10^5\right)\ mm^4$$

$$I_{eff.top.flange} := \left(b_{eff.1} + b_{eff.2}\right) \cdot t \cdot \left(z_{TP.eff.top} - \frac{t}{2}\right)^2 = \left(3.654 \cdot 10^5\right)\ mm^4$$

$$I_{bottom.web.local.z} := \frac{\left(\frac{130\ mm}{\sin(\theta)} - s_n\right)^3 \cdot t}{12}$$

$$I_{bottom.web.global.y} := I_{bottom.web.local.z} \cdot \sin(\theta)^2 \hookleftarrow + \left(\frac{130\ mm}{\sin(\theta)} - s_n\right) \cdot t \cdot \left(z_{TP.eff.bottom} - \left(\frac{\left(\frac{130\ mm}{\sin(\theta)} - s_n\right)}{2} \cdot \sin(\theta)\right) - \frac{t}{2}\right)^2$$

$$I_{seff.1.local.z} := \frac{{s_{eff.1}}^3 \cdot t}{12} = \left(2.022 \cdot 10^3\right)\ mm^4$$

$$I_{seff.1.global.y} := I_{seff.1.local.z} \cdot \sin(\theta)^2 \hookleftarrow + s_{eff.1} \cdot t \cdot \left(z_{TP.eff.top} - \frac{s_{eff.1}}{2} \cdot \sin(\theta) - \frac{t}{2}\right)^2 = \left(1.167 \cdot 10^5\right)\ mm^4$$

$$I_{seff.n.local.z} := \frac{{s_{eff.n}}^3 \cdot t}{12} = \left(6.824 \cdot 10^3\right)\ mm^4$$

$$I_{seff.n.global.y} := I_{seff.n.local.z} \cdot \sin(\theta)^2 \hookleftarrow + s_{eff.n} \cdot t \cdot \left(z_{TP.eff.top} - \left(s_n - \frac{s_{eff.n}}{2}\right) \cdot \sin(\theta) - \frac{t}{2}\right)^2 = \left(4.185 \cdot 10^4\right)\ mm^4$$

$$I_{eff.tot} := 3 \cdot \begin{pmatrix} 2 \cdot I_{eff.bottom.flange} + I_{eff.top.flange} + 2 \cdot I_{bottom.web.global.y} \\ + 2 \cdot I_{seff.1.global.y} + 2 \cdot I_{seff.n.global.y} \end{pmatrix} = \left(3.997 \cdot 10^6\right)\ mm^4$$

$$I_{tot} = \left(4.958 \cdot 10^6\right)\ mm^4$$

$$Reduction := \left(1 - \frac{I_{eff.tot}}{I_{tot}}\right) = 19.377\%$$

$$k := \frac{384 \cdot E \cdot I_{tot}}{5 \cdot L^3} = 370.212\ \frac{kN}{m}$$

$$k_{eff} := \frac{384 \cdot E \cdot I_{eff.tot}}{5 \cdot L^3} = 298.478\ \frac{kN}{m}$$

SUMMARY:

t = 0.7:
- k = 185 kN/m
- keff = 114 kN/m

t = 1.05:
- k = 278 kN/m
- keff = 198 kN/m

t = 1.4:
- k = 370 kN/m
- keff = 298 kN/m

DEPARTMENT OF ARCHITECTURE AND
CIVIL ENGINEERING
CHALMERS UNIVERSITY OF TECHNOLOGY
Gothenburg, Sweden 2025
www.chalmers.se

CHALMERS
UNIVERSITY OF TECHNOLOGY